University of Strathclyde
Department of Mechanical and Aerospace Engineering

Advanced Surface Engineering: Evaluation of SprayStir

Tom Peat

A thesis submitted for the degree of Doctor of Philosophy

2018

Declaration of Authenticity and Author's Rights

This thesis is the result of the author's original research. It has been composed by the author and has not been previously submitted for examination which has led to the award of a degree

Signed:

Date:

Acknowledgements

I wish to extend my sincere thanks to my supervisor, Dr Alexander Galloway, for his continuous support and guidance throughout this PhD. I would also like to thank Dr Athanasios Toumpis for his motivation and advice. Without their tireless efforts, this PhD project would not have been possible.

My thanks to the University of Strathclyde and particularly the Mechanical and Aerospace Engineering Department for financially supporting this project through the Engineering the Future Scholarship, and for providing an engaging and inspiring environment to complete my PhD. I would especially like to thank Mr James Kelly for his advice concerning metallography and Dr Fiona Sillars for her assistance with SEM investigations.

I wish to also thank the external research partners TWI and Megastir for their generous support and technical expertise in the production of test specimens. Dr Philip McNutt, Dr Naveed Iqbal and Mr Levi Rotherham of TWI, and Mr Russell Steel of Megastir; thank you all for your invaluable contribution.

Most importantly, however, I wish to thank my parents, William and Elizabeth, and my partner, Linda, for their constant encouragement and belief.

Abstract

The objective of this study was the development of an innovative surface engineering technology, referred to as SprayStir, which combines two existing surface engineering processes; cold spray (CS) and friction stir processing (FSP). Cold spray facilitated the deposition of particle reinforced metal matrix composite (MMC) coatings, which were subsequently refined and embedded within the near-surface region of the substrate by FSP. SprayStir was employed to produce particle reinforced MMC surfaces that demonstrate superior erosion performance than that of the unreinforced substrate alloy. Throughout this study, SprayStir was applied to several coating and substrate combinations, and their respective erosion performance established through slurry erosion testing. The volume of the resulting wear scars was measured to compare the erosion performance of SprayStirred MMCs containing different particle reinforcements. Furthermore, the microstructure of the as-received substrate alloys, the cold spray deposited coatings, and the SprayStirrred MMCs were characterised to establish the influence of FSP on the distribution of the particle reinforcements within the near-surface region. Whilst the primary aim of this investigation was to enhance the erosion performance of the as-received substrate, the contribution of erosion, corrosion and synergy to the total mass loss was also measured to identify if the corrosion performance of the as-received substrate was adversely affected by the application of SprayStir. The results presented herein show that the erosion performance of the SprayStirred specimens is superior to that of the cold spray deposited coatings and the as-received substrate alloy. The improved erosion performance was attributed to the presence of fine, evenly dispersed reinforcing particles within the near-surface region that restrict the amount of material removed during the slurry erosion testing by altering the erosion mechanisms that operate on the specimen surface. The results from this investigation have therefore provided a proof of concept for the SprayStir technology when applied to the aluminium and steel substrates discussed throughout this study.

Table of Contents

Chapter 1 Thesis Introduction and Structure

1.1 Introduction

Metal Matrix Composites (MMCs) are a somewhat unique family of materials that consist of two or more constituent parts, one of which is a metal. The other constituent may be a different metal, or it may be a different material entirely, for example, aluminium oxide (Al_2O_3). Different constituents are combined as an MMC to create a new material that exhibits superior mechanical or tribological properties when compared with the unreinforced bulk metal.

MMCs have seen considerable advancement over the past four decades due to their ability to offer improved mechanical and tribological properties over unreinforced alloys [1.1–1.7]. Specifically, MMCs have been shown to demonstrate excellent resistance to erosion and corrosion, superior sliding wear performance, as well as unique electrical and thermal properties [1.1, 1.3–1.10]. Consequently, the range of industries concerned with the development of new MMCs is growing; ground transportation [1.4, 1.11–1.13], mineral extraction [1.7, 1.14, 1.15], power generation [1.5] and aerospace [1.3, 1.10, 1.12, 1.16] have all identified practical applications for MMCs due to the enhanced functional performance that they offer [1.1, 1.3–1.7]. For example, MMCs comprising boron carbide (B_4C) reinforcements are of particular interest to the nuclear industry, owing to their high absorption of neutrons in containment systems [1.5]. Equally, Al_2O_3 reinforced MMCs have been employed within the automotive industry to manufacture vehicle components such as drive shafts [1.17]. In this specific application [1.17], the MMC offers increased stiffness over aluminium and steel, while also reducing the mass of the component [1.17].

One of the primary modes of failure within the mineral extraction industry is erosion caused by micro- and macro-scale particles entrained in the fluid that is transported throughout pipeline systems [1.18–1.22]. These small particles are especially abrasive in regions where the flow is accelerated by the geometry of the pipeline or components [1.23, 1.24]. Valves also disturb the laminar flow of fluid and hence generate turbulence which enhances the abrasion (erosion) generated by these particles [1.20, 1.25]. Furthermore, emerging extraction technologies such as fracking involve injecting slurries containing sand particles under high pressure [1.26].

Under these operating conditions [1.20, 1.23–1.26], the materials that comprise the various components are exposed to a highly erosive working environment. Additionally, the combined effects of erosion and corrosion can accelerate the

removal of material and hence diminish the working life of the components [1.25]. In many instances, the components exposed to these highly erosive and corrosive slurries will be situated in inaccessible locations such as wellheads [1.20]. Consequently, there is a considerable financial cost associated with maintaining these systems [1.20, 1.27]. As such, any technologies that enhance the working life of components and reduce their ongoing maintenance costs should be of interest to this industry [1.28].

Currently, a number of surface engineering and coating technologies are employed within different industries to improve the erosion and corrosion performance of materials [1.29–1.34]. Table 1-1 presents some of these technologies and details some of their respective advantages and disadvantages. Some of these technologies will be expanded upon in Chapter 2.

Table 1-1 Overview of existing surface engineering and thermal spraying processes [1.29–1.34]

	Typical applications	Advantages	Disadvantages
Weld Cladding	Pipelines Valves	Controllability Low cost Repeatability	Limited to wire feed coatings Post heat treatment necessary
Hard Chrome Plating	Oil and gas components Automotive Machine tools Aerospace	High hardness Excellent corrosion resistance Good adhesion to the substrate	Inability to produce a comparably hard coating Limited selection of coating materials Toxicity
Flame Spraying	Bearings Shaft repairs	Equipment is portable Applicable to complex geometry	High porosity Low bond strength Inability to spray powder
Laser Cladding	Turbine repair Bearings Valves Aerospace Automotive	Low porosity Excellent bond strength Multitude of coating powders	High capital cost Highly skilled operators Poor reproducibility Low efficiency/processing speed
High Velocity Oxy-Fuel (HVOF)	Pumps and valves Impellers Gas turbine components	High hardness Chemical resistance Uniform coating thickness High deposition rate	Poor fatigue performance High capital cost Line of sight process Coating shows a tendency to chip or spall

The focus of this study is the development of an innovative surface engineering process to manufacture MMCs capable of withstanding the erosive and corrosive conditions typically encountered in systems that transport aqueous slurries such as oil and gas extraction and mining [1.7, 1.18–1.22]. However, the practical applications of this technology may also be extended to the aerospace and automotive industries. This new process aims to overcome many of the disadvantages associated with the existing technologies (Table 1-1) by embedding reinforcing particles into the surface and near-surface region of an alloy, without altering the constituent phases of the substrate or the reinforcements. To achieve this, the new process combines cold gas dynamic spraying (CS) and friction stir processing (FSP); the combination of which will be referred to as SprayStir.

CS is a solid state spraying process that is used to manufacture coatings that retain the material properties of the feedstock powder. Coating deposition is achieved by accelerating the feedstock material to a supersonic velocity using a compressible carrier gas such as nitrogen or helium [1.35]. The particles undergo extensive plastic deformation as they impact on the target surface which promotes bonding with the substrate material [1.35–1.37]. The specific bonding mechanisms that operate during CS will be discussed further in Chapter 2.

Although CS does not represent a direct replacement for all existing thermal spray and surface engineering technologies, it does possess specific advantages that make it suitable for use in certain applications. For example, unlike high temperature coating processes such as HVOF, CS avoids oxidation and the undesirable phase change of the feedstock powder [1.38, 1.39]. Additionally, the temperatures utilised during CS are suitable for spraying thermally sensitive materials such as aluminium or magnesium [1.40, 1.41]. Moreover, the lower temperatures of CS (in contrast to HVOF or Plasma Spray), prevent the development of potentially damaging residual tensile stresses within the deposited coating [1.42]. Additionally, the cold spray process is capable of generating compressive residual stresses that enhance the fatigue performance of coatings [1.43]. These key advantages are expanded upon in subsequent chapters and in the published literature [1.40–144].

FSP is a solid state surface engineering technology that makes use of a rotating tool that is plunged into the surface of a material [1.45] and subsequently traversed along a pre-defined processing path [1.46]. Contact between the shoulder of the rotating tool and the workpiece generates heat [1.47] which is sufficient to plasticise the material without causing melting [1.47]. The rotational motion forces this

softened material from the leading edge around to the rear of the tool where it is consolidated. Within the stir zone, the original grain structure of the alloy is fully recrystallised due to the frictional heat and rotational motion of the tool [1.46, 1.48–1.51]. The recrystallised grain structure within the stir zone is dissimilar to the bulk alloy and typically comprises refined equiaxed grains [1.52–1.55]. In addition to grain refinement, FSP has also been shown to remove any porosity within as-received alloy and redistribute any undesirable inclusions in the matrix [1.46, 1.56].

The first stage of SprayStir involves the deposition of an MMC coating by CS. FSP is subsequently applied to the MMC deposit to disrupt the coating-to-substrate interface and homogenise the distribution of the reinforcing particles, thereby embedding the reinforcements within the substrate. A schematic diagram of the SprayStir process is shown in Fig. 1-1.

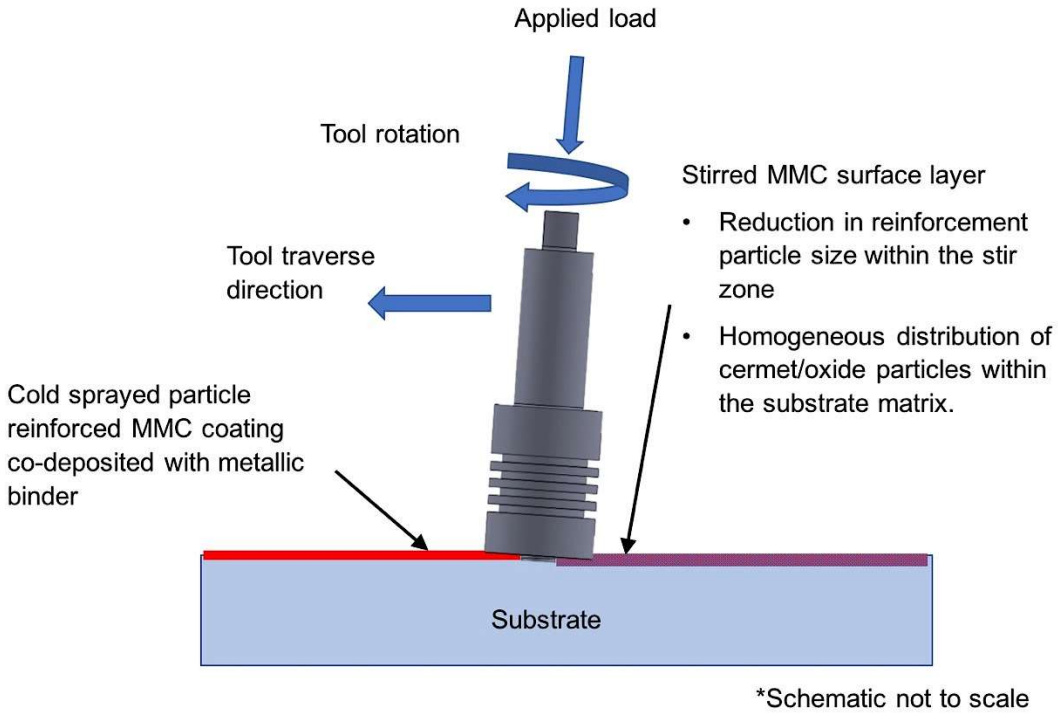

Fig. 1-1 Schematic diagram of the SprayStir process

This thesis contributes to, and advances, the existing knowledge by developing an innovative surface engineering process referred to as SprayStir, that combines two existing surface engineering techniques (CS and FSP). The erosion performance of SprayStirred specimens will be evaluated under slurry erosion test conditions. Further, the test specimens will be impinged at multiple angles of attack and, thereafter, the resulting wear scars examined to identify the different erosion mechanisms that operate on the surface of each specimen. Additionally, the

application of anodic polarisation and cathodic protection will facilitate the identification of the contributing factors of erosion, corrosion and synergy to the mass loss from each specimen. A comprehensive microstructural examination of the SprayStirred coatings will also be conducted, incorporating light optical microscopy, scanning electron microscopy, microhardness and nanoindentation.

1.2 Thesis structure

The layout of this thesis has been structured to express the successive stages completed during the development of SprayStir. Chapter 2 presents a review of several state-of-the-art surface engineering processes that are currently used within different industries to enhance the material properties of various alloys. This is followed by an overview of fundamental erosion and corrosion theory (Chapter 3), relevant to the discussion presented in later chapters. Chapter 4 outlines the various experimental examination and assessment techniques that are used in subsequent chapters to evaluate the SprayStirred specimens.

The first experimental chapter (Chapter 5), examines several High velocity oxy-fuel (HVOF) deposited coatings under slurry erosion-corrosion test conditions. This study (Chapter 5) has been included in the thesis to highlight the different erosion mechanisms that operate at different angles of impingement, on a surface manufactured using a process that is currently used within industry to combat the effects of erosion and corrosion. Furthermore, the erosion data from the HVOF coatings will identify specific coating materials that exhibit enhanced erosion performance and will provide a benchmark with which to measure the erosion performance of the SprayStirred specimens.

Chapter 6 presents the results of a preliminary investigation into combined CS and FSP. This study incorporates several different coating and substrate combinations to assess whether it is feasible to embed reinforcing particles within a substrate matrix. Furthermore, a microstructural examination of the SprayStirred specimens was conducted to confirm the presence of reinforcements within the matrix and assess their distribution throughout the surface and near-surface region.

Based on the results from Chapter 6, the breadth of substrate and reinforcement materials was consolidated in Chapter 7. However, the range of examination and assessment methods employed to evaluate the SprayStirred specimens was significantly increased. Furthermore, Chapter 7 reports on the development of an

innovative co-deposition technique to CS reinforcement particles with a ductile binder to enhance the quantity of material deposited on the surface of the substrate.

The final experimental chapter (Chapter 8) discusses the transition of the SprayStir process from aluminium substrates to steel. This includes the development of suitable CS parameters to successfully co-deposit the reinforcing particles and AISI 316 binder particles. Chapter 8 presents the results from an erosion-corrosion study to measure the contribution of erosion, corrosion and synergy to the mass loss from each specimen. This chapter also expands on the range of analysis methods used to evaluate the microstructure of the SprayStirred specimens.

Chapter 9 summarises the key findings from each of the preceding chapters and indicates some limitations of the present research. Some areas where further work could be useful in advancing the SprayStir technology have been suggested. The research from this project was disseminated through several high impact factor journal publications and conference proceedings. A complete list of published journal articles and conference proceedings is included as an appendix (Appendix A).

1.3 References

[1.1] D.B. Miracle, Metal matrix composites - From science to technological significance, Compos. Sci. Technol. 65 (2005) 2526–2540.

[1.2] T.W. Clyne, P.J. Withers, An Introduction to Metal Matrix Composites, Cambridge University Press, 1993.

[1.3] D. Miracle, Metallic Composites in Space: A Status Report, J. Miner. Met. Mater. Soc. (2001) 2001.

[1.4] N. Chawla, K.K. Chawla, Metal-Matrix Composites in Ground Transportation, J. Miner. Met. Mater. Soc. (2016) 1–5.

[1.5] C.J. Beidler, W.E. Hauth, A. Goel, Development of a B4C/Al Cermet for Use as an Improved Structural Neutron Absorber, J. Test. Eval. 20 (1992) 67–70.

[1.6] M.N. Rittner, Expanding World Markets for MMCs, J. Miner. Met. Mater. Soc. (2004) 6855.

[1.7] A. Neville, F. Reza, S. Chiovelli, T. Revega, Assessing metal matrix composites for corrosion and erosion-corrosion applications in the oil sands industry, J. Sci. Eng. 62 (2006) 657–675.

[1.8] L. Liu, J. Xu, A study of the erosion-corrosion behaviour of nano-Cr2O 3 particles reinforced Ni-based composite alloying layer in aqueous slurry environment, Vacuum. 85 (2011) 687–700.

[1.9] E.J. Wentzel, C. Allen, Erosion-corrosion resistance of tungsten carbide hard metals with different binder compositions, Wear. 181–183 (1995) 63–69.

[1.10] E. Pagounis, V. Lindroos, Processing and properties of particulate reinforced steel matrix composites, Mater. Sci. Eng. A. 246 (1998) 221–234.

[1.11] A. Vencl, A. Rac, I. Bobic, Tribological behaviour of Al-based MMCs and their applications in automotive industry, Tribol. Ind. 26 (2004) 31–38.

[1.12] J.W. Kaczmar, K. Pietrzak, W. Włosiński, The production and application of metal matrix composite materials, J. Mater. Process. Technol. 106 (2000) 58–67.

[1.13] S. V. Prasad, R. Asthana, Aluminum metal-matrix composites for automotive applications: Tribological considerations, Tribol. Lett. 17 (2004) 445–453.
[1.14] A. Neville, F. Reza, S. Chiovelli, T. Revega, Erosion-corrosion behaviour of WC-based MMCs in liquid-solid slurries, Wear. 259 (2005) 181–195.
[1.15] W.H. Kan, Z.J. Ye, Y. Zhu, V.K. Bhatia, K. Dolman, T. Lucey, et al., Fabrication and characterization of microstructure of stainless steel matrix composites containing up to 25 vol% NbC, Mater. Charact. 119 (2016) 65–74.
[1.16] S. Rawal, Metal-matrix composites for space applications, J. Mater. 53 (2001) 14–17.
[1.17] W.H. Hunt, D.R. Herling, Aluminum Metal Matrix Composites, Adv. Mater. Process. 162 (2004) 39–42.
[1.18] N. Barton, Erosion in elbows in hydrocarbon production systems: Review document, Heal. Saf. Exec. TUV NEL Limited, Glas. (2003).
[1.19] M. Parsi, K. Najmi, F. Najafifard, S. Hassani, B.S. McLaury, S.A. Shirazi, A comprehensive review of solid particle erosion modeling for oil and gas wells and pipelines applications, J. Nat. Gas Sci. Eng. 21 (2014) 850–873.
[1.20] L. Nøkleberg, T. Søntvedt, Erosion in choke valves-oil and gas industry applications, Wear. 186–187 (1995) 401–412.
[1.21] X. Hu, R. Barker, A. Neville, A. Gnanavelu, Case study on erosion-corrosion degradation of pipework located on an offshore oil and gas facility, Wear. 271 (2011) 1295–1301.
[1.22] K. Jordan, Erosion in multiphase production of oil and gas, Corrosion. (1998).
[1.23] J. Postlethwaite, S. Nesic, Erosion in Disturbed Liquid/Particle Pipe Flow: Effects of Flow Geometry and Particle Surface Roughness, Corrosion. 49 (1993) 850–857.
[1.24] J.R. Shadley, S.A. Shirazi, E. Dayalan, M. Ismail, E.F. Rybicki, Erosion-Corrosion of a Carbon Steel Elbow in a Carbon Dioxide Environment, Corrosion. 52 (1996) 714–723.
[1.25] R.J.K. Wood, Erosion-corrosion interactions and their effect on marine and offshore materials, Wear. 261 (2006) 1012–1023.
[1.26] H.R. Nasriani, M. Jamiolahmady, Maximizing fracture productivity in unconventional fields; analysis of post hydraulic fracturing flowback cleanup, J. Nat. Gas Sci. Eng. 52 (2018).
[1.27] L. Popoola, A. Grema, G. Latinwo, B. Gutti, A. Balogun, Corrosion problems during oil and gas production and its mitigation, Int. J. Ind. Chem. 4 (2013) 35.
[1.28] Frazer-Nash Consultancy, Case study: Sand erosion – understanding the risks, 2013.
[1.29] B.G. Mellor, Surface coatings for protection against wear, Woodhead Publishing Limited, 2006.
[1.30] P.L. Fauchais, J.V.R. Heberlein, M.I. Boulos, Thermal Spray Fundamentals, 2014.
[1.31] T.S. Sidhu, S. Prakash, State of the Art of HVOF Coating Investigations — A Review, Mar. Technol. Soc. J. 39 (2005) 53–64.
[1.32] L. Pawlowski, The Science and Engineering of Thermal Spray Coatings, 2008.
[1.33] G.A. Lausmann, Electrolytically deposited hardchrome, Surf. Coatings Technol. 86–87 (1996) 814–820.
[1.34] A. Gholipour, M. Shamanian, F. Ashrafizadeh, Microstructure and wear behavior of stellite 6 cladding on 17-4 PH stainless steel, J. Alloys Compd. 509 (2011) 4905–4909.
[1.35] V.K. Champagne, The cold spray materials deposition process:

fundamentals and applications, Woodhead Publishing, 2007.
[1.36] A. Papyrin, V. Kosarev, S. Klinkov, A. Alkhimov, V. Fomin, Cold Spray Technology, Elsevier, 2006.
[1.37] H. Assadi, F. Gärtner, T. Stoltenhoff, H. Kreye, Bonding mechanism in cold gas spraying, Acta Mater. 51 (2003) 4379–4394.
[1.38] D. Toma, W. Brandl, G. Marginean, Wear and corrosion behaviour of thermally sprayed cermet coatings, Surf. Coat. Technol. (2001) 149–158.
[1.39] D.K. Goyal, H. Singh, H. Kumar, V. Sahni, Slurry erosion behaviour of HVOF sprayed WC-10Co-4Cr and Al 2O 3+13TiO 2 coatings on a turbine steel, Wear. 289 (2012) 46–57.
[1.40] Y. Xiong, M.X. Zhang, The effect of cold sprayed coatings on the mechanical properties of AZ91D magnesium alloys, Surf. Coatings Technol. 253 (2014) 89–95.
[1.41] R.N. Raoelison, C. Verdy, H. Liao, Cold gas dynamic spray additive manufacturing today: Deposit possibilities, technological solutions and viable applications, Mater. Des. 133 (2017) 266–287.
[1.42] U. Selvadurai, P. Hollingsworth, I. Baumann, B. Hussong, W. Tillmann, S. Rausch, et al., Influence of the handling parameters on residual stresses of HVOF-sprayed WC-12Co coatings, Surf. Coatings Technol. 268 (2014) 30–35.
[1.43] G. Shayegan, H. Mahmoudi, R. Ghelichi, J. Villafuerte, J. Wang, M. Guagliano, et al., Residual stress induced by cold spray coating of magnesium AZ31B extrusion, Mater. Des. 60 (2014) 72–84.
[1.44] V. Luzin, K. Spencer, M.X. Zhang, Residual stress and thermo-mechanical properties of cold spray metal coatings, Acta Mater. 59 (2011) 1259–1270.
[1.45] J.D. Escobar, E. Velásquez, T.F. a Santos, a. J. Ramirez, D. López, Improvement of cavitation erosion resistance of a duplex stainless steel through friction stir processing (FSP), Wear. 297 (2013) 998–1005.
[1.46] R. Miranda, J. Gandra, P. Vilaca, L. Quintino, T. Santos, Surface Modification by Solid State Processing, Woodhead Publishing Limited, 2008.
[1.47] R.S. Mishra, M.W. Mahoney, Friction stir welding and processing, Mater. Sci. Eng. R Reports. 50 (2007) 360.
[1.48] K. Nakata, Y.G. Kim, H. Fujii, T. Tsumura, T. Komazaki, Improvement of mechanical properties of aluminum die casting alloy by multi-pass friction stir processing, Mater. Sci. Eng. A. 437 (2006) 274–280.
[1.49] C. Lorenzo-Martin, O.O. Ajayi, Rapid surface hardening and enhanced tribological performance of 4140 steel by friction stir processing, Wear. 332–333 (2015) 962–970.
[1.50] S. Mukherjee, A. K. Ghosh, Friction stir processing of direct metal deposited copper-nickel 70/30, Mater. Sci. Eng. A. 528 (2011) 3289–3294.
[1.51] C.I. Chang, X.H. Du, J.C. Huang, Achieving ultrafine grain size in Mg-Al-Zn alloy by friction stir processing, Scr. Mater. 57 (2007) 209–212.
[1.52] R.S. Mishra, M.W. Mahoney, Friction stir welding and processing, Mater. Sci. Eng. R Reports. 50 (2007) 360.
[1.53] D. Yadav, R. Bauri, Effect of friction stir processing on microstructure and mechanical properties of aluminium, Mater. Sci. Eng. A. 539 (2012) 85–92.
[1.54] H.S. Grewal, H.S. Arora, H. Singh, a. Agrawal, Surface modification of hydroturbine steel using friction stir processing, Appl. Surf. Sci. 268 (2013) 547–555.
[1.55] P. Xue, B.L. Xiao, Z.Y. Ma, Achieving ultrafine-grained structure in a pure nickel by friction stir processing with additional cooling, 56 (2014) 848–851.
[1.56] V. Sharma, U. Prakash, B.V.M. Kumar, Surface Composites by Friction Stir Processing: A Review, J. Mater. Process. Technol. 224 (2015) 117–134.

Chapter 2 A Review of Current Surface Engineering Processes

2.1 Introduction

The degradation of metals, when exposed to aqueous slurry, presents challenges for engineers when calculating the expected operational life of components [2.1–2.5]. To combat material degradation, several surface engineering technologies have been developed to enhance the erosion, wear or corrosion performance of metals [2.5–2.11]. This chapter provides an overview of the various processes that are currently employed to increase the operational life of components when subjected to erosive and corrosive operating environments. Later chapters will discuss specific aspects of the individual processes when necessary and elaborate on state-of-the-art research within the existing literature.

In this chapter, Section 2.2 and Section 2.3 provide a review of friction stir processing (FSP) and cold spray (CS). Section 2.4 discusses alternative thermal spray technologies. Surface engineering is defined as the modification of the surface and near-surface regions to enhance specific metallurgical properties over those of the bulk material [2.6, 2.12–2.14]. These properties can be improved mechanically [2.15, 2.16], chemically [2.17, 2.18], or through the deposition of appropriate coating materials [2.6, 2.7, 2.19–2.21]. In this study, the primary aim is to enhance the erosion performance of the as-received alloy. However, surface engineering can also be used to improve the corrosion, electrical, mechanical, wear and thermal performance of materials [2.5–2.11, 2.14, 2.20].

2.2 Friction Stir Processing

FSP is a solid state surface engineering process that has been developed by adapting the concepts of a solid state joining method known as friction stir welding (FSW) [2.22]. The fundamental principles of FSP are discussed in this section, while information relating to the specific processing parameters used throughout this study will be presented in Chapter 3.

2.2.1 Overview of FSP

FSP makes use of a rotating tool that is plunged into a material [2.15] and subsequently traversed along a pre-defined processing path [2.23]. Contact between the shoulder of the rotating tool and the workpiece generates heat [2.24]. While the

amount of heat is not enough to melt the substrate, it is sufficient to plasticise the material beneath the shoulder [2.24]. The rotational motion of the tool forces the softened material from the leading edge around to the rear of the tool where it is consolidated. Fig. 2-1 shows a schematic diagram of the FSP process [2.25].

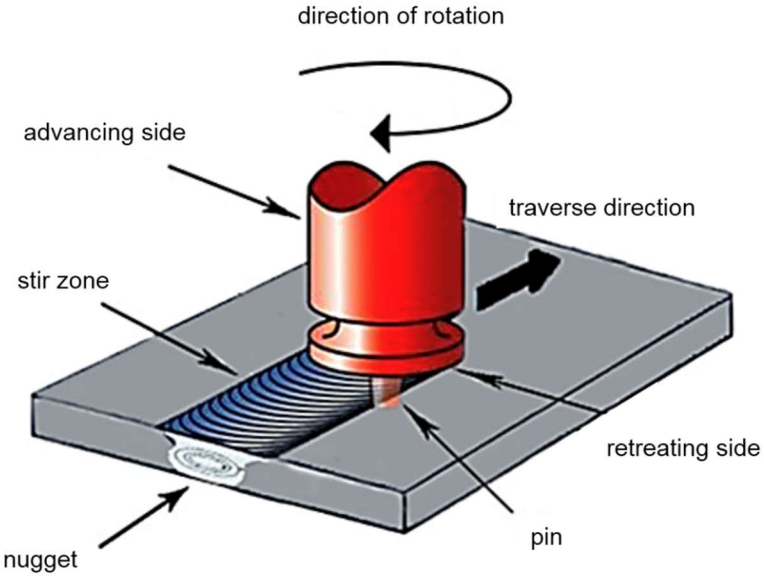

Fig. 2-1 Schematic diagram of the FSP process [2.25]

The FSP process is analogous to forging and typically produces a refined grain structure in the centre of the stir zone [2.16, 2.23, 2.26–2.28]. As an example, Mukherjee and Ghosh [2.16] showed that the application of FSP resulted in complete recrystallisation of the elongated grain structure of the as-received copper-nickel substrate. The authors [2.16] established that the average grain size of the FSPed alloy was approximately 2.5 μm following the application of FSP. Similarly, Chang et al. [2.28] successfully reduced the grain size of Mg-Al-Zn alloy from 75 μm to 0.1 – 0.3 μm with a single FSP pass.

Fig. 2-2 presents a schematic diagram highlighting the change in grain structure as the distance from the centre of the stir zone increases [2.29]. In the region located directly beneath the shoulder, the original grain structure has fully recrystallised due to the frictional heat and rotational motion of the tool [2.16, 2.23, 2.26–2.28]. The recrystallised microstructure typically contains fine, equiaxed grains that are significantly smaller than those present in the bulk alloy [2.22]. This region is commonly referred to as the nugget [2.22].

Outwith the fully recrystallised zone (nugget), the original grain structure of the bulk alloy has been modified; however, complete recrystallisation does not take place

due to insufficient strain [2.30]. This region is referred to as the thermo-mechanically affected zone (TMAZ) [2.30]. Here, the rotational motion of the tool severely deforms the as-received grain structure and often results in an elongated microstructure post-FSP [2.23]. Further, from the weld nugget, the rotating tool does not mechanically affect the microstructure of the parent material. However, depending on the specific grade of alloy being processed, the heat generated within the stir zone is sufficient to cause grain growth, resulting in a heat affected zone (HAZ) that is situated between the as-received parent material and the TMAZ [2.29].

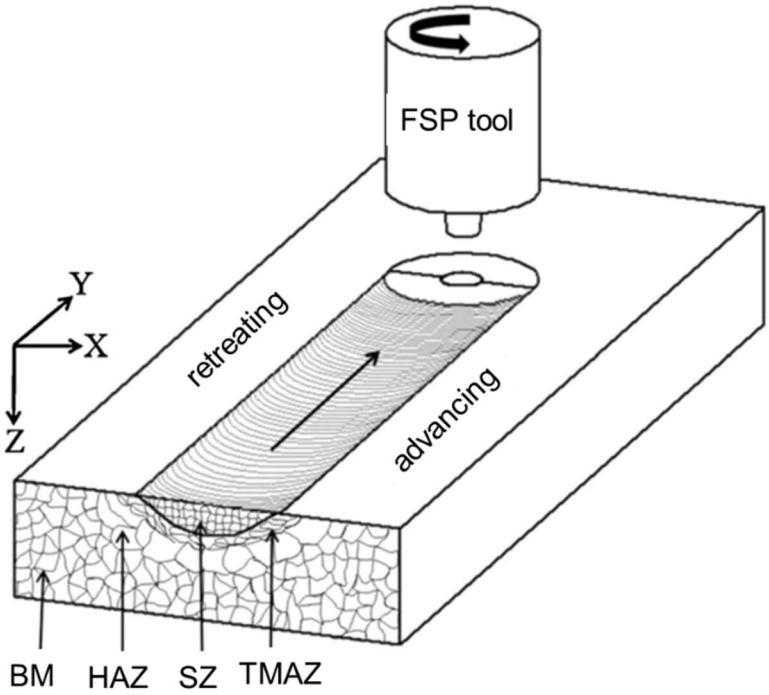

Fig. 2-2 Schematic diagram highlighting the change in microstructure with proximity to the centre of the stir zone [2.29]

Researchers [2.31–2.38] examining the microstructural and mechanical properties of FSP specimens noted that the stir zone demonstrated enhanced mechanical properties over the bulk alloy. For the most part, these studies [2.31–2.38] concluded that the enhanced mechanical properties were a consequence of the refined grain structure in the stir zone.

The mechanism by which grain refinement occurs during FSP was characterised by J Su et al. [2.39]. The authors [2.39] proposed that microstructural modification occurs when nanocrystalline grains form around the probe at the leading edge of the tool, and at the contact surface between the plate and the shoulder. The high temperatures at the contact surfaces encourage dynamic nucleation and

movement of the individual grain boundaries [2.39]. Exposure to the elevated temperatures in the stir zone promotes the growth of the recrystallised grains. Furthermore, the plastic deformation of the softened material generates additional dislocations within larger grains [2.39]. Dynamic recovery subsequently occurs in the grains containing high dislocation density [2.39].

In addition to grain refinement, FSP has been shown to homogenise the distribution of inclusions in the matrix and remove any porosity produced as a by-product of the original manufacturing processes [2.35]. Moreover, Bauri et al. [2.35] highlighted the ability of FSP to homogenise the distribution of titanium carbide (TiC) particles and completely remove casting defects in TiC reinforced aluminium.

Given the localised nature of the FSP process, another advantage it presents over other solid state deformation processes (rolling, extruding, cold working) is that it can be applied to discreet surface areas [2.40]. One potential industrial application of this process could be the modification of the leading edge of turbine blades [40]. Equally, FSP could also be applied to discrete sections of valve bodies in pipelines that transport erosive slurry. The FSP tool and spindle can be attached to a robotic control arm, to facilitate the application of FSP to complex geometries [2.41, 2.42]. Finally, the refined microstructure generated by FSP can be replicated over large surface areas using multiple overlapping FSP passes [2.43].

2.2.2 Influence of tool design on FSP

The FSP tool consists of two main components, the probe (also known as the pin) and the shoulder (Fig. 2-3). The probe is the first point of contact with the workpiece and is responsible for generating heat during the plunge stage [2.44]. Additionally, the probe promotes horizontal stirring and, with the addition of features such as threads, vertical mixing of the material, i.e. from the root of the stir zone to the top surface [2.44], which is essential for the production of a consolidated, pore-free stir zone [2.44]. Incorporating features on the probe can significantly enhance the mixing of material regardless of the total probe length [2.44]. For instance, the “WholrI” probe incorporates either a cylindrical or tapered probe that features threads around its circumference to encourage the vertical mixing of the plasticised material [44]. The presence of threads on the probe also enhances the distribution of oxides and impurities in the stir zone [2.35, 2.44]. However, numerous other tool designs have been manufactured for the processing or welding of specific alloys that incorporate various probe and shoulder geometries [2.44].

Friction between the shoulder of the tool (Fig. 2-3) and the workpiece generates the necessary heat to plasticise the metal [2.22]. However, the geometry of the shoulder is also designed to prevent the softened material from being ejected from the stir zone [2.44]. A concave shoulder encourages the plasticised material to flow into the centre of the stir zone and, in doing so, is prevented from being ejected as flash [2.44]. Moreover, the forging action is enhanced as more material is pushed into the centre where it is forced around to the rear of the tool and consolidated [2.23]. Equally, the addition of scrolls or grooves on a flat shoulder can encourage the movement of plasticised material to the centre of the stir zone [2.44]. A concave design is typically employed in instances where a tilt angle is applied, whereas scrolled shoulder designs feature more commonly in cases where no tilt is applied to the tool [2.44].

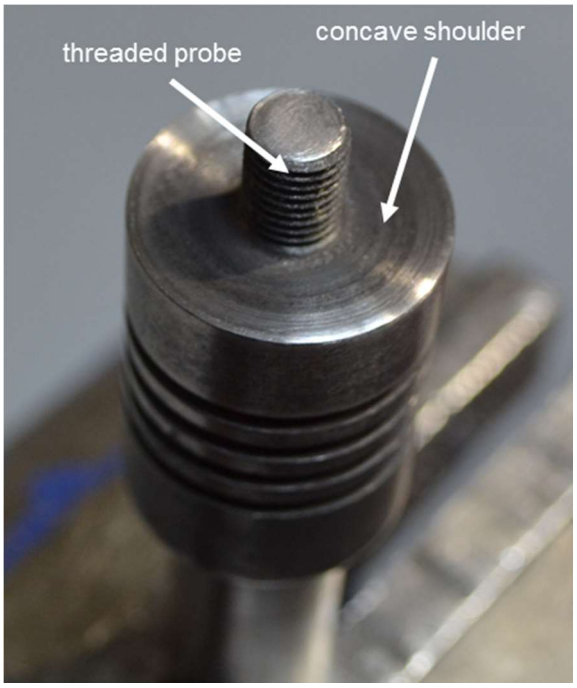

Fig. 2-3 FSP tool with concave shoulder and threaded probe

2.2.3 Heat generation

During FSP, the temperature in the stir zone reaches approximately 80% - 90% of the melting point of the material [2.45]. The source of the heat is contact between the tool shoulder and the workpiece, which is dictated by the friction coefficient between the two surfaces [2.46, 2.47]. Contact between the surface of the probe and the workpiece also generates heat. However, the smaller surface area of the probe leads to this being only a small fraction of the total heat produced [2.24,

2.47]. The plastic deformation of the metal generates additional heat; however, this also accounts for only a small proportion of the total heat produced [2.24].

As the generated heat dissipates into the material, it softens. Consequently, the tool is able to force this softened material around to the rear of the stir zone to form a consolidated processed region (stir zone) [2.24]. As the temperature of the metal increases, the torque force required to move material around to the rear of the tool decreases. Hence, the greatest torque is generated during the plunge stage [2.48]. Thereafter, the temperature of the stir zone plateaus and the torque drops correspondingly to an equilibrium level during the traverse [2.48].

2.2.4 Material flow

The movement of plasticised material within the stir zone is a highly complex process that is directed by the mechanical forces and thermal energy generated by the tool [2.24, 2.44]. Within the published literature [2.49–2.52], there is a wide variety of numerical and experimental techniques employed to assess the flow of material in FSP. These studies [2.49–2.52] confirm that the rotational motion of the tool causes the material on one side of the stir zone to move in the same direction as the tool traverse path (advancing side), while the material on the other side moves in the opposite direction (retreating side) [2.48].

The advancing and retreating sides can be on either the right- or left-hand side of the stir zone (when observing a cross-section of the stir zone) depending on the rotational direction of the tool. Considering the difference in the relative motion of the tool, with respect to the direction of traverse, the thermal and mechanical forces present on each side of the stir zone will be different [2.15]. The dissimilarity in these thermo-mechanical forces gives rise to the asymmetric microstructural features within the resulting stir zone [2.15, 2.49–2.52].

2.3 Cold Spray

2.3.1 Cold spray process overview

Cold spray (CS), also known as cold gas dynamic spraying or kinetic spraying [2.19], is a solid state spraying process in which powder feedstock material is accelerated to a supersonic velocity, ranging from 300 m/s to 1000 m/s [2.53], and impinged onto a target surface (substrate) [2.54–2.57]. Upon contact with the target surface, the feedstock particles undergo severe plastic deformation, and in doing so,

mechanically bond to the substrate [2.58]. Multiple layers are deposited to manufacture thick, well-adhered coatings.

The particles are accelerated using a compressible carrier gas such as nitrogen or helium, passed through a de-Laval nozzle [2.54, 2.57]. A de-Laval nozzle comprises a converging and a diverging section, with the area between the two known as the throat (location of the minimum cross-sectional area) [2.59]. A schematic diagram of a de-Laval nozzle is presented in Fig. 2-4.

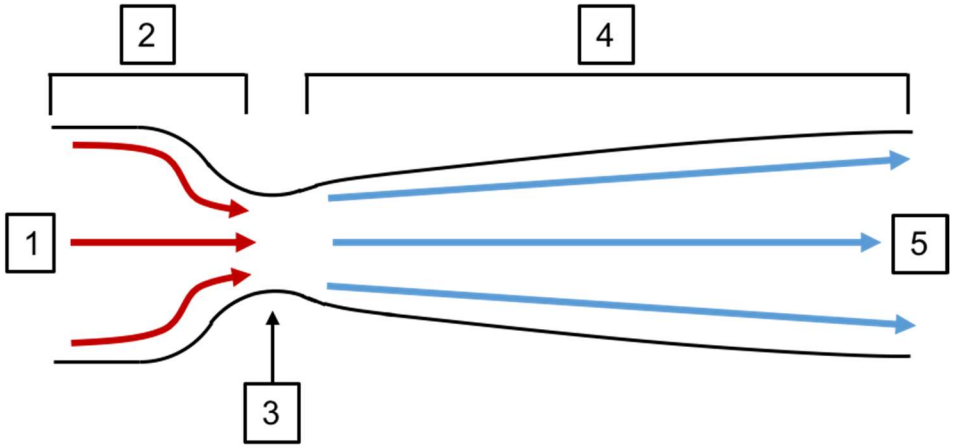

Fig. 2-4 Schematic diagram of a de-Laval nozzle; (1) high pressure, subsonic velocity inlet, (2) converging section, (3) nozzle throat, (4) diverging section, (5) low pressure, supersonic velocity outlet

To achieve sufficient particle velocity, the carrier gas is pressurised and heated to temperatures up to 800°C before entering the nozzle [2.58]. The feedstock powder is introduced into the carrier gas stream using injectors located in the nozzle [2.60]. The powder particles are accelerated as the hot, pressurised gas expands through the converging-diverging nozzle.

The temperature of the carrier gas is increased to facilitate greater particle velocity at the nozzle exit, not to cause melting of the feedstock powder [2.57]. Minimal contact time with the hot gas ensures that the particles do not melt in the jet stream [2.57]. This is in contrast to thermal spraying processes, such as high velocity oxy-fuel (HVOF), in which the feedstock particles are molten (or partially-melted) during deposition [2.61–2.63]. The comparably low temperatures of the cold spray process are not sufficient to induce a phase change in the powder particles [2.54, 2.55]. Thus, the production of brittle phases that can compromise the quality and integrity of the coating is prevented. One example of an undesirable phase change is the formation of W_2C in HVOF sprayed WC-Co coatings [2.64].

The low temperature of the powder also inhibits oxidation of the particles while in the gas stream [2.63]. As such, thermally sensitive materials such as aluminium or magnesium [2.57, 2.65, 2.66] can be deposited without the risk of coating degradation. Furthermore, the absence of any flame or plasma at the cold spray nozzle outlet significantly reduces any thermal input to the substrate, thus preventing any microstructural changes therein [2.65].

The severe plastic deformation of the CS deposited particles at the point of impact with the substrate (or previously deposited material) generates a work hardening (strain hardening) within the flattened particle [2.67]. The particle deformation produces an elongated grain structure, accompanied by an associated build-up of dislocations, thus resulting in this work hardening [2.67, 2.68]. Additionally, the impinging solid state particles impart further deformation, and hence work hardening, into the previously deposited particles through a shot peening effect [2.69–2.73]. This shot-peening effect reduces porosity and generates compressive residual stresses within the coating [2.69, 2.70], and therefore gives rise to improved fatigue performance over thermal spray processes [2.74].

Particles that directly impact the surface of the substrate, and hence experience particularly extensive plastic deformation, exhibit a refined grain structure when compared with the as-received feedstock material [2.68]. Fig. 2-5 presents a schematic diagram depicting the recrystallization of a single particle based on adiabatic shear instability [2.75] and dynamic recrystallization [2.63, 2.76, 2.77].

At the point of impact, shear stresses develop and deform the impinging particle. Depending on the hardness of the substrate and particle, the substrate may also experience deformation when impinged. Adiabatic shear instability occurs, resulting in the significant flattening of the particle and associated material jetting (Fig. 2-6). The particle deformation causes a build-up of dislocations that form elongated subgrains [2.68]. If the strain and temperature (caused by viscous flow) are sufficient, the sub-grains are recrystallised, thus generating a refined microstructure. Similar examples of grain refinement at the particle-to-substrate interface have been reported by two research groups that examined the microstructure of copper particles following impact with the substrate [2.78, 2.79]. Both research groups attributed the recrystallization to the high strain rate deformation of the copper particles at the point of impact [2.80, 2.81].

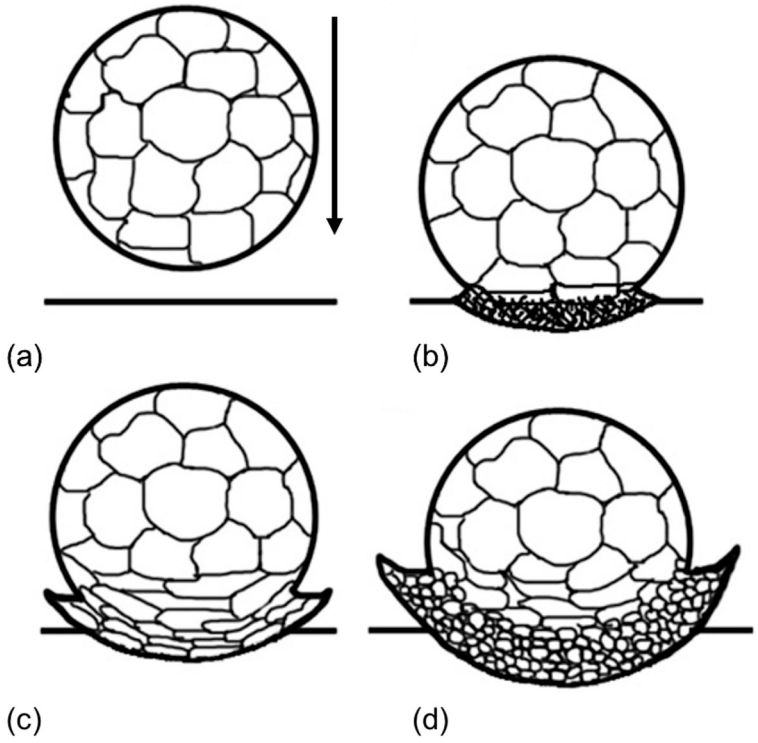

Fig. 2-5 Schematic diagram depicting grain refinement by dynamic recrystallisation; (a) impinging particle before impact; (b) dislocation build-up; (c) development of dislocation cells and re-elongation; (d) recrystallisation of sub-grains by the thermal softening effect [2.68]

2.3.2 Bonding mechanism in cold spray

Two distinct bonding mechanisms have been proposed for the CS process. The first is related to adiabatic shear instabilities that exist at the coating-to-substrate interface that yield direct metal-to-metal contact between the particle and substrate (or previously deposited material) [2.82, 2.83]. The second mechanism is the mechanical interlocking of the particles to the substrate through the production of a jet of highly strained material at the periphery of the impinged material (Fig. 2-5) [2.84].

One of the first investigations to assess the interaction between an impinging particle and the substrate was carried out by Assadi et al. [2.75], who examined the deformation of a copper particle when brought into contact with a copper substrate. The work was later expanded upon by Grujicic et al. [2.65], who employed the same approach as Assadi's group [2.75] to several different material combinations. Both research groups [2.65, 2.75] concluded that the bonding mechanism is ascribed to adiabatic shear instabilities [2.85] which occur at the particle/substrate or particle/particle interface. The kinetic energy of the particles is transferred to thermal

energy at the point of impact [2.65]. This thermal energy softens the particles, thereby enabling them to plastically deform [2.65].

The particle-to-substrate interface was also examined experimentally by several research groups [2.56, 2.58, 2.85–2.87] who identified that material bonding (either particle/substrate or particle/previously deposited material) is achieved through the direct metal-to-metal interaction between the two surfaces, combined with the significant pressure generated at the point of contact [2.87]. The first layer of particles to impinge on the substrate, create craters on the target surface that removes the oxide layer [2.83]. The resulting direct metal-to-metal contact between the two surfaces, combined with significant pressure generates a metallurgical bond between the particle and substrate (or previously deposited particle) [2.58, 2.84, 2.86–2.90]. Chen et al. [2.84] reported the presence of a “jet” of material at the periphery of the deposited particle caused by high strain rate deformation upon contact with the substrate [2.65, 2.87]. Fig. 2-6 provides a schematic representation of the jet phenomenon and Fig. 2-7 shows a micrograph of a single copper particle on the surface of an aluminium substrate, illustrating the jet of material at the periphery of the deformed particle [2.75].

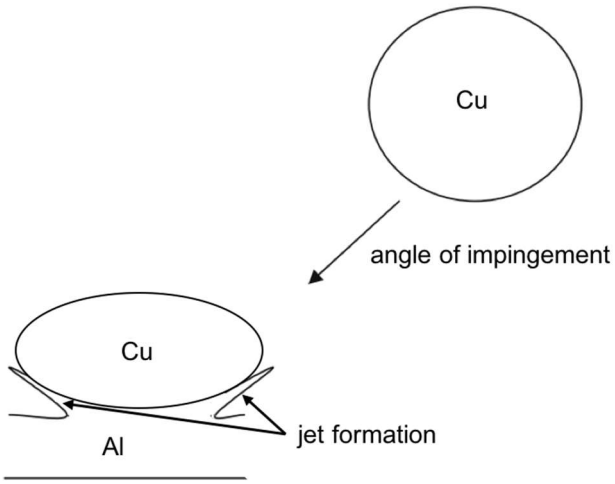

Fig. 2-6 Schematic illustration of the jet formation on an aluminium substrate by an impinging copper particle [2.83]

By examining the interface between the deposited particle and the substrate, Hussain et al. [2.83] proposed that the jet of thinned material, produced by the impinged particle, causes small lips to be produced on the substrate that partially envelope subsequent impinging particles. The authors [2.83] described this phenomenon as “interlocking”. This interlocking provides a mechanical join between

the substrate and the deposited powder particles. The authors [2.83] confirmed mechanical interlocking had occurred by inspecting specimens that had been subjected to coating adhesion testing [2.83]. Examination of the fracture surfaces revealed remnants of the substrate alloy located around the periphery of the deposited particles [2.83].

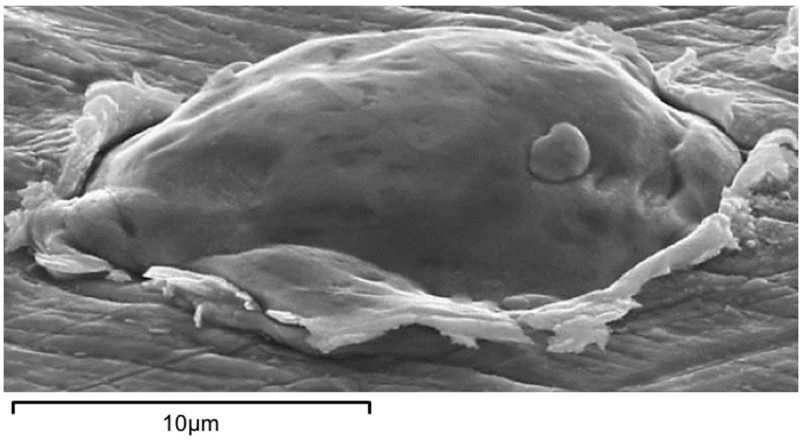

Fig. 2-7 Scanning electron micrographs (secondary electron mode) of a copper particle on a copper substrate, showing the jet formation at the periphery of the particle [2.75]

In summary, the bonding of the cold spray coating to the substrate alloy features two distinct mechanisms. The first is a metallurgical bond that is created by the metal-to-metal contact between substrate and deposit in the jet region [2.58, 2.86, 2.87]. The second mechanism is mechanical interlocking between the powder particles and previously deposited material [2.83]. The contribution of each mechanism to the total adhesive (and cohesive) strength of the coating is dictated by the particular combination of powder and substrate [2.54, 2.89]. While the coating-to-substrate interaction is not the primary area of investigation in this study, it is important to identify the different bonding mechanisms to elucidate the successful (or unsuccessful) deposition of the different powder/substrate combinations examined in later chapters.

2.3.3 Critical velocity of the powder particles

The metal-to-metal contact discussed in Section 2.3.2 is achieved through plastic deformation of the feedstock powder particles and the substrate [84]. However, at the point of impact, different materials will deform to a greater or lesser extent depending on their specific material properties [2.91, 2.92]. For example, titanium particles must be accelerated to greater velocities, in contrast to aluminium particles, to achieve deposition [2.91]. Therefore, the necessary level of plastic deformation

required for the particle to adhere to the target surface will be generated by exceeding a specific particle velocity, unique to each material [91]. The minimum velocity at which the feedstock powder particles must be travelling to adhere to the substrate is known as the critical velocity (V_{crit}) [2.58]. Failure to achieve V_{crit} results in the sprayed material abrading and rebounding from the surface in a similar manner to grit blasting [2.92]. The coating process begins when the velocity of the particles approaches V_{crit}, and by increasing the particle velocity above V_{crit} the deposition rate increases, i.e. the number of impinging particles that adhere to the surface.

Fig. 2-8 illustrates the influence of particle velocity on the deposition rate of an aluminium feedstock powder on a polished copper substrate [2.58]. The micrographs show that no aluminium particles are deposited on the substrate when impinged at 730 m/s (Fig. 2-8a). When the particle velocity is increased to 750 m/s (Fig. 2-8b) some of the impinging particles have rebounded from the surface, as is denoted by the presence of impact craters on the surface (Fig. 2-8b) and some have adhered (Fig. 2-8b). Therefore, for these specific conditions, 750 m/s is the velocity at which CS transitioned from an erosion process to a deposition process and hence, 750 m/s corresponds to V_{crit} [2.58]. Fig. 2-8c indicates that as the particle velocity is increased beyond V_{crit} (to approximately 850 m/s), the number of particles that are successfully deposited on the substrate increases [2.58].

Existing research [2.57, 2.58, 2.93, 2.94] confirms that V_{crit} depends on multiple factors and not simply on the metallurgical properties of the substrate material or the feedstock powder. For example, using the same processing parameters employed to produce the specimen depicted in Fig. 2-8c, Fig. 2-9 shows that the number of aluminium particles deposited on the surface increases when the substrate is grit blasted prior to spraying [2.58]. Correspondingly, the V_{crit} at which point the erosion process shifts to deposition will be lower [2.58]. Moreover, Stoltenhoff et al. [2.57] demonstrated that the deposition efficiency (powder sprayed vs. powder deposited on the substrate) of a copper feedstock powder deposited on aluminium increased linearly with gas temperature, for a constant gas pressure of 2.5 MPa.

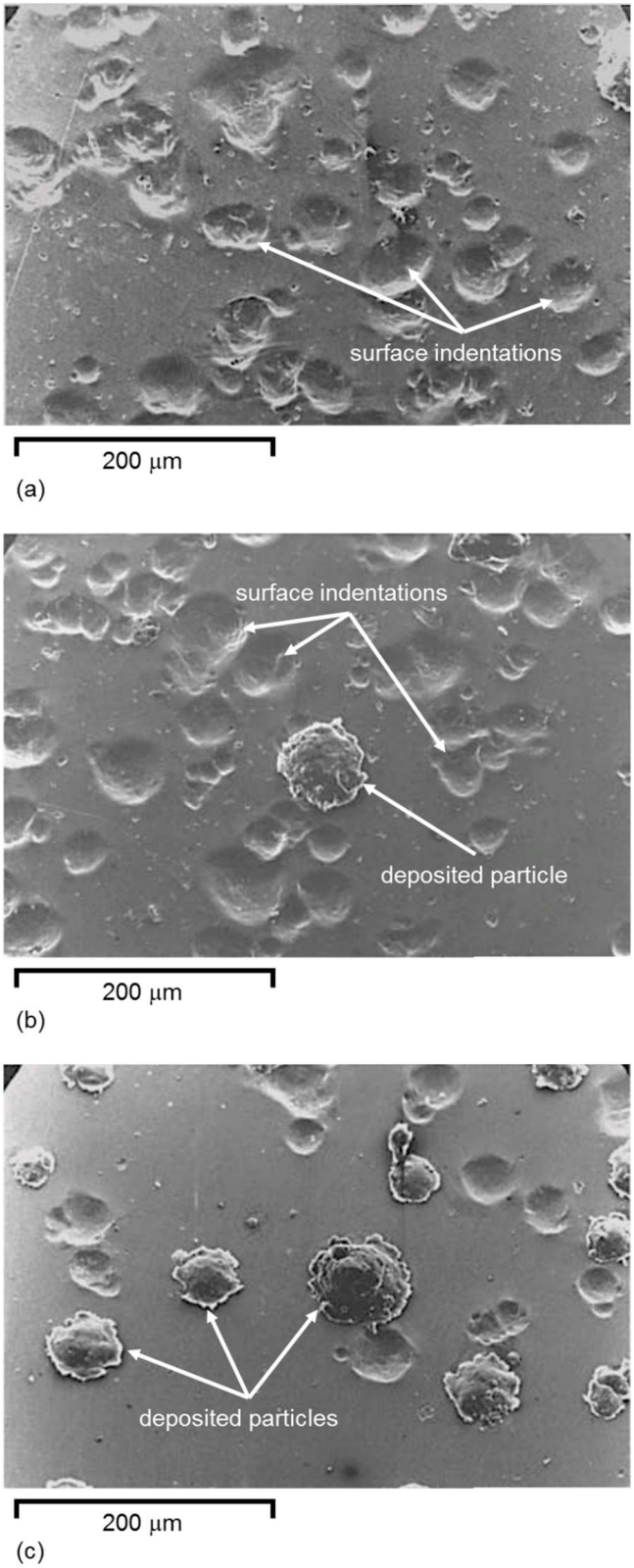

Fig. 2-8 Deposition of aluminium feedstock powder (average diameter of 30.2 μm) on a copper substrate at three particle velocities; (a) 730 m/s; (b) 780 m/s; (c) 850 m/s [2.58]

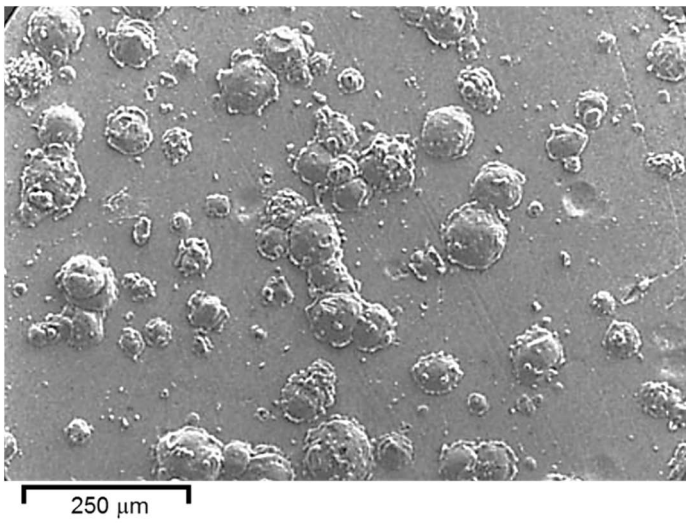

Fig. 2-9 Deposition of aluminium particles travelling at 850 m/s on the grit-blasted copper substrate [2.58]

2.3.4 Overview of cermet powders

Cermet powders were developed for use with thermal spray systems to produce hard, wear resistant coatings to extend the life of components that operate in erosive conditions [2.7]. The term *"cermet"* refers to the mixture of metal/oxide ceramic phase (reinforcement) and a metal phase (binder) [2.7]. Cermet powders typically comprise a reinforcement grain (or grains) surrounded by the metallic binder alloy [2.95]. The size and distribution of the reinforcement grain can be controlled through the manufacturing process to enable the production of bespoke powders that meet the requirements of the coating application [2.95]. Moreover, the chemical composition of the powders can also be modified to provide specific material properties in the deposited coatings [2.7].

There are several methods used in the production of cermet powders, with the choice of process dependent on the desired coating characteristics, the chemical composition of the material and cost [2.95]. The present study concerns the use of agglomerated and sintered cermet powders (WC-CoCr and Cr_3C_2-NiCr), as well as fused and crushed oxide powder (Al_2O_3). Fig. 2-10 highlights the internal morphology of a cross sectioned WC-CoCr cermet particle.

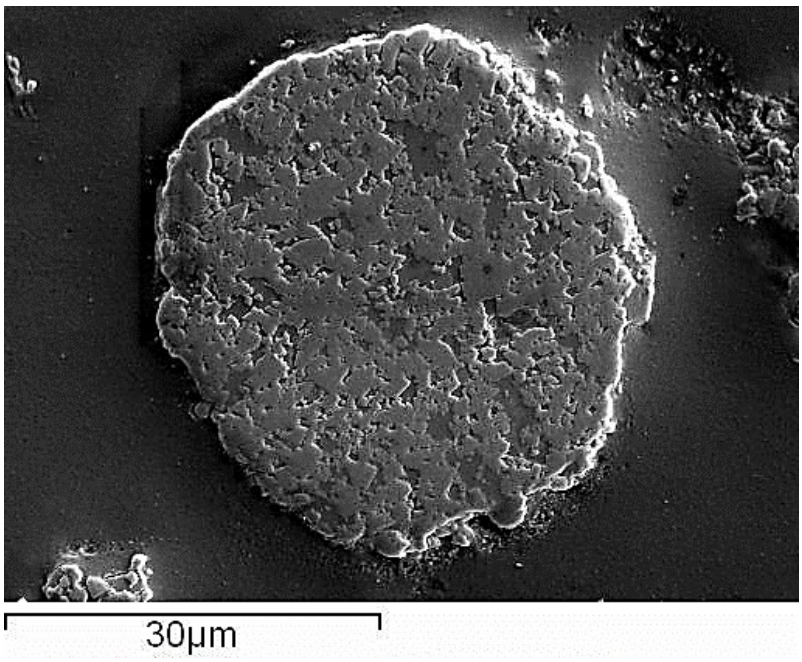

Fig. 2-10 SEM micrograph of a sectioned WC-CoCr cermet powder particle [x2000]

Cermet powders are manufactured by initially powder milling the reinforcement grain (or grains) and binder to obtain an even dispersion of the two constituents [2.7]. The blended powder is subsequently sintered to promote the diffusion of atoms across the boundary between the two phases resulting in permanent bonding between the reinforcement and binder [2.96]. The production of Al_2O_3 is a comparably simple process whereby the powder is manufactured by fusing and crushing [2.95].

2.3.5 Cold spray deposition of cermet powders

Existing research [2.84, 2.87, 2.88] has established that during CS the pressures generated between the impinging particle and the substrate cause the particle to deform and flatten on the surface. Cermet powders contain two or more metallurgically dissimilar phases [2.7]. The reinforcing phase is typically a ceramic or oxide whereas the binder phase is a metallic alloy [2.97]. As such, there is a significant disparity between the mechanical properties (toughness, hardness, Young's modulus) of the different phases [2.97]. Consequently, the size of the reinforcement grain has a strong influence on the deformation of the particle upon contact with the target surface [2.98].

Fig. 2-11 presents a schematic diagram highlighting deformation of a two phase cermet powder following contact with the target surface [2.98]. Under these conditions, the small reinforcements can deform with the binder to produce a flat

particle on the target surface (Fig. 2-11) [2.98]. However, it follows that when the diameter of the reinforcement is larger than the thickness of the deformed particle, the reinforcement protrudes from the surface. Hence, cermet powders composed of many small reinforcements would enable particles to deform uniformly resulting in a greater surface area of metal-to-metal contact [2.98].

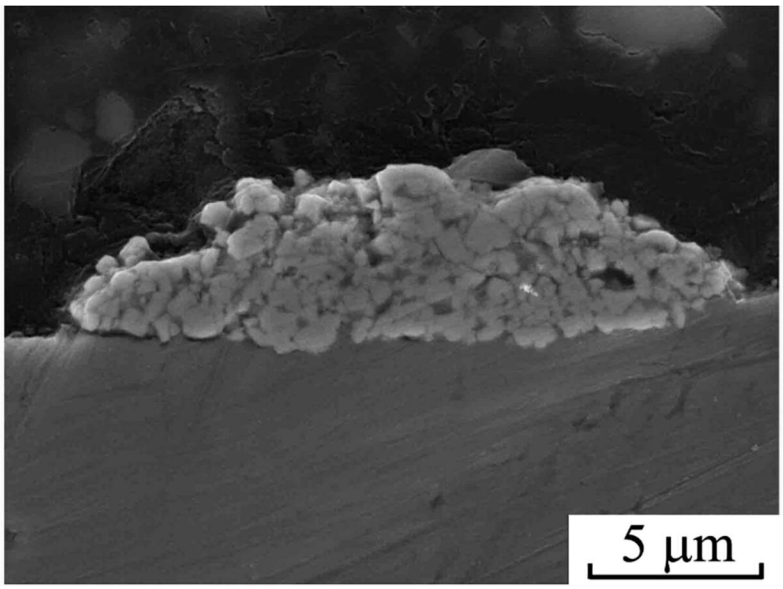

Fig. 2-11 Cold spray deposition of a single WC-Co particle, adapted from [2.98]

2.3.6 Cold spray coating bond strength

Despite the reported benefits associated with CS [2.99–2.103], one drawback of the process is potential delamination of the deposited coating [2.82, 2.104–2.106]. Delamination can occur between coating and substrate, owing to lower adhesive strength (strength of the bond between the coating and the substrate) as a result of the particles remaining below the solidus as they impact the surface of the substrate [2.82]. To investigate this failure mechanism, WC-CoCr and Al_2O_3 were separately co-deposited with AISI 316 onto AISI 316 substrate. These metal matrix composites (MMCs) are evaluated further in Chapter 8. However, the coating bond strength data are presented herein to illustrate the delamination of CS coatings when no FSP is applied.

The bond strength of the as-deposited coatings was evaluated by the pull-off testing method specified in ASTM C633 – 13 [2.107]. The specific parameters employed during the test are presented in Chapter 4, in addition to a schematic diagram of the experimental setup.

Three pull-off tests were completed for each coating type with the maximum load applied prior to the point of failure presented in Table 2-1. Before testing the coated specimens, two of the steel stubs were directly joined together with Araldite AV170 to measure the bond strength of the adhesive. The results confirmed that the Araldite AV170 failed at a load of 48.6 MPa.

Table 2-1 Bond strength test results

Coating material	Test replicate	Max. load before failure (MPa)	Failure mode
WC-Co	1	44.0	AV 170 adhesion
	2	39.9	Coating adhesion
	3	42.6	Coating adhesion
Al_2O_3	1	34.9	AV170 adhesion
	2	55.5	AV170 adhesion
	3	49.7	Coating adhesion

The test results shown in Table 2-1 reveal that the maximum load applied to the coated specimens at the point of failure is close to the bond strength of the adhesive. The variation in the maximum load between the different test specimens is attributed to the minor variations in surface roughness between the individual samples.

Fig. 2-12 presents photographs of the WC-CoCr and Al_2O_3 coated specimens and shows the failed surfaces post-test. Based on the results, the adhesive strength of the WC-CoCr reinforced MMC is less than that of the Araldite AV170. In all but one of the tests on the WC-CoCr MMC, the coating has delaminated, while the adhesive bond (Araldite AV170 bond) has remained intact. The delamination of the WC-CoCr coating is illustrated in Fig. 2-13. Conversely, the Al_2O_3 coated specimens exhibit failure of the Araldite AV170 layer. This finding is characterised by the lack of coating delamination on two of the three test specimens. Specimen 3 (Fig. 2-12f) does, however, exhibit minor coating delamination on the periphery of the test stub.

The increased adhesive strength of the Al_2O_3 coating is attributed to the greater quantity of AISI 316 material in the MMC matrix (reported in Chapter 8). As discussed in Section 2.3.2, the bonding mechanism of CS coatings is attributed to adiabatic shear instabilities that exist at the coating-to-substrate interface [2.83], and

the mechanical interlocking of the particles to the substrate owing to the jet of highly strained material at the periphery of the impinged material [2.84]. Both mechanisms necessitate the deformation of the impinging particles on the substrate. Considering that the Al_2O_3 reinforced coating contains a higher quantity of AISI 316 (Chapter 8, Table 8-3), it is reasonable to conclude that the Al_2O_3 MMC would exhibit increased adhesive strength over the WC-CoCr coating.

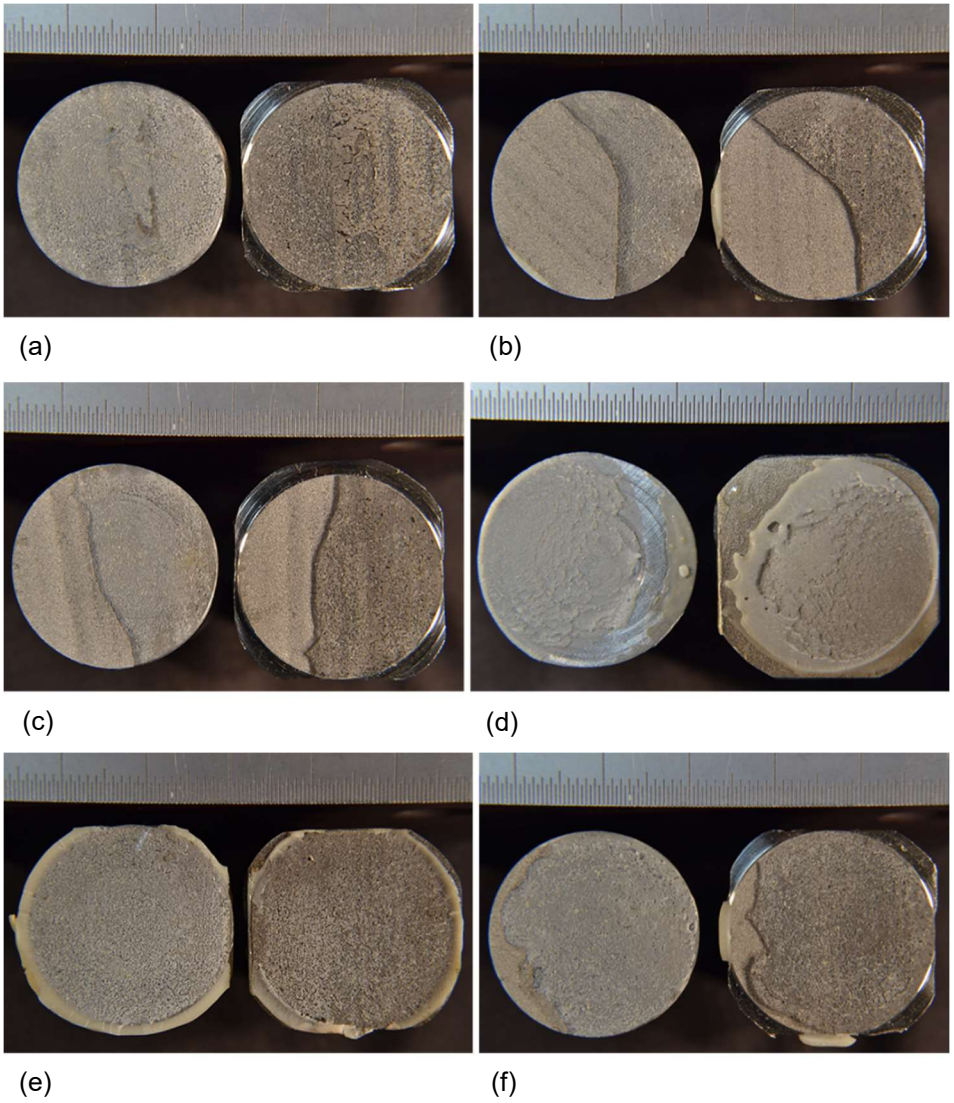

Fig. 2-12 Photographs showing the surface of the test specimens post-test; (a) WC-CoCr 1; (b) WC-CoCr 2; (c) WC-CoCr 3; (d) Al_2O_3 1; (e) Al_2O_3 2; (f) Al_2O_3 3

Fig. 2-13 Photograph illustrating the coating delamination on WC-CoCr test specimen 2

2.4 Alternative Thermal Spraying Processes

To justify the need for the development of a new surface engineering technology, it is first necessary to discuss comparable surface modification methods that are currently employed to improve the erosion and wear performance of components. This section discusses several thermal spraying processes currently used in industry and highlights their respective characteristics.

The term *"thermal spraying"* encompasses several coating deposition techniques that incorporate a high temperature heat source to melt or partially melt the powder or wire feedstock material [2.7]. The softened feedstock material is impinged onto the surface of a chosen substrate and solidifies, forming thick metallic and non-metallic coatings [2.7]. Fig. 2-14 summarises the various thermal spray techniques [2.6]. These different processes can be subdivided into three distinct *"families"*. Combustion thermal spraying processes make use of oxygen and a combustible fuel to generate the necessary heat. The electrical family of processes make use of electricity to produce either a high temperature plasma of an electric arc [2.6]. Cold spray (Section 2.3) is a branch separate from other processes considering that no melting or partial melting of the particles takes place during deposition [2.6].

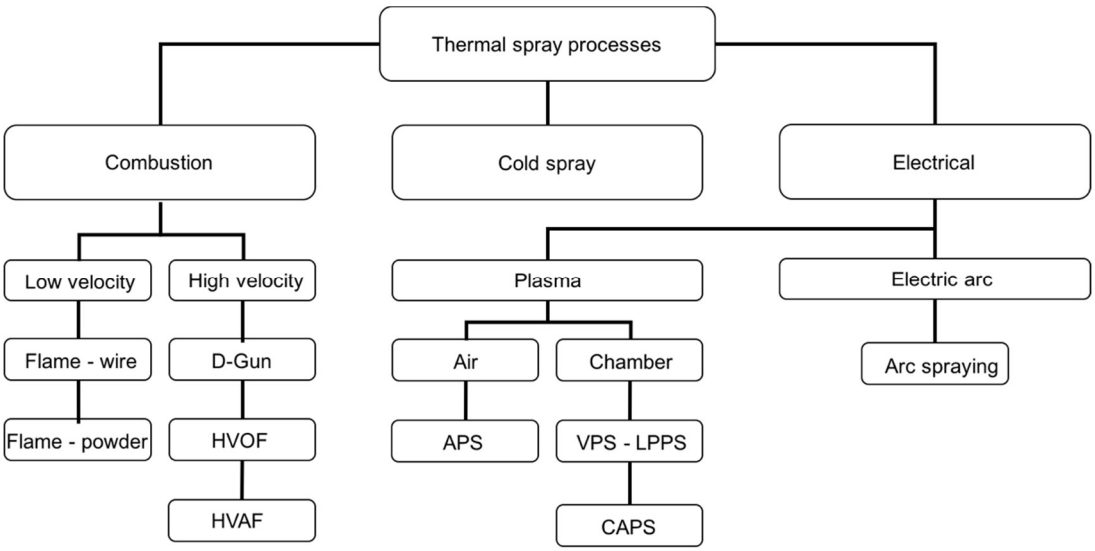

Fig. 2-14 Current range of thermal spraying processes [2.6]

2.4.1 High velocity oxy-fuel (HVOF)

HVOF makes use of oxygen and a combustible gas to melt or partially melt the feedstock material [2.61] and a compressible carrier gas to propel the molten particles onto the target surface at a high velocity [2.61]. The molten material experiences substantial deformation upon impact with the target surface [2.61], resulting in a dense coating [2.108] that is highly resistant to wear and erosion [2.8].

During HVOF spraying, a combustible gas (typically hydrogen or propane) is fed into a chamber where it is mixed with oxygen and ignited [2.61]. Thereafter, the hot gases are accelerated through a nozzle. The chosen feedstock material is fed into the hot gas stream using a suitable carrier gas (nitrogen or helium) where it is softened and accelerated onto the target surface [2.61].

Several different HVOF gun designs have been developed to offer improved coatings depending on the feedstock material [2.7]. By accurately controlling the location at which the powder is fed into the gas stream, the type of fuel used or the nozzle dimensions, the temperature and velocity of the feedstock material can be controlled [2.7]. For example, the Top-Gun system (Fig. 2-15) supplies the feedstock powder axially into the rear of the combustion chamber [2.7]. This exposes the powder to the high temperatures encountered in the combustion chamber. As a result, the particles reach a higher temperature before being deposited on the substrate [2.7].

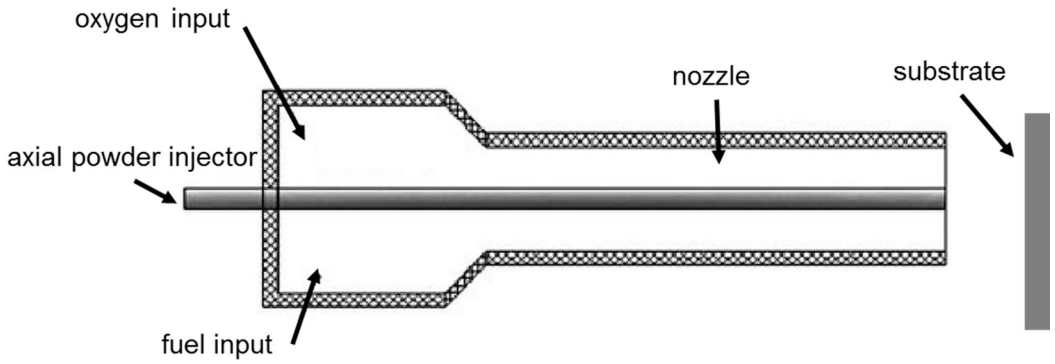

Fig. 2-15 Schematic diagram showing the Top Gun HVOF gun, adapted from [2.17]

The JP-5000 system (Fig. 2-16) incorporates a converging-diverging nozzle and supplies the powder to the gas stream as it flows through the nozzle. Based on this arrangement, the maximum particle temperature is lower than in the Top-Gun system [2.7]. However, the particle velocity is increased due to the incorporation of the de-Laval nozzle. Consequently, the particles experience significant deformation upon contact with the target surface [2.17]. The JP-5000 system (Fig. 2-16) would, therefore, be more appropriate for the deposition of powders that may be adversely affected by particularly high process temperatures [2.17].

Considerable research [2.6, 2.9, 2.10, 2.102, 2.108–2.115] has been carried out on the HVOF process and on the coatings produced using the HVOF technique. Studies [2.6, 2.9, 2.10] have highlighted, through microstructural analysis, corrosion, erosion and fatigue testing that HVOF coatings exhibit superior corrosion, erosion and fatigue performance when compared with other thermal spray processes - as well as traditional coating techniques.

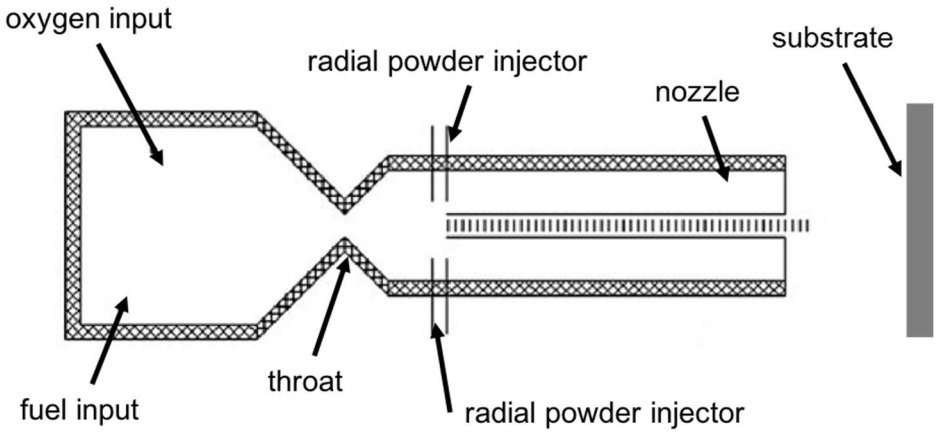

Fig. 2-16 Schematic diagram showing the JP-5000 HVOF gun, adapted from [2.17]

Despite being adopted within various industries (mineral extraction and aerospace), HVOF does exhibit notable disadvantages [2.116]. One main drawback is the modification of the constituent phases within the feedstock powder, i.e. the phases that are present within the deposited coating are dissimilar to those found in the feedstock material [2.7]. One material that is particularly susceptible to this phenomenon is tungsten carbide (WC) [2.94, 2.117]. Existing studies show that following HVOF spraying, some of the primary WC phase (contained in the feedstock powder) undergoes a phase transformation and forms undesirable tertiary phases [2.94, 2.117]. Studies have shown that the presence of these tertiary phases (W_2C and W) reduce the sliding wear performance of the coating [2.117].

The high temperature maintained throughout the process also gives rise to oxidation within the deposited coating [2.10]. The oxides prevent the particles from deforming as extensively [2.10] and, consequently, the cohesive strength between adjacent particles is reduced [2.10]. Other noteworthy disadvantages include the development of undesirable residual stresses within the deposited layer [2.103] and the risk of coating delamination [2.118].

2.4.2 Flame spraying

Flame spraying utilises an oxy-acetylene flame to melt powder or wire feedstock material in a combustion chamber, and an appropriate carrier gas to spray the molten particles onto the target surface [2.20]. The technology is similar to HVOF, however, impinges the feedstock material at a comparably lower velocity [2.20]. An inert gas, such as argon or nitrogen, is typically employed to minimise the oxidation of the molten particles [2.20]. Upon contact with the substrate, the molten material deforms and rapidly solidifies forming a coating [2.20]. A schematic diagram of the powder flame spraying nozzle can be seen in Fig. 2-17 [2.20].

Flame spraying has been widely adopted in industrial applications due to its ability to produce erosion and corrosion resistant coatings using low-cost and portable spraying equipment [2.7]. By using comparably course feedstock powder, flame spraying can achieve a high coating deposition rate (mass of deposited material divided by the mass of sprayed material) [2.17], in contrast to other thermal spray methods.

However, flame spraying is often employed in relatively low-tech applications as coatings suffer from high porosity owing to the insufficient deformation of the feedstock material upon contact with the substrate [2.119]. Moreover, the feedstock

material exhibits increased oxidation [2.17] as a consequence of the increased dwell time of the powder in the combustion chamber [2.17]. The presence of oxides within the deposited layer reduces the overall bond strength of the coating, hence limiting the applicability of this technology to highly erosive operating conditions [2.17]. Rodriguez et al. [2.120] demonstrated that post-spray heat treatment improved the wear performance of the flame sprayed coatings beyond that of plasma spray. The fusion heat treatment reduced the surface roughness, moving from 20-30 μm to 2-4 μm. This, combined with the increased hardness of the flame spray coating resulted in a significant reduction in mass loss under sliding wear tests [2.120]. Despite this, flame spraying as a stand-alone process produces coatings that are inferior to those produced by plasma spraying or high velocity deposition methods.

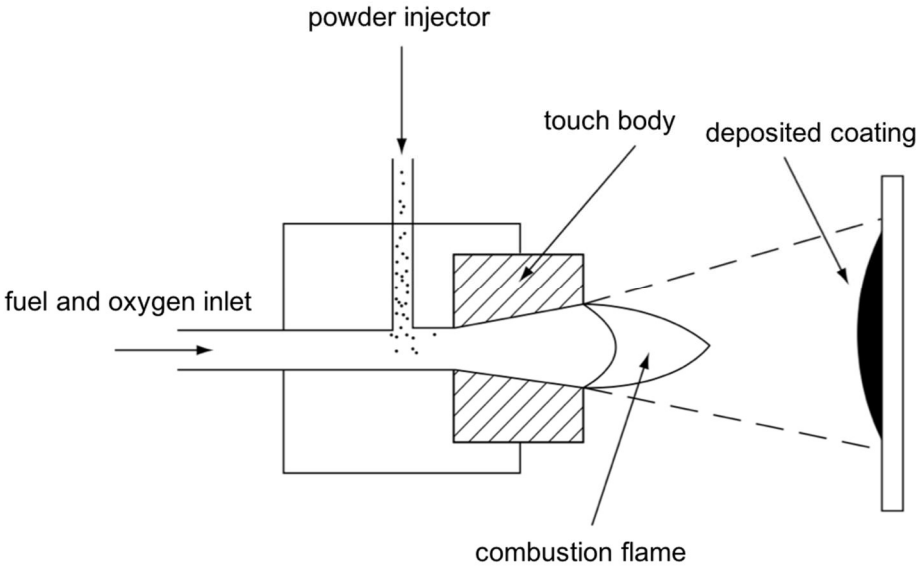

Fig. 2-17 Schematic diagram of the powder flame spraying system [2.20]

2.4.3 Plasma spray

During plasma spray, a direct current is passed between two electrodes contained within a nozzle to create an electric arc [2.7]. A gas such as argon [2.121] or nitrogen [2.122] is ignited by the arc to generate the plasma. The feedstock material is fed into the plasma jet causing immediate melting [2.58]. The inert powder carrier gas is heated by the plasma and rapidly expands, thereby generating a high velocity jet that accelerates the molten powder towards the substrate at speeds in the range of 500 to 700 m/s [2.58]. Fig. 2-18 presents a schematic diagram of the Praxair-TAFA SG100 plasma spray torch [2.7].

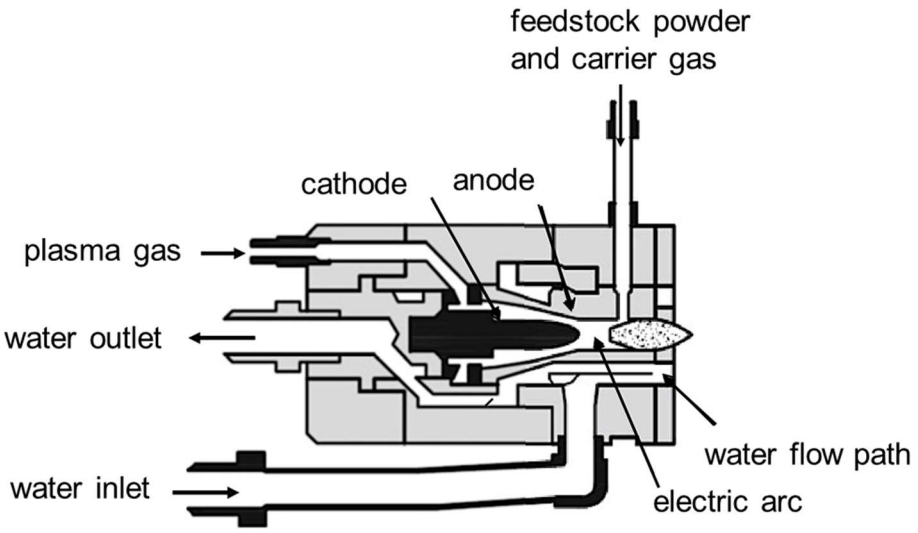

Fig. 2-18 Schematic diagram of the SG100 plasma spray torch manufactured by Praxair-TAFA [2.7]

The temperatures generated during plasma spraying are capable of melting any material [2.58]. As such, plasma spray is particularly appropriate for the deposition of materials with a high melting point, such as erosion resistant cermet's and ceramics [2.123]. However, careful selection of feedstock powder and processing parameters are necessary to successfully produce a suitable coating [2.123]. For instance, the considerable temperature of the plasma (approximately 2800°C – 16800°C) [2.58] can vaporise the powder if the diameter of the particle is particularly small [2.123].

Another drawback of the plasma spray process is that the manufactured coatings contain dissimilar phases to those present in the feedstock material [2.123, 2.124]. The melting of the feedstock material stimulates diffusion within the particles and hence, the formation of new phases [2.124]. Upon rapid cooling and solidification, these new phases are trapped within the deposited coating [2.124]. Moreover, exposure of the molten particles to the atmosphere oxidises the material [2.125]. The presence of oxides within the layer act as nucleation sites for cracking and reduce the contact area between the molten particles [2.125]. Due to the development of these undesirable features (new phases and oxides), the transition region between the coating and substrate is susceptible to failure under cyclic loading [2.126].

To overcome the aforementioned deficiencies in plasma spray, two modifications of the standard process have been developed. Vacuum plasma spray (VPS) and low pressure plasma spray (LPPS) take place in chambers that remove oxygen from the spraying environment [2.127]. In doing so, the undesirable

microstructural features within the coating are reduced or eliminated [2.127]. However, VPS and LPPS are both considerably more expensive than the standard plasma spray process. Therefore components that are coated using either of these techniques are typically high value, for example, aircraft turbine blades [2.123].

2.5 Chapter Summary

Fig. 2-19 [2.58] presents a chart highlighting the difference in the temperature and particle velocity between the various spray deposition processes (thermal and CS). The temperatures and velocities, as well as the coating properties associated with each of the spray process [2.6], are presented in Table 2-2.

For each of the processes in Table 2-2, there are specific drawbacks that limit the performance of each engineered surface. This may include, but are not restricted to, delamination of coating with low bond strength [2.118], the formation of undesirable brittle phases from high temperatures in the process [2.7, 2.117], the development of detrimental residual stresses at the coating-to-substrate interface or presence of oxides in the deposited material [2.54, 2.55, 2.63, 2.69, 2.146]. Considering these various disadvantages, there is an opportunity for the development of a new surface engineering technology that overcomes the issues associated with the existing processes.

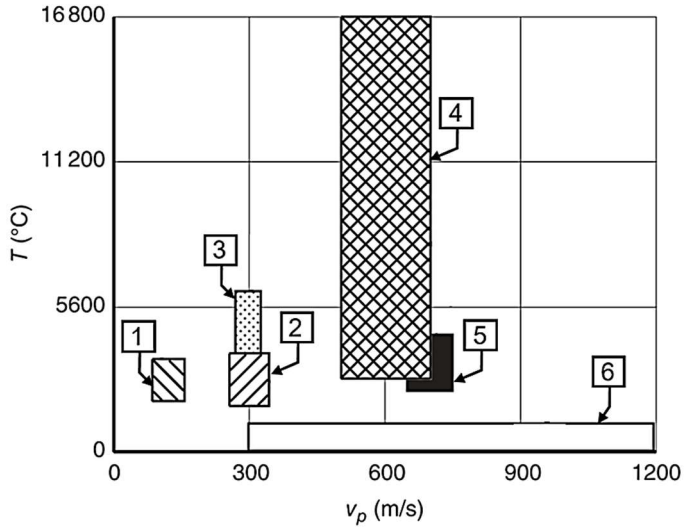

Fig. 2-19 Chart highlighting the difference in particle velocity and gas temperature employed in the various thermal spraying processes; (1) power flame, (2) wire flame, (3) wire arc, (4) plasma, (5) HVOF, (6) cold spray [2.58]

Table 2-2 Comparison of cold spray and high temperature (HVOF and Plasma) spray parameters and the associated coating characteristics [2.6]

Spray process	Gas temp. (K)	Gas velocity (m/s)	Particle temp. (K)	Particle velocity (m/s)	Coating density (%)	Oxidation
Cold spray	300 - 900	1000 – 2500	<800	300 – 1200	>95	none
HVOF	2700	500 – 1200	2000	200 – 1000	>95	moderate
Plasma	15000	300 – 1000	>3800	200 – 300	90 – 95	moderate /elevated

FSP is a solid-state surface engineering process that utilises a rotating tool to modify the microstructure within the processed region of an alloy [2.22, 2.23, 2.27]. The elevated temperature, combined with the plastic deformation generated by the rotating tool typically yields a highly refined microstructure within the stir zone [2.22, 2.23, 2.27]. The mechanisms that promote this refined grain structure have been discussed in Section 2.2. The existing research [2.35] suggests FSP as an effective method of removing manufacturing defects from the material, as well as improving the dispersion of any inclusions contained within the microstructure of the alloy [2.23]. Moreover, FSP has been shown to improve the mechanical properties of the bulk material [2.29].

Based on the information presented in this Chapter, CS offers one of the most suitable methods for producing coatings on different alloys. Considering that the heat input to the substrate material is low, CS is appropriate for the spraying of thermally sensitive materials that may be adversely affected by the high temperatures in thermal spraying approaches [2.65]. Moreover, the range of materials that can be successfully sprayed without oxidation or the development of undesirable phases is wider given the low heat input to the feedstock material [2.54, 2.55, 2.62]. Additionally, the cold spray process is capable of imparting compressive residual stresses within the deposited coating through the shot peening effect of the impinging material [2.69]. Compressive residual stresses offer improved fatigue performance [2.74] in contrast to the tensile stresses generated by thermal spraying processes.

Despite these advantages, CS coatings adhere to the substrate through metallurgical and mechanical bonds that exist between the individually deposited particles and the substrate [2.58, 2.83, 2.86, 2.87]. The contribution of each mechanism to the total adhesive (and cohesive) strength of the coating is dictated by the particular combination of powder and substrate materials [2.54, 2.89]. As such,

CS coatings will be prone to delamination [2.118], thus exposing the underlying substrate to potentially erosive and corrosive operating environments. This study investigates the ability of FSP to remove this coating-to-substrate interface entirely and embed the CS deposited material within the substrate alloy, thereby resulting in a particle reinforced metal matrix composite (MMC) surface layer.

2.6 References

[2.1] B. Lu, Erosion-Corrosion in Oil and Gas Production, Res. Rev. Mater. Sci. Chem. 2 (2013) 19–60.

[2.2] R. Tarodiya, B.K. Gandhi, Hydraulic performance and erosive wear of centrifugal slurry pumps - A review, Powder Technol. 305 (2017) 27–38.

[2.3] M.C. Roco, G.R. Addie, Erosion wear in slurry pumps and pipes, Powder Technol. 50 (1987) 35–46.

[2.4] S. Chandel, S.N. Singh, V. Seshadri, Experimental study of erosion wear in a centrifugal slurry pump using coriolis wear test rig, Part. Sci. Technol. 30 (2012) 179–195.

[2.5] X. Luo, H. Xu, J. Liu, L. Qi, Abrasive Erosion Comparison for a Ceramics and a High Chrome Cast Iron Applied in a Slurry Pump, (2008) 894–897.

[2.6] B.G. Mellor, Surface coatings for protection against wear, Woodhead Publishing Limited, 2006.

[2.7] P.L. Fauchais, J.V.R. Heberlein, M.I. Boulos, Thermal Spray Fundamentals, 2014.

[2.8] R. Pileggi, M. Tului, D. Stocchi, S. Lionetti, Tribo-corrosion behaviour of chromium carbide based coatings deposited by HVOF, Surf. Coatings Technol. 268 (2015) 247–251.

[2.9] S. Abdi, S. Lebaili, Alternative to chromium, a hard alloy powder NiCrBCSi (Fe) coatings thermally sprayed on 60CrMn4 steel. Phase and comportements, Phys. Procedia. 2 (2009) 1005–1014.

[2.10] G. Bolelli, R. Giovanardi, L. Lusvarghi, T. Manfredini, Corrosion resistance of HVOF-sprayed coatings for hard chrome replacement, Corros. Sci. 48 (2006) 3375–3397.

[2.11] K. Winter, J. Kalucki, D. Koshel, Process technologies for thermochemical surface engineering, in: Thermochem. Surf. Eng. Steels, Woodhead Publishing Limited, 2015: pp. 141–206.

[2.12] T. Bell, Surface engineering of austenitic stainless steel, Surf. Eng. 18 (2002) 415–422.

[2.13] H. Dong, A. Bloyce, P.H. Morton, T. Bell, Surface engineering to improve tribological performance of Ti–6Al–4V, Surf. Eng. 13 (1997) 402–406.

[2.14] T. Burakowski, T. Wierzchon, Surface Engineering of Metals: Principles, Equipment, Technologies, CRC Press LLC, Boca Raton, 1999.

[2.15] J.D. Escobar, E. Velásquez, T.F. a Santos, a. J. Ramirez, D. López, Improvement of cavitation erosion resistance of a duplex stainless steel through friction stir processing (FSP), Wear. 297 (2013) 998–1005.

[2.16] S. Mukherjee, A. K. Ghosh, Friction stir processing of direct metal deposited copper-nickel 70/30, Mater. Sci. Eng. A. 528 (2011) 3289–3294.

[2.17] R.J.K. Wood, R. Manish, Surface Engineering for Enhanced Performance against Wear, Springer, 2013.

[2.18] K. Winter, J. Kalucki, D. Koshel, Process technologies for thermochemical surface engineering, in: Thermochem. Surf. Eng. Steels, Woodhead

Publishing Limited, 2015: pp. 141–206.
[2.19] J.R. Davis, Introduction to Thermal Spray Processing, in: D.E. Crawmer (Ed.), Handb. Therm. Spray Technol., ASM International, 2004: pp. 54–76.
[2.20] L. Pawlowski, The Science and Engineering of Thermal Spray Coatings, 2008.
[2.21] A. Brown, Weld overlay cladding - The solution to pump corrosion?, World Pumps. (2005) 50–53.
[2.22] R.S. Mishra, M.W. Mahoney, Friction stir welding and processing, Mater. Sci. Eng. R Reports. 50 (2007) 360.
[2.23] R. Miranda, J. Gandra, P. Vilaca, L. Quintino, T. Santos, Surface Modification by Solid State Processing, Woodhead Publishing Limited, 2008.
[2.24] R.S. Mishra, M.W. Mahoney, Friction stir welding and processing, Mater. Sci. Eng. R Reports. 50 (2007) 360.
[2.25] A. Fattah-Alhosseini, M. Vakili-Azghandi, M. Sheikhi, M.K. Keshavarz, Passive and electrochemical response of friction stir processed pure Titanium, J. Alloys Compd. 704 (2017) 499–508.
[2.26] K. Nakata, Y.G. Kim, H. Fujii, T. Tsumura, T. Komazaki, Improvement of mechanical properties of aluminum die casting alloy by multi-pass friction stir processing, Mater. Sci. Eng. A. 437 (2006) 274–280.
[2.27] C. Lorenzo-Martin, O.O. Ajayi, Rapid surface hardening and enhanced tribological performance of 4140 steel by friction stir processing, Wear. 332–333 (2015) 962–970.
[2.28] C.I. Chang, X.H. Du, J.C. Huang, Achieving ultrafine grain size in Mg-Al-Zn alloy by friction stir processing, Scr. Mater. 57 (2007) 209–212.
[2.29] D. Yadav, R. Bauri, Effect of friction stir processing on microstructure and mechanical properties of aluminium, Mater. Sci. Eng. A. 539 (2012) 85–92.
[2.30] T.S. Mahmoud, Surface modification of A390 hypereutectic Al-Si cast alloys using friction stir processing, Surf. Coatings Technol. 228 (2013) 209–220.
[2.31] R. Kapoor, K. Kandasamy, R.S. Mishra, J. a. Baumann, G. Grant, Effect of friction stir processing on the tensile and fatigue behavior of a cast A206 alloy, Mater. Sci. Eng. A. 561 (2013) 159–166.
[2.32] J.S. De Jesus, A. Loureiro, J.M. Costa, J.M. Ferreira, Effect of tool geometry on friction stir processing and fatigue strength of MIG T welds on Al alloys, J. Mater. Process. Technol. 214 (2014) 2450–2460.
[2.33] H.S. Grewal, H.S. Arora, H. Singh, a. Agrawal, Surface modification of hydroturbine steel using friction stir processing, Appl. Surf. Sci. 268 (2013) 547–555.
[2.34] Y. Chen, H. Ding, J. Li, Z. Cai, J. Zhao, W. Yang, Influence of multi-pass friction stir processing on the microstructure and mechanical properties of Al-5083 alloy, Mater. Sci. Eng. A. 650 (2016) 281–289.
[2.35] R. Bauri, D. Yadav, G. Suhas, Effect of friction stir processing (FSP) on microstructure and properties of Al-TiC in situ composite, Mater. Sci. Eng. A. 528 (2011) 4732–4739.
[2.36] B.L. Xiao, Q. Yang, J. Yang, W.G. Wang, G.M. Xie, Z.Y. Ma, Enhanced mechanical properties of Mg-Gd-Y-Zr casting via friction stir processing, J. Alloys Compd. 509 (2011) 2879–2884.
[2.37] K. Sillapasa, S. Surapunt, Y. Miyashita, Y. Mutoh, N. Seo, Tensile and fatigue behavior of SZ, HAZ and BM in friction stir welded joint of rolled 6N01 aluminum alloy plate, Int. J. Fatigue. 63 (2014) 162–170.
[2.38] A. Toumpis, A. Galloway, S. Cater, N. McPherson, Development of a process envelope for friction stir welding of DH36 steel - A step change, Mater. Des. 62 (2014) 64–75.
[2.39] J.-Q. Su, T.W. Nelson, C.J. Sterling, Grain refinement of aluminum alloys by

friction stir processing, J. Mater. Sci. Lett. 86 (2006) 1–24.
[2.40] M. Mehranfar, K. Dehghani, Producing nanostructured super-austenitic steels by friction stir processing, Mater. Sci. Eng. A. 528 (2011) 3404–3408.
[2.41] B.T. Gibson, D.H. Lammlein, T.J. Prater, W.R. Longhurst, C.D. Cox, M.C. Ballun, et al., Friction stir welding: Process, automation, and control, J. Manuf. Process. 16 (2014) 56–73.
[2.42] N. Mendes, P. Neto, A. Loureiro, A.P. Moreira, Machines and control systems for friction stir welding: A review, Mater. Des. 90 (2016) 256–265.
[2.43] Z.Y. Ma, S.R. Sharma, R.S. Mishra, Effect of multiple-pass friction stir processing on microstructure and tensile properties of a cast aluminum-silicon alloy, Scr. Mater. 54 (2006) 1623–1626.
[2.44] Y.N. Zhang, X. Cao, S. Larose, P. Wanjara, Review of tools for friction stir welding and processing, Can. Metall. Q. 51 (2012) 250–261.
[2.45] Y. Chao, X. Qi, W. Tang, Heat Transfer in Friction Stir Welding — Experimental and Numerical Studies, 125 (2003) 138–145.
[2.46] V. Sharma, U. Prakash, B.V.M. Kumar, Surface Composites by Friction Stir Processing: A Review, J. Mater. Process. Technol. 224 (2015) 117–134.
[2.47] M. Durdanovic, M. Mijajlovic, D. Milcic, D. Stamenkovi, Heat Generation During Friction Stir Welding Process, Tribol. Ind. 31 (2009) 8–14.
[2.48] P. Asadi, M. Akbari, H. Karimi-Nemch, Simulation of friction stir welding and processing, Woodhead Publishing Limited, 2014.
[2.49] H. Schmidt, J. Hattel, Modelling heat flow around tool probe in friction stir welding Modelling heat flow around tool probe in friction stir welding, Sci. Technol. Weld. Join. 10 (2013).
[2.50] H. Pashazadeh, A. Masoumi, J. Teimournezhad, A study on material flow pattern in friction stir welding using finite element method, Proc. Inst. Mech. Eng. Part B J. Eng. Manuf. 227 (2013) 1453–1466.
[2.51] S. Xu, X. Deng, A.P. Reynolds, T.U. Seidel, Finite element simulation of material flow in friction stir welding, 6 (2001).
[2.52] A.N. Albakri, B. Mansoor, H. Nassar, M.K. Khraisheh, Thermo-mechanical and metallurgical aspects in friction stir processing of AZ31 Mg alloy—A numerical and experimental investigation, J. Mater. Process. Technol. 213 (2013) 279–290.
[2.53] W.-Y. Li, C. Zhang, X. Guo, C.-J. Li, H. Liao, C. Coddet, Study on impact fusion at particle interfaces and its effect on coating microstructure in cold spraying, Appl. Surf. Sci. 254 (2007) 517–526.
[2.54] S. Grigoriev, A. Okunkova, A. Sova, P. Bertrand, I. Smurov, Cold spraying: From process fundamentals towards advanced applications, Surf. Coatings Technol. 268 (2015) 77–84.
[2.55] A. Papyrin, V. Kosarev, S. Klinkov, A. Alkhimov, V. Fomin, Cold Spray Technology, Elsevier, 2006.
[2.56] R.C. Dykhuizen, M.F. Smith, Gas Dynamic Principles of Cold Spray, J. Therm. Spray Technol. 7 (1998) 205–212.
[2.57] T. Stoltenhoff, H. Kreye, H.J. Richter, An Analysis of the Cold Spray Process and Its Coatings, J. Therm. Spray Technol. 11 (2002) 542–550.
[2.58] V.K. Champagne, The cold spray materials deposition process: fundamentals and applications, Woodhead Publishing, 2007.
[2.59] L. Pawlowski, The Science and Engineering of Thermal Spray Coatings, 2008.
[2.60] R. Lupoi, W. O'Neill, Powder stream characteristics in cold spray nozzles, Surf. Coatings Technol. 206 (2011) 1069–1076.
[2.61] T.S. Sidhu, S. Prakash, State of the Art of HVOF Coating Investigations — A Review, Mar. Technol. Soc. J. 39 (2005) 53–64.

[2.62] Y. Xiong, W. Zhuang, M. Zhang, Effect of the thickness of cold sprayed aluminium alloy coating on the adhesive bond strength with an aluminium alloy substrate, Surf. Coatings Technol. 270 (2015) 259–265.
[2.63] C. Borchers, F. Gärtner, T. Stoltenhoff, H. Assadi, H. Kreye, Microstructural and macroscopic properties of cold sprayed copper coatings, J. Appl. Phys. 93 (2003) 10064–10070.
[2.64] D.A. Stewart, P.H. Shipway, Microstructural evolution in thermally sprayed WC-Cr coatings: comparison between nanocomposite and conventional starting powders, 48 (2000) 1593–1604.
[2.65] M. Grujicic, C.L. Zhao, W.S. Derosset, D. Helfritch, Adiabatic shear instability based mechanism for particles / substrate bonding in the cold-gas dynamic-spray process, Mater. Des. 25 (2004) 681–688.
[2.66] K. Spencer, D.M. Fabijanic, M.X. Zhang, The use of Al-Al2O3 cold spray coatings to improve the surface properties of magnesium alloys, Surf. Coatings Technol. 204 (2009) 336–344.
[2.67] X.T. Luo, G.J. Yang, C.J. Li, Multiple strengthening mechanisms of cold-sprayed cBNp/NiCrAl composite coating, Surf. Coatings Technol. 205 (2011) 4808–4813.
[2.68] K. Kim, M. Watanabe, J. Kawakita, S. Kuroda, Grain refinement in a single titanium powder particle impacted at high velocity, Scr. Mater. 59 (2008) 768–771.
[2.69] K. Spencer, V. Luzin, N. Matthews, M.-X. Zhang, Residual stresses in cold spray Al coatings: The effect of alloying and of process parameters, Surf. Coatings Technol. 206 (2012) 4249–4255.
[2.70] E.J.T. Pialago, C.W. Park, Cold spray deposition characteristics of mechanically alloyed Cu-CNT composite powders, Appl. Surf. Sci. 308 (2014) 63–74.
[2.71] P. Coddet, C. Verdy, C. Coddet, F. Debray, F. Lecouturier, Mechanical properties of thick 304L stainless steel deposits processed by He cold spray, Surf. Coatings Technol. 277 (2015) 74–80.
[2.72] S.A. Alidokht, P. Manimunda, P. Vo, S. Yue, R.R. Chromik, Cold spray deposition of a Ni-WC composite coating and its dry sliding wear behavior, Surf. Coatings Technol. 308 (2016) 424–434.
[2.73] F. Sevillano, P. Poza, C.J. Múnez, S. Vezzù, S. Rech, A. Trentin, Cold-sprayed Ni-Al2O3 coatings for applications in power generation industry, J. Therm. Spray Technol. 22 (2013) 772–782.
[2.74] R. Ghelichi, S. Bagherifard, D. Macdonald, I. Fernandez-Pariente, B. Jodoin, M. Guagliano, Experimental and numerical study of residual stress evolution in cold spray coating, Appl. Surf. Sci. 288 (2014) 26–33.
[2.75] H. Assadi, F. Gärtner, T. Stoltenhoff, H. Kreye, Bonding mechanism in cold gas spraying, Acta Mater. 51 (2003) 4379–4394.
[2.76] Y. Zou, W. Qin, E. Irissou, J.G. Legoux, S. Yue, J.A. Szpunar, Dynamic recrystallization in the particle/particle interfacial region of cold-sprayed nickel coating: Electron backscatter diffraction characterization, Scr. Mater. 61 (2009) 899–902.
[2.77] C.J. Li, W.Y. Li, Y.Y. Wang, Formation of metastable phases in cold-sprayed soft metallic deposit, Surf. Coatings Technol. 198 (2005) 469–473.
[2.78] U. Andrade, M.A. Meyers, K.S. Vecchio, A.H. Chokshi, Dynamic recrystallization in high-strain, high-strain-rate plastic deformation of copper, Acta Metall. Mater. 42 (1994) 3183–3195.
[2.79] L.E. Murr, C.-S. Niou, E.P. Garcia, E. Ferreyra, T.J.M. Rivas, J.C. Sanchez, Comparison of jetting-related microstructures associated with hypervelocity impact crater formation in copper targets and copper shaped charges, Mater.

Sci. Eng. A. 222 (1997) 118–132.
[2.80] U. Andrade, M.A. Meyers, K.S. Vecchio, A.H. Chokshi, Dynamic recrystallization in high-strain, high-strain-rate plastic deformation of copper, Acta Metall. Mater. 42 (1994) 3183–3195.
[2.81] L.E. Murr, C.-S. Niou, E.P. Garcia, E. Ferreyra, T.J.M. Rivas, J.C. Sanchez, Comparison of jetting-related microstructures associated with hypervelocity impact crater formation in copper targets and copper shaped charges, Mater. Sci. Eng. A. 222 (1997) 118–132.
[2.82] R. Ghelichi, D. MacDonald, S. Bagherifard, H. Jahed, M. Guagliano, B. Jodoin, Microstructure and fatigue behavior of cold spray coated Al5052, Acta Mater. 60 (2012) 6555–6561.
[2.83] T. Hussain, D.G. McCartney, P.H. Shipway, D. Zhang, Bonding Mechanisms in Cold Spraying : The Contributions of Metallurgical and Mechanical Components, J. Therm. Spray Technol. 18 (2009) 364–379.
[2.84] C. Chen, Y. Xie, S. Yin, M.P. Planche, S. Deng, R. Lupoi, et al., Evaluation of the interfacial bonding between particles and substrate in angular cold spray, Mater. Lett. 173 (2016) 76–79.
[2.85] T.W. Wright, The Physics and Mathematics of Adiabatic Shear Bands, Cambridge University Press, 2002.
[2.86] T.H. Van Steenkiste, J.R. Smith, R.E. Teets, Aluminum coatings via kinetic spray with relatively large powder particles, Surf. Coatings Technol. 154 (2002) 237–252.
[2.87] R.C. Dykhuizen, M.F. Smith, D.L. Gilmore, R.A. Neiser, X. Jiang, S. Sampath, Impact of High Velocity Cold Spray Particles, J. Therm. Spray Technol. 8 (1999) 559–564.
[2.88] T. Hussain, A study of bonding mechanisms and corrosion behaviour of cold sprayed coatings, (2011).
[2.89] T. Hussain, D.G. McCartney, P.H. Shipway, D. Zhang, Bonding mechanisms in cold spraying: The contributions of metallurgical and mechanical components, J. Therm. Spray Technol. 18 (2009) 364–379.
[2.90] T.S. Price, P.H. Shipway, D.G. McCartney, E. Calla, D. Zhang, A method for characterizing the degree of inter-particle bond formation in cold sprayed coatings, J. Therm. Spray Technol. 16 (2007) 566–570.
[2.91] T. Schmidt, F. Gartner, H. Assadi, H. Kreye, Development of a generalized parameter window for cold spray deposition, Acta Mater. 54 (2006) 729–742.
[2.92] D. Seo, M. Sayar, K. Ogawa, SiO 2 and MoSi 2 formation on Inconel 625 surface via SiC coating deposited by cold spray, Surf. Coatings Technol. 206 (2012) 2851–2858.
[2.93] D.L. Gilmore, R.C. Dykhuizen, R.A. Neiser, T.J. Roemer, M.F. Smith, Particle Velocity and Deposition Efficiency in the Cold Spray Process, J. Therm. Spray Technol. 8 (1999) 576–582.
[2.94] C.J. Li, G.J. Yang, Relationships between feedstock structure, particle parameter, coating deposition, microstructure and properties for thermally sprayed conventional and nanostructured WC-Co, Int. J. Refract. Met. Hard Mater. 39 (2013) 2–17.
[2.95] Oerlikon Metco, Thermal Spray Materials Guide, 2015.
[2.96] G. Braichotte, G. Cizeron, Sintering of (alumina + titanium) powder mixtures and elaboration of the corresponding cermets, J. Mater. Sci. 24 (1989) 3123–3136.
[2.97] J. Zackrisson, U. Rolander, H.-O. Andren, Development of cermet microstructures during sintering and heat-treatment, Metall. Mater. Trans. A. 32 (1999) 1–48.

[2.98] P. Gao, C. Li, G. Yang, Y. Li, C. Li, Influence of substrate hardness on deposition behaviour of single porous WC-12Co particle in cold spraying, Surf. Coatings Technol. 203 (2008) 348–390.
[2.99] Y. Xiong, M.X. Zhang, The effect of cold sprayed coatings on the mechanical properties of AZ91D magnesium alloys, Surf. Coatings Technol. 253 (2014) 89–95.
[2.100] R.N. Raoelison, C. Verdy, H. Liao, Cold gas dynamic spray additive manufacturing today: Deposit possibilities, technological solutions and viable applications, Mater. Des. 133 (2017) 266–287.
[2.101] D. Toma, W. Brandl, G. Marginean, Wear and corrosion behaviour of thermally sprayed cermet coatings, Surf. Coat. Technol. (2001) 149–158.
[2.102] D.K. Goyal, H. Singh, H. Kumar, V. Sahni, Slurry erosion behaviour of HVOF sprayed WC-10Co-4Cr and Al 2O 3+13TiO 2 coatings on a turbine steel, Wear. 289 (2012) 46–57.
[2.103] U. Selvadurai, P. Hollingsworth, I. Baumann, B. Hussong, W. Tillmann, S. Rausch, et al., Influence of the handling parameters on residual stresses of HVOF-sprayed WC-12Co coatings, Surf. Coatings Technol. 268 (2014) 30–35.
[2.104] M. Couto, S. Dosta, M. Torrell, J. Fernández, J.M. Guilemany, Cold spray deposition of WC-17 and 12Co cermets onto aluminum, Surf. Coatings Technol. 235 (2013) 54–61.
[2.105] E. Irissou, J.G. Legoux, B. Arsenault, C. Moreau, Investigation of Al-Al 2O 3 cold spray coating formation and properties, J. Therm. Spray Technol. 16 (2007) 661–668.
[2.106] S. Dosta, M. Couto, J.M. Guilemany, Cold spray deposition of a WC-25Co cermet onto Al7075-T6 and carbon steel substrates, Acta Mater. 61 (2013) 643–652.
[2.107] I.A. Standard, ASTM C633 − 13: Standard Test Method for Adhesion or Cohesion Strength of Thermal Spray Coatings, 2001.
[2.108] M.R. Ramesh, S. Prakash, S.K. Nath, P.K. Sapra, B. Venkataraman, Solid particle erosion of HVOF sprayed WC-Co/NiCrFeSiB coatings, Wear. 269 (2010) 197–205.
[2.109] W. Liu, F. Shieu, W. Hsiao, Enhancement of wear and corrosion resistance of iron-based hard coatings deposited by high-velocity oxygen fuel (HVOF) thermal spraying, Surf. Coat. Technol. 249 (2014) 24–41.
[2.110] L. Thakur, N. Arora, A comparative study on slurry and dry erosion behaviour of HVOF sprayed WC-CoCr coatings, Wear. 303 (2013) 405–411.
[2.111] L. Thakur, N. Arora, R. Jayaganthan, R. Sood, An investigation on erosion behavior of HVOF sprayed WC-CoCr coatings, Appl. Surf. Sci. 258 (2011) 1225–1234.
[2.112] S. Matthews, B. James, M. Hyland, The role of microstructure in the mechanism of high velocity erosion of Cr3C2-NiCr thermal spray coatings: Part 1 - As-sprayed coatings, Surf. Coatings Technol. 203 (2009) 1086–1093.
[2.113] M. Manjunatha, R.S. Kulkarni, M. Krishna, Investigation of HVOF Thermal sprayed Cr 3 C 2 -NiCr Cermet Carbide Coatings on Erosive Performance of AISI 316 Molybdenum steel, 5 (2014) 622–629.
[2.114] H.S. Grewal, H. Singh, A. Agrawal, Understanding Liquid Impingement erosion behaviour of nickel-alumina based thermal spray coatings, Wear. 301 (2013) 424–433.
[2.115] M. Akhtari Zavareh, A.A.D.M. Sarhan, B.B. Razak, W.J. Basirun, The tribological and electrochemical behavior of HVOF-sprayed Cr3C2-NiCr ceramic coating on carbon steel, Ceram. Int. 41 (2015) 5387–5396.

[2.116] C.N. Machio, G. Akdogan, M.J. Witcomb, S. Luyckx, Performance of WC-VC-Co thermal spray coatings in abrasion and slurry erosion tests, Wear. 258 (2005) 434–442.
[2.117] P.H. Shipway, D.G. McCartney, T. Sudaprasert, Sliding wear behaviour of conventional and nanostructured HVOF sprayed WC-Co coatings, Wear. 259 (2005) 820–827.
[2.118] R. Ahmed, Contact fatigue failure modes of HVOF coatings, Wear. 253 (2002) 473–487.
[2.119] B. Prawara, H. Yara, Y. Miyagi, T. Fukushima, Spark plasma sintering as a post-spray treatment for thermally-sprayed, Surf. Coat. Technol. 162 (2003) 234–241.
[2.120] J. Rodríguez, a. Martín, R. Fernández, J.E. Fernández, An experimental study of the wear performance of NiCrBSi thermal spray coatings, Wear. 255 (2003) 950–955.
[2.121] K. Ghosh, T. Troczynski, A.C.D. Chaklader, Aluminum-Silicon Carbide Coatings by Plasma Spraying, 7 (1998) 78–86.
[2.122] T. Bacci, L. Bertamini, F. Ferrari, F.P. Galliano, E. Galvanetto, Reactive plasma spraying of titanium in nitrogen containing plasma gas, Mater. Sci. Eng. A. 283 (2000) 189–195.
[2.123] P. Fauchais, Understanding plasma spraying, J. Phys. D. Appl. Phys. 37 (2004) R86–R108.
[2.124] L.L. Shaw, D. Goberman, R. Ren, M. Gell, S. Jiang, Y. Wang, et al., The dependency of microstructure and properties of nanostructured coatings on plasma spray conditions, Surf. Coatings Technol. 130 (2000) 1–8.
[2.125] W.R. Chen, X. Wu, B.R. Marple, P.C. Patnaik, Oxidation and crack nucleation/growth in an air-plasma-sprayed thermal barrier coating with NiCrAlY bond coat, Surf. Coatings Technol. 197 (2005) 109–115.
[2.126] E. Tzimas, H. Müllejans, S.D. Peteves, J. Bressers, W. Stamm, Failure of thermal barrier coating systems under cyclic thermomechanical loading, Acta Mater. 48 (2000) 4699–4707.
[2.127] M.E. Vinayo, F. Kassabji, J. Guyonnet, P. Fauchais, Plasma sprayed WC-Co coatings: Influence of spray conditions (atmospheric and low pressure plasma spray) on the crystal structure, porosity, and hardness, J. Vac. Sci. Technol. A Vacuum, Surfaces, Film. 3 (1998).
[2.128] S. Salim, Effects of boronizing process on the surface roughness and dimensions of AISI 1020, AISI 1040 and AISI 2714, J. Mater. Process. Technol. 209 (2008) 1736–1741.
[2.129] W. Möller, S. Parascandola, T. Telbizova, R. Günzel, E. Richter, Surface processes and diffusion mechanisms of ion nitriding of stainless steel and aluminum, Surf. Coatings Technol. 136 (2001) 73–79.
[2.130] F.A.P. Fernandes, A. Lombardi Neto, L.C. Casteletti, A.M. de Oliveira, G.E. Totten, Stainless Steel Property Improvement By Ion Nitriding and Nitrocarburizing, Heat Treat. Prog. 8 (2008) 41–43.
[2.131] S. Dodds, A.H. Jones, S. Cater, Tribological enhancement of AISI 420 martensitic stainless steel through friction-stir processing, Wear. 302 (2013) 863–877.
[2.132] P. Kochmański, J. Nowacki, Activated gas nitriding of 17-4 PH stainless steel, Surf. Coat. Technol. 200 (2006) 6558–6562.
[2.133] P. Kochmański, J. Nowacki, Activated gas nitriding of 17-4 PH stainless steel, Surf. Coatings Technol. 200 (2006) 6558–6562.
[2.134] V. Lacaille, V. Peres, C. Langlade, C. Morel, E. Feulvarch, J.M. Bergheau, et al., Combination of mechanical and chemical pre-treatments to improve nitriding efficiency on pure iron, Appl. Surf. Sci. 414 (2017) 73–81.

[2.135] D. Kundalkar, M. Mavalankar, A. Tewari, Effect of gas nitriding on the thermal fatigue behavior of martensitic chromium hot-work tool steel, Mater. Sci. Eng. A. 651 (2016) 391–398.
[2.136] D. Kundalkar, M. Mavalankar, A. Tewari, Effect of gas nitriding on the thermal fatigue behavior of martensitic chromium hot-work tool steel, Mater. Sci. Eng. A. 651 (2016) 391–398.
[2.137] R.F. Smart, Selection of surfacing treatments, Tribol. Int. 11 (1978) 97–104.
[2.138] G.A. Lausmann, Electrolytically deposited hardchrome, Surf. Coatings Technol. 86–87 (1996) 814–820.
[2.139] K. Hughes, M.E. Meek, L.J. Seed, J. Shedden, Chromium and its compounds: Evaluation of risks to health from environmental exposure in Canada, J. Environ. Sci. Heal. Part C. 12 (1994) 237–255.
[2.140] T. Sahraoui, N. Fenineche, G. Montavon, C. Coddet, Alternative to chromium: characteristics and wear behavior of HVOF coatings for gas turbine shafts repair (heavy-duty), 152 (2004) 43–55.
[2.141] J.A. Picas, A. Forn, G. Matthaus, HVOF coatings as an alternative to hard chrome for pistons and valves, Wear. 261 (2006) 477–484.
[2.142] A. Ibrahim, C.C. Berndt, Fatigue and deformation of HVOF sprayed WC-Co coatings and hard chrome plating, Mater. Sci. Eng. A. 456 (2007) 114–119.
[2.143] G. Bolelli, V. Cannillo, L. Lusvarghi, S. Riccò, Mechanical and tribological properties of electrolytic hard chrome and HVOF-sprayed coatings, Surf. Coatings Technol. 200 (2006) 2995–3009.
[2.144] A. Gholipour, M. Shamanian, F. Ashrafizadeh, Microstructure and wear behavior of stellite 6 cladding on 17-4 PH stainless steel, J. Alloys Compd. 509 (2011) 4905–4909.
[2.145] A. Robinson, S. Bonell, Longer life with welded claddings, World Pumps. 2010 (2010) 42–45.
[2.146] R.H. Leggatt, Residual stresses in welded structures, Int. J. Press. Vessel. Pip. 85 (2008) 144–151.

Chapter 3 Relevant Erosion and Corrosion Theory

Erosion and corrosion are two of the most common failure modes associated with components that transport aqueous slurry [3.1, 3.2]. This study aims to develop a surface engineering process (SprayStir) that increases an alloys resistance to the combined effects of erosion and corrosion. However, to discuss the erosion and corrosion performance of the manufactured surfaces in subsequent chapters, it is first necessary to consider the supporting theory of erosion and corrosion.

In this Chapter, Section 3.1 provides an overview of erosion and Section 3.2 discusses corrosion. The combined effects of these two mechanisms (erosion and corrosion) can enhance the level of damage caused by the slurry, through a process known as synergy [3.3, 3.4]. Synergy is the additional mass loss generated when both erosion and corrosion operate on the surface of metal [3.3, 3.4]. Failure to account for the enhanced material loss produced by synergy can lead to the catastrophic breakdown of components well in advance of the predicted number of hours to failure [3.5]. Consequently, Section 3.3 presents a brief overview of synergy theory that will be expanded upon, where necessary, in subsequent chapters.

Some of the references incorporated in this Chapter discuss materials that do not necessarily reflect the materials examined in the experimental section of this thesis. Furthermore, some references may comment on the effects of erosion, corrosion or synergy on surfaces produced by several different surface engineering or coating processes. These references have been included to demonstrate the erosion, corrosion and synergy phenomenon and do not necessarily explain the influence of these phenomena on SprayStirred specimens.

3.1 Overview of Erosion

Erosion is a wear process in which a surface is degraded by the frictional forces generated between the material and an erosive surface or by the impingement of erodent particles [3.6]. The aim of this study is to develop a new process (SprayStir) by which to manufacture erosion resistant surfaces. Therefore, it is necessary to identify and examine the erosion mechanisms that operate on the surfaces discussed in subsequent chapters. Consequently, this section presents an overview of the erosion phenomenon and will introduce terms that will be used to explain the erosion response of the materials discussed in later Chapters.

The variables that affect the erosion mechanisms that operate on the surface of a material can be split into two groups. The first group comprises the properties related to the target (impinged) material, i.e. Young's modulus, microstructural properties and hardness [3.10–3.12]. The toughness of the target surface is also an important variable as it influences whether the impinged surface exhibits brittle or ductile erosion [3.13–3.15]. The second set of variables includes the properties associated with the erodent and include the hardness, size and shape of the impinging material [3.7–3.9]. As this study examines the slurry erosion performance of materials, the effect of slurry impact angle will also be considered.

This section will not discuss state-of-the-art studies that examine erosion performance of different materials. Instead, the following sub-sections will make use of published literature to describe the various erosion mechanisms and their associated features. These features will be used to characterise the erosion taking place on the surface of specimens examined in later chapters. Information concerning the current state-of-the-art research on the erosion of aluminium and steel alloys will be included in their respective chapters.

3.1.1 Influence of the target material on the erosion properties

The specific erosion mechanism that operates on a surface is related to several interconnected mechanical properties; Young's modulus, yield strength, fracture toughness, microstructural composition. These properties typically dictate whether ductile [3.16] or brittle erosion [3.5] occurs. Numerous research groups [3.6, 3.16–3.19] have investigated the variation in erosion mechanisms between ductile and brittle materials and have reported important differences in the way in which material is removed (eroded) from the surface.

However, for the purpose of this study, ductility is defined as the amount of plastic deformation that can occur on a surface prior to failure. A ductile material is, therefore, one that plastically deforms when impinged by solid particles, whereas a brittle material is one in which the impinging particles initiate cracks on the target surface [3.6, 3.16–3.19]. The influence of the target material on the erosion response is of particular interest in this study considering that many of the materials examined are metal matrix composites (MMCs). The MMCs examined throughout this thesis (Chapter 5 to Chapter 8) comprise a brittle reinforcing material, (i.e. tungsten carbide) that is embedded within a comparably ductile matrix. Therefore, the MMCs can be considered both brittle and ductile concurrently. The chapters that examine the

surface of the material post-erosion testing will discuss the influence of the brittle reinforcements within the matrix. However, it is first necessary to discuss ductile erosion and brittle erosion as independent mechanisms. This section will conclude by presenting and considering some of the existing research into the erosion performance of MMCs

3.1.1.1 Ductile erosion

Ductile erosion is characterised as a forging and extrusion process, initiated by impinging erodent particles [3.16]. When an erodent particle strikes the target surface, the contact face of that particle acts as a cutting surface, extruding the ductile material (target surface) at its leading edge [3.16]. This deformation process results in the formation of what are commonly referred to as platelets on the surface of the target material [3.16, 3.20]. Fig. 3-1 presents a schematic diagram of the ductile erosion process [3.17] and Fig. 3-2 demonstrates an extruded platelet that has formed on AA1100 following impingement by a spherical particle [3.16]. As discussed in Section 3.1.2, this phenomenon only occurs when the hardness of the impinging particle is greater than that of the target surface [3.9].

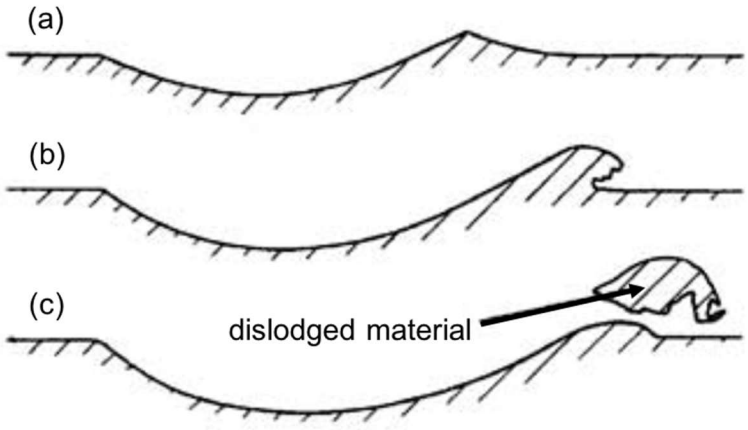

Fig. 3-1 Schematic diagram of the ductile erosion mechanism; (a) initial impact generating surface indentation; (b) continued deformation generating highly strained lip feature; (c) removal of weakened material with successive impacts [3.17]

The extruded material is thin and highly strained, and is, therefore, weak in contrast to the bulk alloy [3.12]. As a result, successive particle impacts cause this weakened material to detach from the surface through a low cycle fatigue process [3.12]. Under greater impact angles, i.e. approaching 90°, the extrusion (often referred to as ploughing) caused by the impinging particle becomes less evident [3.6]. Instead, impact craters are produced on the surface of the ductile material comprising a central

indentation, typically reflecting the shape of the impinging particle, surrounded by a ring of highly strained material [3.16]. As with low impact angles, the highly strained material is weak and is therefore easily detached by subsequent particle strikes. Existing research [3.16] has shown that the formation of platelets and craters is not unique to aluminium and that several grades of steel also experience this form of damage. The alloys investigated (AA1020, AA4340 and SS304) formed platelets of similar size and shape to those observed in the aluminium alloy [3.16].

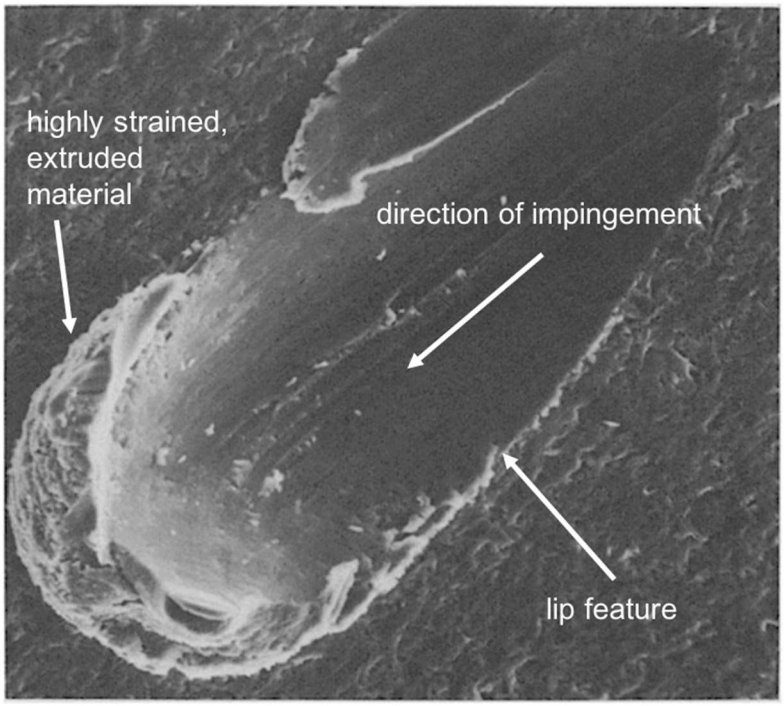

Fig. 3-2 Single particle impact on AA1100 [3.16]

While the extrusion model is widely accepted for shallow impingement, several different erosion mechanisms have been proposed for steep (near 90°) impact angles. These include low cycle fatigue by repeated plastic deformation [3.12], embrittlement of the target material by strain hardening [3.21]. Within recirculating slurry systems, additional erosion from the fractured impinging particles (following their initial impact) can also increase the rate of mass loss [3.22].

3.1.1.2 Brittle erosion

Brittle materials cannot plastically deform when impinged by a solid particle because of their low toughness and, as such, are prone to cracking upon impact [3.5]. Therefore, the removal of material from brittle surfaces typically occurs through crack generation and propagation [3.5, 3.14, 3.23]. When an impinging particle strikes the

target, small lateral and radial cracks form on the surface. Once the initial fracture has occurred, repeated impacts cause the cracks to propagate through the material until they intersect other fracture surfaces [3.5].

The damage experienced by brittle surfaces is closely linked to the size and shape of the impinging particles [3.23]. Large, spherical particles travelling at low velocity generate only minimal elastic deformation on the surface. However, when the force exerted by the particle exceeds a critical value, cracks will propagate from flaws on the target surface [3.17]. Substantial material loss occurs when multiple fracture surfaces intersect [3.5].

Conversely, small, faceted particles travelling at high velocities create a small region of plastically deformed material even in highly brittle materials such as ceramic or glass [3.5, 3.23]. The size of the plastic zone increases until the material can deform no more, and the particle reaches its maximum penetration depth [3.5, 3.23]. At this point, radial and transverse cracks develop on the surface owing to the inability of the material to undergo further plastic deformation (Fig. 3-3) [3.23]. Significant material loss occurs when cracks propagate and fracture surfaces intersect [3.5]. A schematic diagram illustrating the erosion damage generated on brittle surfaces can be seen in Fig. 3-4.

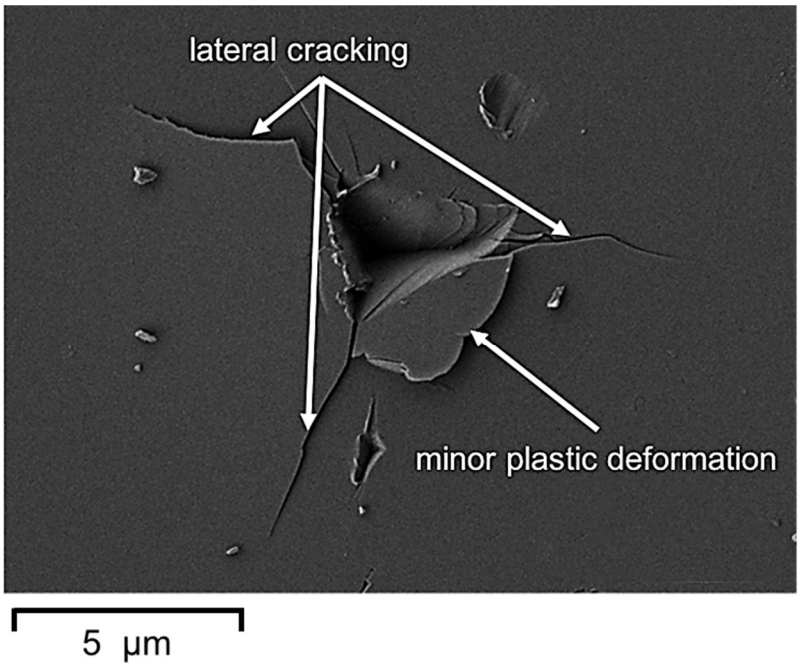

Fig. 3-3 Surface of a brittle material (quartz glass) following impingement by faceted particles [3.23]

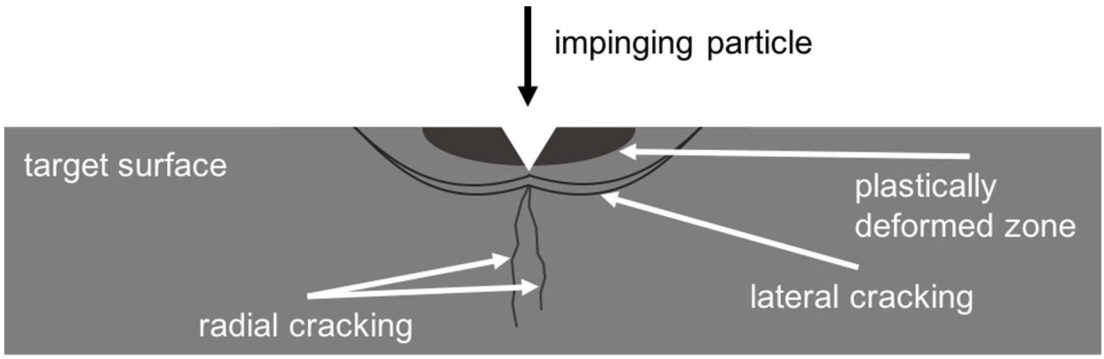

Fig. 3-4 Schematic diagram of a single particle impact on a brittle target material

3.1.2 Effect of the erodent properties on erosion

The properties associated with the impinging material also have a considerable effect on the erosion that occurs on the target surface [3.7–3.9]. The experimental test programme employed during this investigation does not examine the influence of different erodent materials on the material loss from the SprayStirred surface. However, to present a detailed overview of the erosion process, it is necessary to discuss the influence of the erodent material on the resulting mass and volume loss.

3.1.2.1 Erodent Size

As reported by several research groups [3.7, 3.8, 3.24–3.26], the size of the erodent particle has considerable influence over the erosion rate experienced by the impinged material. Neville et al. [3.26] investigated the influence of two different sizes of silica particle on a WC-CoCr based metal matrix composite (MMC) produced by plasma transferred arc (PTA) weld overlay process [3.27] on AISI316L. The study [3.26] concluded that impingement of the coarse particles caused greater mass loss from the target surface than the comparably fine particles. Conversely, the mass loss of the uncoated steel was higher than the MMCs, when both specimens were impinged by fine eroding particles [3.26].

To elucidate their findings, the authors [3.26] examined micrographs of the impinged region and identified discrete erosion mechanisms generated by the coarse and fine particles. The fine particles attacked either the matrix or the reinforcement phase separately, whereas the coarse particles impinged on both matrix and reinforcement simultaneously. The damage caused by the coarse particles was attributed to their larger diameter and, thus, a greater contact area on the surface [3.26]. Consequently, the erosion performance was directly related to the cohesive

strength between the reinforcement phase and the matrix, when impinged by coarse particles [3.26].

The influence of particle size on the slurry erosion of stainless steel (S304) was assessed experimentally and numerically by Nguyen et al. [3.8]. The authors [3.8] measured the erosion rate of specimens when impinged by coarse particles then repeated the experiment with fine particles. As in the study by Neville et al. [3.26], the authors [3.8] reported that both numerical and experimental results demonstrate an increase in the erosion rate when coarse sand particles are present in the slurry. Moreover, Nguyen at al. [3.8] noted that during their investigation, the erosion rate varied depending on the size of the eroding particles. The maximum erosion rate was attained when the average size of the eroding particles was 150 μm, however, a further increase in the particle size did not correspond to an increase in the erosion rate [3.8].

The authors [3.8] attributed their finding to the distribution of erodent particles within the slurry jet. Specifically, as the particles increase in size, they are less prone to deviate from the centre of the jet stream and hence are concentrated at the centre of the jet. This observation accounts for the increased erosion rate as the particle size increases [3.8]. However, above 150 μm, the particles exhibit almost no deviation from the centre of the jet stream. Therefore, when they impinge, they rebound back along the path of impingement into the route of the incoming particles [3.8]. Consequently, the impinging particles are prevented from impacting the target surface, thus reducing the erosion rate [3.8]. The lower erosion rate associated with fine particles is a consequence of the particles dispersing over a wider area leading to a reduction in the number of successive impacts on the same surface region. Additionally, the fine particles exert less force on the surface as they possess less kinetic energy [3.8].

3.1.2.2 Erodent Geometry

Several research groups have identified that the shape (geometry) of the erodent particle influences the plastic deformation and thus the erosion performance of the impinged surface [3.20, 3.24, 3.28]. Levy and Chik [3.20] examined the effect of particle shape on the erosion performance of AISI 1020 steel by calculating the erosion rate when impinged by faceted particles. The experiment was repeated with spherical particles to establish the variation in erosion rate [3.20]. To maintain consistency between the experiments, the faceted and spherical particles were comprised of the same grade of steel and were equal in size [3.20].

The study reported that the erosion rate of specimens impinged by the faceted particles demonstrated a 300% increase over specimens impinged by spherical particles [3.20]. Examination of the eroded surfaces showed that the faceted erodent produced deep angular craters on the target surface [3.20]. The spherical particles did not extrude the material to the same extent as the faceted erodent, and instead produced shallow, rounded craters on the surface. The enhanced erosion rate measured on specimens impinged by the faceted erodent was attributed by Levy and Chik [3.20] to the production, and subsequent removal, of greater quantities of highly strained, extruded material.

While examining several characteristics of erosive particles, Liebhard and Levy [3.7] established that the erosion rate exhibited a direct correlation with particle size, up to a peak particle diameter, for specimens impinged by spherical particles. Thereafter, the erosion rate dropped as the particle size was further increased [3.7]. The authors [3.7] postulated that the decrease in mass loss above this diameter (300 μm) is due to the decrease in the number of particles striking the surface. Equally, Liebhard and Levy [3.7] suggested that these larger particles (>300 μm) were unable to penetrate the surface of the specimen to the same extent as the smaller particles, and hence cause less plastic deformation on the surface [3.7].

Contrastingly, the erosion rate produced by faceted material continued to increase with particle size and exhibited no “maximum particle diameter”, over which the erosion rate dropped [3.7]. However, the erosion rate for faceted particles did plateau. The increase in erosion rate between faceted and spherical erodent was nearly a factor of 10 for the small particles (250 – 355 μm) and up to almost 40 times for the large particles (495 – 600 μm) [3.7].

3.1.2.3 Erodent Hardness

The influence of erodent hardness on the erosion rate of AISI316 was assessed by Arabnejad et al. [3.9] under submerged slurry jet conditions. The authors [3.9] identified a correlation between hardness and erosion rate by measuring the mass loss generated by several different erodents under consistent test conditions. Erosion rate was defined as the mass loss of the specimen divided by the total mass of erodent that was impinged on the surface throughout the experiment (Equation 3-1). While the erodent hardness was found to affect the erosion rate, the kinetic energy and morphology of the particle were also identified as key factors [3.9]. The normalised erosion rate was obtained by dividing the erosion rate by the particle

velocity (V) squared and a factor that accounted for the particle morphology (δ). Hence, Equation 3-2 correlates erosion rate to the erodent hardness [3.9].

$$\text{Erosion Rate} = \frac{\text{total mass loss}}{\text{total mass of impinged erodent}} \qquad \text{Equation 3-1}$$

$$\frac{\text{Erosion Rate}}{V^2\delta} \propto \text{hardness}^{0.89} \qquad \text{Equation 3-2}$$

The erosivity of a particle is dependent on its ability to transfer a concentrated force directly onto the target surface [3.9]. Eroding particles that have a lower hardness compared with the target surface, deform upon contact [3.9]. Hence, their kinetic energy is not effectively transferred to the target surface. Moreover, the authors [3.9] established that above a specific hardness value, further increasing the erodent hardness did not translate to a corresponding increase in the erosion rate.

3.1.3 Influence of slurry impact angle

In slurry erosion conditions, the angle at which the slurry impinges on the target material is dependent on the geometry of the surrounding pipework or components. Therefore, it is necessary to consider the influence of different angles of impingement when establishing the erosion performance of a material. Hence, subsequent chapters will examine near-perpendicular (90°) impingement and comparably shallow impingement to determine the effect of the angle of attack on the erosion properties of the MMCs (and other examined materials). To provide context for this examination, the influence of impingement angle will be discussed herein, by referring to the existing published literature.

Studies [3.14, 3.21, 3.29–3.31] investigating particle impact on ductile and brittle materials indicate that the angle at which the particles strike the surface dictates the rate at which erosion occurs on the surface. Ductile materials experience the highest erosion rate at shallow angles, typically less than 30° [3.30, 3.31]. Conversely, brittle materials such as ceramics and glass experience their highest erosion rates when impinged at angles approaching 90° [3.14]. This relationship between the angle of attack and the properties of the target material was first established by Finnie [3.18] and expanded on by several research groups [3.14, 3.21, 3.29, 3.30]. Fig. 3-5 [3.18] demonstrates the correlation between the angle of attack and the erosion rate for brittle and ductile materials.

The increased erosion rate of ductile materials at low impact angles is attributed to the enhanced quantities of plastically deformed material produced as the particles plough (extrude) and cut the target surface [3.30]. This deformation process generates weakened material that is removed by subsequent impacts, thus promoting the greater erosion rate (Fig. 3-5) [3.18]. Conversely, brittle materials exhibit low erosion rates at low angles of impingement as the eroding particles are unable to plastically deform the surface [3.14, 3.18]. As the angle approaches 90°, the force applied by the particle is applied perpendicular to the target surface [3.23]. Consequently, cracks develop on the surface and propagate radially and transverse from the point of impact [3.23]. Material loss occurs when fracture surfaces intersect, and material is dislodged from the surface [3.5].

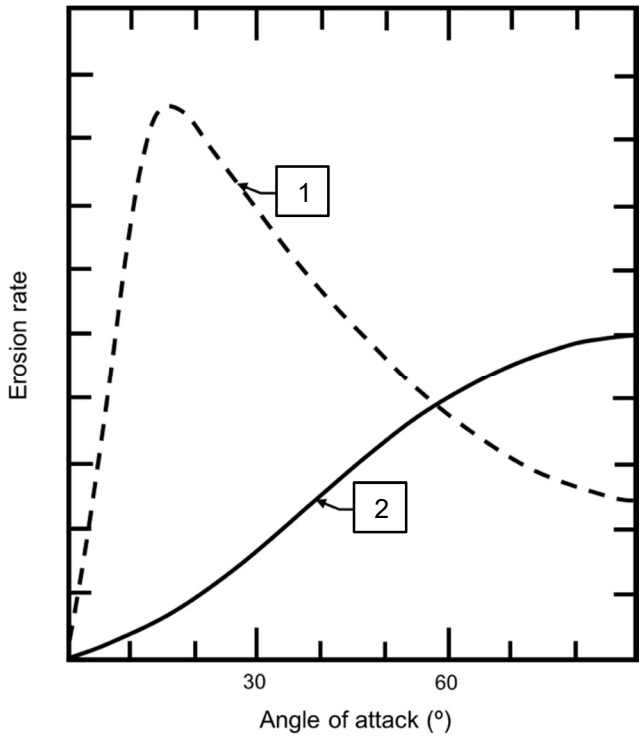

Fig. 3-5 Variation in erosion rate with respect to impact angle for; (1) ductile material, (2) brittle material [3.18]

The influence of impingement angle on the erosion rate of different materials has been investigated by numerous research groups [3.14, 3.30, 3.32]. For example, Oka et al. [3.32] studied the erosion rate of a range of metallic alloys, a ceramic (alumina) and a polymer (nylon 6) when impinged at several different angles of attack. The authors [3.32] discovered that the steel and polymer materials exhibited a ductile response, demonstrating increased erosion rates at shallow angles of attack. Correspondingly, as the ductility of the respective alloys decreased, the angle at which

maximum erosion took place increased. The maximum erosion rate of the brittle alumina specimen occurred at 90°, and hence aligned with Finnie's model (Fig. 3-5) [3.18].

Similarly, Wellman and Allen [3.14] reported that the maximum erosion rate of a range of ceramic materials occurred at 90°. The authors [3.14] highlighted lateral fracture surfaces leading to the formation and subsequent removal of chips from the target surface. These surface features align with the brittle erosion mechanism discussed in Section 3.1.1

Al-Bukhaiti et al. [3.30] explored the influence of impingement angle on the erosion performance of 1017 steel and high-chromium cast iron under slurry test conditions. The authors [3.30] mounted test coupons on a rotating arm positioned under a slurry (silica sand and water) jet that impinged on the surface at 1.62 m/s [3.30]. The test rig incorporated two slurry agitator tanks to improve the homogeneity of the solid particle-liquid mixture. The mass loss from the test coupons was measured and the impinged region was inspected by optical and scanning electron microscopy.

The authors [3.30] also conducted additional short-duration erosion tests to better examine the individual particle impacts and, hence, establish the mechanisms of material removal. The results of the study [3.30] revealed that under shallow angles of impingement (≤15°), the primary erosion mechanism on the steel specimens was ploughing of the material. At near-perpendicular angles, surface indentation and extrusion became the dominant erosion processes [3.30]. For the specimens containing high levels of chromium, the erosion mechanism was a combination of plastic deformation and brittle fracture of the matrix and carbides respectively [3.30]. The results showed that for the steel and high-chromium specimens, the maximum erosion rate occurred at approximately 45° and 90° respectively [3.30].

3.1.4 Slurry erosion of metal matrix composites

The scope of the present study extends to the examination of particle reinforced metal matrix composite (MMC) materials. Therefore, it is important to elaborate on how the erosion mechanisms vary between materials that demonstrate either purely ductile or purely brittle erosion, or those that comprise a ductile matrix and brittle reinforcement phase [3.33].

The influence of impingement angle on the erosion performance of a thermally sprayed Ni-Al_2O_3 coating deposited on CA6NM steel was investigated by Grewal at al. [3.34]. Within their study [3.34], the coated specimens, containing approximately

40 wt.% Al_2O_3 reinforcements, enhanced the erosion performance of the steel by two to four times. The primary erosion mechanism was identified as cracking of the Al_2O_3 particles leading to the removal of large volumes of material [3.34]. The erosion was further enhanced by the removal of Al_2O_3 particles caused by subsurface crack propagation through the nickel matrix [3.34].

An extensive study into the erosion of carbide-metal composites was completed by Ninham and Levy [3.15]. The authors [3.15] assessed several carbide reinforced materials under consistent erosion conditions to evaluate the erosion mechanisms operating on the surface. The influence of reinforcement quantity (vol.%) on the resulting erosion mechanisms was also examined by evaluating different ratios of matrix to reinforcement [3.15]. For specimens containing a low quantity of reinforcement (<25 vol.%), the erosion rate increased as the amount of reinforcement increased [3.15]. This relationship was attributed to a reduction in the ductility of the matrix and fracturing of the carbide reinforcements [3.15]. At approximately 80% reinforcement content, the authors [3.15] discovered that the erosion mechanisms operating on the surface were no longer governed by the properties of the ductile matrix, and were instead dictated by the material properties of the reinforcements. Moreover, the authors [3.15] concluded that when the erosion mechanism is dominated by the fracture of carbide reinforcements, it is the size and distribution of these reinforcements that dictate the erosion performance of the MMC.

Wood et al. [3.35] investigated tungsten carbide (WC) based coatings deposited via detonation gun spraying. The specimens were examined following exposure to slurry impingement at 30° and 90° [3.35]. At 30°, the authors [3.35] observed ploughing of the ductile binder alloy which subsequently exposed the reinforcement phase (WC) to the slurry jet [3.35]. Without any binder to retain them within the matrix, the reinforcements were removed from the surface by the impinging slurry [3.35]. The researchers [3.35] also noted that the detached reinforcements caused additional erosion of the target surface as they functioned as a secondary erodent within the slurry [3.35]. Under 90° impingement, the erosion mechanism was dominated by crack propagation and subsequent spalling of the particle reinforced MMC. Specifically, the eroding particles produce sub-surface cracks, which propagate with successive impacts [3.35]. When these micro-cracks intersect one another, or any pre-existing defects in the MMC, substantial quantities of material were removed [3.35].

Based on the reviewed literature [3.15, 3.34, 3.35], the key variables that dictate the erosion mechanism of a specific particle reinforced composite are the quantity of reinforcing particles, the size of the reinforcements relative to the size of the impinging particles and the distribution of the reinforcing particles throughout the matrix. These variables will, therefore, be examined when investigating the erosion mechanisms that operate on the various particle reinforced specimens examined in later chapters.

3.2 Overview of Corrosion

When metals corrode in an aqueous environment (seawater, fresh water, damp atmosphere, wet soil), the degradation experienced by the alloy is caused by an electrochemical reaction between the solution and the alloy [3.2, 3.36–3.38]. For corrosion to take place in neutral aqueous solutions (e.g. seawater), the process necessitates the transfer of an electrical charge between the anode (the corroding surface) and the cathode (the aqueous solution) [3.37]. Considering that the materials discussed in later chapters were assessed under erosive and corrosive environments, it is necessary to explore their corrosion properties. This section provides a brief overview of the corrosion phenomenon and will be expanded on, where necessary, in relevant chapters.

3.2.1 Anodic and cathodic reactions

The corrosion process comprises two simultaneous reactions; an anodic reaction in which electrons move from the solid metal (anode) to the aqueous solution (cathode) and a corresponding cathodic reaction which involves the reduction of either hydrogen ions or oxygen from the aqueous solution [3.39].

The rate at which a metal corrodes in an aqueous solution is governed by the rate of charge transfer between the anode and cathode [3.40]. As such, the amount of material loss experienced by the metal is directly proportional to the magnitude of the electrical current (I_{corr}), in accordance with Faraday's laws of electrolysis [3.40, 3.41]. Therefore, the precise measurement of I_{corr} enables the rate of material loss to be monitored [3.42].

3.2.2 Electrode potential

The electrode potential of a metal can be measured to establish its corrosion rate [3.41]. To measure the electrode potential, a reference electrode is connected

via a high impedance voltmeter to measure the voltage across the working electrode (the corroding material of interest), with respect to the reference electrode [3.39]. Typically, a silver/silver chloride electrode (Ag/AgCl) or a saturated calomel electrode serves as the reference electrode [3.39].

When a metal is exposed to an aqueous environment, there is a point at which further metal dissolution is prevented by the build-up of electrons that electrostatically oppose the anodic reaction [3.39]. This point is known as the equilibrium potential (E_o) [3.43]. For each reaction (cathodic and anodic), the value of E_o depends on the temperature and concentration of elements that are present during the reaction [3.39].

The rate at which corrosion takes place is a function of the current flowing through the cell with respect to time (charge transfer) [3.44]. As previously stated, if the electrode potential of a metal is equal to E_o, the driving force promoting the transfer of electrons is balanced, and hence, no charge transfer will occur [3.39]. As the electrode potential is moved from E_o in the positive direction, the electrons move from the metal to the solution (anodic reaction). Correspondingly, if the electrode potential across the metal surface is less than E_o, the reaction is driven in the cathodic direction [3.39]. The change in potential with respect to the reference electrode is known as polarisation [3.44]. Polarisation is the driving force behind the anodic and cathodic reactions on the surface of the metal and hence controls the rate of these reactions [3.44]. Furthermore, the greater difference between the electrode potential and E_o yields a greater driving force and hence increases the rate of the anodic reaction [3.39]. This relationship [3.39] is also applicable to the cathodic reaction.

While the occurrence of change transfer is associated with the potential of the metal, the rate of the reaction is related to the number of electrons moving from the metal to the solution, i.e. the current [3.39]. Therefore, the rate of corrosion can be expressed in terms of the current flowing in the circuit [3.39]. This “corrosion current” can be converted to metal loss (mm of thickness loss or mg loss per year) using Faraday’s law [3.40, 3.41].

The relationship between current and potential can be expressed using the Tafel relation (Equation 3-3), where $(E - E_0)$ is the difference between the measured and reference potentials, (b_a) is the Tafel constant, (I_a) is the current and (I_o) is the exchange current density [3.44]. This relationship is typically illustrated on a polarisation diagram (Fig. 3-6), where the gradient of the line is the Tafel constant [3.44].

$$(E - E_o) = b_a \log_{10}\left(\frac{i_a}{i_o}\right)$$ Equation 3-3

3.2.3 Polarisation measurements

The material discussed thus far concerns the spontaneous anodic and cathodic reactions that take place on the surface of an alloy when exposed to a corroding solution. However, this theory can be extended and used to determine the corrosion rate of a particular material [3.41]. The point at which the anodic and cathodic reactions are balanced is known as the corrosion potential (E_{corr}). When the potential of a specimen is at E_{corr}, the anodic and cathodic currents are balanced, and hence there is no net transfer of charge [3.44]. To clarify, this does not mean that no corrosion is taking place on the metal, but rather that the rate of the oxidation and reduction reactions (Section 3.2.1) are equal [3.44]. Polarisation measurements involve shifting the potential in either the anodic or cathodic directions in relation to E_{corr} [3.45]. Shifting the potential more positive to E_{corr}, causes the anodic current to dominate at the expense of the cathodic current. The cathodic current becomes negligible as the potential across the specimen is increased further from E_{corr}. Correspondingly, by shifting the potential negative to $E_{corr,}$ the anodic current becomes negligible [3.45].

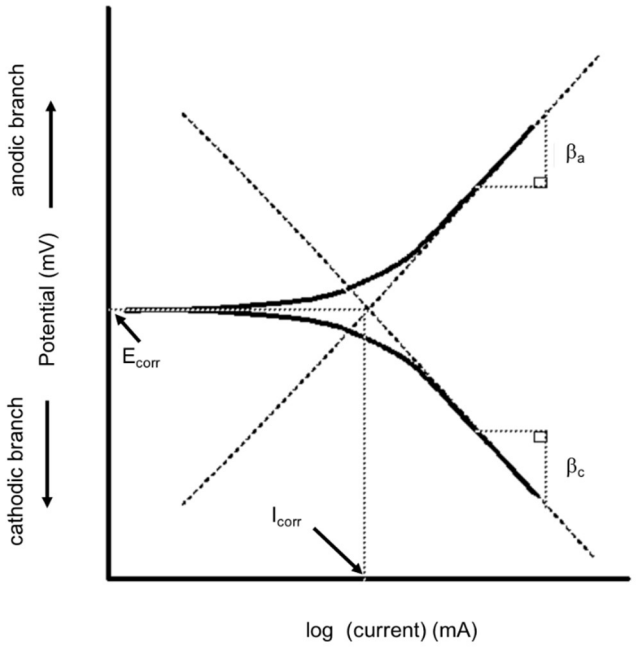

Fig. 3-6 Example of a typical Tafel plot of potential against current [3.44]

The potential across the working electrode is controlled using a potentiostat [3.39, 3.41]. The potentiostat varies the potential across the specimen by making minor adjustments to an applied current. The sample (working electrode) is connected to the potentiostat along with two other electrodes [3.39, 3.46]. A silver/silver chloride electrode (Ag/AgCl) acts as the reference, against which the potential difference across the specimen is measured [3.42, 3.47, 3.48]. A third electrode (counter electrode) is added to provide an electrical connection between the potentiostat and the working electrode. The counter electrode is typically a highly corrosion resistant material (such as platinum) to prevent any changes to the chemistry of the corroding solution over the course of the experiment [3.42].

The potentiostat shifts the potential at a constant rate by approximately 300 mV in the anodic and cathodic directions with respect to E_{corr} [3.41]. The results of the polarisation scans are plotted on a Tafel diagram (Fig. 3-6), where the logarithm of the applied current is plotted along the x-axis, and the measured potential is plotted on the y-axis [3.44]. β_a and β_c represent the gradient of the anodic and cathodic Tafel slopes [3.44].

3.2.4 Corrosion rate

The corrosion rate of the working electrode can be determined using the data presented in the Tafel plot [3.44]. The corrosion current is established by extending the slope of the linear regions of both the anodic and cathodic curves to the point where the two lines intersect. Fig. 3-6 illustrates the linear regions of the anodic and cathodic branches of the polarisation curve [3.44]. A line is extrapolated from the point of intersection towards the x-axis to establish the corrosion current (I_{corr}) [3.44]. Often, the corrosion current is made dimensionless by dividing by the surface area of the specimen to yield the corrosion current density [3.44. 3.47]. The corrosion potential (E_{corr}) can be found by extrapolating a line from the point of intersection towards the y-axis [3.44].

The extent of material loss, in terms of mass and volume loss, from corrosion is calculated by inputting the established current density (I_{corr}) to the relationships derived from Faraday's law [3.40, 3.41]. Faraday's law states that the level of mass loss during the reaction is directly proportional to the amount of charge transferred during the anodic reaction [3.40, 3.41]. As such, the mass loss varies directly with the corrosion current (I_{corr}) [3.42]. Furthermore, Faraday states that the mass loss (Equation 3-4) is proportional to the equivalent weight of a particular element [3.49].

Hence, mass loss (M_{loss}) is dependent on the corrosion current (I_{corr}) as identified using the Tafel diagram, and Faraday's constant (K_2) [3.41, 3.44, 3.50].

$$M_{loss} = K_2 i_{corr} EW$$ Equation 3-4

The discussion thus far has only accounted for pure metals. However, experiments are rarely conducted on pure metals and instead, are typically performed on alloys [3.34, 3.40, 3.42–3.43, 3.51]. To determine the corrosion rate of an alloy, it is first necessary to establish the equivalent weight (EW) of each element within the alloy [3.49]. EW is equal to the atomic weight of an element divided by its respective valence [3.41, 3.44]. Equation 3-5 accounts for the different elements in the alloy by calculating EW, where (f_i) is the atomic weight fraction of the element, (n_i) is the valence value associated with the particular element and (W_I) is the atomic weight of the sample [3.41, 3.44].

$$EW = \left(\sum \frac{f_i n_i}{W_i} \right)^{-1}$$ Equation 3-5

3.2.5 Cathodic protection

One of the most widely adopted techniques employed to mitigate the effects of corrosion is cathodic protection [3.36, 3.39]; of which there are two types: galvanic cathodic protection (GCP) and impressed current cathodic protection (ICCP) [3.38]. GCP is implemented by connecting a more noble element (anode) to the material requiring protection (cathode). In doing so, the sacrificial galvanic anode corrodes preferentially with respect to the cathode, until it must be replaced [3.38].

During ICCP the potential of the corroding material is shifted more negative with respect to E_{corr}. This is achieved by connecting a DC power source to the circuit and varying the current to generate the required potential [3.39]. When ICCP is applied to a specimen, the negative potential suppresses the anodic reaction necessary for electrochemical corrosion [3.36]. In subsequent chapters (Chapter 5 and Chapter 8), ICCP will be employed to prevent corrosion occurring on the surface of the specimens, to establish the mass loss from erosion alone.

3.3 Erosion, corrosion and synergy

Under slurry erosion conditions, the target surface is subjected to a highly destructive environment in which two mechanisms contribute to material removal; mechanical wear from particulates within the slurry impacting on the material surface and electrochemical corrosion from the fluid [3.3–3.4, 3.42, 3.52]. Under these conditions, the degradation process is known as erosion-corrosion.

It is well established that the total material loss experienced by a specimen under combined erosion-corrosion is typically greater than the sum of the material removed by corrosion and erosion separately [3.26, 3.43, 3.49, 3.53–3.55]; and is attributed to the synergistic effect (synergy) of the electrochemical (corrosion) and erosion processes. Synergy can be caused by corrosion effects that enhance mechanical damage from the particulates [3.56]. Equally, the damage from corrosion can be enhanced by the erosive particles through the continuous removal of the passivating layer [3.57]. Regardless, the total mass loss experienced by the specimen (M_{total}) is the sum of the mass loss from erosion (E), corrosion (C) and synergy (S) and is represented by Equation 3-6 [3.3].

$$M_{total} = E + C + S \qquad \text{Equation 3-6}$$

3.4 References

[3.1] E.S. Venkatesh, Erosion Damage in Oil and Gas Wells, in: SPE Rocky Mt. Reg. Meet, Society of Petroleum Engineers, 1986.

[3.2] M.B. Kermani, D. Harr, The Impact of Corrosion on Oil and Gas Industry, SPE Prod. Oper. 11 (1995) 186–190.

[3.3] L. Giourntas, T. Hodgkiess, A.M. Galloway, Comparative study of erosion–corrosion performance on a range of stainless steels, Wear. 332–333 (2015) 1051–1058.

[3.4] A. Neville, X. Hu, Mechanical and electrochemical interactions during liquid–solid impingement on high-alloy stainless steels, Wear. 251 (2001) 1284–1294.

[3.5] E. Bousser, L. Martinu, J.E. Klemberg-Sapieha, Solid particle erosion mechanisms of hard protective coatings, Surf. Coatings Technol. 235 (2013) 383–393.

[3.6] I. Finnie, Erosion of surfaces by solid particles, Wear. 3 (1960) 87–103.

[3.7] M. Liebhard, A. Levy, Effect of erodent particle characteristics on the erosion of metals, Wear. 151 (1991) 381–390.

[3.8] V.B. Nguyen, Q.B. Nguyen, Y.W. Zhang, C.Y.H. Lim, B.C. Khoo, Effect of particle size on erosion characteristics, Wear. 348–349 (2016) 126–137.

[3.9] H. Arabnejad, S.A. Shirazi, B.S. McLaury, H.J. Subramani, L.D. Rhyne, The effect of erodent particle hardness on the erosion of stainless steel, Wear. 332–333 (2015) 1098–1103.

[3.10] S. Lathabai, M. Ottmüller, I. Fernandez, Solid particle erosion behaviour of

thermal sprayed ceramic, metallic and polymer coatings, Wear. 221 (1998) 93–108.
[3.11] M.A. Islam, T. Alam, Z.N. Farhat, A. Mohamed, A. Alfantazi, Effect of microstructure on the erosion behavior of carbon steel, Wear. 332–333 (2015) 1080–1089.
[3.12] A. V. Levy, The solid particle erosion behavior of steel as a function of microstructure, Wear. 68 (1981) 269–287.
[3.13] L. Thakur, N. Arora, R. Jayaganthan, R. Sood, An investigation on erosion behavior of HVOF sprayed WC-CoCr coatings, Appl. Surf. Sci. 258 (2011) 1225–1234.
[3.14] R.G. Wellman, C. Allen, The effects of angle of impact and material properties on the erosion rates of ceramics, Fuel Energy Abstr. 37 (1996) 213.
[3.15] A.J. Ninham, A. V Levy, The erosion of carbide-metal composites, Wear. 121 (1988) 347–361.
[3.16] A. V. Levy, The platelet mechanism of erosion of ductile metals, Wear. 108 (1986) 1–21.
[3.17] D. Aquaro, E. Fontani, Erosion of ductile and brittle materials, Meccanica. 36 (2001) 651–661.
[3.18] I. Finnie, Some Reflections on the Past and Future of Erosion, Wear. 186–187 (1995) 1–10.
[3.19] P. Kulu, I. Hussainova, R. Veinthal, Solid particle erosion of thermal sprayed coatings, Wear. 258 (2005) 488–496.
[3.20] A. V. Levy, P. Chik, The effects of erodent composition and shape on the erosion of steel, Wear. 89 (1983) 151–162.
[3.21] I. Finnie, G.R. Stevick, J.R. Ridgely, The influence of impingement angle on the erosion of ductile metals by angular abrasive particles, Wear. 152 (1992) 91–98.
[3.22] G.P. Tilly, A two stage mechanism of ductile erosion, Wear. 23 (1973) 87–96.
[3.23] E. Bousser, L. Martinu, J.E. Klemberg-Sapieha, Effect of erodent properties on the solid particle erosion mechanisms of brittle materials, J. Mater. Sci. 48 (2013) 5543–5558.
[3.24] S. Lynn, K. Wong, On the particle size effect in slurry erosion, Wear. 149 (1991) 55–71.
[3.25] H.M. Clark, R.B. Hartwich, A re-examination of the ‘particle size effect’ in slurry erosion, Wear. 248 (2001) 147–161.
[3.26] A. Neville, F. Reza, S. Chiovelli, T. Revega, Erosion-corrosion behaviour of WC-based MMCs in liquid-solid slurries, Wear. 259 (2005) 181–195.
[3.27] K. Bobzin, F. Ernst, K. Richardt, T. Schlaefer, C. Verpoort, G. Flores, Thermal spraying of cylinder bores with the Plasma Transferred Wire Arc process, Surf. Coatings Technol. 202 (2008) 4438–4443.
[3.28] H.Y. Lee, S.H. Jung, S.Y. Lee, Y.H. You, K.H. Ko, Correlation between Al2O3 particles and interface of Al-Al2O3 coatings by cold spray, Appl. Surf. Sci. 252 (2005) 1891–1898.
[3.29] N. Andrews, L. Giourntas, A.M. Galloway, A. Pearson, Effect of impact angle on the slurry erosion-corrosion of Stellite 6 and SS316, Wear. 320 (2014) 143–151.
[3.30] M.A. Al-Bukhaiti, S.M. Ahmed, F.M.F. Badran, K.M. Emara, Effect of impingement angle on slurry erosion behaviour and mechanisms of 1017 steel and high-chromium white cast iron, Wear. 262 (2007) 1187–1198.
[3.31] Y.I. Oka, H. Ohnogi, T. Hosokawa, M. Matsumura, The impact angle dependence of erosion damage caused by solid particle impact, Wear. 203–

204 (1997) 573–579.
[3.32] Y.I. Oka, H. Ohnogi, T. Hosokawa, M. Matsumura, The impact angle dependence of erosion damage caused by solid particle impact, Wear. 203–204 (1997) 573–579.
[3.33] P.L. Fauchais, J.V.R. Heberlein, M.I. Boulos, Thermal Spray Fundamentals, 2014.
[3.34] H.S. Grewal, A. Agrawal, H. Singh, B.A. Shollock, Slurry erosion performance of Ni-Al2O3 based thermal-sprayed coatings: Effect of angle of impingement, J. Therm. Spray Technol. 23 (2014) 389–401.
[3.35] R.J.K. Wood, B.G. Mellor, M.L. Binfield, Sand erosion performance of detonation gun applied tungsten carbide/cobalt-chromium coatings, Wear. 211 (1997) 70–83.
[3.36] N. Muthukumar, Petroleum Products Transporting Pipeline Corrosion-A Review, Elsevier B.V., 2014.
[3.37] L. Popoola, A. Grema, G. Latinwo, B. Gutti, A. Balogun, Corrosion problems during oil and gas production and its mitigation, Int. J. Ind. Chem. 4 (2013) 35.
[3.38] D. Brondel, R. Edwards, A. Hayman, D. Hill, T. Semerad, Corrosion in the Oil Industry, Oilf. Rev. (1994) 4–18.
[3.39] D. Landolt, Corrosion and surface chemistry of metals, 2007.
[3.40] H. Xu, A. Neville, An electrochemical and microstructural assessment of erosion-corrosion of austenitic cast iron for marine applications, Mater. Corros. 53 (2002) 5–12.
[3.41] International ASTM Standard, ASTM G102 - 89 Standard Practice for Calculation of Corrosion Rates and Related Information from Electrochemical Measurements, 2015.
[3.42] V.A.D. Souza, A. Neville, Corrosion and synergy in a WC-Co-Cr HVOF thermal spray coating - Understanding their role in erosion-corrosion degradation, Wear. 259 (2005) 171–180.
[3.43] C. Hodge, M.M. Stack, Tribo-corrosion mechanisms of stainless steel in soft drinks, Wear. 270 (2010) 104–114.
[3.44] D.G. Enos, L.L. Scribner, The Potentiodynamic Polarization Scan Technical Report 33, 1997.
[3.45] A. Neville, T. Hodgkiess, J.T. Dallas, A study of the erosion-corrosion behaviour of engineering steels for marine pumping applications, Wear. 186–187 (1995) 497–507.
[3.46] R. Pileggi, M. Tului, D. Stocchi, S. Lionetti, Tribo-corrosion behaviour of chromium carbide based coatings deposited by HVOF, Surf. Coatings Technol. 268 (2015) 247–251.
[3.47] W. Liu, F. Shieu, W. Hsiao, Enhancement of wear and corrosion resistance of iron-based hard coatings deposited by high-velocity oxygen fuel (HVOF) thermal spraying, Surf. Coat. Technol. 249 (2014) 24–41.
[3.48] H. Koivuluoto, J. Näkki, P. Vuoristo, Corrosion properties of cold-sprayed tantalum coatings, J. Therm. Spray Technol. 18 (2009) 75–82.
[3.49] M. Abedini, H.M. Ghasemi, Synergistic erosion–corrosion behavior of Al–brass alloy at various impingement angles, Wear. 319 (2014) 49–55.
[3.50] E. Principles, P. Polarization, Application Note CORR-1 Subject : Basics of Corrosion Measurements, (n.d.).
[3.51] M.N. Ilman, Analysis of internal corrosion in subsea oil pipeline, Case Stud. Eng. Fail. Anal. 2 (2014) 1–8.
[3.52] V.A.D. Souza, A. Neville, Aspects of microstructure on the synergy and overall material loss of thermal spray coatings in erosion – corrosion

environments, Wear. 263 (2007) 339–346.
[3.53] M. Bjordal, E. Bardal, T. Rogne, T.G. Eggen, Combined erosion and corrosion of thermal sprayed WC and CrC coatings, Surf. Coatings Technol. 70 (1995) 215–220.
[3.54] B.G. Mellor, Surface coatings for protection against wear, Woodhead Publishing Limited, 2006.
[3.55] E.J. Wentzel, C. Allen, Erosion-corrosion resistance of tungsten carbide hard metals with different binder compositions, Wear. 181–183 (1995) 63–69.
[3.56] Y. Zhao, F. Zhou, J. Yao, S. Dong, N. Li, Erosion–corrosion behavior and corrosion resistance of AISI 316 stainless steel in flow jet impingement, Wear. 328–329 (2015) 464–474.
[3.57] S.S. Rajahram, T.J. Harvey, R.J.K. Wood, Erosion-corrosion resistance of engineering materials in various test conditions, Wear. 267 (2009) 244–254.

Chapter 4 Experimental Apparatus and Evaluation Methods

This chapter provides an overview of the various cold spray (CS) (Section 4.1) and friction stir processing (FSP) (Section 4.2) equipment utilised during the preparation of the SprayStir specimens. The apparatus used in the production of the high velocity oxy-fuel (HVOF) specimens is described in Section 4.3. Section 4.4 details the various microstructural examination techniques employed to characterise the manufactured specimens, and Section 4.5 describes the experimental methods employed to evaluate their erosion performance and corrosion properties.

4.1 Cold Spray Deposition

The present section details the apparatus used to manufacture the CS coatings throughout this investigation. Additionally, the procedure employed to develop optimised spraying parameters is presented herein. Information relating to the specific properties of the coating and substrate combinations are introduced in the relevant chapters.

4.1.1 Cold spray apparatus

A CGT Kinetiks 4000 CS system was used to deposit (and co-deposit) various powder combinations onto aluminium and steel substrates. Fig. 4-1 presents a schematic diagram of the CS setup and illustrates the different pieces of equipment that comprise the system. Fig. 4-2 depicts the CS equipment located in the dedicated spray booth.

The configuration (Fig. 4-1) incorporates a control cabinet to monitor and adjust the pressure and temperature of the process gas (Nitrogen). The primary gas heater, located immediately after the control cabinet (Fig. 4-1), raises the temperature of the process gas to the specified value (t_{max} of 450°C). The secondary heater, contained within the cold spray gun, enables the gas temperature to be further increased up to 800°C. The two powder feeders (Kinetiks 4000 Comfort) can operate independently or in parallel to supply the binder and reinforcing particles simultaneously to the CS nozzle.

A Type 24 de-Laval nozzle, constructed from tungsten carbide was employed in this study. The nozzle comprised an exit diameter of 6.1 mm and a throat diameter of 2.7 mm. A schematic diagram of the nozzle is presented in Chapter 2 (Section 2.3.1). A water-cooling system was secured over the nozzle to prevent any thermal

damage from the secondary heater. The cold spray gun was manipulated using a 6-axis industrial robot (OTC FD-V50).

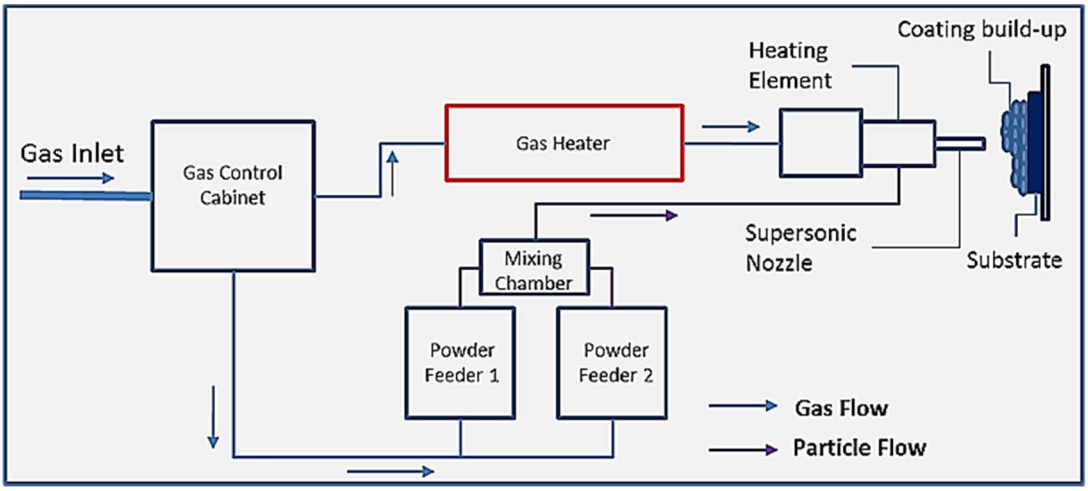

Fig. 4-1 Schematic diagram of the cold spray apparatus

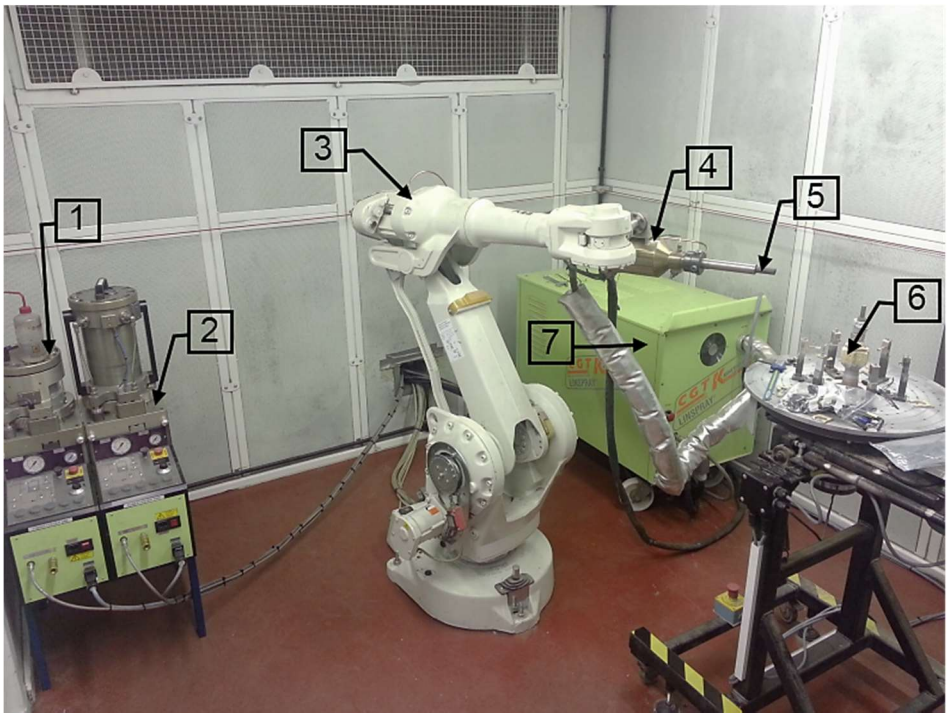

Fig. 4-2 Image of the cold spray apparatus; (1) powder feeder 1, (2) powder feeder 2, (3) Industrial robot, (4) cold spray gun, (5) cold spray nozzle, (6) specimen stage, (7) gas heater

In the current setup (Fig. 4-1), the process gas (Nitrogen) was supplied from external storage cylinders into the control cabinet via fixed pipework. The majority of the gas was directed to the primary gas heater while a small percentage was diverted to the powder feeders. The gas was heated and thereafter flowed to the secondary heating element, located in the CS gun. Afterwards, the hot process gas entered the

nozzle pre-chamber where the feedstock powders were introduced. The combined stream of gas and powder particles were accelerated through the de-Laval nozzle and onto the surface of the substrate.

The substrate plates were secured to the specimen stage using fabricated mounting brackets. The industrial robot, with the CS gun attached, scanned across the surface of the plates at the specified standoff distance to spray multiple layers of powder.

4.1.2 Cold spray co-deposition process development

The difference in the density of the various reinforcing and binder powders necessitated the use of volume ratio, as opposed to mass ratio, to supply the feedstock powder to the CS nozzle. The aperture dimensions of the powder feeders were measured and the volumetric aperture ratio (AR) between the two feeders calculated. The measured values were used to define the volumetric feed rate necessary to supply the desired ratio of reinforcing particle and binder. For clarity, when referring to the co-deposited ductile particles, the term “binder” is used for pre-deposition, with “matrix” used for post-deposition.

The rotational velocity of the feeder required to supply the specified ratio of binder to reinforcement was calculated using Equation 4-1, where ω_r is the rotational velocity of the powder feeder containing the reinforcing particles and ω_m is the velocity of the feeder containing the binder powder.

$$\omega_r = \omega_m \left(\frac{\text{Vol.}\,\%_r}{\text{Vol.}\,\%_m}\right) \text{AR} \qquad \text{Equation 4-1}$$

The spraying parameters identified as having the greatest influence on the quality of the deposited coating were gas temperature and gas pressure; the speed at which the CS nozzle traverses across the surface of the substrate and the CS nozzle standoff distance [4.1]. For this study, a high quality coating was one with no spalling of the deposited (or co-deposited) material and a minimum coating thickness of 0.1 mm.

An iterative approach was adopted to determine the optimal spraying conditions to achieve a dense, well-adhered coating. The adhesion strength of the coating was not measured via pull-off testing at this stage, but rather by visual examination of the coating surface.

The amount of material deposited on the surface of the substrate was evaluated for three reinforcement to binder ratios; 30/70, 60/40, and 90/10 by

measuring the coating thickness and mass increase following deposition onto a series of test coupons. In each case, the quantity of reinforcement phase within the coating was measured using suitable image analysis software (ImageJ). These ratios (30/70, 60/40, and 90/10) were selected in an attempt to deposit the greatest quantity of reinforcement on the surface whilst not creating a surface that was impossible, or extremely difficult to FSP.

4.2 Friction Stir Processing

4.2.1 Process parameters

FSP consists of four distinct stages: the plunge, dwell, traverse and retract. During the initial plunge stage, the rotating tool was brought into contact with the workpiece, and a load subsequently applied to drive the tool into the metal. Position (fixed depth) or force (fixed force) control, or a combination of both, can be used to manipulate the plunge depth [4.3]. In this study, the aluminium specimens (Chapter 6 and Chapter 7) were manufactured using position control, and the steel specimens (produced at a different facility) were manufactured using force control (Chapter 8).

Thereafter, the rotating tool was held (i.e. the tool bed remained stationary) at the desired plunge depth to increase the temperature within the stir zone and allow the forces acting on the tool to stabilise (the dwell stage [4.2]). During the dwell, the shoulder was fully in contact with the workpiece and, as such, considerable heat was generated in the stir zone [4.4].

The increase in temperature locally plasticised the metal, thereby allowing the tool to progress forward through the plate (traverse stage) [4.5]. During the traverse, the rotating tool plasticised the metal immediately in front of the stir zone [4.6] and forced the softened material around and to the rear of the tool, where it consolidated forming the stir zone [4.7]. The retraction of the tool from the plate marked the fourth stage and the conclusion of the FSP process [4.2].

A total of six FSP passes were completed on each substrate plate, which measured 500 x 125 x 6 mm. A maximum of three parallel FSP passes were completed on each plate with each pass offset by a minimum of 10 mm to prevent subsequent passes affecting adjacent stir zones. When processing the coated plates, the tool path commenced at the uncoated section of the substrate and traversed onto the cold sprayed coating, where it continued for a total distance of 100 mm.

4.2.2 Equipment

Friction stir processing (FSP) was performed using a TTI precision spindle, friction stir welding/processing machine; an image of which is presented in Fig. 4-3.

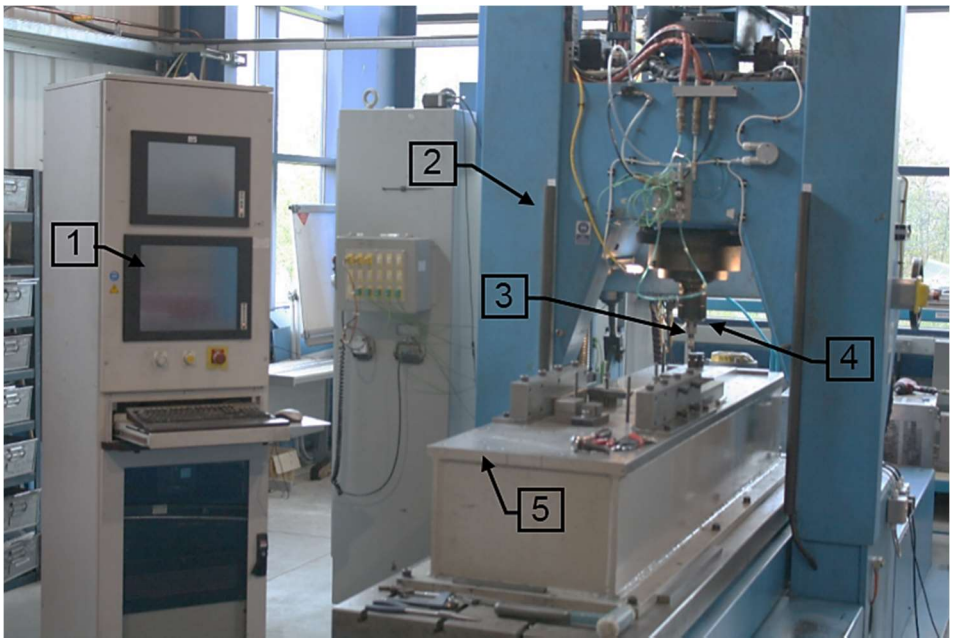

Fig. 4-3. Image of the FSP apparatus; (1) control cabinet, (2) TTI FSP rig, (3) FSP tool, (4) rotating spindle, (5) mobile specimen bed

The control cabinet is the primary interface with the machine and enables the operator to input the specific FSP processing parameters. Various sensors mounted in the FSP rig measure the forces on the tool in the transverse, longitudinal and vertical directions and the temperatures at specified points in the workpiece (when suitable thermocouples are installed), and relay this real-time data to the monitor on the control cabinet. The resulting data can be exported to an Excel data file to correlate the loads, temperatures and displacements that were recorded during the process, to physical changes in the processed region.

The FSP rig houses the motor, spindle head and cooling jacket. A cooling jacket was necessary for processing of steel substrates (Chapter 8), owing to the higher temperatures involved. Without a cooling system, the tool would likely overheat, resulting in increased tool wear [4.8]. Xue et al. [4.9] examined the influence of a cooling system when conducting FSP on a Nickel alloy. The authors [4.9] noted the complete failure of the FSP tool when the cooling system was not employed, while the use of a cooling system resulted in a defect-free stir zone. For processing aluminium substrates (Chapter 6 and Chapter 7), no cooling system was required.

Any movement within the FSP rig may alter the contact conditions between the tool and workpiece, thereby potentially disrupting the path the tool takes through the material (processing path) [4.10]. Consequently, the rig must be capable of remaining rigid to ensure that a consistent load or plunge depth was applied to the tool [4.11]. The FSP machine bed acted as an anvil providing a hard, solid surface on which to process the alloy while also offering a clamping point on which to secure the workpiece [4.10]. The setup employed in this study consisted of a heavy-duty steel backing plate and clamps that were bolted to the tool bed. The backing plate was necessary to protect the bed from the high temperatures within the workpiece.

4.2.3 Tool design

The FSP tool is one of the most important aspects of the FSP process. The tool comprises two main components; a shoulder and a pin. The purpose of the shoulder is to frictionally heat the surface of the workpiece, provide the forging action required to consolidate the plasticised material at the rear of the stir zone [4.5], and also constrain the plasticised material beneath the surface of the shoulder (as discussed in Chapter 2). The pin provides additional frictional heating and encourages the movement of the plasticised material [4.6, 4.12].

There are numerous variants of tool geometry and material; however, all tools fall into one of two categories: fixed or adjustable [4.12]. Fixed tools are constructed from a single piece of material with fixed probe and shoulder geometry. If the fixed tool becomes damaged, the entire tool must be replaced. Adjustable tools comprise two distinct pieces - the shoulder and the pin. Both (pin and shoulder) can be constructed from the same, or dissimilar materials. The pin can be replaced if damaged, while the shoulder can be reused. The FSP tools utilised in this study include both fixed (Chapter 6 and Chapter 7) and adjustable tools (Chapter 6 and 8).

The selection of an appropriate tool material is critical for FSP. Improper selection of the tool material can lead to excessive wear, resulting in a change to its dimensions and, hence, increase the likelihood of defects within the stir zone [4.12, 4.13]. Equally, as the tool wears, the tool material can become embedded within the matrix of the workpiece, thus compromising the integrity of the stir zone [4.14]. Researchers [4.15] have noted that, in some cases, tool wear can create a self-optimised tool geometry that suffers no additional tool wear, and is capable of creating a defect-free processed region.

H13 is a chromium-molybdenum steel that is widely used in hot work and cold work tooling applications [4.12]. One property of H13 steel is that it is resistant to thermal fatigue cracking which can occur as a result of cyclic heating and cooling cycles. Due to its high toughness [4.12] and resistance to thermal fatigue cracking, H13 is commonly used for FSP of aluminium alloys [4.12] and has been employed in this study (Chapter 6 and 7) to process the aluminium specimens.

Tools can also be manufactured from tungsten carbide (WC) and other refractory materials (niobium, molybdenum) for high temperature FSP applications. A WC tool was trialled for the FSP of AISI316 in Chapter 8. While the WC tool was capable of processing the as-received AISI316, the addition of the reinforcements within the SprayStirred layer generated excessive tool wear, rendering the tool unusable after only one or two passes. Consequently, it was necessary to explore polycrystalline cubic boron nitride (pcBN) tools for processing the SprayStirred AISI316 specimens (Chapter 8).

The pcBN based tool was originally developed for machining tool steels and superalloys [4.12]; and is now widely accepted as the standard for FSP tooling, owing to its excellent mechanical and thermal performance [4.12]. However, pcBN tools suffer from low fracture toughness and poor machinability. This limits the range of geometries that can be manufactured. Furthermore, the production process (sintering under high temperature and pressure) is considerably more costly than when using other tooling materials (i.e. H13 or refractory materials) [4.12]. The specific details of the FSP tools employed at each stage of this study will be presented within the associated chapter.

4.3 High Velocity Oxy-Fuel (HVOF)

HVOF spraying was completed using three different HVOF systems. The Tafa Model JP-5000 HVOF system [4.16], produced by Praxair was used to deposit the chromium carbide (CrC) feedstock powder while the Diamond Jet HVOF system developed by Oerlikon Metco facilitated the deposition of the tungsten carbide (WC) based cermet powder. The JP-5000 system was used to deposit the CrC based MMCs due to the reduced dwell time of the feedstock powder in the combustion chamber when compared to other systems [4.17]. The reduced dwell time yields fewer oxides in the deposited coating and is thus beneficial for coatings intended for use in corrosive environments.

The TopGun HVOF system [4.16], produced by Ibeda, was used to deposit the Al_2O_3 powder due to the higher flame temperatures generated by this equipment. The increase in temperature is sufficient to elevate the Al_2O_3 particles above the solidus thereby enabling the particles to flatten upon contact with the surface of the substrate, hence yielding lower porosity in the coating. This is particularly necessary for Al_2O_3 powder due to the lack of any inherent metallic binder. The specific deposition parameters associated with each of the three HVOF systems are detailed in Chapter 5.

All of the three systems (JP-5000, Diamond Jet and TopGun) incorporate an HVOF gun, control cabinet, powder feeder and cooling system. Additionally, the HVOF gun was mounted on a six-axis industrial robot (ABB) to improve the repeatability of the deposition process. The robot moved in the vertical plane while the specimens rotated in the horizontal plane (Fig. 4-4). Before spraying, the surface of the substrate was prepared by grit blasting. Brown alumina with an average particle size of 260 μm was impinged on the specimen surface to remove any contaminants. The plates were subsequently de-greased using methylated spirit. Square samples of the substrate were mounted on a rotating rig to increase the number of test coupons that could be sprayed simultaneously.

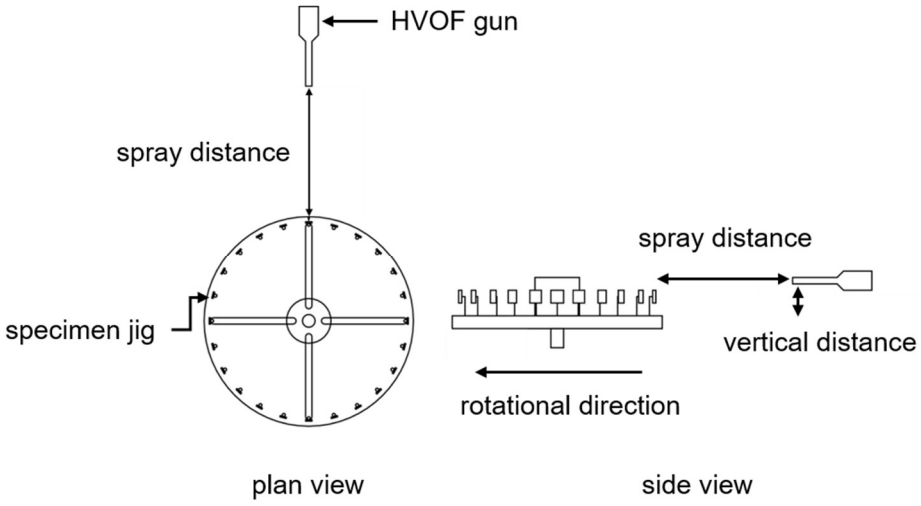

Fig. 4-4 Schematic diagram of the HVOF spraying setup (not to scale)

4.4 Specimen Characterisation Techniques

Section 4.4 details the various characterisation and assessment techniques that were employed to evaluate the microstructure and metallurgical properties of the specimens examined throughout this study. The method used to measure the coating bond strength (presented in Chapter 2) is also discussed herein.

4.4.1 Metallographic preparation

A precision cutting wheel (Accutom 5) was used to cut cross sections of the FSP tracks to examine their respective microstructures. The samples were mounted in either epoxy resin or Bakelite powder to enable the surface of interest to be polished. Epoxy resin was used for aluminium specimens as exposure to the high temperatures present in the Bakelite mounting process has the potential to alter their microstructure.

Standard metallographic preparation techniques were used to prepare the sectioned specimens to a 0.05 μm finish. Due to the dissimilar hardness of the reinforcing and matrix phases, incorrect grinding had the potential to cause pull-out of the reinforcing particles, leading to an inaccurate representation of the porosity within the coatings [4.18]. Several alternative preparation steps were explored to eliminate pull-out of the reinforcing particles. The influence of these different preparation stages on the microstructure of the MMCs was examined, and an optimised preparation process was developed. This optimised process is detailed in the following paragraphs.

Specimens were ground using 220-grade silicon carbide (SiC) paper to remove any small layers of Bakelite, epoxy or surface damage caused by the cutting process. Thereafter, the samples were ground progressively using SiC papers of decreasing grit size from 500 to 1200. At each grinding stage, the SiC papers gradually remove and replace the larger surface scratches with smaller ones.

The samples were then prepared using 15 μm and 9 μm lapping disks to remove any relief produced as a consequence of the dissimilar hardness between the matrix and the reinforcements. The specimens were subsequently polished on fibre cloths using 6 μm and 3 μm diamond suspension. The duration of the polishing stages was kept to a minimum to reduce the risk of reinforcements being plucked from the matrix by the fibres in the cloth. A 0.05 μm OP-S silica suspension was employed for the final polishing stage. The polished surface was washed using soap and water to remove any residual polishing solution and dried thoroughly to prevent oxidation of

the specimen surface. To increase the uniformity of the surface finish, the specimens were secured in a sample holder and prepared using an automated grinding/polishing machine (Struers Rotopol-21).

To observe the grain size in the as-received, cold sprayed, and SprayStirred specimens, the surface of interest was etched using an appropriate reagent. The AA5083 and AISI 316 specimens were submerged in Barker's reagent (5 ml HBF_4, 200 ml water) and 10% oxalic acid respectively. To highlight the grain structure, electrolytic etching was required. The specimens were submerged in their respective etchants for approximately 30 seconds, while a potential of 1 V was applied across each sample. The voltage was kept to a minimum to reduce the speed of the reaction to prevent over-etching. The grain size of the various specimens was resolved using optical microscopy.

4.4.2 Optical microscopy

An Olympus G51X optical microscope was used to capture images of the samples at different magnification levels to highlight the microstructure of the specimens. Optical microscopy provided an indication as to how the reinforcing particles were refined and redistributed by FSP. Additionally, the images highlighted various microstructural features associated with the stir zone such as banding (layers of particle-rich and particle-free regions within stir zone) [4.19] or inhomogeneous particle distribution. The images were subjected to quantitative inspection to establish the interparticle spacing, and detailed volume fraction analysis to determine the ratio of reinforcing particles to matrix. Specimens were not etched prior to image analysis or measurement of the interparticle spacing. However, micrographs of etched specimens were captured to highlight the grain structure where necessary.

4.4.3 Scanning electron microscopy

A Hitachi S-3700 series scanning electron microscope (SEM), operating at 15 kV facilitated a detailed examination of the reinforcing particles and matrix in the MMCs. The SEM has two operational modes, either of which may be selected depending on which produces the highest resolution image. In the first of the two operational modes, the SEM fires electrons at the surface of the specimen and records the energy of those electrons after they have rebounded from the target surface. This approach is known as electron backscatter diffraction (EBSD) [4.20]. The second method bombards the target surface with electrons and measures the energy of the electrons ejected by the target surface. This method is referred to as

secondary electron imagery [4.20]. In the present study, EBSD and secondary electron detection modes were employed to highlight features within the microstructure of the specimens. The SEM can achieve significantly greater magnification and improved resolution over an optical microscope owing to the shorter wavelength of the electrons when compared to the wavelength of the visible light used in optical microscopy [4.20].

4.4.4 Energy dispersive spectroscopy

Energy dispersive spectroscopy (EDS) software (Oxford Instruments INCA) was used in conjunction with the SEM to analyse the elemental composition of the specimens. During EDS, the sample is bombarded by a high-energy electron beam which excites the atoms within the material. The elements within the sample were identified by detecting the emission of an x-ray energy spectrum from the surface that is unique to a particular element.

EDS was able to generate maps depicting the position of elements within the matrix and was also used to measure the quantity (wt.%) of a particular element within a scanned region. These capabilities were very useful for determining the distribution of the reinforcing particles throughout the matrix. In this study, the sample preparation for SEM microscopy was the same as for optical microscopy (Section 4.4.2). However, the SEM equipment required the specimen to hold a positive charge to attract the electrons. Therefore, specimens mounted in epoxy resin were gold coated using a magnetron sputtering system [4.21].

4.4.5 Grain size measurement

The grain size was established using the circular intercept procedure (Abrams Three-Circle Procedure) outlined in ASTM E112-12 [4.22]. This approach [4.22] estimates the average grain size by counting the number of grain boundaries that intercept concentric circles overlaid on an etched optical micrograph depicting the microstructure of interest. It is possible to overlay five parallel lines of known length; however, this method is not appropriate for un-equiaxed grains (such as a cold rolled microstructure).

The test pattern (Fig. 4-5) consists of three concentric circles, with circumferences of 250 mm, 166.7 mm and 83.3 mm, giving a total circumference of 500 mm. The test pattern was overlaid on five randomly selected areas within each region of interest on the micrograph; i.e. the root of the stir zone, the near-surface region and the as-received substrate.

For each region, a magnification level was selected that allowed between 40 and 100 grain boundary intercepts to be counted. For example, the larger grain size of the as-received AISI 316 necessitated the use of [x500] magnification. However, [x1000] magnification was more appropriate when examining the stir zone as it was not possible to accurately discern grain boundaries at [x500].

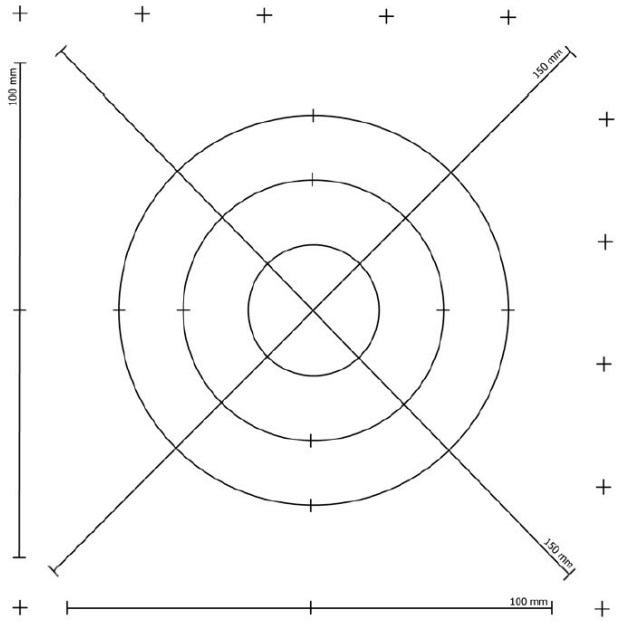

Fig. 4-5 The Abrams Three-Circle Procedure test pattern [4.22]

Using the equations detailed in [4.22], the mean lineal intercept (N_L) was calculated (number of intercepts per unit length of test circles) and, using Equation 4-2, the ASTM grain size (G) was calculated. This value was subsequently converted to grain size (in microns) using a conversion table in [4.22]. To ensure that there was suitable consistency in the measurements, standard deviation was used to calculate the "percent relative accuracy" (%RA) of the measurements. According to the standard [4.22], the %RA should be no greater than 10%. In the measurements presented in later chapters, the maximum %RA recorded was 7.9%.

$$G = (6.643856 \log_{10} N_L) - 3.288 \qquad \text{Equation 4-2}$$

4.4.6 Microhardness

The microhardness of the as-received, CS desposited and SprayStirred specimens was evaluated using a Mitutoyo MVK-G1 microhardness tester with a 4-sided, pyramidal diamond indenter. The hardness tester was calibrated before each use by taking three microhardness measurements of a calibration sample. The three

measurements were averaged and compared with the known hardness of the calibration sample. In all cases, the examined specimens were prepared using the method outlined in Section 4.4.1.

The measurement process began when the diamond indenter established contact with the surface of the specimen. When in contact, a specified load was applied to the indenter causing the tip to penetrate the surface. Loads of 100 gf and 200 gf were used for the aluminium alloys and AISI316 respectively. The higher load was applied to the AISI316 to ensure the indents on the surface could be resolved on the monitor used to view the indentations.

The load was applied for a predefined dwell time (10 seconds), following which, the indenter was withdrawn from the surface. When the dimensions of the diamond indenter are known, the dimensions, d1 and d2 of the indent correspond to the depth of the indent and thus, the hardness of the material. The hardness is expressed in terms of Vickers (HV) and is calculated using Equation 4-3, where F is the force applied to the indenter (N), and d is the average length of the two diagonals, d1 and d2.

$$\mathrm{HV} = \frac{2\mathrm{F}\sin(\frac{136}{2})}{\mathrm{d}^2} \qquad \text{Equation 4-3}$$

The hardness of the as-received substrate alloys was measured 1 mm from the edge of the polished surface. For the CS deposited and HVOF coatings, measurements were recorded at a distance of 0.1 mm from the top surface of the sample. To determine the hardness within the SprayStirred material, five hardness measurements were taken on the advancing side, the retreating side and centre of the stir zone, giving a total of fifteen measurements across the width of the stir zone (at 0.1 mm from the surface). Fig. 4-6 presents a macroscopic cross-section of the stir zone and depicts the approximate location of the hardness indents.

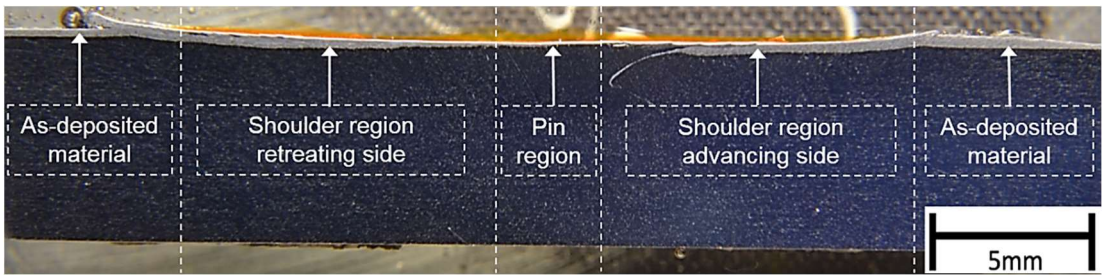

Fig. 4-6 Macroscopic cross section of SprayStirred MMC layer

4.4.7 Nanoindentation analysis

The microhardness indenter described in Section 4.4.5 has a diameter greater than the size of the reinforcing particles. Therefore, the microhardness measurements represent the average hardness of the reinforcements and the surrounding matrix. To accurately assess the hardness of the reinforcing particles and the matrix independently, a more precise measuring system was required. Therefore, a nanoindentation system (Agilent Nano Indenter G200) (Fig. 4-7) was employed to establish the specific hardness of the reinforcements and matrix respectively

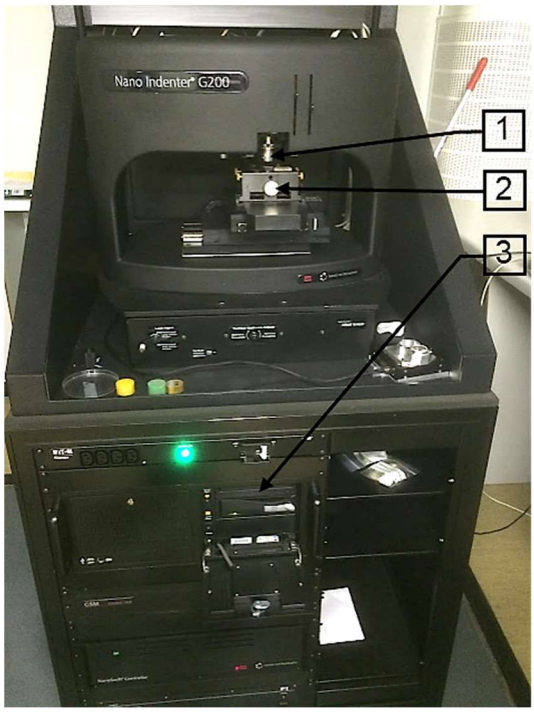

Fig. 4-7 Agilent Nano Indenter G200; (1) Berkovich indenter, (2) specimen stage, (3) data logging

In nanoindentation testing, the size of the residual impression left by the diamond indenter is of the order of microns and too small to be conveniently measured visually (as in microhardness testing). Thus, the area of contact is established by measuring the depth of penetration of the indenter into the specimen surface. This, together with the known geometry of the indenter, provides an indirect measurement of contact area at full load and hence, indicates the hardness of the indented material.

The indentation process commenced when the Berkovich indenter [4.23] was brought into contact with the surface of the test sample. An increasing load was applied to the indenter causing the tip to penetrate the target surface. Upon reaching the predefined maximum indentation depth (250 nm), the indenter was withdrawn.

Throughout the indentation process, the changes in applied load and indentation depth were continuously monitored. Analysis of the elastic recovery portion of the unloading curve, in accordance with the model for the elastic contact problem [4.23], establishes Young's modulus, E, of the examined material. Thereafter, the hardness of the test sample is determined by calculating the maximum load divided by the contact area, which is related to the indentation depth. The extended methodology for this process was developed by Oliver and Pharr, and is discussed in detail in the published literature [4.23, 4.24].

The surface of each specimen was indented at 10 μm intervals with the indentations covering a total surface area of 100 μm^2. The nanohardness measurements were converted to HV using the conversion factor stated in ASTM E92 – 16 [4.25] to enable a direct comparison with the microhardness results.

4.4.8 Interparticle spacing

The distribution of reinforcing particles has a significant impact on the resulting mechanical and erosion properties of the MMC [4.26–4.29]. Therefore, it was necessary to quantify the difference in interparticle spacing between the reinforcements in the CSed and SprayStirred specimens. A quantitative dispersion characterisation method was applied to assess the distribution of reinforcing particles in the present study. The chosen method was developed by Khare & Burris [4.30] to measure nanocomposite dispersion [4.30] as this method [4.30] accounts for the presence of particle agglomerates unlike other techniques [4.31–4.33].

The process [4.30] measures the free-space length, which is defined as the width of the largest randomly placed square for which the average number of intersecting reinforcing particles is zero. Optical micrographs of the CSed, and SprayStirred specimens were captured at [x500] magnification. The micrographs were converted to binary (black and white) images by manually modifying the threshold, with black pixels representing the reinforcing phase, and white pixels representing the matrix phase. The binary image was loaded into Matlab and the statistical analysis performed.

The analysis method randomly places a specified number of squares onto the binary image and records the number of black pixels present within each square. The size of the square is progressively reduced until the average number of intersecting black pixels is zero. In this study, the number of randomly placed squares was 10,000, and the initial estimate for the length of the square was 5 μm.

4.4.9 Coating bond strength

The bond strength of the AISI 316 cold sprayed coatings (presented in Chapter 2) was evaluated in line with the pull-off testing method specified in ASTM C633 – 13 [4.34], using tensile testing equipment (Instron 8801). A schematic diagram of this method is presented in Fig. 4-8. During the test, steel stubs (Fig. 4-8) 25 mm in diameter were bonded to the coated and uncoated surfaces of the specimen.

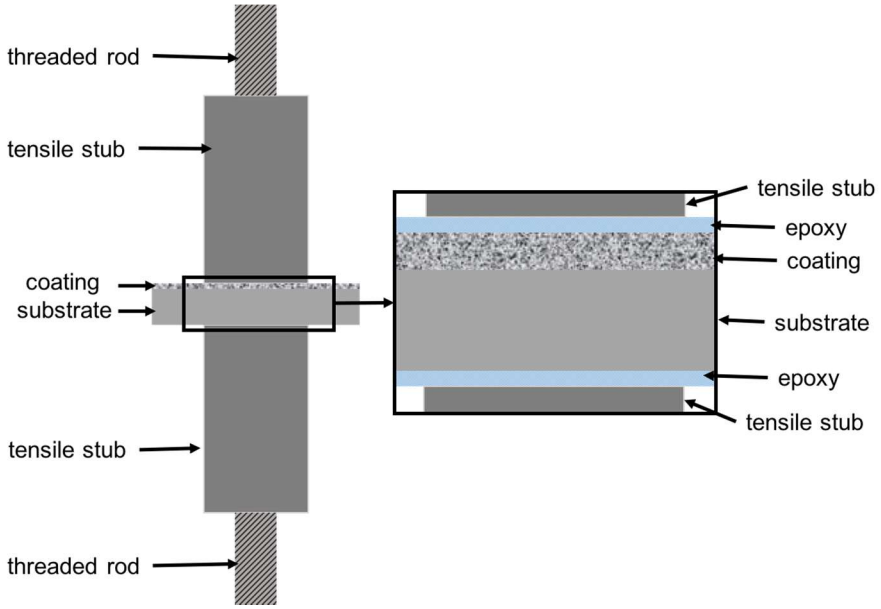

Fig. 4-8 Schematic diagram of the specimen setup for pull-off testing (not to scale)

The surfaces of the coated samples and the steel stubs were prepared using p220 SiC paper to remove any surface roughness, and cleaned with acetone. A thermally curing epoxy resin (Huntsman Araldite AV170) was used to bond steel stubs to the coated and uncoated sides of the specimen and was applied to the contact surface of the steel stubs. The steel stubs and the coated samples were secured in a self-aligning jig incorporating a 90° V-block and jubilee clips, to ensure that both stubs were concentric. The jig was placed in an oven for two hours at 160°C, while a 50 N weight was positioned on top of the jig to apply light compression while the epoxy cured. Before testing, the coating material out with the diameter of the stub was machined from the specimen surface to ensure that no portion of the load applied by the tensile testing equipment was transferred to the coating outwith the diameter of the steel stub.

The Instron machine applied a constant tensile force to the specimens, extending them up to the point of failure. The rate of extension used in this study was 1 mm/min. The maximum load applied to the specimens prior to failure was recorded.

Three pull-off tests were completed for each coating type with the average and range of these results reported. The fracture surfaces were examined using the SEM to evaluate the mechanisms leading to the failure of the coating.

4.5 Slurry Erosion and Corrosion Analysis

4.5.1 Slurry erosion investigation

A closed loop solid-liquid impingement test rig was used to assess the erosion performance of the various test specimens examined throughout this investigation. A schematic diagram of the apparatus is exhibited in Fig. 4-9.

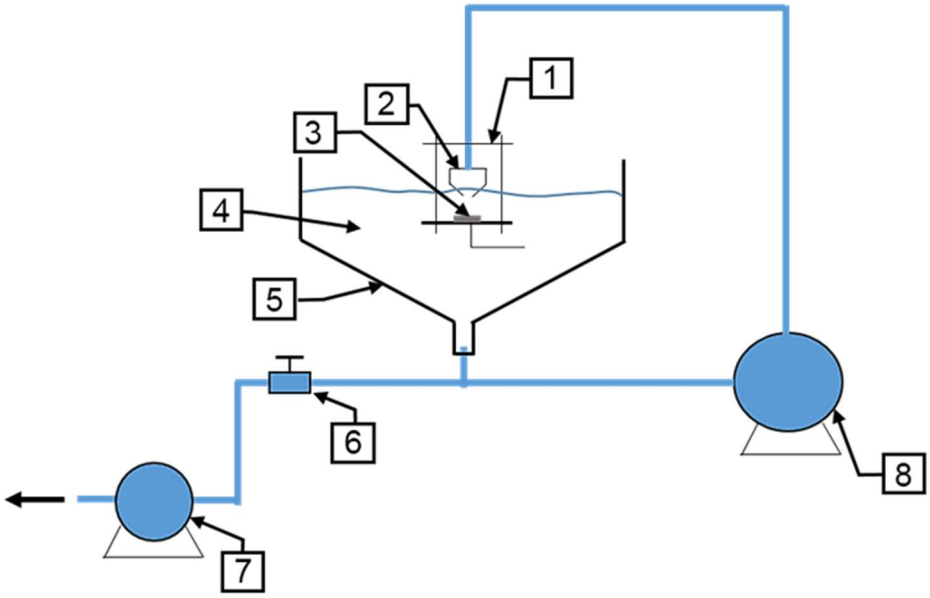

Fig. 4-9. Schematic diagram of recirculating liquid impingement test rig (not to scale); (1) sample holder, (2) jet impingement nozzle, (3) specimen, (4) slurry solution, (5) slurry tank, (6) drain valve, (7) drain pump, (8) recirculating pump

This particular design of the test rig was chosen due to its frequent use by researchers examining the erosion and corrosion properties of materials within a slurry environment [4.26, 4.35, 4.36]. Furthermore, a closed-loop system offers the ability to modify the concentration of erosive particles within the slurry, control the flow velocity and set the standoff distance between the nozzle exit and the surface of the specimen. Additionally, this testing environment provides a more accurate approximation of the conditions experienced by the MMCs when transporting erosive slurry [4.37], in contrast to pin on disk.

The slurry used throughout the study was comprised of a 3.5% sodium chloride (NaCl) solution and FS9 grade silica particles with an average particle size

of 0.4 mm. Fig. 4-10 shows a macroscopic view of the silica particles highlighting their faceted morphology.

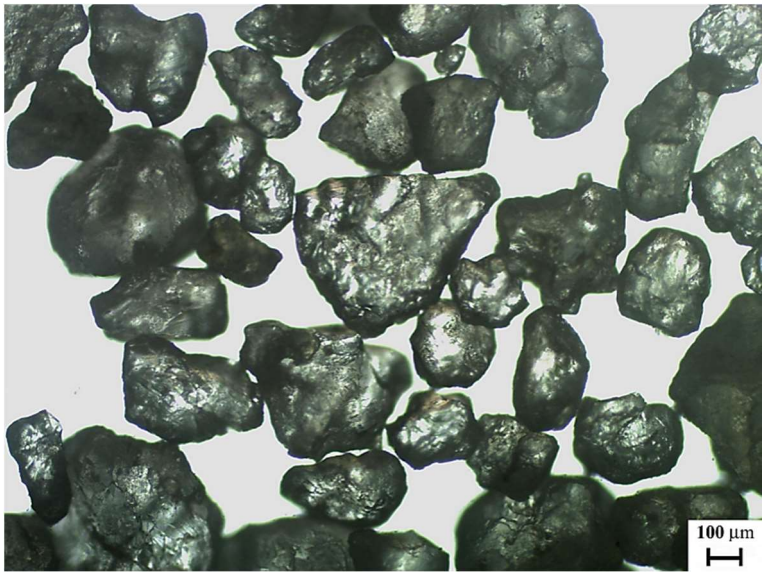

Fig. 4-10 Silica sand particles, pre-erosion testing [x50]

4.5.1.1 Test procedure

The coupons were prepared for the erosion test by first removing any minor surface roughness using 500-grit SiC paper. The mass was established pre- and post-testing using a calibrated mass balance (Sartorius S224I) to an accuracy of 0.1 mg, to calculate the total mass loss. Three replicates were assessed for each specimen to establish the average mass loss.

The slurry tank was filled with 33 litres of water and 1.15 kg of NaCl to produce the 3.5% NaCl solution. Mixing was facilitated by operating the test rig for approximately 20 minutes prior to the first test. The silica particles were added to the solution within the first few seconds of the test. To prevent settling of the silica particles, the slurry was agitated periodically during the test regime.

Test specimens were positioned directly beneath the jet nozzle, using a suitable mounting jig (Fig. 4-11). The sample holders were constructed from acrylic to ensure they would not influence the mass loss experienced by the test coupons. The test coupon and holder were fully submerged in the slurry for the duration of the experiment. The erosion performance of the MMCs and coatings were evaluated at different angles of impingement. The specific impingement angles examined during each section of this study will be detailed in the relevant chapter.

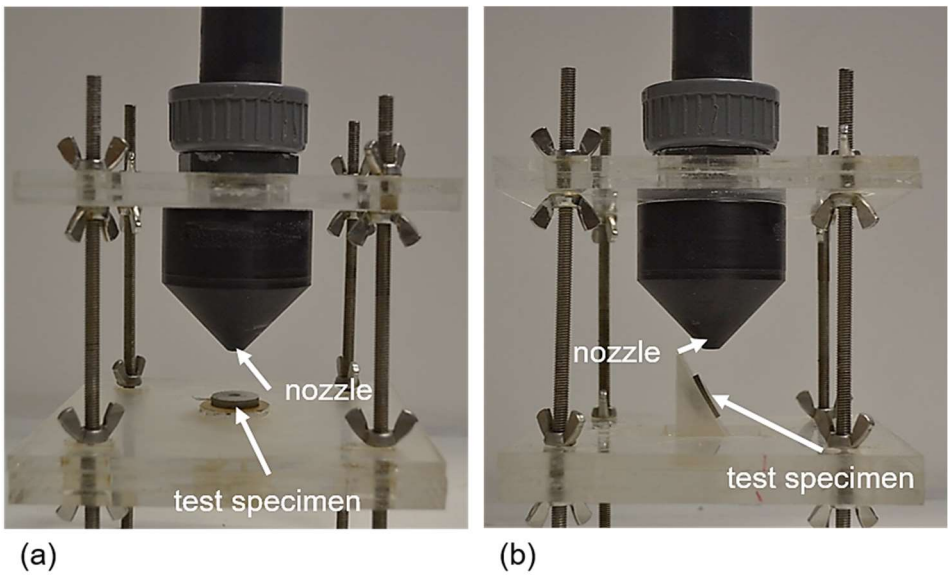

Fig. 4-11. Jet nozzle and test specimen in situ for slurry erosion testing at; (a) 90°; (b) 30° impingement

The standoff distance between the nozzle and sample was initially set to 20 mm (Chapter 5 and Chapter 7). However, to generate a measurable amount of mass loss in the AISI316 study (Chapter 8), the standoff was reduced to 5 mm. The distance between the nozzle and specimen was held constant between test replicates using a spacer disk cut to the appropriate thickness. The duration of the slurry erosion test was one hour; however, this was reduced for the AA5083 study as the cold sprayed coatings were breached before the conclusion of the experiment. Therefore, the test duration in the AA5083 study (Chapter 7) was reduced to 20 minutes.

Following the completion of each test, the drainage pump (Fig. 4-9) removed the slurry. The system was subsequently flushed with fresh water to remove any trace silica particles, thereby ensuring consistent test conditions. Silica particles were examined post-testing to identify any change in the particle size distribution following impingement on the surface of the specimen. The mass loss of a control sample was measured prior to the assessment of the test coupons to ensure consistent erosive conditions. The specific test parameters for each substrate are detailed within their respective chapters.

4.5.2 Slurry velocity and silica concentration calculation

The velocity of the slurry at the nozzle exit was calculated using Equation 4-4, where V is the flow velocity, Q is the volume flow rate, and r is the radius of the nozzle exit. The volume flow rate was established by attaching a hose to the end of the

submerged nozzle while the pump was operating. The total mass of water that passed through the nozzle into a 20 litre plastic container after 20 seconds was measured and the volumetric flow rate per second calculated by dividing the mass flow per second, by the density of water (1000 kg/m^3). The concentration of silica at the nozzle exit was established using a metal sieve to extract the particles from the slurry as they passed from the nozzle into the 20 litre plastic container. The sieve and the trapped silica were dried for one hour at 160°C. The silica particles were subsequently poured into a measuring beaker and weighed on a mass balance, to an accuracy of 0.1 mg.

$$V = \frac{Q}{\pi r^2} \qquad \text{Equation 4-4}$$

4.5.3 Corrosion evaluation and synergy calculation

In this investigation, the influence of corrosion on the resulting mass and volume loss was established using the electrochemical measurement techniques discussed in Chapter 3. The application of cathodic protection and anodic/cathodic polarisation was necessary to isolate the effects of pure erosion and pure corrosion to determine the impact of synergy on the resulting mass loss. Synergy (S) is the additional mass loss experienced by a material due to the combined effect of erosion and corrosion and is represented by Equation 4-5, where TML is the total mass loss, C is the mass loss owing to pure corrosion, and E is the mass loss due to pure erosion.

$$S = TML - (E + C) \qquad \text{Equation 4-5}$$

The testing procedure was kept consistent with free erosion corrosion testing, with identical liquid impingement setup used. A WaveNow potentiostat, manufactured by Pine Instruments, in conjunction with Aftermath data acquisition software facilitated the electrochemical analysis. A three-electrode configuration was connected to the potentiostat to monitor and record the current and potential within the circuit (Fig. 4-12). The working electrode is the specimen under investigation. Throughout this study, platinum foil served as the auxiliary electrode, while a double junction silver/silver chloride (Ag/AgCl) electrode served as the reference electrode. The cathodic protection was applied for the same duration as the free erosion corrosion test, to enable a direct comparison between the two results.

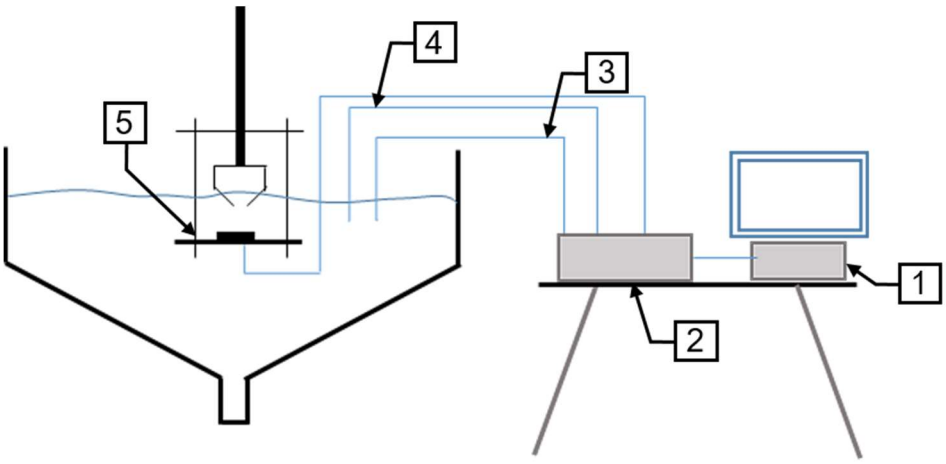

Fig. 4-12 Schematic diagram of the three-electrode potentiostat setup (not to scale); (1) data logging, (2) potentiostat, (3) reference electrode (Ag/AgCl), (4) auxiliary electrode (platinum), (5) working electrode (specimen)

4.5.3.1 Cathodic protection

Cathodic protection was applied to the test coupons to establish the component of mass loss relating to pure erosion, by inhibiting any electrochemical reaction between the specimen and the slurry. A potential of -1 V was applied across the working electrode, thereby suppressing any anodic reaction and preventing the occurrence of corrosion on the surface of the sample.

4.5.3.2 Anodic polarisation scans

Mass loss from corrosion alone was determined through DC anodic/cathodic polarisation scans under static and flowing conditions. The E_{corr} value (corrosion current) for each coating type was established for both conditions, with scans conducted for 40 minutes in order to allow sufficient time for the potential to settle. Static conditions refer to the specimen submerged in 3.5% NaCl solution while flowing conditions refer to the slurry impinging on the surface of the test coupon.

For the polarisation scans, the applied potential was swept from E_{corr} -300 mV (cathodic) to E_{corr} +300 mV (anodic) at a sweep rate of 14 mV/min; this provided sufficient potential range to determine the corrosion current density using Tafel extrapolation from both the cathodic and anodic curves. The calculated values were used to determine the corresponding corrosion mass loss rate using the method outlined in ASTM G102 - 89(2010) [4.38].

Since the coatings included a mixture of elements, the equivalent weight of each constituent was evaluated using Equation 4-6. Valence values were obtained from published literature [4.39]. The mass loss rate was calculated using Equation 4-7,

incorporating the respective equivalent weight values determined for each coating. The mass loss from corrosion and erosion was subtracted from the total mass loss under free erosion-corrosion conditions to establish the mass loss attributed to the synergistic effect of combined erosion-corrosion. In Equation 4-6, EW is the equivalent weight, f_i represents the mass fraction of the specific element, n_i is the valance value of the specific element, and W_i is the atomic weight of the specific element. K_2 is a contestant from Faraday's equation and is equal to 8.954 x 10^{-3} g cm^2/ μA m^2 d [4.38].

$$EW = \left(\sum \frac{f_i n_i}{W_i}\right)^{-1} \quad \text{Equation 4-6}$$

$$MR = K_2 i_{corr} EW \quad \text{Equation 4-7}$$

4.5.4 Mass and volume loss analysis

The mass loss of each specimen was measured using a calibrated mass balance (Sartorius S224I) to an accuracy of 0.1 mg. However, due to the different densities of the various reinforcing particles examined throughout this study, the mass loss does not provide a suitable metric with which to compare the different MMCs and coatings. For example, tungsten carbide (WC) has a greater density than alumina (Al_2O_3). Therefore, WC reinforced specimens may exhibit greater mass loss than Al_2O_3 reinforced specimens (low density), despite less of the WC reinforced material being removed from the surface by the erosive slurry.

Similar issues have been encountered by research groups [4.40, 4.41] examining the erosion performance of two or more dissimilar materials. In these studies [4.40, 4.41], the authors establish the volume loss by simply dividing the mass loss by the density of each material, thereby allowing a direct comparison of the relative erosivity of the different materials.

While this method is appropriate for materials of known density, there is no suitably accurate mathematical method to determine the volume loss for specimens in which density is not known. Considering the density of the MMCs examined in this study is unknown, another method must be used to establish the volume loss, thereby enabling the relative erosivity of the different MMCs to be compared.

In this study, a focal variation microscope (Alicona Infinite Focus G4) [4.42] was used to establish the volume of the wear scars produced by the impinging slurry. Fig. 4-13 displays an image of the Alicona imaging system used in this study.

Fig. 4-13 Alicona Infinite Focus G4 focal variation microscope; (1) automated specimen stage, (2) lens selection turret, (3) data logging

The Alicona system makes use of focus variation technology to construct a 3D model of the wear scar by layering multiple images of the impinged region, captured at different focal lengths [4.42]. As with an optical microscope, white light is reflected off the material surface from a suitable light source. However, in the Alicona imaging system, the reflected light is subsequently split using a photoelectric detector to distinguish the colour, brightness and contrast of the image. This data is gathered by the light sensor located behind the beam splitting mirror [4.43]. Focal variation technology only captures in-focus images of small regions of the surface at one time, due to the small depth of field examined by the light sensor. The Alicona generates a complete image of the wear scar by precisely shifting the lens in the vertical direction from the lowest to the highest point of the wear scar, while continuously capturing information on the specimen surface. Hence, a sharp image of the entire damaged region (wear scar) is obtained. Native software in the Alicona imaging system converts this information into a 3D dataset which can be inspected using the Alicona software (IF-MeasureSuite).

Each test specimen was evaluated at [x5] magnification, with a vertical resolution of 2.5 µm. The lateral resolution was set to 6 µm to ensure the measurements were of high accuracy. The resulting 3D model contains numerous data points that were measured in relation to a reference plane representing the

original top surface of the specimen. The Alicona software calculated the volume of the wear scar by measuring the relative distance between each data point and the reference plane.

The depth of the wear scars was also measured using a Mitutoyo SV 2000 profilometer to validate the results of the Alicona. This mechanical measuring system operates by traversing a stylus across the surface of the specimen while recording the change in the vertical position of the stylus tip. Comparison of the Alicona and profilometer values yielded negligible variation between the two sets of results.

4.5.5 Wear scar analysis

Microscopic examination of the wear scars generated by the slurry erosion testing was carried out to identify the degradation mechanisms leading to the removal of material from the surface of each specimen. The Alicona imaging system (Section 4.5.4) was used to capture low magnification images of the wear scar, with high magnification images subsequently taken using the SEM (Section 4.4.3). The damage caused by the impinging particles was examined and compared with the features that are reported on materials exhibiting brittle and ductile erosion mechanisms (as discussed in Chapter 3), as well as those that operate on metal matrix composite (MMC) materials.

4.6 References

[4.1] H. Assadi, T. Schmidt, H. Richter, J.O. Kliemann, K. Binder, F. Gartner, et al., On parameter selection in cold spraying, J. Therm. Spray Technol. 20 (2011) 1161–1176.

[4.2] M. Durdanovic, M. Mijajlovic, D. Milcic, D. Stamenkovi, Heat Generation During Friction Stir Welding Process, Tribol. Ind. 31 (2009) 8–14.

[4.3] N. Mendes, P. Neto, A. Loureiro, A.P. Moreira, Machines and control systems for friction stir welding: A review, Mater. Des. 90 (2016) 256–265.

[4.4] S. Mukherjee, a. K. Ghosh, Friction stir processing of direct metal deposited copper-nickel 70/30, Mater. Sci. Eng. A. 528 (2011) 3289–3294.

[4.5] R.S. Mishra, M.W. Mahoney, Friction stir welding and processing, Mater. Sci. Eng. R Reports. 50 (2007) 360.

[4.6] R.S. Mishra, Z.Y. Ma, Friction stir welding and processing, Mater. Sci. Eng. R. 50 (2005) 1–78.

[4.7] C.I. Chang, X.H. Du, J.C. Huang, Achieving ultrafine grain size in Mg-Al-Zn alloy by friction stir processing, Scr. Mater. 57 (2007) 209–212.

[4.8] V. Sharma, U. Prakash, B.V.M. Kumar, Surface Composites by Friction Stir Processing: A Review, J. Mater. Process. Technol. 224 (2015) 117–134.

[4.9] P. Xue, B.L. Xiao, Z.Y. Ma, Achieving ultrafine-grained structure in a pure nickel by friction stir processing with additional cooling, 56 (2014) 848–851.

[4.10] B.T. Gibson, D.H. Lammlein, T.J. Prater, W.R. Longhurst, C.D. Cox, M.C. Ballun, et al., Friction stir welding: Process, automation, and control, J.

Manuf. Process. 16 (2014) 56–73.
[4.11] E.F. Shultz, E.G. Cole, C.B. Smith, M.R. Zinn, N.J. Ferrier, F.E. Pfefferkorn, Effect of Compliance and Travel Angle on Friction Stir Welding With Gaps, J. Manuf. Sci. Eng. 132 (2010) 41010–41019.
[4.12] Y.N. Zhang, X. Cao, S. Larose, P. Wanjara, Review of tools for friction stir welding and processing, Can. Metall. Q. 51 (2012) 250–261.
[4.13] J.S. De Jesus, a. Loureiro, J.M. Costa, J.M. Ferreira, Effect of tool geometry on friction stir processing and fatigue strength of MIG T welds on Al alloys, J. Mater. Process. Technol. 214 (2014) 2450–2460.
[4.14] O.S. Salih, H. Ou, W. Sun, D.G. Mccartney, A review of friction stir welding of aluminium matrix composites, Mater. Des. 86 (2015) 61–71.
[4.15] R.A. Prado, L.E. Murr, K.F. Soto, J.C. McClure, Self-optimization in tool wear for friction-stir welding of Al 6061+20% Al2O3 MMC, Mater. Sci. Eng. A. 349 (2003) 156–165.
[4.16] R.J.K. Wood, R. Manish, Surface Engineering for Enhanced Performance against Wear, Springer, 2013.
[4.17] P.L. Fauchais, J.V.R. Heberlein, M.I. Boulos, Thermal Spray Fundamentals, 2014.
[4.18] Struers, Metallographic preparation of thermal spray coatings, 2014.
[4.19] M. Bahrami, K. Dehghani, M.K. Besharati Givi, A novel approach to develop aluminum matrix nano-composite employing friction stir welding technique, Mater. Des. 53 (2014) 217–225.
[4.20] R.F. Egerton, Physical Principles of Electron Microscopy: An Introduction to TEM, SEM and AEM, 2005.
[4.21] P. J. Kelly, R. D. Arnell, Magnetron sputtering: a review of recent developments and applications, Vacuum. 56 (2000) 159–172.
[4.22] ASTM International, ASTM E112-13: Standard test methods for determining average grain size, ASTM Int. (2013) 1–28.
[4.23] A.C. Fischer-Cripps, Mechanical Engineering Series: Nanoindentation, 2011.
[4.24] W.C. Oliver, G.M. Pharr, An improved technique for determining hardness and elastic modulus using load and displacement sensing indentation experiments, J. Mater. Res. 7 (1992) 1564–1583.
[4.25] International ASTM Standard, ASTM E92-16 Standard Test Methods for Vickers Hardness and Knoop Hardness of Metallic, 2016.
[4.26] A. Neville, F. Reza, S. Chiovelli, T. Revega, Erosion-corrosion behaviour of WC-based MMCs in liquid-solid slurries, Wear. 259 (2005) 181–195.
[4.27] H. Gül, F. Kili, M. Uysal, S. Aslan, A. Alp, H. Akbulut, Effect of particle concentration on the structure and tribological properties of submicron particle SiC reinforced Ni metal matrix composite (MMC) coatings produced by electrodeposition, Appl. Surf. Sci. 258 (2012) 4260–4267.
[4.28] R. Casati, M. Vedani, Metal Matrix Composites Reinforced by Nano-Particles—A Review, Metals (Basel). 4 (2014) 65–83.
[4.29] B.G. Mellor, Surface coatings for protection against wear, Woodhead Publishing Limited, 2006.
[4.30] H.S. Khare, D.L. Burris, A quantitative method for measuring nanocomposite dispersion, Polymer (Guildf). 51 (2010) 719–729.
[4.31] M. Yourdkhani, P. Hubert, Quantitative dispersion analysis of inclusions in polymer composites, ACS Appl. Mater. Interfaces. 5 (2013) 35–41.
[4.32] Z.P. Luo, J.H. Koo, Quantification of the layer dispersion degree in polymer layered silicate nanocomposites by transmission electron microscopy, Polymer (Guildf). 49 (2008) 1841–1852.
[4.33] M. Kouzeli, A. Mortensen, Size dependent strengthening in particle

reinforced aluminium, Acta Mater. 50 (2002) 39–51.
[4.34] I.A. Standard, ASTM C633 − 13: Standard Test Method for Adhesion or Cohesion Strength of Thermal Spray Coatings, 2001.
[4.35] J. Yao, F. Zhou, Y. Zhao, H. Yin, N. Li, Investigation of erosion of stainless steel by two-phase jet impingement, Appl. Therm. Eng. (2014) 1–10.
[4.36] A. Neville, T. Hodgkiess, J.T. Dallas, A study of the erosion-corrosion behaviour of engineering steels for marine pumping applications, Wear. 186–187 (1995) 497–507.
[4.37] Y. Zhao, F. Zhou, J. Yao, S. Dong, N. Li, Erosion–corrosion behavior and corrosion resistance of AISI 316 stainless steel in flow jet impingement, Wear. 328–329 (2015) 464–474.
[4.38] International ASTM Standard, ASTM G102 - 89 Standard Practice for Calculation of Corrosion Rates and Related Information from Electrochemical Measurements, 2015.
[4.39] M. Pourbaix, Atlas of Electrochemical Equilibria in Aqueous Solutions, 1974.
[4.40] S. Lathabai, M. Ottmüller, I. Fernandez, Solid particle erosion behaviour of thermal sprayed ceramic, metallic and polymer coatings, Wear. 221 (1998) 93–108.
[4.41] M. Moazami-goudarzi, F. Akhlaghi, Wear behavior of Al 5252 alloy reinforced with micrometric and nanometric SiC particles, Tribiology Int. 102 (2016) 28–37.
[4.42] R.S. Bolton-King, J.P.O. Evans, C.L. Smith, J.D. Painter, D.F. Allsop, W.M. Cranton, What are the Prospects of 3D Profiling Systems Applied to Firearms and Toolmarks Identification?, AFTE J. 42 (2010) 23–33.
[4.43] R. Danzl, F. Helmli, S. Scherer, Focus variation - A robust technology for high resolution optical 3D surface metrology, Stroj. Vestnik/Journal Mech. Eng. 57 (2011) 245–256.

Chapter 5 Examination of High Velocity Oxy-Fuel (HVOF) Coatings

5.1 Introduction

Before commencing the development of SprayStir, high velocity oxy-fuel (HVOF) coatings were examined to assess their erosion and corrosion performance under the test conditions used, in later chapters, to evaluate the erosion and corrosion performance of SprayStirred specimens. HVOF has been selected over other thermal spraying methods (discussed in Chapter 2) as it can successfully deposit erosion resistant coatings onto a variety of metallic substrates [5.1]. Moreover, HVOF has been adopted in several industries as their standard method of surface property enhancement [5.2] and component repair [5.3].

5.1.1 State-of-the-art HVOF research

As discussed in Chapter 2, the HVOF process involves spraying molten or semi-molten powder particles at high velocities onto a target surface [5.4]. The high kinetic energy generated by the spraying process deforms these molten and semi-molten particles upon impact with the substrate, resulting in a dense coating that is well bonded to the substrate material, and resistant to sliding wear, erosion and corrosion [5.5–5.10]. There have been numerous studies examining the erosion performance of HVOF coatings, most notably tungsten carbide (WC) and chromium carbide (CrC) based cermets [5.10–5.18].

Thakur et al. [5.11] investigated the erosion behaviour of HVOF sprayed WC-CoCr coatings deposited on AISI304 stainless steel. The research group [5.11] examined the impact of reinforcement carbide size on the slurry erosion performance of the coating. Additionally, the authors [5.11] also examined the effect of erodent particle size and slurry concentration on the coating's erosion performance. Their results [5.11] indicated that feedstock powder containing a nanoscale carbide phase yields higher erosion resistance, which the authors attributed to increased hardness and toughness.

Similarly, Goyal et al. [5.13] investigated the erosion mechanisms of WC-CoCr and Al_2O_3 coatings following pot-type slurry erosion testing. The research team [5.13] measured the volume loss in the impinged region and employed scanning electron microscopy (SEM) to examine the eroded surface to investigate the wear mechanisms operating thereon. The study [5.13] identified a correlation between increased coating hardness and reduced volume loss. The researchers attributed the

increased volume loss of the Al_2O_3 specimen to the presence of large, un-melted particles within the coating [5.13].

Conversely, Ramesh et al. [5.12] reported the reduced erosion performance of HVOF deposited WC-CoCr when compared with the uncoated SA210 substrate alloy. The study [5.12] examined the impact of HVOF spraying parameters on the erosion resistance of the coating under dry jet impingement, and the wear damage was characterised using a similar approach to Goyal et al. [5.13]. The increased volume loss measured on the coated specimens was attributed to both ductile and brittle erosion mechanisms (as discussed in Chapter 3) operating on the WC-CoCr coating [5.12]. Furthermore, the comparably lower hardness of the uncoated SA210 alloy enabled the impinging SiC particles to embed on the surface. The authors proposed that the embedded SiC acted as a protective barrier, thus preventing the impinging SiC particles from causing further damage to the surface of the SA210 [5.12].

Thakur and Arora [5.18] examined the erosion performance of HVOF deposited, WC coatings under pot-type slurry impingement and dry-jet erosion. The investigation [5.18] concluded that the cermet coatings significantly enhanced the erosion performance of the uncoated substrate. Moreover, by examining the same coating under two different testing regimes, the authors [5.18] demonstrated that dry erosion generated greater mass loss when compared with slurry erosion. The increased volume loss associated with dry erosion testing was primarily attributed to higher erodent particle velocity. Additionally, the angle at which the eroding material impacts the substrate is more consistent in dry erosion testing; this consequently leads to considerable damage to the target surface. However, it should be noted that the impact angle between the two test regimes (dry erosion and pot-slurry erosion) was not the same [5.18]. Hence, a direct comparison of the two datasets does not deliver a meaningful conclusion considering the significant influence of impingement angle as demonstrated in the existing literature [5.19–5.21].

The existing research [10–21] demonstrates the considerable variation in the erosion performance of different HVOF coatings, with the level of erosion contingent on both the testing environment and the spraying parameters. Therefore, it is necessary to ensure that, where possible, the testing conditions used to evaluate the HVOF coatings are consistent with those used to assess the specimens produced by the new surface engineering process.

5.1.2 State-of-the-art erosion-corrosion research

As mentioned in Chapter 2, two mechanisms dictate the amount of material removed from the surface of a specimen under slurry erosion-corrosion conditions [5.23]; mechanical wear caused by erosive particles and corrosion from the slurry solution [5.22]. Moreover, combined erosion and corrosion yields greater mass loss than is produced by each process (erosion and corrosion) when they operate independently [5.24]. The additional mass loss generated by the compounded effects of erosion and corrosion is known as “synergy” [5.25].

The combined erosion-corrosion of various grades of steel is well documented, with the effects of erodent size, flow velocity and angle of attack all reported [5.20, 5.27–5.32]. These studies [5.20, 5.27–5.32] report different corrosion rates of steel under static corrosion and when exposed to slurry impingement. The variation in mass loss between the static and flowing environments is typically attributed, by the authors, to the presence of erosive particles within the slurry [5.20, 5.27–5.32]. As the particles impact the surface, they remove the passive film, thus accelerating the rate of electrochemical charge transfer (corrosion) [5.33, 5.34].

Studies examining the erosion-corrosion properties of HVOF deposited coatings have increased significantly in recent years, owing to the uptake of this technology within industry. Earlier investigations [5.35] typically considered the effects of erosion and corrosion separately, thus failing to establish the influence of synergy on the total material loss from the specimen. For example, Shabana et al. [5.35] evaluated the wear properties of the HVOF deposited coatings using pin-on-disk apparatus. The authors [5.35] calculated the corrosion rate using electrochemical test equipment, with the specimen submerged in a sodium chloride (NaCl) solution. While the results of this study are of interest, the analysis [5.35] fails to establish the influence of synergy and as such does not report the actual performance of the HVOF deposited coatings under aqueous, flowing conditions.

Souza and Neville [5.36] measured the erosion, corrosion and synergy values for HVOF coating under slurry impingement testing. The study aimed to evaluate the effect of microstructure created by HVOF and super detonation gun (SDG) spraying [5.37] methods, on the corrosion and synergy properties of the specimen [5.36]. The findings from the study indicate that the HVOF coatings demonstrated inferior resistance to corrosion when compared with the SDG deposited material. However, the HVOF coating measured considerably lower total volume loss under free erosion-corrosion conditions [5.36]. The poor erosion-corrosion performance of the SDG

coating was attributed to lower toughness caused by the production of brittle secondary phases by the SDG process [5.36].

Tan et al. [5.39] completed a comprehensive investigation into the erosion-corrosion properties of an HVOF deposited nickel-aluminium bronze. The authors [5.39] quantified the contribution of synergy to the total mass loss under several slurry test conditions. In instances where the kinetic energy of the impinging particles was relatively low, the corrosive film generated by the saline slurry acted as a protective barrier on the surface of the specimen [5.39]. Hence, the synergistic effect of combined erosion and corrosion led to a reduction in the total mass loss. The authors [5.39] referred to this phenomenon as “negative synergy”. Conversely, when high energy particles impact the surface, they break up the protective barrier, thereby resulting in “positive synergy” [5.39].

The existing published literature [5.20, 5.22, 5.25–5.39] highlights the considerable variation in the erosion-corrosion properties of HVOF deposited coatings. The results obtained by the various research groups are unique to the test conditions employed in each study and the chemical or microstructural composition of the respective coatings.

The work presented herein evaluates the erosion-corrosion performance of HVOF deposited coatings on low carbon steel when impinged by a slurry solution containing silica particles. The contribution of erosion, corrosion and synergy to the total mass loss was calculated for each coating. The erosion mechanisms operating on the surfaces of the test specimens were subsequently characterised by examining the wear scars generated by the erosive slurry. Additionally, dry jet erosion testing was employed to establish the variation in mass loss associated with the same HVOF coating, when exposed to two dissimilar erosion regimes.

5.2 Experimental Methods

The various evaluation techniques used to assess the HVOF coatings are presented in Chapter 4. However, this section details the specific materials examined in the present study as well as the particular test parameters employed herein.

5.2.1 Materials

Tungsten carbide (WC-CoCr) and chromium carbide (Cr_3C_2-NiCr) reinforced cermet powders were selected for this study, as both exhibit beneficial erosion

properties [5.36, 5.38]. An alumina (Al_2O_3) coating was also included in the study, as Al_2O_3 reinforced MMCs have been shown to offer enhanced erosion properties [5.40].

The three powders were individually sprayed onto 40 x 40 x 6 mm S355 steel (EN:10025) test coupons, and subsequently, grit blasted with alumina and de-greased with methylated spirit to remove any surface contaminants. The chemical composition of the feedstock powder and the substrate can be found in Table 5-1 and Table 5-2. The information concerning the average particle size range was gathered from the powder manufacturers' data sheets [5.41–5.43]. The size distribution (Table 5-1) indicates the size of the entire cermet or oxide particle, whereas the "reinforcement grain" relates to the size of the carbide reinforcement within the cermet particle.

Table 5-1 Properties of the feedstock powder [5.41–5.43]

Coating material	Composition (wt.%)	Size distribution (μm)	Reinforcement grain
WC-CoCr	80.6W - 10Co - 4Cr - 5.2C - 0.2Fe	-45 +15	fine
Cr_3C_2-NiCr	69.9Cr - 20Ni - 9.6C - 0.5Fe	-45 +15	coarse
Al_2O_3	100Al_2O_3	-22 +5	N/A

Table 5-2 Chemical composition of the S355 substrate [5.44]

Element	C	Mn	P	S	Si
wt.%	0.23	1.35	0.03	0.03	0.4

*maximum values unless otherwise stated

The WC-CoCr feedstock is an agglomerated-sintered cermet powder comprising nanoscale tungsten carbides distributed within a cobalt-chromium binder [5.41]. The Cr_3C_2-NiCr feedstock powder was manufactured using the same production method; however, in contrast to WC-CoCr, the particles comprise coarse carbide grains surrounded by a nickel-chromium binder [5.42]. The Al_2O_3 particles are comparably larger and contain no metallic binder. The shape and relative size of the three powders can be seen in Fig. 5-1. Micrographs exhibiting the internal morphology of the two cermet particles are presented in Fig. 5-2.

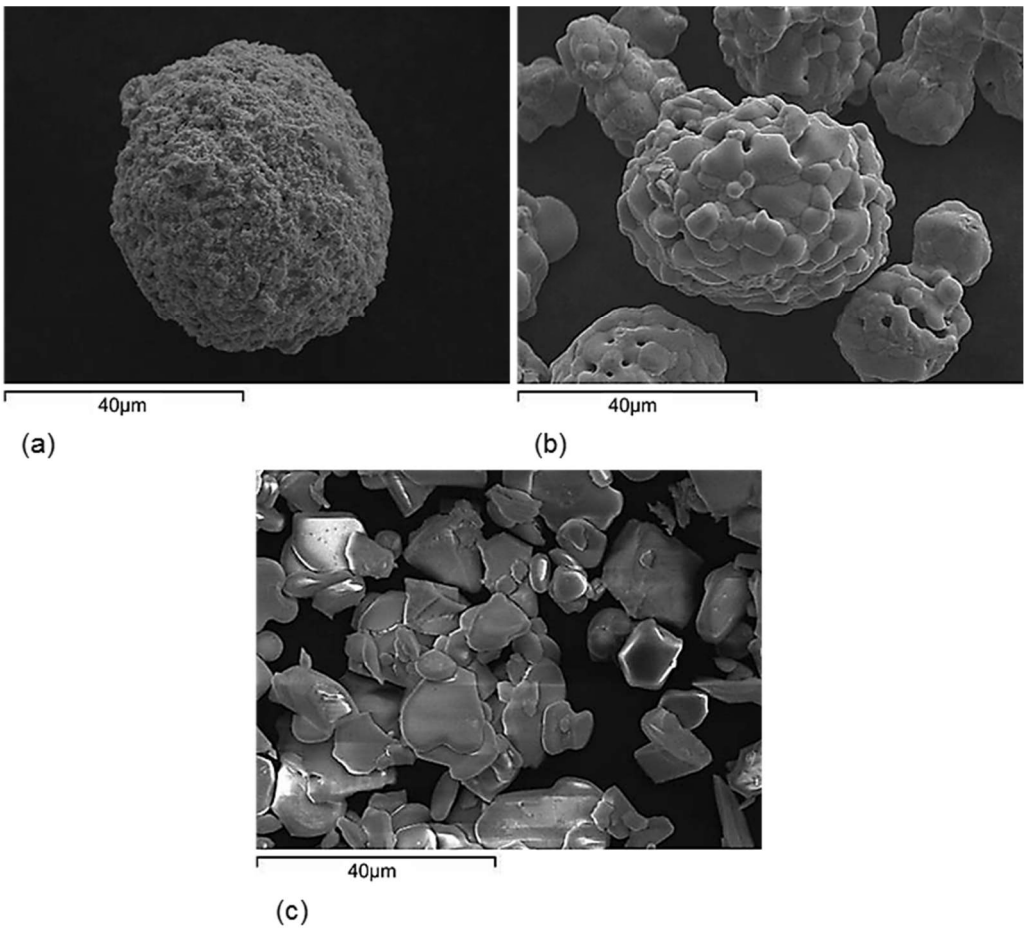

Fig. 5-1 Scanning electron micrographs of the feedstock powder particle pre-deposition; (a) WC-CoCr; (b) Cr_3C_2-NiCr; (c) Al_2O_3 [x1500]

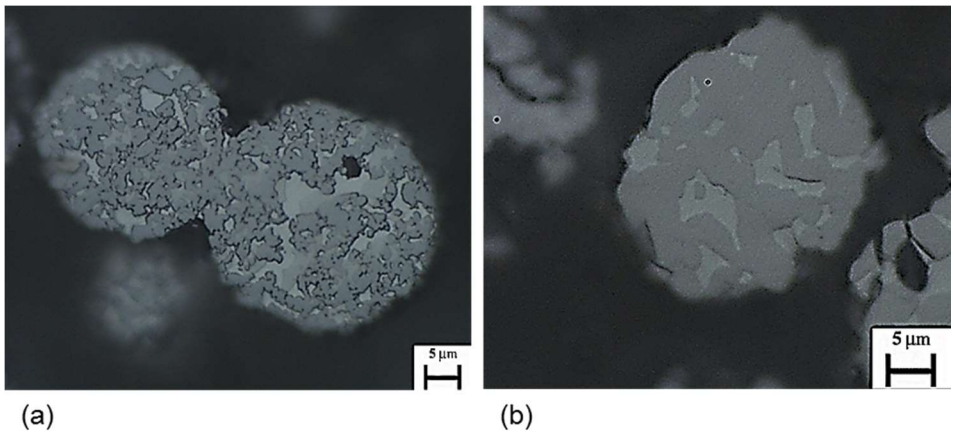

Fig. 5-2 Micrographs showing the internal morphology of the feedstock powder particles; (a) WC-CoCr; (b) Cr_3C_2-NiCr [x1000]

5.2.2 HVOF deposition parameters

Deposition of the three feedstock powders was facilitated by three different HVOF systems due to the particular spraying requirements for each powder. The Al_2O_3 coating was deposited using the UTP Top Gun system [5.1]; as this particular HVOF system exposes the feedstock material to the hot gas for an extended length of time. Therefore, the particles are at a higher temperature when they exit the nozzle. The increased particle temperature was necessary to achieve deposition of Al_2O_3 coating considering the high melting point of this oxide material [5.1]. Equally, the location of the powder injectors on the JP5000 system [5.1] yields favourable spray conditions for the deposition of Cr_3C_2-NiCr powder. By injecting the feedstock powder immediately after the combustion chamber, the likelihood of undesirable phase transformations taking place is reduced, owing to a lower particle temperature [5.1]. Additional information relating to the three HVOF systems is included in Chapter 2. Table 5-3 contains the various spray parameters used to deposit the three powders onto the S355 steel substrate.

Table 5-3 HVOF spray parameters

	WC-CoCr	Cr_3C_2-NiCr	Al_2O_3
Spray gun	DJ-2600	Tafa JP5000	UTP Top Gun
Standoff distance (mm)	229	355	178
Spray angle (°)	90	90	90
Vertical traverse speed (mm/s)	1.8	1.8	3
Horizontal traverse speed (mm/s)	1.13	1.33	1.13
No. of passes	40	74	70
Fuel flow rate (l/min)	681.5	0.455	732
Oxygen flow rate (l/min)	229.8	860	262
Carrier gas flow rate (l/min)	369.4	9.911	23.6

5.2.3 Characterisation of HVOF deposited coatings

5.2.3.1 Microstructural characterisation

The coated specimens were sectioned using a precision cutting wheel (Accutom 5) to examine the microstructure of the deposited WC-CoCr, Cr_3C_2-NiCr and Al_2O_3. Standard metallographic preparation techniques were employed to prepare the specimens to a 0.05 µm finish. The explicit steps taken to prepare the specimens are outlined in Chapter 4. The microstructure of the three coatings was

characterised using light optical and SEM, facilitated by an Olympus G51X light optical microscope and a Hitachi S-3000N SEM. Energy Dispersive Spectroscopy (EDS) provided an elemental analysis of the deposited material through spot analysis of specific regions within the coating.

The hardness of the three coatings was established using a Mitutoyo MVK-G1 microhardness indenter. Indents were made using an applied load of 200 gf at several locations within the deposited layer. The porosity was measured by Mercury Intrusion Porosimetry (Quantachrome Poremaster 60). To ensure that the porosity measurements were not skewed by the presence of the substrate, a precision cutting wheel (Accutom 5) removed the bulk substrate material. Any remaining traces of the S355 steel were removed by submerging the bottom surface of the specimen in a nitric acid bath. Optical porosity measurements, recorded in accordance with ASTM E2109 - 01(2014) [5.45], validated the porosimetry results.

5.2.4 Experimental analysis of erosion and corrosion

5.2.4.1 Dry erosion testing

A sandblasting gun with inverted particle feeder, shown as a schematic in Fig. 5-3, facilitated the dry erosion testing. Erosion testing was carried out at room temperature using a method based on GE-E50TF121 specification [5.48].

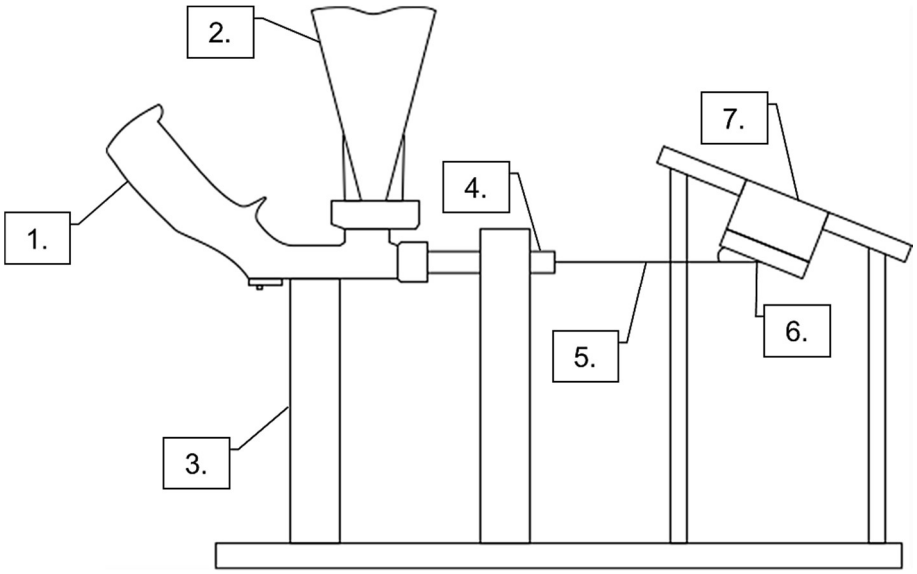

Fig. 5-3 Schematic diagram of dry erosion test rig (not to scale); (1) sandblasting gun, (2) particle hopper, (3) rig fixture, (4) jet nozzle, (5) particle stream, (6) test specimen, (7) sample holder.

The test samples were mounted at 20° to the jet stream at a standoff distance of 100 mm. Alumina, with an average particle size of 50 μm, was accelerated onto the surface at a feed rate of 5.3 g/s, with the test concluded when 300 g of alumina had passed through the jet nozzle.

5.2.4.2 Slurry erosion assessment

A closed loop jet impingement rig, as detailed in Chapter 4, was used to evaluate the slurry erosion performance of the three coatings. The test parameters used throughout the experimental programme are listed in Table 5-4.

Table 5-4 Liquid impingement test parameters

flow velocity (m/s)	sand concentration (g/l)	nozzle standoff distance (mm)	nozzle exit diameter (mm)	sample diameter (mm)	test duration (min)
23	2.3	20	4	20	60

Prior to testing, the surface of each sample was lightly abraded with 500-grit SiC paper to produce a uniform surface finish. The specimen was located directly beneath the nozzle while fully submerged in the slurry solution. The angle at which slurry impinged the coated surface was modified to measure the mass loss for 30° and 90° impingement. Each sample was weighed pre- and post-testing using a mass balance (accuracy 0.1 mg) to establish the total mass loss. Three test replicates of each coating, as well as uncoated S355, were evaluated to provide an average mass loss. A focal variation microscope (Alicona Infinite Focus G4) [5.52] was used to measure the volume of the wear scars produced by the impinging slurry.

5.2.4.3 Corrosion measurement

To establish the contribution of erosion, corrosion and synergy to the total mass loss, it was necessary to employ cathodic protection (CP) and anodic/cathodic polarisation. Specifically, CP was applied to eliminate the effects of corrosion, thereby establishing the contribution of pure erosion [5.26]. A potential of -1 V was applied to the specimen (working electrode) which suppressed any anodic reaction and prevented any corrosion developing on the surface.

Anodic/cathodic polarisation scans were conducted under slurry impingement test conditions to establish the corrosion mass loss rate of each specimen; in accordance with the method outlined in ASTM G102 - 89 (2010) [5.54]. The details of the specific measurement equipment and test methodology are included in Chapter 4.

The mass loss attributed to the synergistic effect of combined erosion-corrosion was calculated by subtracting the mass loss from pure erosion (CP) and corrosion (anodic polarisation) from the mass loss measured under free erosion-corrosion conditions (total mass loss).

5.3 Results and Discussion

5.3.1 Light optical microscopy

The HVOF coatings were examined using light optical microscopy to characterise the microstructure of the deposited coatings. For WC-CoCr (Fig. 5-4a-b), the microstructure exhibited a homogenous distribution of carbide reinforcing particles within the cobalt-chromium binder. Moreover, there was no visible evidence of cracking defects within the coating.

When the coating was examined at high magnification (Fig. 5-4b), porosity was evident within the deposited layer. These pores typically occur when the sprayed particles do not possess sufficient heat to plastically deform and bond with adjacent particles [5.56]. At the coating-to-substrate interface region (Fig. 5-4a) there was evidence of inclusions within the microstructure. These inclusions reduce the area of metal-to-metal contact [5.57] with the substrate, thereby decreasing the adhesive strength of the coating-to-substrate bond [5.57]. In general, regions void of any inclusions or defects exhibit a homogenous distribution of tungsten carbide particles within the cobalt chromium binder.

Fig. 5-5 presents micrographs of the Cr_3C_2-NiCr coating. Fig. 5-5a is a low magnification view of the coating, illustrating the thickness and coating-to-substrate interface, while Fig. 5-5b highlights the distribution of reinforcements within the nickel-chromium binder. Both images (Fig. 5-5) show that the coating layer exhibits only minor porosity. However, Fig. 5-5b shows small pores that form along the interface between carbide and binder material [5.56]. As with the WC-CoCr coating, some of the deposited particles have not sufficiently deformed upon contact with the surface leading to minor cavities between adjacent particles.

The structure of the deposited Al_2O_3 coating (Fig. 5-6) is dense and reveals no evidence of porosity or inclusions within the layer. This is attributed to the high particle impact velocity in addition to the elevated particle temperature generated by the UTP Top Gun HVOF system; which produces significant flattening [5.58] of the alumina particles at the point of impact.

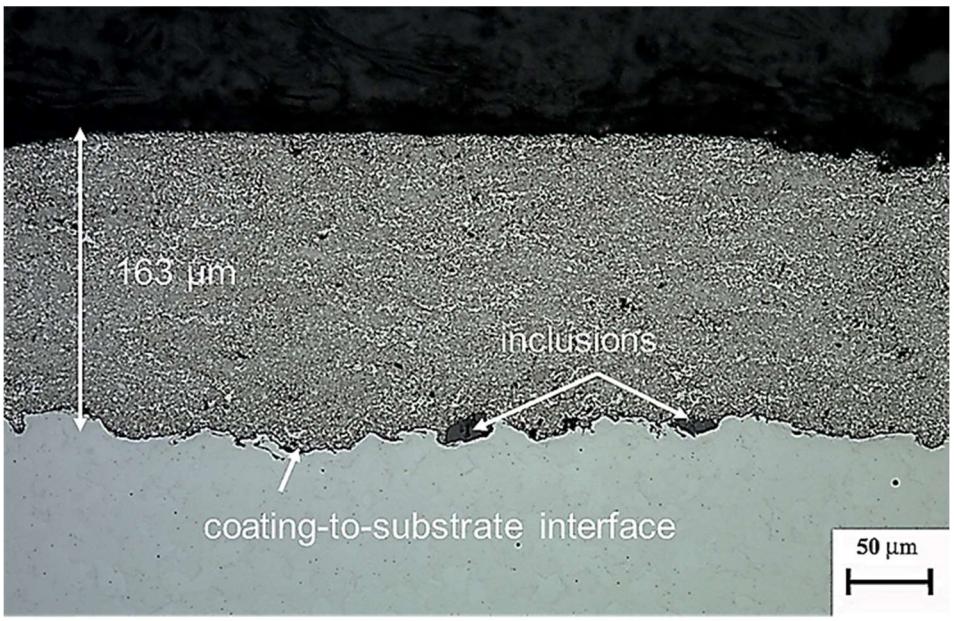

(a)

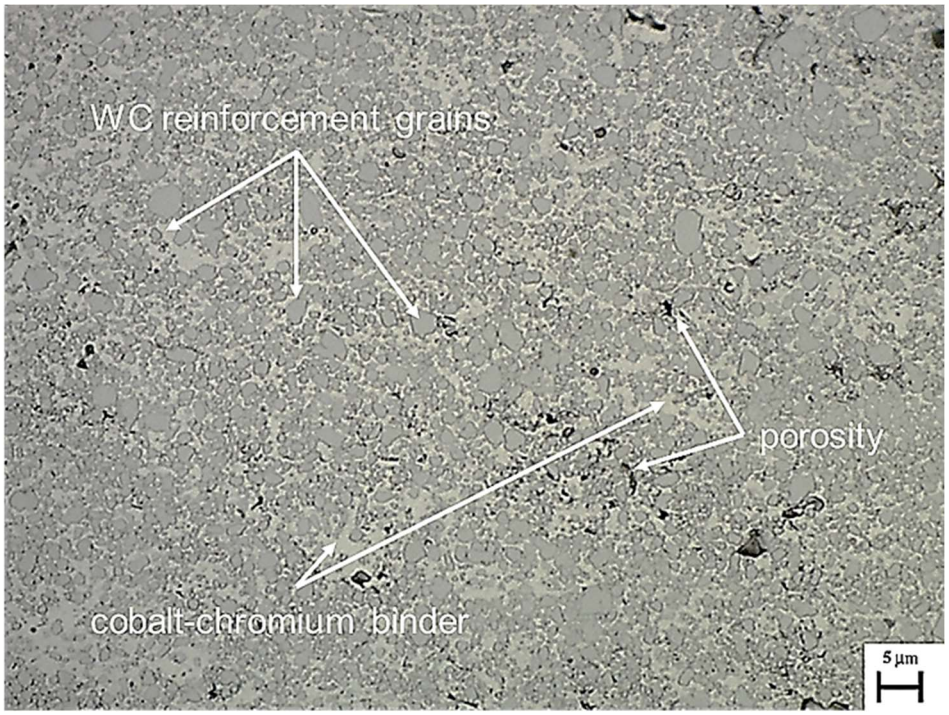

(b)

Fig. 5-4 Optical micrograph of the WC-CoCr coated specimen; (a) low magnification micrograph showing the coating thickness and coating-to-substrate interface [x200, Unetched]; (b) high magnification micrograph showing the distribution of WC reinforcement grains within the WC-CoCr coating [x1000, Unetched]

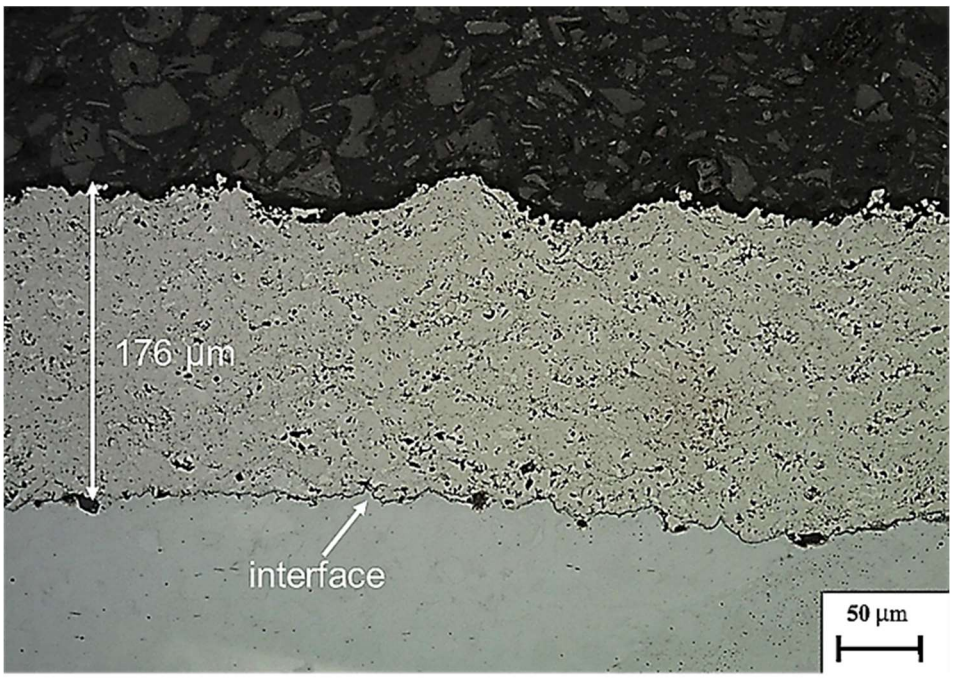

(a)

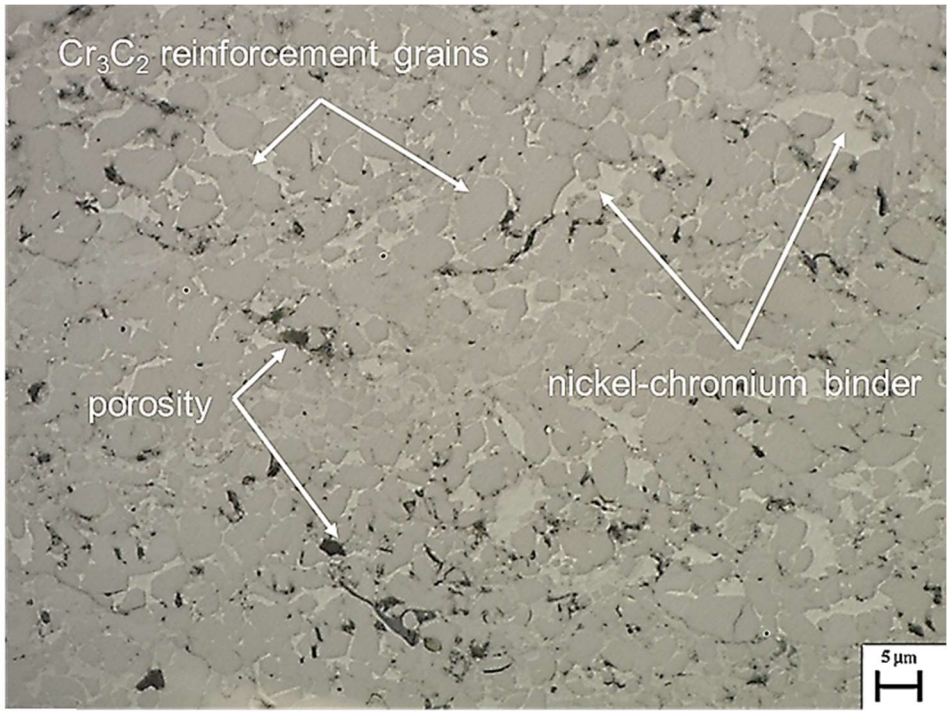

(b)

Fig. 5-5 Optical micrograph of the Cr_3C_2-NiCr coated specimen; (a) low magnification micrograph interface [x200, Unetched]; (b) high magnification micrograph showing the distribution of Cr_3C_2 reinforcement grains within the Cr_3C_2-NiCr coating [x1000, Unetched]

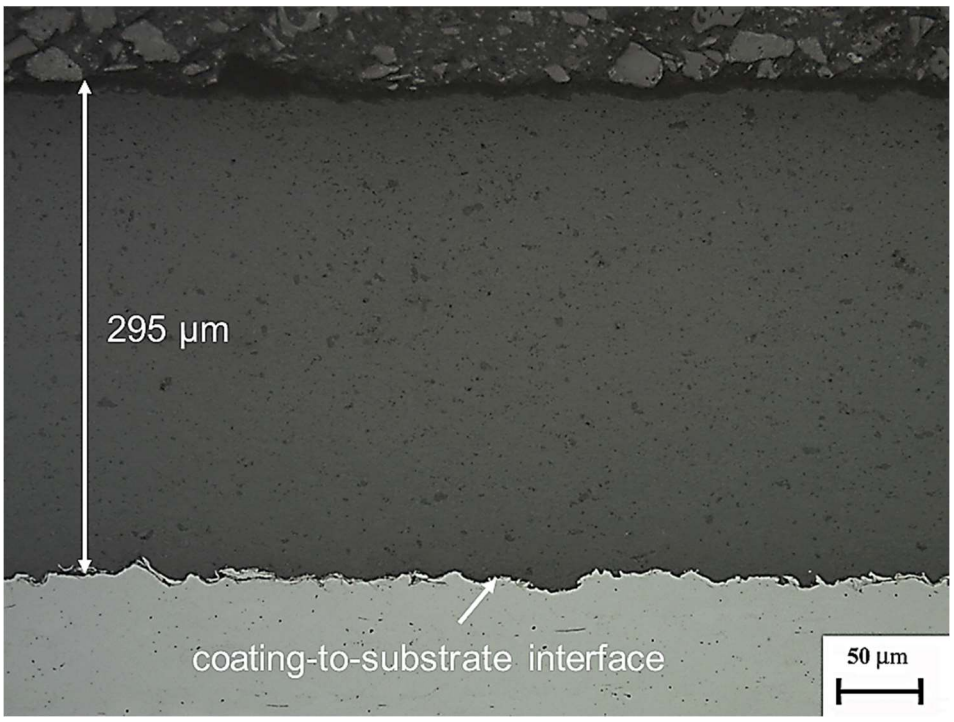

Fig. 5-6 Optical micrograph of the Al_2O_3 coated specimen showing the coating thickness and coating-to-substrate interface [x200, Unetched]

5.3.2 Scanning electron microscopy

The three coatings were examined by SEM to characterise the microstructure at the interface between reinforcement and binder (in the case of the WC-CoCr and Cr_3C_2-NiCr coatings). Moreover, Electron Dispersive Spectroscopy (EDS) was used to verify several of the features highlighted through optical microscopy.

Using EDS spot analysis, the respective chemical compositions of the dark and light coloured regions depicted in Fig. 5-4 and Fig. 5-5 were established. When examining the WC-CoCr coating, the EDS analysis revealed high quantities (>80%) of tungsten in the dark coloured regions and no tungsten in the light coloured regions. Therefore, the EDS results confirm that the dark regions are the carbide reinforcements and the light areas represent the binder. The same approach was used to verify that the dark regions on the Cr_3C_2-NiCr specimen depict the carbide reinforcements, while the light coloured region is the nickel-chromium binder. Fig. 5-7 illustrates the locations in which EDS scanning was conducted. The corresponding chemical composition recorded by EDS is presented in Table 5-5.

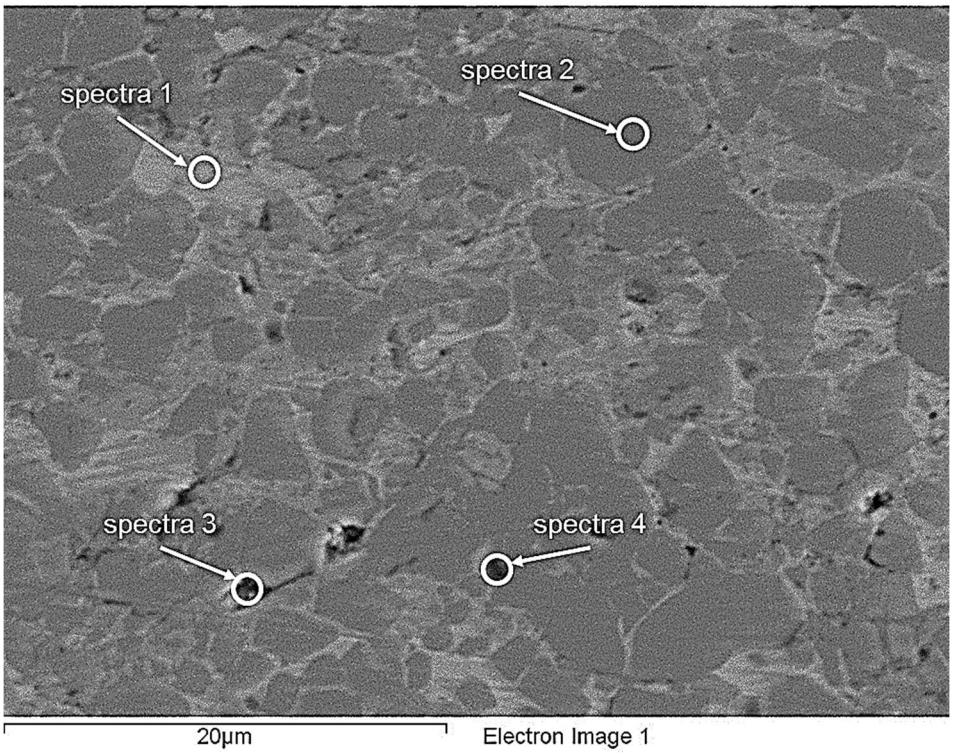

Fig. 5-7 SEM micrograph of the Cr_3C_2-NiCr coating showing the location of EDS analysis [x4000]

Table 5-5 Chemical composition of the locations depicted in Fig. 5-7

	Cr	C	Ni
Spectrum 1	81.7	18.3	
Spectrum 2	15.1	4.8	77.3

EDS was also employed to determine whether the dark regions on the micrographs depict pores or inclusions within the matrix. EDS scanning of these regions (spectra 3 and 4 on Fig. 5-7) recorded comparatively low dead-time readings, thereby indicating that the dark areas on the micrograph are indeed voids in the microstructure.

5.3.3 Porosity

The porosity of each coating was measured experimentally by mercury intrusion porosimetry (MIP) and optically using ImageJ image analysis software to determine the density of the deposited material. By comparing the two sets of results (MIP and optical measurements), it was possible to determine if the pores evidenced by the micrographs were a consequence of the metallographic preparation, or if they were generated during the HVOF deposition process. If the results from the

experimental and optical measurements are analogous, it can be concluded that the pores exist in the as-deposited HVOF coating and are not produced by the metallographic preparation. However, if the optical measurements denote considerably greater porosity, the pores are likely a consequence of the metallographic preparation process. Table 5-6 presents the average porosity values for each coating when measured by MIP and by optical microscopy.

Analysis of the three coatings reveals that the WC-CoCr layer has the highest density and exhibits 85% lower porosity in contrast to the Cr_3C_2-NiCr. This finding is attributed to two factors. The first is differences associated with the HVOF systems used to deposit each powder. The Tafa JP5000 system, used to spray the Cr_3C_2-NiCr material, injects the feedstock powder downstream of the combustion chamber and as such does not raise the particle temperature to the same level as the system used to deposit the WC-CoCr coating (DJ-2600). Consequently, the Cr_3C_2-NiCr particles are unable to deform to the same extent as the WC-CoCr material, hence resulting in small void spaces (pores) between adjacent particles.

Table 5-6 Coating porosity values

	MIP porosity (vol.%)	ImageJ porosity (vol.%)
WC-CoCr	0.2	0.2
Cr_3C_2-NiCr	1.3	2.1
Al_2O_3	1.4	1.3

*results are an average of three test replicates

The second factor that accounts for the difference in porosity between the coatings is the difference in the reinforcing grain size within the cermet powders (WC-CoCr and Cr_3C_2-NiCr). The WC-CoCr feedstock material comprises nanoscale carbides distributed throughout a cobalt chromium binder (Fig. 5-2a). Conversely, the Cr_3C_2-NiCr powder comprises larger microscale reinforcement grains surrounded by a nickel-chromium binder (Fig. 5-2b); as presented in Table 5-1.

In the case of the Cr_3C_2-NiCr powder, the presence of larger carbide grains limits the particle deformation upon contact with the substrate surface [5.59] and, hence, results in void spaces where the particles have failed to agglomerate with surrounding particles. A similar trend has been observed in existing studies [5.4, 5.59, 5.60], with the authors attributing increased particle deformation at the point of impact to the presence of smaller reinforcement grains within the feedstock powder [5.59].

The comparably low density of the Al_2O_3 coating is also a consequence of reinforcement grain size. Unlike the cermet powders, which contain reinforcement grains surrounded by a metallic binder, the entire Al_2O_3 particle is the reinforcement grain. The size of the Al_2O_3 particles is considerably larger than the reinforcements contained in the WC-CoCr and Cr_3C_2-NiCr powders. Consequently, the HVOF system is required to impart considerable heat into these particles to cause partial melting. While the UTP Top Gun system is capable of partially melting the Al_2O_3 feedstock material, the extent to which the particles are softened is less than the cermets that contain a metallic binder. Accordingly, the amount of deformation experienced by the Al_2O_3 particles at the point of impact is less than is experienced by either of the cermet powders. Hence, the porosity of the Al_2O_3 coating is greater than that of WC-CoCr and Cr_3C_2-NiCr.

The two measurement techniques (MIP and optical) recorded different values of porosity for the Cr_3C_2-NiCr specimen. ImageJ indicated a coating 1.6 times more porous than that determined through porosimetry. Therefore, the Cr_3C_2-NiCr coating is more susceptible to pull-out [5.61] during the preparation process compared to the WC-CoCr coating.

5.3.4 Coating microhardness

Fig. 5-8 presents the average microhardness values measured in the three HVOF deposited coatings. The WC-CoCr coating possesses the highest overall average hardness at 1364 HV. This result constitutes a substantial increase (approximately 580%) over the S355, which was found to have a hardness value of 200 HV. This result is in agreement with previous work which attributes the increased hardness to the presence of evenly dispersed nanoscale carbides [5.62]. Due to the even distribution of the carbides, the load from the diamond indenter is distributed across the reinforcements and the ductile matrix. Consequently, the microhardness of the MMC is an average of both hardness values (reinforcements and matrix alloy) [5.63].

Optical microscopy of hardness indents illustrates a direct relationship between reinforcement concentration and the indicated hardness. For example, the lowest hardness measurements are obtained when indenting on binder alloy, whereas the highest hardness values are measured in regions with high concentrations of carbides.

The Cr_3C_2-NiCr coating exhibited an average microhardness of 850 HV, representing a 325% increase over the S355 steel. While this result demonstrates a considerable increase over the as-received substrate, the increase is not as substantial as the WC-CoCr coating. This smaller hardness increase measured in the Cr_3C_2-NiCr coating (as compared with the WC-CoCr) was attributed to the differences in the hardness of the respective reinforcing particles. The chromium carbides (1200 HV) [5.42], while hard in contrast to metallic alloys, do not possess the same hardness as tungsten carbide (1450 HV) [5.41]. Therefore, it is unsurprising that the Cr_3C_2-NiCr would fail to match the hardness of WC-CoCr. Moreover, based on a visual examination of each coatings' microstructure, the distribution of the chromium carbides does not appear as homogeneous as the tungsten carbides. Consequently, in regions void of reinforcing particles, the load from the indenter is predominantly applied to binder alloy only. Hence, the average hardness of the coating would drop accordingly.

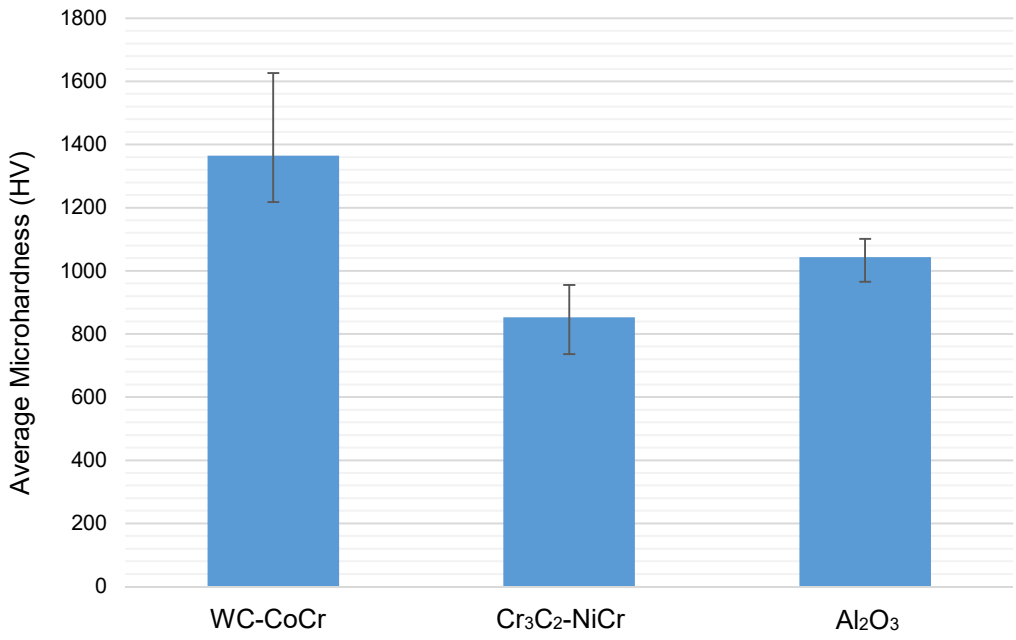

Fig. 5-8 Average microhardness values of the three HVOF deposited coatings (average of 5 measurements)

The microhardness measurements from the Al_2O_3 specimen present the smallest range of hardness values out of the three examined coatings. The more consistent data set is a consequence of the coating comprising a single phase (Al_2O_3), with no metallic binder. Considering that the hardness of the cermet powders is an average of the binder and alloy, the disparity in the respective hardness values of

each phase leads to a broad scatter of microhardness results. As the Al_2O_3 coating has only a single phase (no binder), the individual microhardness measurements do not vary significantly from the average hardness of the coating.

5.3.5 Mass loss from dry erosion

The variation in mass and volume loss between the three coatings following dry erosion testing is presented in Fig. 5-9. The results show that WC-CoCr and Cr_3C_2-NiCr experience similar levels of mass loss, with Al_2O_3 exhibiting comparably less mass loss. However, considering the dissimilar densities of the three coatings, the mass loss does not provide a suitable metric with which to compare the erosion performance of the three coatings. When the coating density is taken into account, the volume loss of the three coatings presents a different relationship (Fig. 5-9). The low density of Al_2O_3 and the comparatively high density of WC-CoCr result in both coatings yielding similar volume loss, with Cr_3C_2-NiCr specimens experiencing approximately double the volume loss. Based on these findings and those outlined in Fig. 5-9, it can be concluded that, under dry erosion testing, coatings possessing higher hardness perform favourably under impingement at 20°. This outcome is in agreement with existing studies on the erosion of materials at shallow angles of attack [5.64, 5.65].

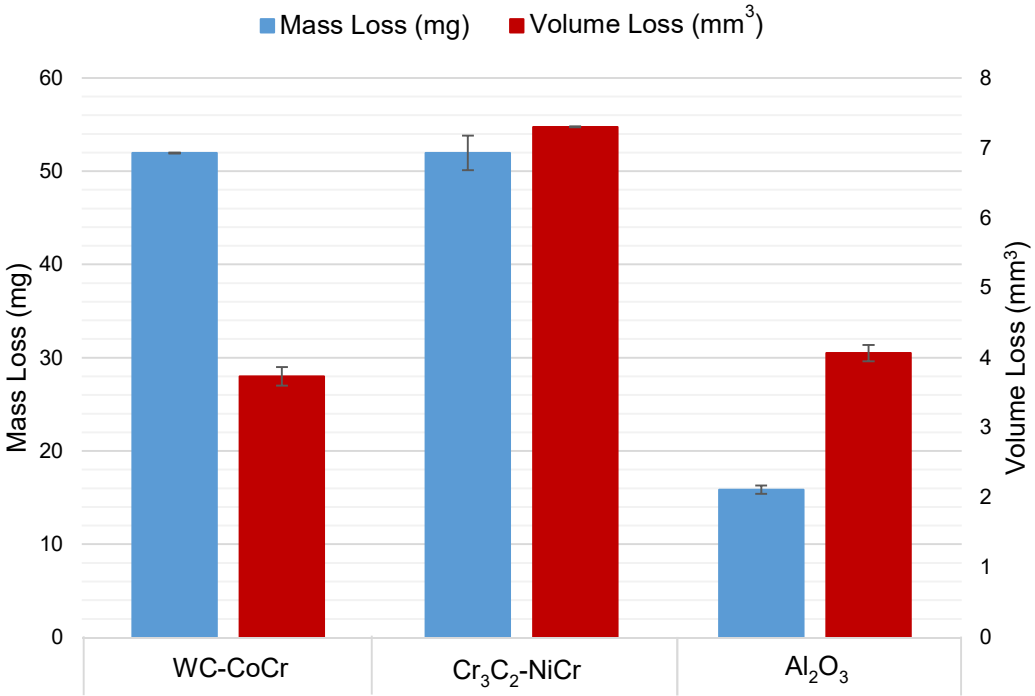

Fig. 5-9 Measured mass and volume loss from dry erosion testing

The superior erosion performance of the WC-CoCr and Al_2O_3 specimens is attributed to the greater hardness of the coating (Fig. 5-8). The variation in the structure of the feedstock powders also contributes to the comparably poor performance of the Cr_3C_2-NiCr specimen. The large microscale reinforcement grains contained in the Cr_3C_2-NiCr cermet yield increased the spacing between the reinforcements within the coating. Consequently, a greater surface area of nickel chromium binder is exposed to the impinging slurry. In contrast to the reinforcements, the binder is soft and is, therefore, more susceptible to erosive damage from the impinging material. Furthermore, the shallow impingement angle (20°) employed in this study has been shown to produce a greater material loss on ductile alloys as a result of the cutting and ploughing erosion mechanisms [5.66] (as discussed in Chapter 3).

Based on these findings (Fig. 5-9), it can be concluded that, under dry erosion testing, the coatings that exhibit higher hardness demonstrate superior erosion performance under impingement at 20°. This outcome is in agreement with existing studies on the erosion of materials at shallow angles of attack [5.64, 5.65].

5.3.6 Mass and volume loss from slurry impingement

5.3.6.1 Free erosion-corrosion conditions

Mass Loss

Fig. 5-10 presents the average mass loss (three test replicates at 90° and 30° impingement) from the three coatings and the as-received S355 substrate. The error bars indicate the range of the individual test results. It should be noted that the measured mass loss for Cr_3C_2-NiCr and Al_2O_3 specimens include mass loss from the substrate material, due to the coatings being breached under the highly aggressive test environment.

The results show that the comparably ductile S355 substrate experiences elevated mass loss at a shallower angle of attack. In contrast, the coated specimens experience significantly increased mass loss under 90° attack. This outcome is attributed to the presence of the hard reinforcement phase within the coating and is in agreement with the work of Andrews et al. [5.20]. The research team [5.20] previously demonstrated that alloys with higher carbide content experience increased mass loss at higher angles of attack, with more ductile steels experiencing their most substantial mass loss at shallower angles of attack. This finding was attributed, by the

authors [5.20], to the hard reinforcements limiting the depth and extent of cutting damage caused by the impinging material.

Despite its high hardness, the Al_2O_3 coating has experienced significant mass loss under 90° impingement, with the average mass loss being close to that of uncoated S355. However, under 30° impingement, the mass loss from the Al_2O_3 coating was comparably less. This result is also in agreement with the published findings [5.20] in which an increased quantity of carbides resulted in maximum damage occurring at higher (near-90°) angles of attack. A similar mechanism operates within the Cr_3C_2-NiCr coating, with attack at 90° causing a greater mass loss when compared with the mass loss from the uncoated specimen. Consequently, Cr_3C_2-NiCr proved the poorest performing coating of the three. The high mass loss associated with the Cr_3C_2-NiCr specimen is attributed to the removal of the large reinforcement grains from the matrix. Later sections examine and discuss the microstructure within the impinged region to confirm that carbide removal is the primary erosion mechanism.

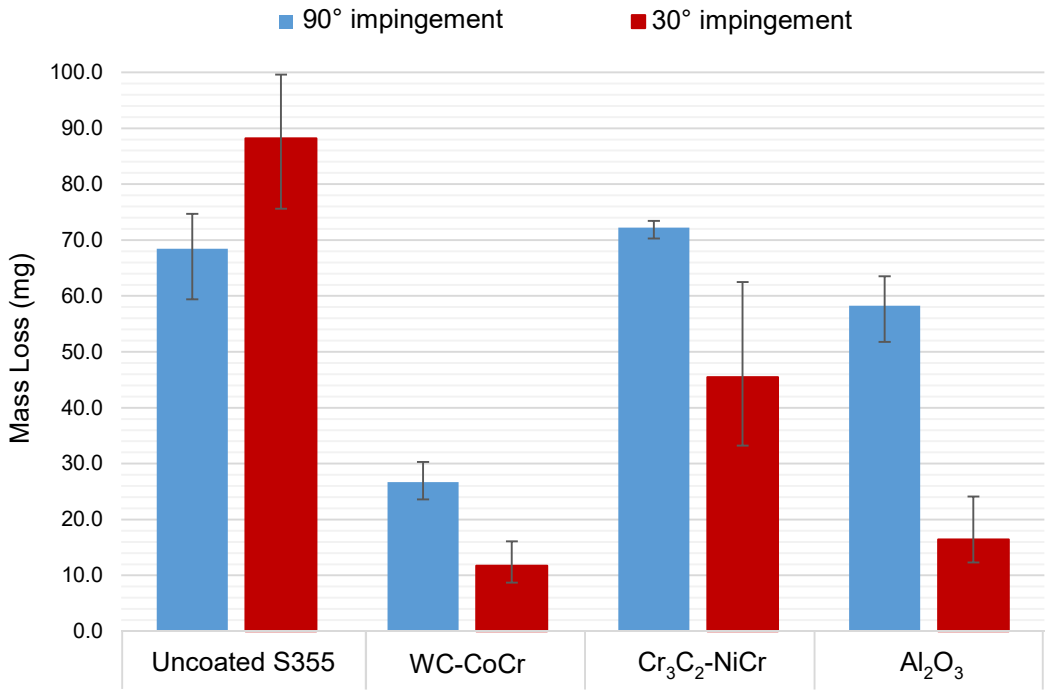

Fig. 5-10 Mass loss under free erosion-corrosion conditions at 90° and 30° impingement

The reduced mass loss measured on the WC-CoCr coating, in contrast to the Cr_3C_2-NiCr and Al_2O_3 coated specimens, demonstrates the ability of the binder to retain nanoscale carbide grains within the coating matrix. This, combined with the increased hardness of the coating, has resulted in WC-CoCr functioning as an

effective protective layer for S355 steel under erosion-corrosion conditions at both 90° and 30° angle of attack. The findings support previous work on the erosion-corrosion of HVOF coatings under multiple angles of attack [5.20, 5.21, 5.67–5.69].

The results demonstrate a link between high average coating hardness (Fig. 5-8) and low mass loss (Fig. 5-10). The recorded data show the mass loss to be inversely related to coating hardness. This is true for both angles of attack and is in agreement with existing published results [5.15, 5.70].

Additionally, Fig. 5-11 highlights the variation in mass loss between 30° and 90° angle of attack. In the case of uncoated steel, the lack of any reinforcement grains yields a comparably ductile coating [5.71]. Fig. 5-11 demonstrates a negative gradient linking the average mass loss at 30° and 90° angle of attack, i.e. the steel experiences increased mass loss at shallower angles of attack.

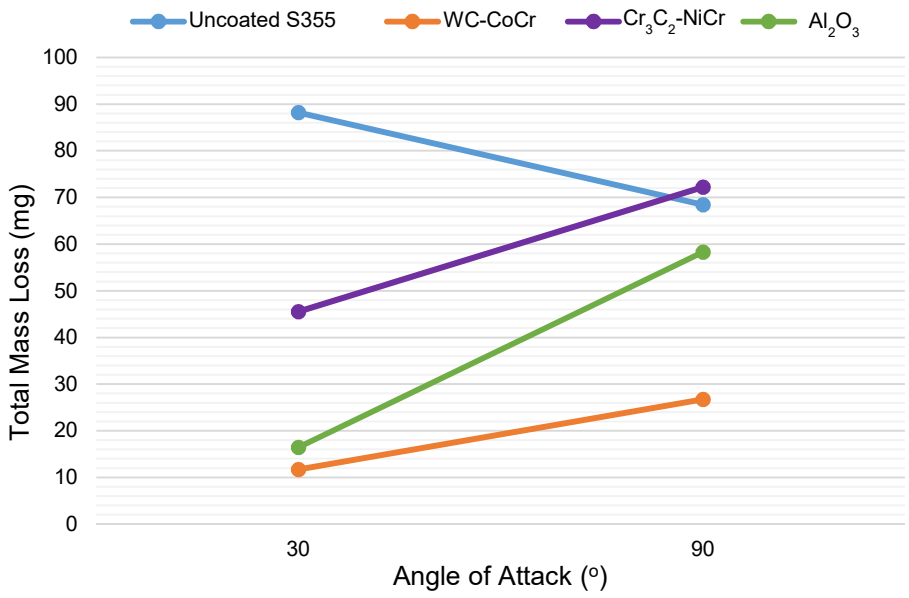

Fig. 5-11 Correlation between the angle of attack and total mass loss for each coating type

Volume Loss

Fig. 5-12 presents the volume loss for each coating and the uncoated substrate. For specimens in which the coating was breached during the test, the chart (Fig. 5-12) shows the combined volume of material removed from the coating and the substrate.

The WC-CoCr was the only coating not to be penetrated following one hour of exposure to the impinging slurry. The total volume loss recorded in the WC-CoCr coating was approximately 20% of the value recorded for the uncoated material. Both

Cr_3C_2-NiCr and Al_2O_3 specimens sustained substantial damage to the substrate material immediately beneath the directly impinged zone.

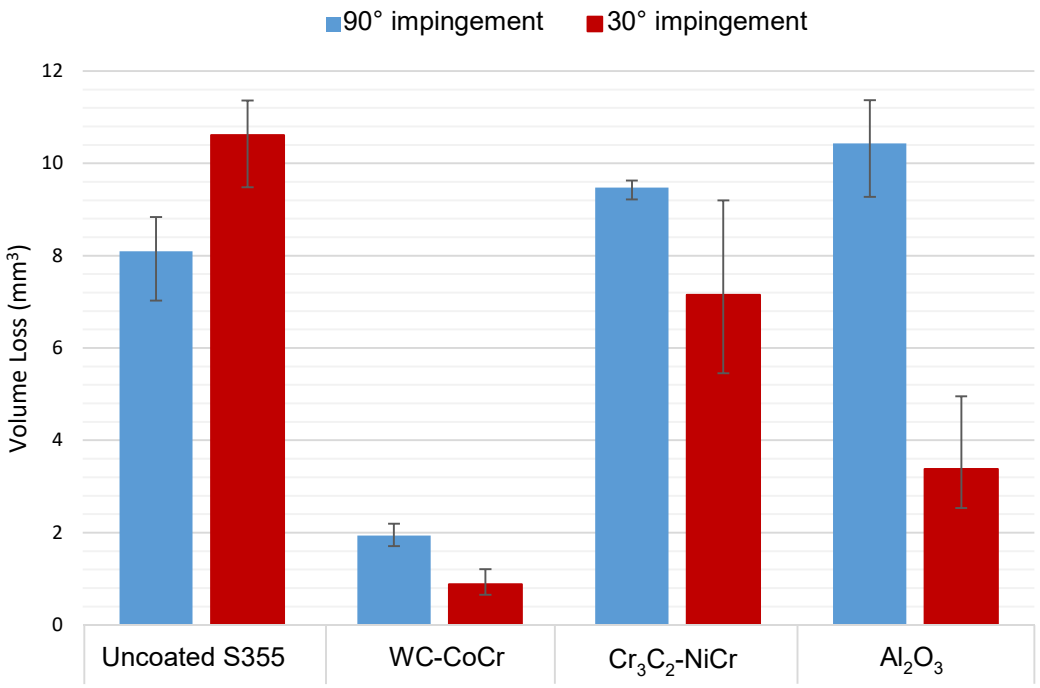

Fig. 5-12 Volume loss under free erosion-corrosion conditions at 90° and 30° impingement

5.3.6.2 Impressed current cathodic protection (ICCP)

Mass Loss

The slurry erosion test was repeated with applied CP to prevent any corrosion occurring on the surface of the specimen. The measured mass loss, therefore, represented the quantity of material removed by mechanical erosive wear, as opposed to combined erosion-corrosion [5.23]. Fig. 5-13 presents the mass loss measured with and without applied CP under 90° impingement and highlights the extent to which applied CP reduces the amount of material removed from each respective coating.

The results (Fig. 5-13) show that the uncoated S355 and Al_2O_3 specimens exhibit the most significant reduction in the mass loss with applied CP. Considering corrosion and synergy account for the difference between the free erosion-corrosion mass loss and mass loss with applied CP, the results indicate that the uncoated S355 and Al_2O_3 specimens suffer most from corrosion and synergy. While this is to be expected for the uncoated S355 given the poor corrosion performance of low carbon steel, this is a surprising outcome for the Al_2O_3 coated specimen considering that

Al_2O_3 does not electrochemically interact with the slurry. The considerable drop in mass loss measured in the Al_2O_3 specimen with applied CP is attributed to the protective Al_2O_3 coating being breached during the test. As a consequence, the slurry is corroding the uncoated S355 material for the majority of the test and thus exhibits a similar drop in the mass loss with applied CP.

A negligible difference in the mass loss with and without applied CP was measured on the Cr_3C_2-NiCr specimen (Fig. 5-13). Cr_3C_2-NiCr is known for its superior corrosion properties and is one of the reasons why this particular coating is selected for use in corrosive operating environments [5.72].The negligible difference in the mass loss with and without applied CP demonstrates the superior corrosion performance of Cr_3C_2-NiCr and is in agreement with the published literature [5.72, 5.73].

The WC-CoCr coated specimen measured the lowest overall mass loss under free erosion-corrosion conditions and with applied CP. This finding is attributed to the high hardness of the WC-CoCr coating and the homogenous distribution of carbide reinforcements. The poor corrosion properties of the WC-CoCr are not significantly detrimental to the erosion-corrosion performance of the coating considering the damage caused by the impinging slurry is dominated by mechanical erosion.

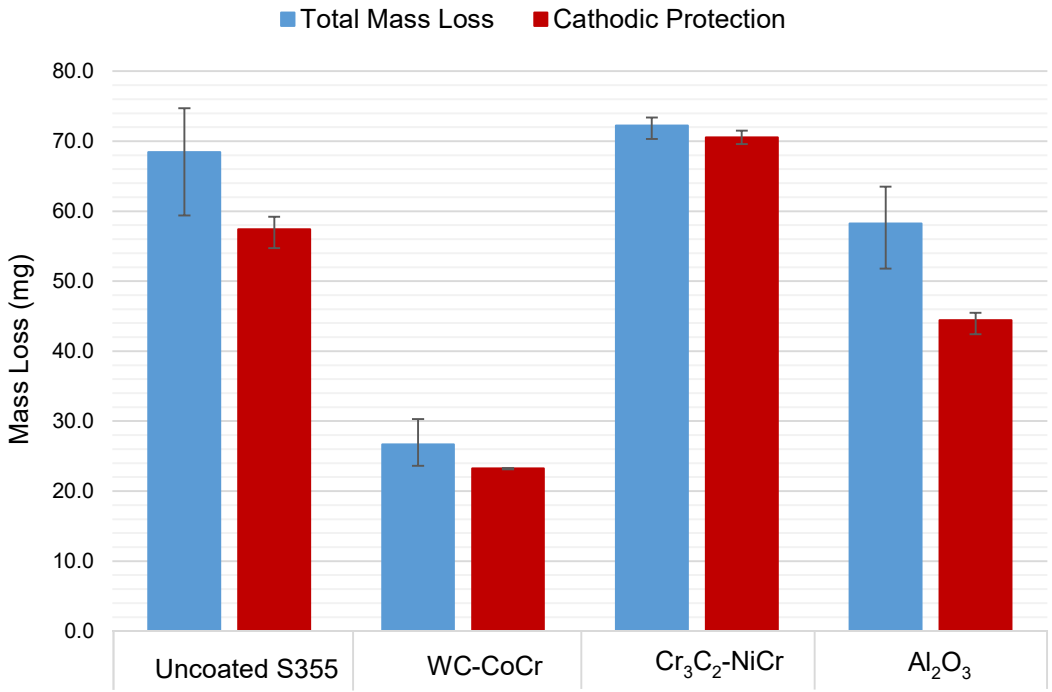

Fig. 5-13 Mass loss following one hour of exposure to the slurry under free erosion-corrosion conditions and with applied CP (90° impingement)

Comparison of dry and slurry erosion results

The slurry erosion performance of the three coatings was measured with applied CP, under 20° impingement, to facilitate direct comparison with the dry erosion results (Section 5.3.5). By comparing the volume loss under slurry and dry erosion (Fig. 5-14), the results show significantly increased levels of material loss under dry erosion conditions. The increased volume loss associated with dry erosion testing was attributed to the variation in the impact velocity and the particle morphology of the impinging material between the two testing regimes [5.74–5.76].

Existing research [5.74, 5.75] has shown particle velocity under slurry conditions to be significantly reduced as a consequence of squeeze film effects. Squeeze film is the phenomenon whereby the slurry acts as a barrier between the impinging particles and the surface [5.74, 5.75]. Energy is required to break this barrier, which in turn, decreases the particle impact velocity. As a result, the cumulative erosive damage is reduced. Conversely, the particle velocity under dry erosion will reflect the gas velocity emanating from the nozzle [5.76].

The variation in particle morphology also accounts for the increased volume loss under dry jet erosion, with Levy et al. [5.77] demonstrating a rise in the erosion rate with increased erodent hardness. Numerous studies [5.46, 5.77–5.79] also report the influence of erosive particle material, size and shape on the recorded erosion rate.

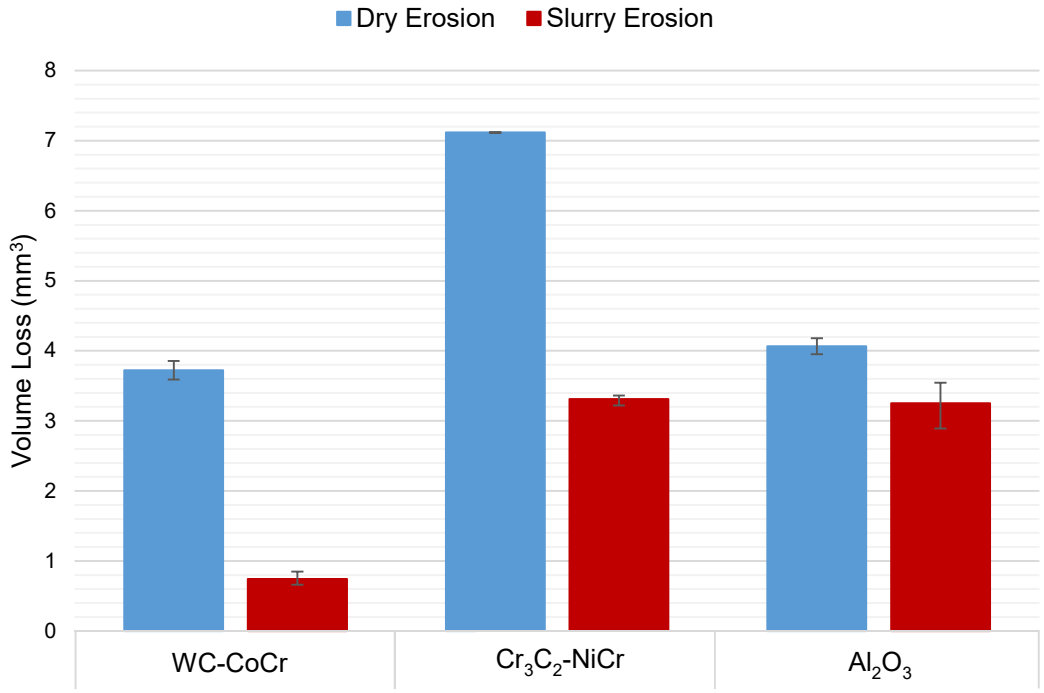

Fig. 5-14 Average volume loss following dry and slurry erosion testing (20° impingement)

Under dry erosion conditions, the WC-CoCr and Al_2O_3 coatings experience similar volume loss. However, under slurry erosion conditions the Al_2O_3 coating exhibits similar volume loss to the Cr_3C_2-NiCr coating. Two observations can be drawn from this data (Fig. 5-14). The first is that the Cr_3C_2-NiCr coating has resulted in the highest volume loss under both test regimes. Considering that the Cr_3C_2-NiCr coating measured the lowest overall hardness of the three coatings, it can be said that coating hardness is inversely proportional to volume loss at shallow angles of attack. This outcome is in agreement with the work of several research groups [5.12, 5.20, 5.64, 5.65, 5.69].

The second observation concerns the variation in the volume loss between each coating type under the two test regimes. The data (Fig. 5-14) shows that WC-CoCr and Cr_3C_2-NiCr coatings behave differently under dry erosion and slurry erosion. Specifically, the WC-CoCr and Cr_3C_2-NiCr specimens demonstrate comparably high volume loss under dry erosion. Conversely, the Al_2O_3 coating exhibits similar volume loss under both erosion regimes. Thus, for ceramic-based coatings, dry erosion testing does not necessarily reflect the erosion mechanisms and associated material losses that are encountered under slurry erosion. Therefore, dry erosion testing does not provide a suitable benchmark with which to assess the erosion performance of coatings that typically operate within a slurry based flowing environment.

5.3.7 Measurement of corrosion rate and synergy

5.3.7.1 Corrosion rate

The study has, thus far, recorded the mass loss of specimens under free erosion-corrosion conditions and with applied CP. However, to establish the contributing factor synergy, it is necessary to measure the mass loss attributed to pure corrosion. The method for determining the mass loss generated by corrosion is discussed in detail in Chapter 4.

To perform the anodic and cathodic polarisation sweeps, it was first necessary to measure the E_{corr} of each specimen under static and flowing conditions. After 200 seconds of exposure to the flowing slurry, the E_{corr} value of the Cr_3C_2-NiCr specimen dropped to approximately -600 mV. Considering that -600 mV is equal to the E_{corr} of uncoated S355, the result suggests that the coating has been damaged to such an extent that current could flow between the slurry and the substrate.

When the Al_2O_3 coating was exposed to the impinging slurry, no current was detected for 100 s. However, after 100 s a -80 mV voltage was measured across the

working electrode. Given that the Al_2O_3 coating has been shown to prevent the flow of current, the identified -80 mV voltage is ascribed to the coating being damaged to such an extent that the current was able to flow between the substrate and the slurry. Continued impingement by the erosive particles led to an increase in the detected voltage, thus indicating that a larger area of the substrate material had been exposed to the slurry. After approximately 420 s, the E_{corr} of the specimen fell immediately to -480 mV and remained constant at this value (-480 mV) for the remainder of the test.

The results show that following 80 seconds of exposure, the impinging jet had damaged the coating to such an extent that current could flow between the substrate and the slurry. Further impingement of the erosive particles resulted in the complete removal of the Al_2O_3 layer after approximately 420 s, at which point the E_{corr} of the specimen dropped to a value similar to that of the uncoated S355 substrate. This outcome corroborates the results discussed in Section 5.3.6.2 and further highlights the poor performance of Al_2O_3 and Cr_3C_2-NiCr as protective surface coatings when exposed to high velocity slurry.

Considering that the coating layer was breached by the slurry in such a short period of time, it was not possible to measure the corrosion rate under flowing conditions. Thus, the mass loss from corrosion under flowing conditions was determined for the uncoated S355 and WC-CoCr specimens only. However, the corrosion rate for each coating was established under static conditions to provide some indication as to the corrosion performance of each material.

Under static conditions, the Al_2O_3 coating prevented the flow of current between the slurry and the electrode; hence, no corrosion data is presented for the Al_2O_3 specimen.

Table 5-7 and Table 5-8 present the extrapolated corrosion current density for each material under static and flowing conditions. The corrosion current density was calculated by dividing the corrosion current by the specimen area (3.14 cm^2). The polarisation curves for uncoated S355 and WC-CoCr are shown in Fig. 5-15. The fluctuations in the current density exhibited in Fig. 5-15 are indicative of particle impingement, which disrupted the passive layer [5.80].

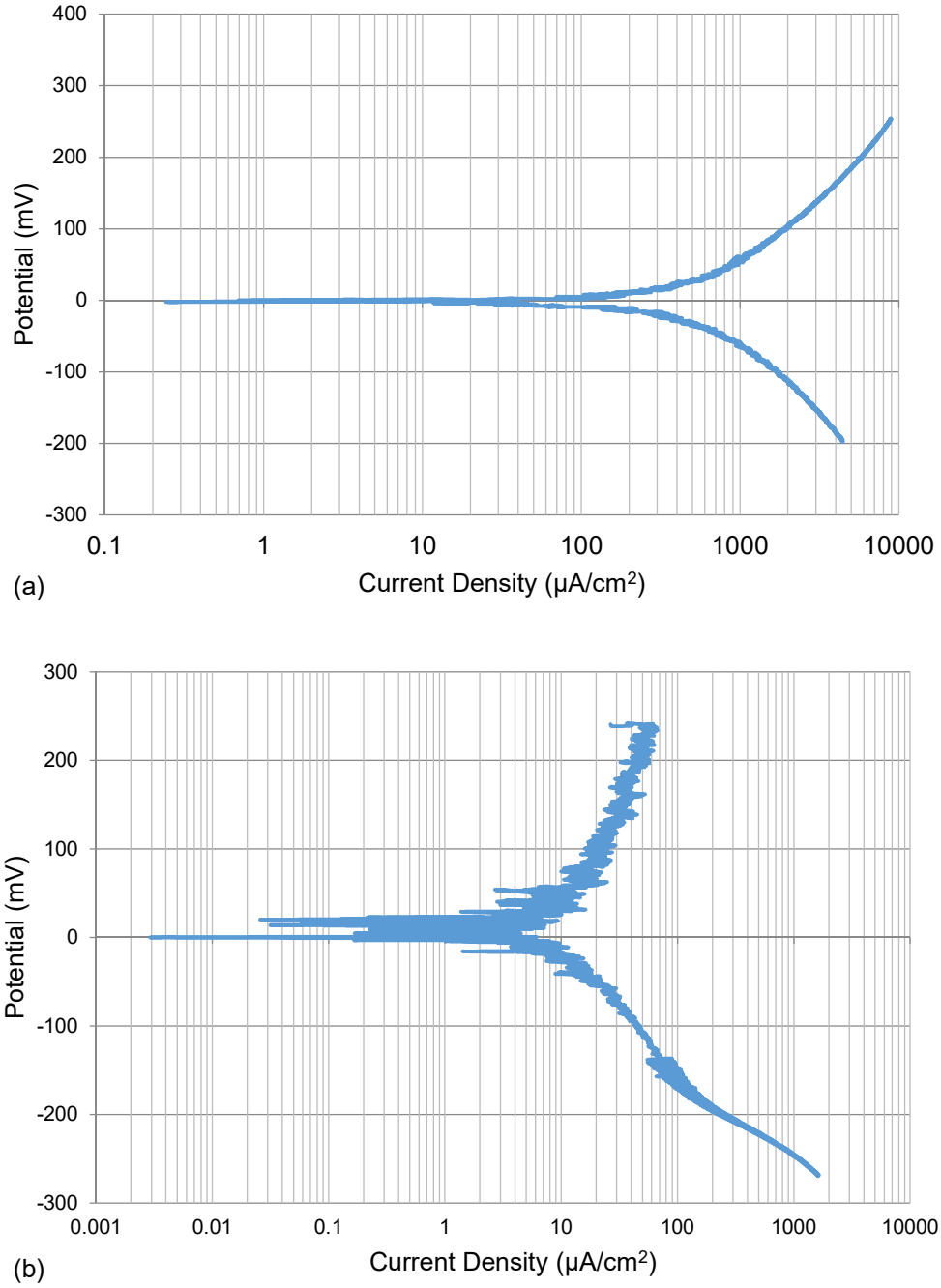

Fig. 5-15 Anodic/cathodic polarisation sweeps of; (a) Uncoated; (b) WC-CoCr, specimens under flowing liquid impingement conditions

Table 5-7 Corrosion current density for specimens under static corrosion test conditions

	Uncoated	WC-CoCr	Cr_3C_2-NiCr
total anodic current (μA)	47.9	6.2	1.8
current density (μA/cm^2)	15.3	2.0	0.6

Table 5-8 Corrosion current density for specimens under flowing test conditions

	Uncoated	WC-CoCr
total anodic current (μA)	2331.6	44.7
current density (μA/cm^2)	742.5	14.2

5.3.7.2 Mass loss due to synergy

The anodic/cathodic polarisation sweeps reveal a significant variance in the current density for each of the three coatings (Table 5-7 and Table 5-8). The results show that the corrosion rate of the Cr_3C_2-NiCr coating is significantly lower when compared with the other examined coatings.

The method outlined in ASTM G102 - 89(2010) [5.54, 5.55] was employed to calculate hourly mass loss rate for each coating material from the extrapolated current density. The particular calculation steps are detailed in Chapter 4. Table 5-9 shows the contribution of each wear mechanism (erosion, corrosion and synergy) to the total mass loss under flowing erosion-corrosion conditions. The results (Table 5-9) indicate that the mass loss caused by the flowing slurry is highly erosion dominant, with the synergistic effect of combined corrosion and erosion contributing approximately 10% of the total mass loss in the case of uncoated S355.

Table 5-9 Percentage contribution of pure erosion, pure corrosion and synergy to total mass loss under flowing conditions

	Total mass loss (%)	Erosion (%)	Corrosion (%)	Synergy (%)
Uncoated	100	84	5	11
WC-CoCr	100	87	0.2	12.8

Based on the results of the static corrosion test, the Cr_3C_2-NiCr coated specimen is the most resistant to corrosion. However, due to the comparatively poor erosion performance when exposed to the impinging slurry, the coating has not provided suitable protection under the erosive conditions. Despite not exhibiting the same level of corrosion resistance as Cr_3C_2-NiCr, WC-CoCr demonstrates a

substantial reduction in current density for flowing and static conditions over the uncoated specimen (S355). This, in combination with high resistance to erosive wear, results in the WC-CoCr coating providing exceptional protection of the S355 substrate under flowing erosion-corrosion conditions.

5.3.8 Post-test wear scar examination

5.3.8.1 Macro observations

High-resolution images of the impinged region on each coating were captured using an Alicona focal variation microscope to measure the depth of each respective wear scar. Fig. 5-16 depicts the wear scar on each coating, and on the uncoated S355.

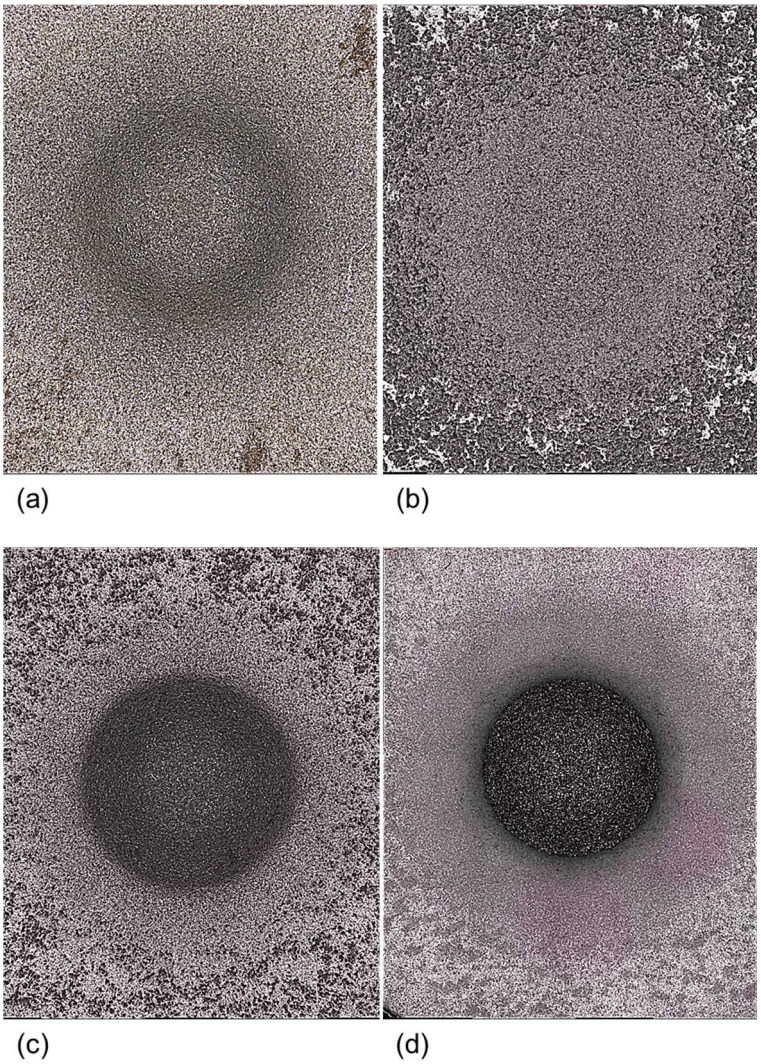

Fig. 5-16 Macro images of the wear scar on; (a) uncoated S355; (b) WC-CoCr; (c) Cr_3C_2-NiCr; (d) Al_2O_3 following one-hour slurry erosion testing

It is immediately clear that the Cr_3C_2-NiCr and Al_2O_3 specimens have experienced the most severe damage as, for both specimens (Fig. 5-16c and Fig. 5-16d), the underlying substrate is visible, confirming that the entire coating thickness has been penetrated. Fig. 5-17 illustrates the wear scar depth of each coated specimen and the uncoated S355 following one-hour slurry erosion impingement. The depth of the wear scars was measured using a surface profilometer (Mitutoyo SV 2000). The depth of each wear scar was subsequently corroborated using an Alicona with the results shown Table 5-10.

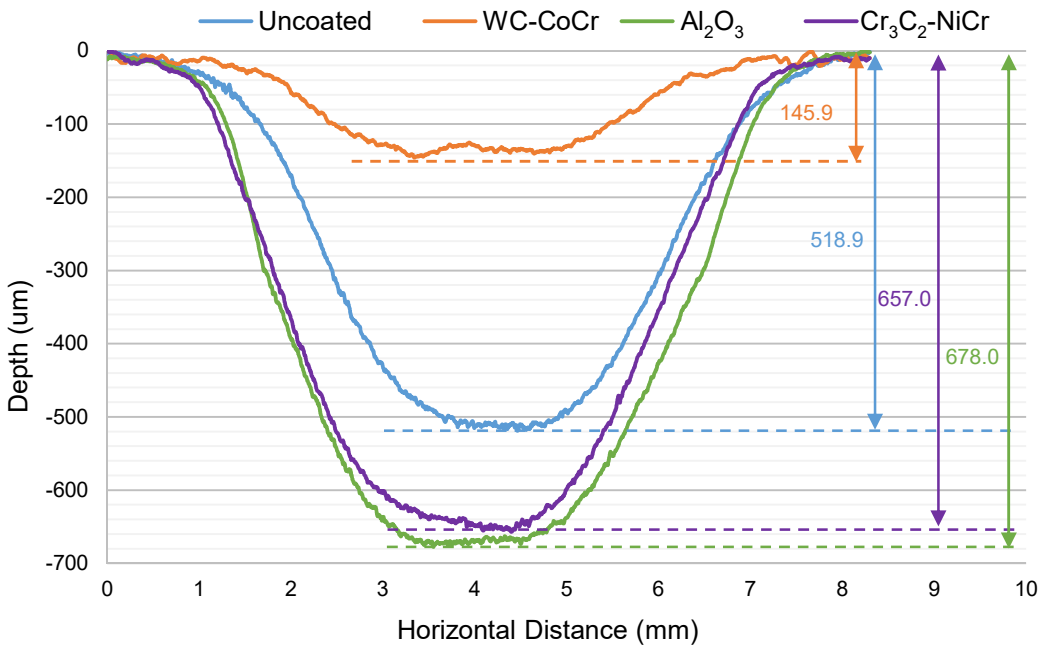

Fig. 5-17 Wear scar depth profiles for the three coatings and uncoated substrate following 1-hour free erosion-corrosion test

Based on the results shown in Fig. 5-17, the impinging slurry has generated the deepest wear scar (approximately 680 µm) on the Al_2O_3 coated specimens. The scar depth for Cr_3C_2-NiCr was shown to be marginally shallower. Table 5-10 indicates that the coating thickness on the Al_2O_3 specimen was approximately 120 µm greater than the Cr_3C_2-NiCr coating. Considering that there is only a marginal difference in the depth of the wear scar on each coating, the Al_2O_3 coating can be considered the poorest performing coating given its greater thickness prior to the start of the slurry erosion test (Fig. 5-6).

The recorded maximum wear scar depth for WC-CoCr was 141.7 µm. With an indicated coating thickness of 180 µm, the results verify that the coating layer was not penetrated during the slurry erosion test. The reduction in wear scar depth (when

compared with the other examined coatings) demonstrates that WC-CoCr has provided superior protection of the S355 substrate.

For Cr_3C_2-NiCr and Al_2O_3, the presence of the coating increased the total mass loss and resulted in a larger wear scar produced on the impinged surface. This outcome is attributed to the erosive effect of the previously removed coating particulates that act as a secondary erodent within the recirculating impinging slurry [5.81].

Table 5-10 Average coating thickness and wear scar depth

	Coating thickness (μm)	Profilometer indicated scar depth (μm)	Alicona indicated scar depth (μm)	Average depth of substrate wear scar (μm)
Uncoated	N/A	518.9	518.5	518
WC-CoCr	163	145.9	141.7	0
Cr_3C_2-NiCr	176	657.0	653.7	481
Al_2O_3	294	680.0	678.0	386

5.3.8.2 Wear scar surface characterisation

SEM microscopy facilitated the evaluation of the eroded surfaces to identify the wear mechanisms that led to the removal of coating and substrate material from each specimen. Examination of the impinged region highlighted the dissimilar erosion mechanisms operating at a high (near 90°) and a low (near 20°/30°) impingement. All the specimens examined in this section were exposed to free erosion-corrosion tests lasting one hour.

90° impingement

Under 90° impingement, the eroded surface of the uncoated S355 sample (Fig. 5-18) exhibits considerable plastic deformation (ploughing) of the impinged surface from the eroding particle. Impact craters are visible on the surface of the S355 and comprise a central indentation on the specimen surface. The faceted shape and volume of impinged material have produced a roughened surface comprising numerous intertwined and overlapping indents.

Lips of highly strained and thinned material are visible at the periphery of the plastically deformed material (indents). These lips consist of weak, highly strained material. Consequently, successive particle impact causes this weakened material to detach from the surface through a low cycle fatigue process [5.82]. The erosive wear

on the surface of the uncoated S355 specimen is in agreement with the widely reported erosion mechanism that takes place on ductile materials under a high (near 90°) angle of attack [5.66].

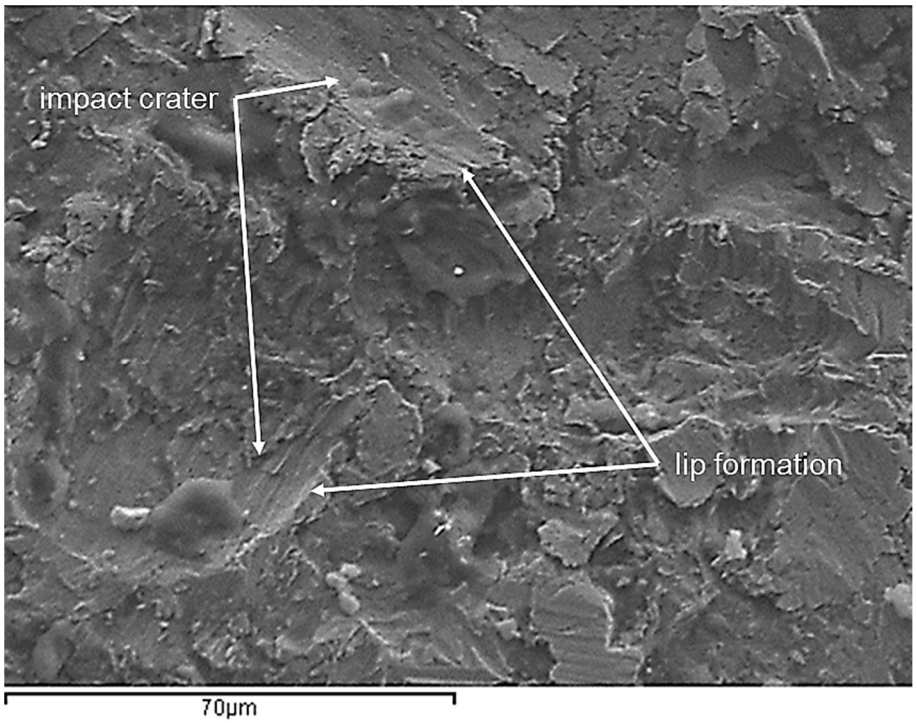

Fig. 5-18 SEM micrograph of the worn surface on the uncoated S355 specimen following slurry erosion test at 90° impingement [x900]

Fig. 5-19 illustrates the worn surface of the WC-CoCr coating. In contrast to the uncoated specimen (Fig. 5-18), the WC-CoCr coating depicts no evidence of plastic deformation such as impact craters or extruded material within the impinged region. Additionally, there is no evidence of scoring on the surface that is typically indicative of ductile erosion. Instead, the worn WC-CoCr surface indicates that brittle erosion has occurred due to the presence of cracks and small voids. With continued impingement, the cracks propagate and intersect resulting in the removal of material. Corroborating results have been obtained by Thakur et al. [5.11].

Following the removal of the carbides, the remaining cobalt binder is of insufficient hardness to withstand the erosive conditions and is eventually also removed. The superior erosion performance of the WC-CoCr coating (Fig. 5-10 and Fig. 5-12) can be attributed to the higher hardness of the coating (a consequence of the carbide reinforcements) and the ability of the cobalt binder to effectively retain the carbide grains within the matrix.

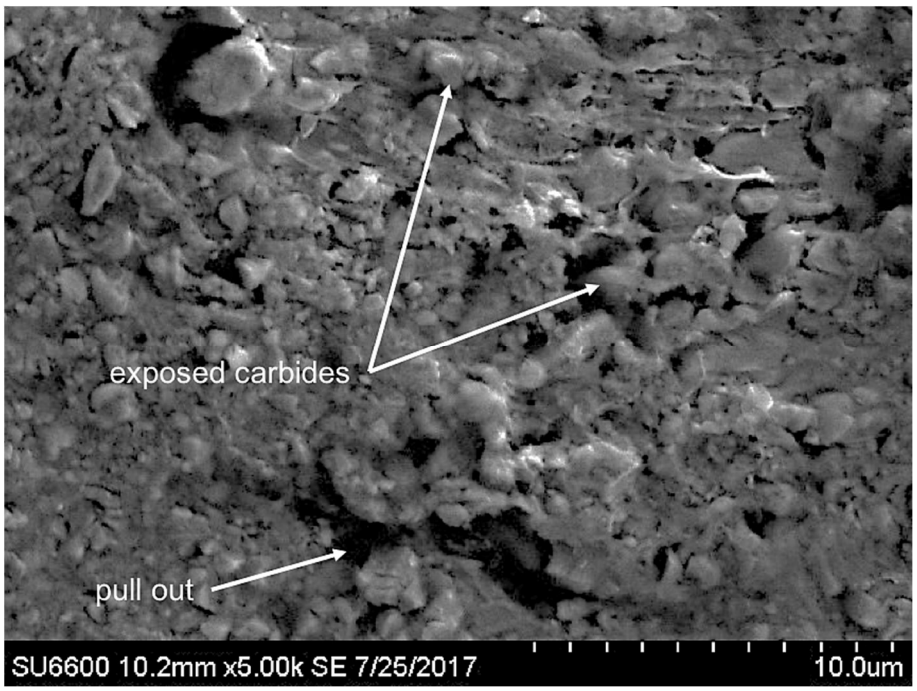

Fig. 5-19 SEM micrograph of the worn surface on the WC-CoCr specimen following slurry erosion test at 90° impingement [x5000]

The damage to the Cr_3C_2-NiCr coated specimen is depicted in Fig. 5-20. Considering that the coating has been breached during the one hour test (Fig. 5-16c), the micrograph (Fig. 5-20) shows the eroded Cr_3C_2-NiCr material at the interface between the coating and the exposed substrate. EDS was employed to confirm that the examined region was the Cr_3C_2-NiCr coating, as opposed to the substrate. The EDS results measured a normalised wt.% of approximately 45% chromium, 25% nickel and 4% iron, thereby confirming that the image depicted in Fig. 5-20 is the Cr_3C_2-NiCr material.

Fig. 5-20 highlights evidence of ductile and brittle erosion on the surface of the coating. As in the uncoated S355 specimen, evidence of ductile erosion is demonstrated by plastic deformation on the impinged surface [5.83]. Impact craters are visible on the surface accompanied by lips of highly strained and thinned material on the outer edge of the craters. However, the Cr_3C_2-NiCr coating also exhibits surface damage associated with a brittle erosion mechanism such as cracking and pull-out. Moreover, the brittle fracture and removal of the carbide reinforcements accelerate material removal by acting as an additional erodent within the recirculating slurry. The combination of the two erosion mechanisms (ductile and brittle) is responsible for the substantial volume of material removed by the slurry in contrast to the WC-CoCr, Al_2O_3 and uncoated specimens.

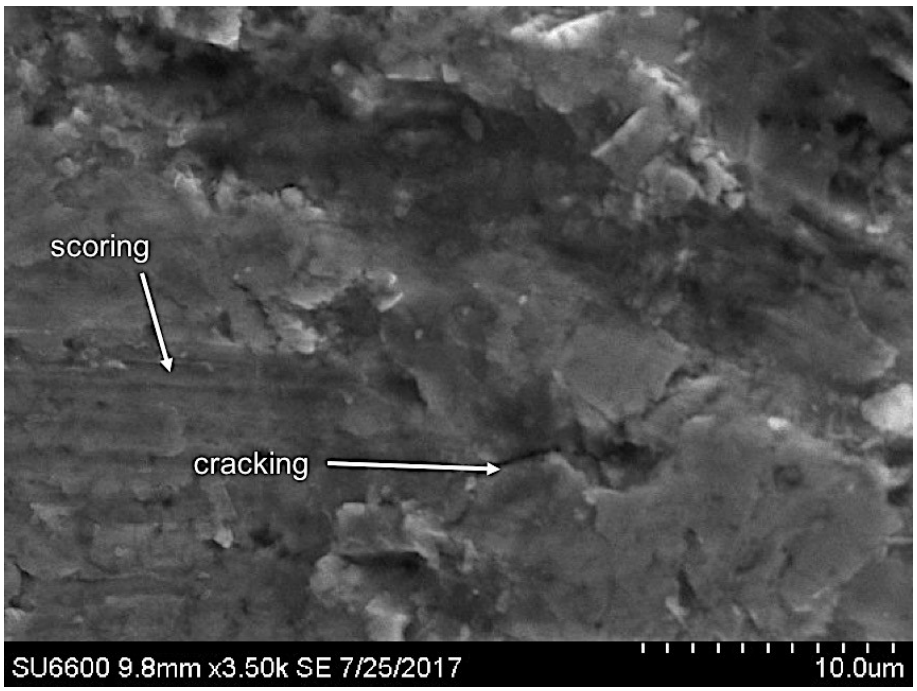

Fig. 5-20 SEM micrograph of the worn surface on the Cr_3C_2-NiCr coated specimen following slurry erosion test at 90° impingement [x3500]

Fig. 5-21 depicts the exposed surface of the S355 substrate following the removal of the Cr_3C_2-NiCr coating. When compared to the uncoated specimen (Fig. 5-18), the exposed substrate exhibits deeper surface indents and more extensive plastic deformation.

The eroded surface of the Al_2O_3 sample is shown in Fig. 5-22. The lack of any ductile binder in the deposited layer leads to the coating exhibiting a brittle response to the impinging erodent [5.67, 5.84, 5.85]. The platelets depicted in the image (Fig. 5-22) are the deformed Al_2O_3 particles. The impinging silica particles crack the interface between the bonded oxides. These cracks intersect, consequently leading to the oxide being dislodged from the surface by the flow of the slurry. Further, void spaces where Al_2O_3 particles have been dislodged are also evident on the eroded surface (Fig. 5-22).

The lack of binder has resulted in the rapid removal of the protective Al_2O_3 coating with the dislodged alumina particles causing further damage to the exposed S355 substrate. Erosion by these particles contributes to the enhanced mass and volume loss over uncoated S355. It is widely accepted that the most severe erosion of brittle materials occurs at high (near 90°) angle of attack [5.64]. Thus, the identified erosion mechanisms that operate on the three coatings from the examination are in agreement with the existing research [5.64, 5.86, 5.87].

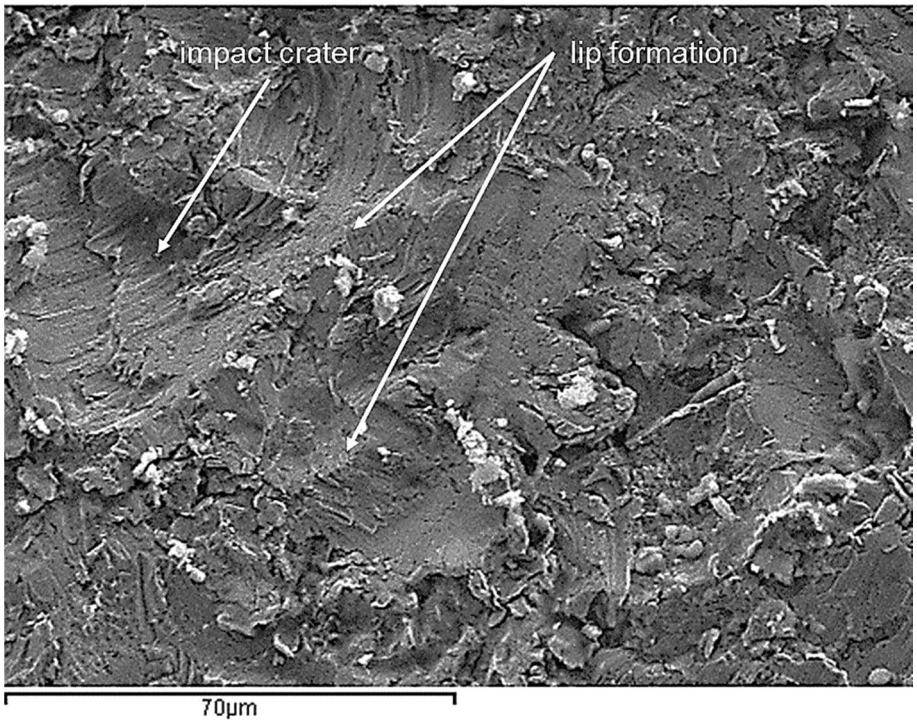

Fig. 5-21 SEM micrograph of the exposed substrate on the Cr_3C_2-NiCr coated specimen following slurry erosion test at 90° impingement [x900]

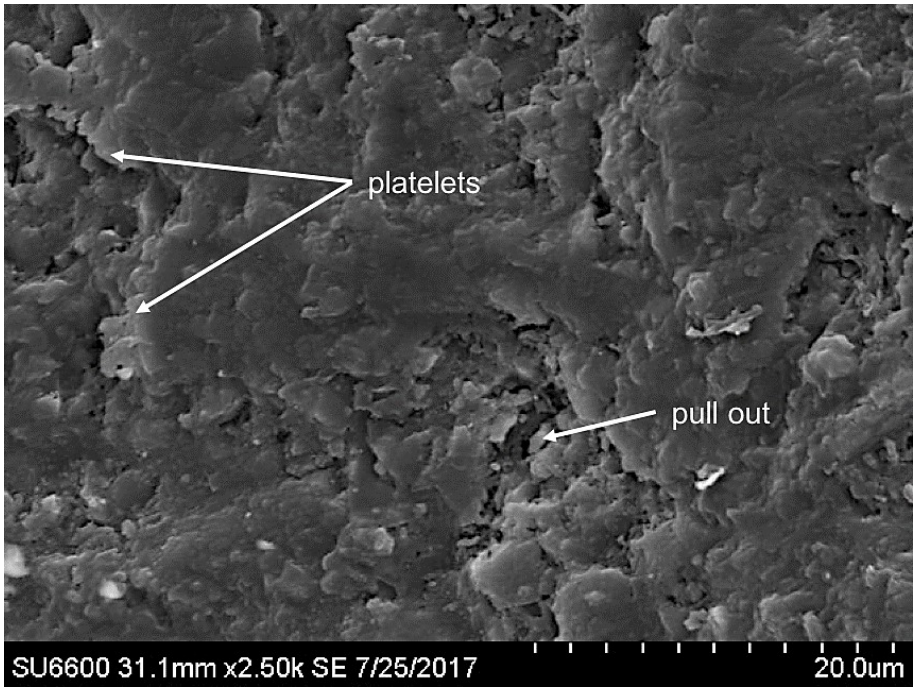

Fig. 5-22 SEM micrograph of the worn surface on the Al_2O_3 coated specimen following slurry erosion test at 90° impingement [x2500]

Shallow impingement

Fig. 5-23 presents an image of the impinged region on the uncoated S355 specimen and shows evidence of substantial ploughing. As discussed in Chapter 3, ploughing refers to the plastic deformation of the ductile material by the leading edge of the eroding particle [5.66]. Following the initial impact, the silica particles score the surface of the specimen in line with the direction of the slurry jet. Moreover, the image also shows signs of lip formation at the periphery of particle impact craters [5.66]. This wear pattern is consistent with the erosion of ductile materials as noted by Finnie [5.88]. The micrograph (Fig. 5-23) also confirms that the mechanisms of material removal at shallow impact angles are noticeably different from the attack at 90° [5.20, 5.21].

The repeated impact of the silica particles led to the formation of lips at the periphery of the impact crater as indicated in Fig. 5-23. Continued exposure to the high velocity jet resulted in the removal of these lips leading to extensive material loss of the uncoated S355 steel. Fig. 5-23 also highlights the directionality within the wear scar, with evidence of parallel scratch patterns and ploughing within the impinged region.

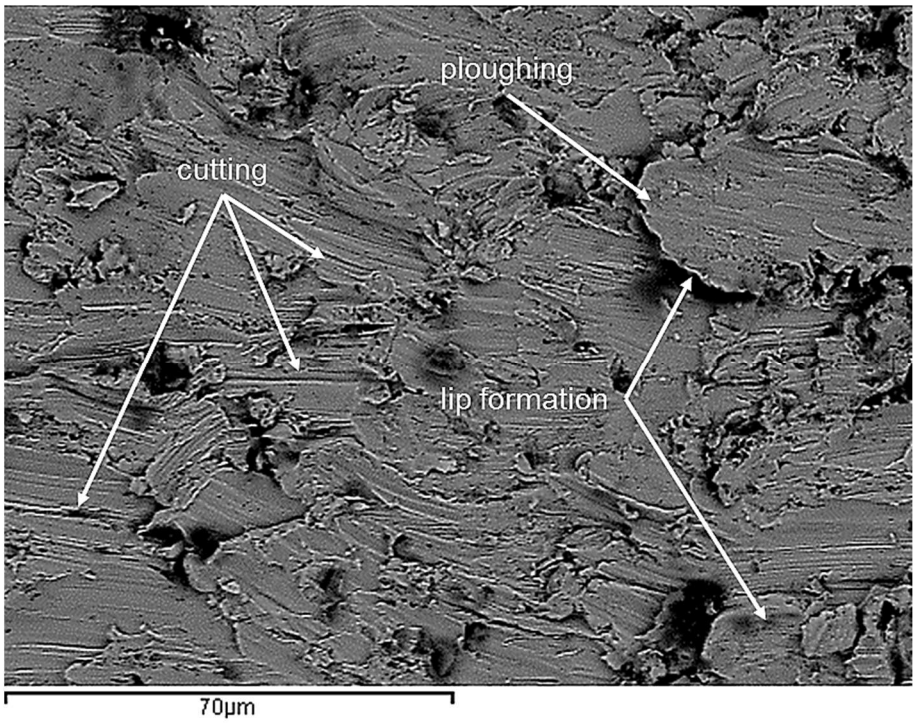

Fig. 5-23 SEM micrograph of the worn surface on the uncoated S355 specimen following slurry erosion test at 20° impingement [x900]

The impinged region on the WC-CoCr coated specimen is depicted in Fig. 5-24. The image (Fig. 5-24), reveals extensive carbide removal with noticeably less scoring and ploughing when compared with the damage observed on the uncoated sample (Fig. 5-23). Also, the depth of the scratch pattern appears shallower than was observed on the surface of the uncoated S355. The reduced depth of the scratches is likely a consequence of the subsurface nanoscale carbide reinforcements that increase the overall hardness of the MMC. Moreover, the scoring is restricted to the binder phase of the coating due to the comparably low hardness of cobalt when compared with the tungsten carbide reinforcements. Repeated impact by the impinging particles causes the breakdown of the binder phase, typically initiating at the carbide-binder interface [5.22]. Without sufficient binder alloy to retain the carbides within the matrix, they are dislodged from the surface by the impinging slurry. These observations align with the widely accepted breakdown mechanism of WC-CoCr based coatings under slurry erosion [5.23, 5.89–5.91].

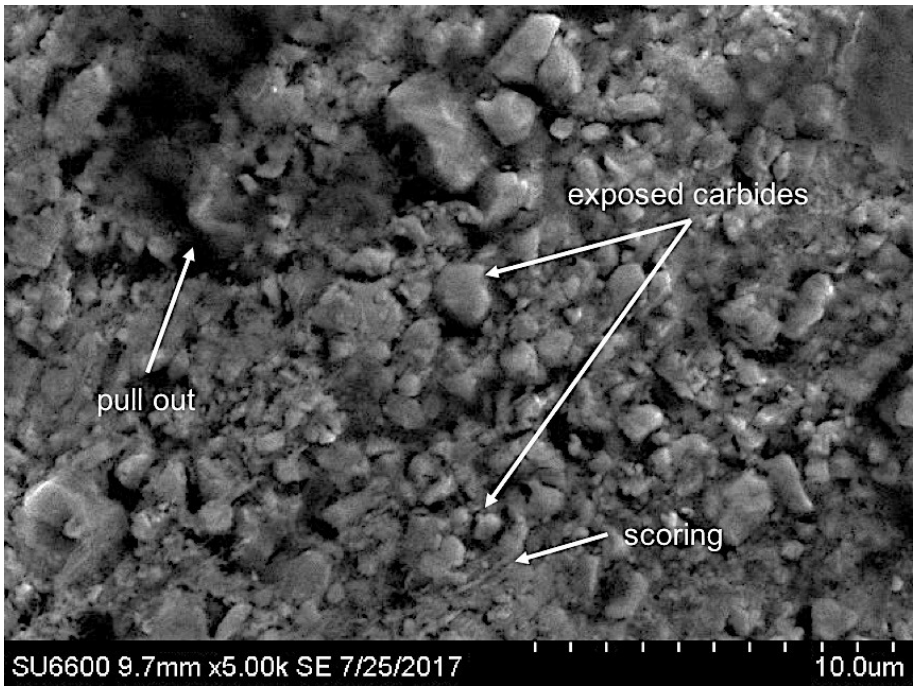

Fig. 5-24 SEM micrograph of the worn surface on the WC-CoCr coated specimen following slurry erosion test at 20° impingement [x5000]

Fig. 5-25 depicts the impinged region of the Cr_3C_2-NiCr coated specimen and highlights the existence of both ductile and brittle mechanisms of material removal. Specifically, the image (Fig. 5-25) highlights evidence of scoring and ploughing, as well as pull-out. The presence of these features indicates that the Cr_3C_2-NiCr exhibits both brittle and ductile erosion mechanisms. Corresponding features were identified

by Zavareh et al. [5.16] following tribological and electrochemical assessment of an HVOF sprayed Cr_3C_2-NiCr coating.

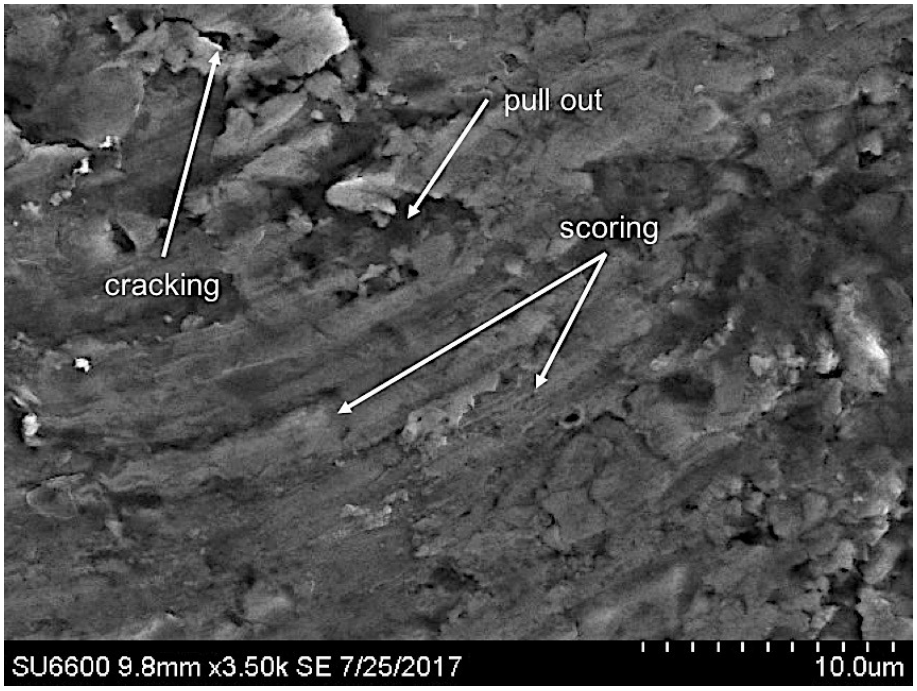

Fig. 5-25 SEM micrograph of the worn surface on the Cr_3C_2-NiCr coated specimen following slurry erosion test at 20° impingement [x3500]

The worn surface of the Al_2O_3 coating is depicted in Fig. 5-26. Due to the lack of any metallic binder, the pure ceramic coating exhibits a brittle response to the impinging slurry. Erosion is characterised by microcracking and delamination of splats, (plastically deformed particles) [5.57], from the surface. Fig. 5-26 depicts these features within the impinged region. The lack of binder yields low cohesive strength between deposited Al_2O_3 particles [5.93]. The impinging slurry generates cracks on the surface of the coating that propagate, leading to the removal of “flakes” from the surface. An extensive study by Yang et al. [5.93] recorded a similar outcome on Al_2O_3 coatings with varying levels of Cr_2O_3 (binder). The addition of Cr_2O_3 was shown to increase the cohesive strength of the layer thereby improving its erosion resistance [5.93].

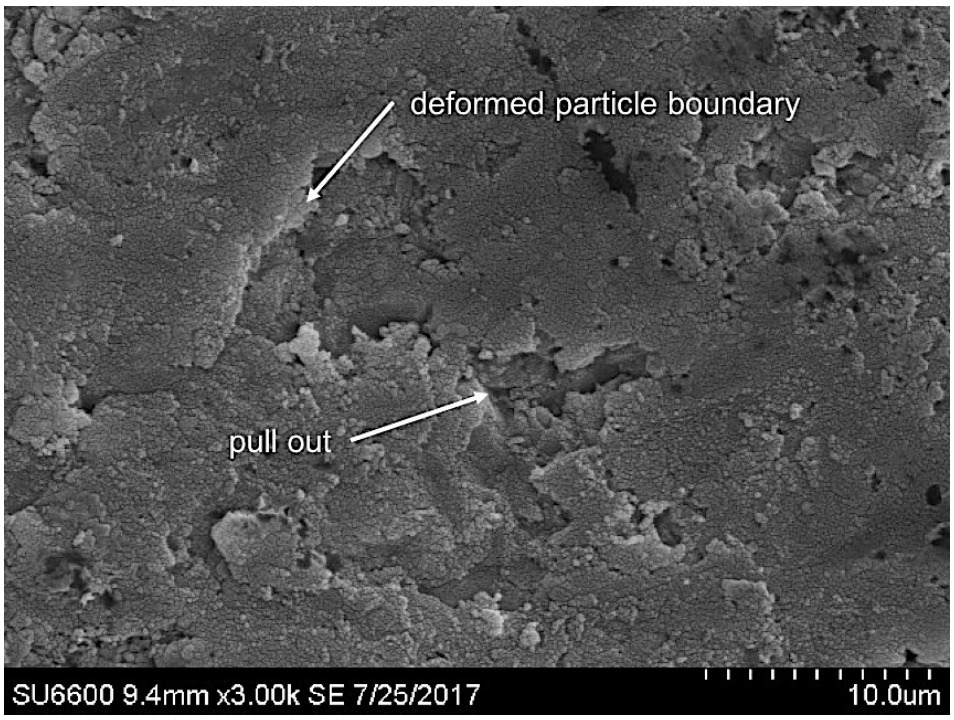

Fig. 5-26 SEM micrograph of the worn surface on the Al_2O_3 coated specimen following slurry erosion test at 20° impingement [x2500]

5.4 Conclusions

This chapter has investigated the slurry erosion performance of three HVOF deposited coatings (WC-CoCr, Cr_3C_2-NiCr and Al_2O_3) and uncoated S355 steel. The specimens were exposed to dry jet and slurry test conditions to identify the influence of the erosive environment on the resulting erosion performance. The breadth of experimental analysis was furthered through the application of cathodic protection and anodic polarization to determine the contributing factors or erosion, corrosion and synergy to the total mass loss under slurry test conditions. The mass and volume loss for each coating material was established with the mechanisms causing coating degradation evaluated through examination of the resulting wear scars.

For the WC-CoCr coating, volume loss under dry erosion was found to be more than five times greater than volume loss under slurry conditions. Squeeze film effects [5.23], which reduce impinging particle impact velocity in the presence of a slurry erosion environment, and variation in erodent particle size and hardness, account for the recorded increase to volume loss under dry erosion conditions.

Based on the results presented herein, simply measuring the mass loss does not provide a suitable metric with which to compare the erosion performance of MMC coatings considering the different densities of the reinforcement grains. Hence, the

determination of volume loss is necessary for a comparative evaluation of dissimilar MMCs.

The WC-CoCr and Cr_3C_2-NiCr coatings both exhibit different erosion characteristics under slurry and dry erosion, with both demonstrating a comparably high volume loss under dry erosion and low volume loss under slurry erosion. Considering that under dry erosion testing, the impinging particles impact the surface of the substrate at a higher velocity, this outcome is to be expected. However, this result does imply that, for the coatings examined in the present study, dry erosion test conditions do not reflect the erosion mechanisms encountered under slurry erosion.

The results from the electrochemical analysis confirmed that the specimens were subject to an erosion dominant wear regime, with pure corrosion contributing no more than 6% to the total mass loss in the case of uncoated S355. Under flowing conditions, pure corrosion contributed only 0.34% to the mass loss of WC-CoCr coated specimens.

The WC-CoCr coating has exhibited the lowest overall volume loss and wear scar depth of all the examined specimens at all examined impingement angles (20°, 30°, 90°) under both dry jet and slurry erosion. The minimal volume loss and wear scar depth are attributed to the high coating hardness, and the ability of the cobalt binder to retain the carbide reinforcements within the matrix.

5.5 References

[5.1] R.J.K. Wood, R. Manish, Surface Engineering for Enhanced Performance against Wear, Springer, 2013.

[5.2] R.S. Lima, B.R. Marple, Thermal spray coatings engineered from nanostructured ceramic agglomerated powders for structural, thermal barrier and biomedical applications: A review, J. Therm. Spray Technol. 16 (2007) 40–63.

[5.3] C.-P. Hubs, L. Pitch, S. Lever, U.S.H. Chrome, A. Team, Validation of WC / Co , WC / CoCr HVOF or Tribaloy 800 Thermal Spray Coatings as a Replacement for Hard Chrome Plating on, (1999).

[5.4] C.J. Li, G.J. Yang, Relationships between feedstock structure, particle parameter, coating deposition, microstructure and properties for thermally sprayed conventional and nanostructured WC-Co, Int. J. Refract. Met. Hard Mater. 39 (2013) 2–17.

[5.5] A. Ibrahim, C.C. Berndt, Fatigue and deformation of HVOF sprayed WC-Co coatings and hard chrome plating, Mater. Sci. Eng. A. 456 (2007) 114–119.

[5.6] G. Bolelli, L. Lusvarghi, M. Barletta, HVOF-sprayed WC-CoCr coatings on Al alloy: Effect of the coating thickness on the tribological properties, Wear. 267 (2009) 944–953.

[5.7] G. Bolelli, R. Giovanardi, L. Lusvarghi, T. Manfredini, Corrosion resistance of HVOF-sprayed coatings for hard chrome replacement, Corros. Sci. 48 (2006) 3375–3397.

[5.8] J.R. García, J.E. Fernández, J.M. Cuetos, F.G. Costales, Fatigue effect of WC coatings thermal sprayed by HVOF and laser treated, on medium carbon steel, Eng. Fail. Anal. 18 (2011) 1750–1760.
[5.9] J.G. La Barbera-Sosa, Y.Y. Santana, C. Villalobos-Gutiérrez, D. Chicot, J. Lesage, X. Decoopman, et al., Fatigue behavior of a structural steel coated with a WC-10Co-4Cr/Colmonoy 88 deposit by HVOF thermal spraying, Surf. Coatings Technol. 220 (2013) 248–256.
[5.10] S. Matthews, B. James, M. Hyland, The role of microstructure in the mechanism of high velocity erosion of Cr3C2-NiCr thermal spray coatings: Part 1 - As-sprayed coatings, Surf. Coatings Technol. 203 (2009) 1086–1093.
[5.11] L. Thakur, N. Arora, R. Jayaganthan, R. Sood, An investigation on erosion behavior of HVOF sprayed WC-CoCr coatings, Appl. Surf. Sci. 258 (2011) 1225–1234.
[5.12] M.R. Ramesh, S. Prakash, S.K. Nath, P.K. Sapra, B. Venkataraman, Solid particle erosion of HVOF sprayed WC-Co/NiCrFeSiB coatings, Wear. 269 (2010) 197–205.
[5.13] D.K. Goyal, H. Singh, H. Kumar, V. Sahni, Slurry erosion behaviour of HVOF sprayed WC-10Co-4Cr and Al 2O 3+13TiO 2 coatings on a turbine steel, Wear. 289 (2012) 46–57.
[5.14] M. Manjunatha, R.S. Kulkarni, M. Krishna, Investigation of HVOF Thermal sprayed Cr 3 C 2 -NiCr Cermet Carbide Coatings on Erosive Performance of AISI 316 Molybdenum steel, 5 (2014) 622–629.
[5.15] H.S. Grewal, H. Singh, A. Agrawal, Understanding Liquid Impingement erosion behaviour of nickel-alumina based thermal spray coatings, Wear. 301 (2013) 424–433.
[5.16] M. Akhtari Zavareh, A.A.D.M. Sarhan, B.B. Razak, W.J. Basirun, The tribological and electrochemical behavior of HVOF-sprayed Cr3C2-NiCr ceramic coating on carbon steel, Ceram. Int. 41 (2015) 5387–5396.
[5.17] W. Liu, F. Shieu, W. Hsiao, Enhancement of wear and corrosion resistance of iron-based hard coatings deposited by high-velocity oxygen fuel (HVOF) thermal spraying, Surf. Coat. Technol. 249 (2014) 24–41.
[5.18] L. Thakur, N. Arora, A comparative study on slurry and dry erosion behaviour of HVOF sprayed WC-CoCr coatings, Wear. 303 (2013) 405–411.
[19] M.A. Islam, T. Alam, Z.N. Farhat, A. Mohamed, A. Alfantazi, Effect of microstructure on the erosion behavior of carbon steel, Wear. 332–333 (2015) 1080–1089.
[5.20] N. Andrews, L. Giourntas, A.M. Galloway, A. Pearson, Effect of impact angle on the slurry erosion-corrosion of Stellite 6 and SS316, Wear. 320 (2014) 143–151.
[5.21] Z.B. Zheng, Y.G. Zheng, W.H. Sun, J.Q. Wang, Erosion-corrosion of HVOF-sprayed Fe-based amorphous metallic coating under impingement by a sand-containing NaCl solution, Corros. Sci. 76 (2013) 337–347.
[5.22] V.A.D. Souza, A. Neville, Corrosion and synergy in a WC-Co-Cr HVOF thermal spray coating - Understanding their role in erosion-corrosion degradation, Wear. 259 (2005) 171–180.
[5.23] A. Neville, F. Reza, S. Chiovelli, T. Revega, Erosion-corrosion behaviour of WC-based MMCs in liquid-solid slurries, Wear. 259 (2005) 181–195.
[5.24] L. Giourntas, T. Hodgkiess, A.M. Galloway, Enhanced approach of assessing the corrosive wear of engineering materials under impingement, Wear. 338–339 (2015) 155–163.
[5.25] R. Malka, S. Nešić, D.A. Gulino, Erosion-corrosion and synergistic effects in disturbed liquid-particle flow, Wear. 262 (2007) 791–799.

[5.26] H. Xu, A. Neville, An electrochemical and microstructural assessment of erosion-corrosion of austenitic cast iron for marine applications, Mater. Corros. 53 (2002) 5–12.
[5.27] Y. Zhao, F. Zhou, J. Yao, S. Dong, N. Li, Erosion–corrosion behavior and corrosion resistance of AISI 316 stainless steel in flow jet impingement, Wear. 328–329 (2015) 464–474.
[5.28] M.S. Jellesen, T.L. Christiansen, L.R. Hilbert, P. Møller, Erosion-corrosion and corrosion properties of DLC coated low temperature gas-nitrided austenitic stainless steel, Wear. 267 (2009) 1709–1714.
[5.29] F. Mohammadi, J. Luo, Effects of particle angular velocity and friction force on erosion enhanced corrosion of 304 stainless steel, Corros. Sci. 52 (2010) 2994–3001.
[5.30] D. López, N.A. Falleiros, A.P. Tschiptschin, Corrosion-erosion behaviour of austenitic and martensitic high nitrogen stainless steels, Wear. 263 (2007) 347–354.
[5.31] S. Aribo, R. Barker, X. Hu, A. Neville, Erosion-corrosion behaviour of lean duplex stainless steels in 3.5% NaCl solution, Wear. 302 (2013) 1602–1608.
[5.32] M.A. Islam, T. Alam, Z.N. Farhat, A. Mohamed, A. Alfantazi, Effect of microstructure on the erosion behavior of carbon steel, Wear. 332–333 (2015) 1080–1089.
[5.33] A. Neville, T. Hodgkiess, J.T. Dallas, A study of the erosion-corrosion behaviour of engineering steels for marine pumping applications, Wear. 186–187 (1995) 497–507.
[5.34] D. Landolt, Corrosion and surface chemistry of metals, 2007.
[5.35] Shabana, M.M.M. Sarcar, K.N.S. Suman, S. Kamaluddin, Tribological and Corrosion behavior of HVOF Sprayed WC-Co, NiCrBSi and Cr3C2-NiCr Coatings and analysis using Design of Experiments, Mater. Today Proc. 2 (2015) 2654–2665.
[5.36] V.A.D. Souza, A. Neville, Aspects of microstructure on the synergy and overall material loss of thermal spray coatings in erosion – corrosion environments, Wear. 263 (2007) 339–346.
[5.37] J.R. Davis, Introduction to Thermal Spray Processing, in: D.E. Crawmer (Ed.), Handb. Therm. Spray Technol., ASM International, 2004: pp. 54–76.
[5.38] M. Bjordal, E. Bardal, T. Rogne, T.G. Eggen, Combined erosion and corrosion of thermal sprayed WC and CrC coatings, Surf. Coatings Technol. 70 (1995) 215–220.
[5.39] K.S. Tan, J.A. Wharton, R.J. Wood, Solid particle erosion – corrosion behaviour of a novel HVOF nickel aluminium bronze coating for marine applications — correlation between mass loss and electrochemical measurements, Wear. 258 (2004) 629–640.
[5.40] H.S. Grewal, H.S. Arora, A. Agrawal, H. Singh, S. Mukherjee, Slurry erosion of thermal spray coatings: Effect of sand concentration, Procedia Eng. 68 (2013) 484–490.
[5.41] Oerlikon Metco, Material Product Data Sheet Tungsten Carbide – 10 % Cobalt 4 % Chromium Powders, (2015) 1–7.
[5.42] Oerlikon Metco, Material Product Data Sheet Chromium Carbide – Nickel Chromium Powder Blends, 2 (2014) 2–7.
[5.43] Praxair, Materials Product Data Sheet Al-1110-HP, (1999) 1–4.
[5.44] International ASTM Standard, ASTM A572/A572M - 15: Standard Specification for High-Strength Low-Alloy Columbium-Vanadium Structural, 2015.
[5.45] International ASTM Standard, ASTM E2109 − 01: Standard Test Methods for Determining Area Percentage Porosity in Thermal Sprayed Coatings,

(2006) 1–8.
[5.46] F. Cernuschi, S. Capelli, C. Guardamagna, L. Lorenzoni, D.E. Mack, A. Moscatelli, Solid particle erosion of standard and advanced thermal barrier coatings, Wear. 348–349 (2015) 43–51.
[5.47] R.E. Vieira, A. Mansouri, B.S. McLaury, S.A. Shirazi, Experimental and computational study of erosion in elbows due to sand particles in air flow, Powder Technol. 288 (2016) 339–353.
[5.48] GE Aircraft Engines, E50TF121 - S2: Room Temperature Erosion Test Method for Coatings, (1995) 1–11.
[5.49] L. Giourntas, T. Hodgkiess, A.M. Galloway, Comparative study of erosion–corrosion performance on a range of stainless steels, Wear. 332–333 (2015) 1051–1058.
[5.50] M.M. Stack, G.H. Abdulrahman, Mapping erosion-corrosion of carbon steel in oil-water solutions: Effects of velocity and applied potential, Wear. 274–275 (2012) 401–413.
[5.51] M. Abedini, H.M. Ghasemi, Synergistic erosion–corrosion behavior of Al–brass alloy at various impingement angles, Wear. 319 (2014) 49–55.
[5.52] R.S. Bolton-King, J.P.O. Evans, C.L. Smith, J.D. Painter, D.F. Allsop, W.M. Cranton, What are the Prospects of 3D Profiling Systems Applied to Firearms and Toolmarks Identification?, AFTE J. 42 (2010) 23–33.
[5.53] D.G. Enos, L.L. Scribner, The Potentiodynamic Polarization Scan Technical Report 33, 1997.
[5.54] International ASTM Standard, ASTM G102 - 89 Standard Practice for Calculation of Corrosion Rates and Related Information from Electrochemical Measurements, 2015.
[5.55] M. Pourbaix, Atlas of Electrochemical Equilibria in Aqueous Solutions, 1974.
[5.56] C. Sun, L. Guo, G. Lu, Y. Lv, F. Ye, Interface bonding between particle and substrate during HVOF spraying, Appl. Surf. Sci. 317 (2014) 908–913.
[5.57] R. Ahmed, Contact fatigue failure modes of HVOF coatings, Wear. 253 (2002) 473–487.
[5.58] A. Kulkarni, J. Gutleber, S. Sampath, A. Goland, W.B. Lindquist, H. Herman, et al., Studies of the microstructure and properties of dense ceramic coatings produced by high-velocity oxygen-fuel combustion spraying, Mater. Sci. Eng. A. 369 (2004) 124–137.
[5.59] C.J. Li, Y.Y. Wang, G.J. Yang, A. Ohmori, K.A. Khor, Effect of solid carbide particle size on deposition behaviour, microstructure and wear performance of HVOF cermet coatings, Mater. Sci. Technol. 20 (2004).
[5.60] W. Tillmann, B. Hussong, T. Priggemeier, S. Kuhnt, N. Rudak, H. Weinert, Influence of parameter variations on WC-Co splat formation in an HVOF process using a new beam-shutter device, J. Therm. Spray Technol. 22 (2013) 250–262.
[5.61] Struers, Metallographic preparation of thermal spray coatings, 2014.
[5.62] A.M. Redsten, E.M. Klier, A.M. Brown, D.C. Dunand, Mechanical properties and microstructure of cast oxide-dispersion-strengthened aluminum, Mater. Sci. Eng. A. 201 (1995) 88–102.
[5.63] B. Chen, S. Li, H. Imai, L. Jia, J. Umeda, M. Takahashi, Load transfer strengthening in carbon nanotubes reinforced metal matrix composites via in-situ tensile tests, Compos. Sci. Technol. 113 (2015) 1–8.
[5.64] I. Finnie, Some Reflections on the Past and Future of Erosion, Wear. 186–187 (1995) 1–10.
[5.65] P. Kulu, I. Hussainova, R. Veinthal, Solid particle erosion of thermal sprayed coatings, Wear. 258 (2005) 488–496.
[5.66] A. V. Levy, The platelet mechanism of erosion of ductile metals, Wear. 108

(1986) 1–21.
[5.67] R.G. Wellman, C. Allen, The effects of angle of impact and material properties on the erosion rates of ceramics, Fuel Energy Abstr. 37 (1996) 213.
[5.68] Y. Purandare, M. Stack, P. Hovsepian, A study of the erosion-corrosion of PVD CrN/NbN superlattice coatings in aqueous slurries, Wear. 259 (2005) 256–262.
[5.69] Y.I. Oka, H. Ohnogi, T. Hosokawa, M. Matsumura, The impact angle dependence of erosion damage caused by solid particle impact, Wear. 203–204 (1997) 573–579.
[5.70] A.J. Gant, M.G. Gee, Wear modes in slurry jet erosion of tungsten carbide hardmetals: Their relationship with microstructure and mechanical properties, Int. J. Refract. Met. Hard Mater. 49 (2015) 192–202.
[5.71] A.J. Ninham, A. V Levy, The erosion of carbide-metal composites, Wear. 121 (1988) 347–361.
[5.72] J.A. Picas, A. Forn, G. Matthaus, HVOF coatings as an alternative to hard chrome for pistons and valves, Wear. 261 (2006) 477–484.
[5.73] Zimmerman, S., Chromium carbide coatings produced with various HVOF spray systems, Proeedings 7th Natl. Therm. Spray Conf. Bost. 147 (1996).
[5.74] H.M. Clark, L.C. Burmeister, The influence of the squeeze film on particle impact velocities in erosion, Int. J. Impact Eng. 12 (1992) 415–426.
[5.75] K.K. Wong, H.M. Clark, A model of particle velocities and trajectories in a slurry pot erosion tester, Wear. 160 (1993) 95–104.
[5.76] H.M. Hawthorne, B. Arsenault, J.P. Immarigeon, J.G. Legoux, V.R. Parameswaran, Comparison of slurry and dry erosion behaviour of some HVOF thermal sprayed coatings, Wear. 225–229 (1999) 825–834.
[5.77] A. V. Levy, P. Chik, The effects of erodent composition and shape on the erosion of steel, Wear. 89 (1983) 151–162.
[5.78] S. Lathabai, M. Ottmüller, I. Fernandez, Solid particle erosion behaviour of thermal sprayed ceramic, metallic and polymer coatings, Wear. 221 (1998) 93–108.
[5.79] M. Liebhard, A. Levy, Effect of erodent particle characteristics on the erosion of metals, Wear. 151 (1991) 381–390.
[5.80] International ASTM Standard, ASTM G46 - 94 (2013): Standard Guide for Examination and Evaluation of Pitting Corrosion, 2017.
[5.81] R.J.K. Wood, B.G. Mellor, M.L. Binfield, Sand erosion performance of detonation gun applied tungsten carbide/cobalt-chromium coatings, Wear. 211 (1997) 70–83.
[5.82] A. V. Levy, The solid particle erosion behavior of steel as a function of microstructure, Wear. 68 (1981) 269–287.
[5.83] D. Aquaro, E. Fontani, Erosion of ductile and brittle materials, Meccanica. 36 (2001) 651–661.
[5.84] E. Bousser, L. Martinu, J.E. Klemberg-Sapieha, Solid particle erosion mechanisms of hard protective coatings, Surf. Coatings Technol. 235 (2013) 383–393.
[5.85] E. Bousser, L. Martinu, J.E. Klemberg-Sapieha, Effect of erodent properties on the solid particle erosion mechanisms of brittle materials, J. Mater. Sci. 48 (2013) 5543–5558.
[5.86] M.A. Al-Bukhaiti, S.M. Ahmed, F.M.F. Badran, K.M. Emara, Effect of impingement angle on slurry erosion behaviour and mechanisms of 1017 steel and high-chromium white cast iron, Wear. 262 (2007) 1187–1198.
[5.87] Y.I. Oka, H. Ohnogi, T. Hosokawa, M. Matsumura, The impact angle dependence of erosion damage caused by solid particle impact, Wear. 203–

204 (1997) 573–579.
[5.88] I. Finnie, Erosion of surfaces by solid particles, Wear. 3 (1960) 87–103.
[5.89] V. Fervel, B. Normand, H. Liao, C. Coddet, E. Beche, R. Berjoan, Friction and wear mechanisms of thermally sprayed ceramic and cermet coatings, Surf. Coatings Technol. 111 (1999) 255–262.
[5.90] C. Verdon, A. Karimi, J.L. Martin, Microstructural and analytical study of thermally sprayed WC-Co coatings in connection with their wear resistance, Mater. Sci. Eng. A. 234–236 (1997) 731–734.
[5.91] R.J.K. Wood, Tribology of thermal sprayed WC-Co coatings, Int. J. Refract. Met. Hard Mater. 28 (2010) 82–94.
[5.92] S. Hong, Y. Wu, Q. Wang, G. Ying, G. Li, W. Gao, et al., Microstructure and cavitation-silt erosion behavior of high-velocity oxygen-fuel (HVOF) sprayed Cr3C2-NiCr coating, Surf. Coatings Technol. 225 (2013) 85–91.
[5.93] K. Yang, J. Rong, C. Liu, H. Zhao, S. Tao, C. Ding, Study on erosion-wear behavior and mechanism of plasma-sprayed alumina-based coatings by a novel slurry injection method, Tribol. Int. 93 (2016) 29–35.

Chapter 6 Preliminary Analysis of Cold Spray with Subsequent FSP

6.1 Introduction

This chapter presents the results of a preliminary study on Cold Spray (CS) deposited coatings with subsequent Friction Stir Processing (FSP). The findings of this chapter provide a proof of concept for combined CS and FSP (SprayStir).

The CS deposition of coatings is primarily restricted to ductile alloys due to the specific bonding mechanisms that operate in CS [6.1–6.7]. These bonding mechanisms are discussed in Chapter 2; however, in summary, bonding occurs through two distinct mechanisms. The first is the metallurgical bond that is created by the direct metal-to-metal contact between the substrate and the deposited material in the jet region [6.5–6.7]. The second mechanism is mechanical interlocking between the powder particles and previously deposited material (or the substrate) [6.2].

Deposition of ceramic materials by CS is difficult to achieve as ceramic particles are unable to deform upon impact with the substrate [6.8]. Consequently, the sprayed particles are prone to rebounding from the surface. Despite this, several research groups [6.9–6.12] have attempted to deposit ceramic and oxide particles through optimisation of the CS parameters or by blending the ceramic or oxide particles with a comparably ductile alloy.

In one study [6.9], a research group examined the effect of FSP on a CS deposited blend of aluminium and Al_2O_3 particles, deposited onto 6061-grade aluminium. The aim of the research [6.9], was to determine the influence of the Al_2O_3 (reinforcement) content on the microstructure of the FSPed coating. Hodder et al. [6.9] concluded that homogeneous dispersal of the Al_2O_3 reinforcing particles (by FSP) led to increased hardness (approximately 60%) when compared with the as-deposited CS coating. Moreover, the researchers noted that the greatest hardness was recorded where the mean free particle distance of the reinforcements was below 5 µm [6.9].

In a similar study, Huang et al. [6.10] deposited a metal matrix composite (MMC) coating comprising SiC reinforcing particles (45 vol.%) and 5056-grade aluminium onto a pure aluminium substrate (Fig. 6-1a). The research group [6.10] subsequently modified the deposited layer by FSP to assess the changes in the microstructure and wear performance of the MMC following FSP (Fig. 6-1b).

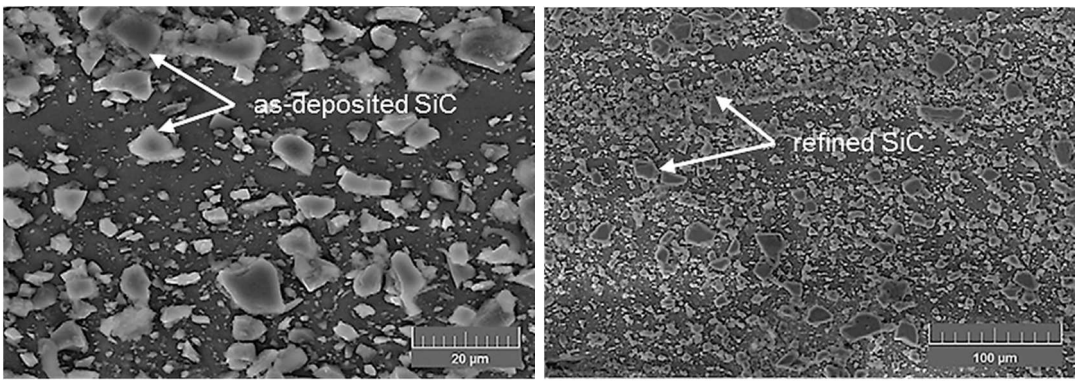

Fig. 6-1 SEM micrographs adapted from [6.10], showing; (a) the as-deposited SiC particles; (b) the refined SiC particles post-FSP

Their results [6.10] show that the as-deposited particles were refined from an average size of 12.2 µm to 4.4 µm following a single FSP pass at 1400 rpm, traversing at 100 mm/min. The authors attributed this refinement to fragmentation of the SiC particles caused by the intense plastic deformation within the stir zone [6.10]. Furthermore, the refined particles were homogeneously distributed across the stir zone. The refinement and homogeneous distribution of the SiC particles yielded a 100% hardness increase over the as-deposited coating [6.10]. The sliding wear performance of the FSPed specimen exhibited a corresponding improvement. The authors [6.10] attributed this result to the increased hardness in the near-surface region, originating from the homogeneous distribution of the refined SiC reinforcements [6.10]. Additionally, the authors [6.10] also noted that the CS and FSP processes did not alter the constituent phases of the feedstock powders.

The breadth of research that has been conducted on combined CS and FSP is limited. Therefore, to elucidate the findings from this study, it was necessary to compare the results with those obtained by researchers examining FSP combined with other spraying techniques, such as high velocity oxy-fuel (HVOF) [6.13, 6.14] or similar process [6.13, 6.15–6.19]. Specifically, these studies [6.13, 6.16] have been reviewed to establish if the microstructure within the stir zone exhibits similar features when the coating is deposited via CS or by thermal spray processes.

In one study [6.13], a coating comprising WC-Cr_3C_2-Ni was deposited on H13 steel by HVOF and subsequently FSPed. The aim of the study [6.13], was to characterise any changes to the microstructure post-FSP and determine if the combination of the two surface modification processes (HVOF and FSP) offered any advantages over HVOF alone.

The authors' [6.13] results confirmed that the sintered WC-Co FSP tool was capable of stirring the deposited WC-Cr_3C_2-Ni. The FSPed layer exhibited a considerable hardness increase (>65%) over the as-deposited coating. Furthermore, FSP successfully homogenised the distribution of the WC reinforcements leading to a reduction in the average interparticle spacing and eliminated porosity identified in the as-deposited coating [6.13]. Finally, the research group [6.13] concluded that the interface between the coating and substrate was successfully improved post-FSP owing to the disruption of the as-deposited coating-to-substrate interface.

In a similar study, Rahbar-kelishami et al. [6.16] investigated the effects of FSP on a flame sprayed WC-CoCr coating. The authors [6.16] utilised a novel multilayer technique to enhance the deposition efficiency of the WC-CoCr coating by first spraying a Ni-Al intermediate layer. Subsequently, they [6.16] measured the wear performance of the as-deposited coating and FSPed layer to evaluate whether the combination of the two processes offered enhanced wear resistance when compared to flame spraying alone. Additionally, the research group [6.16] examined the interface between the coating and substrate using optical and scanning electron microscopy (SEM) and highlighted the successful disruption of the coating-to-substrate interface by FSP. Their results [6.16] confirmed the elimination of porosity and increase in hardness (120% increase over the as-received base material). Interestingly, the hardness of the as-deposited WC-CoCr coating was approximately 42% greater than the FSPed coating; unfortunately, this result was not explained by the authors [6.16].

By measuring the wear track depth following sliding erosion tests, the authors [6.16] confirmed that the combination of the two surface modification processes offers improved wear performance over the flame sprayed coating alone. The coefficient of friction of the FSPed specimen was approximately 50% greater than the as-deposited coating. Equally, the wear rate (mm^3/m) of the as-deposited coating was 47% greater than the FSPed specimen [6.16].

Based on the results from these two studies [6.13, 6.16], and similar studies on CS combined with FSP [6.9, 6.10], it can be deduced that the application of FSP to either a thermally sprayed coating or a CS coating can successfully embed the deposited reinforcements within the stir zone. Additionally, post-FSP, both the CS and thermal sprayed coatings exhibit refinement and redistribution of the reinforcing particles, when compared with the as-deposited layers [6.13, 6.16].

The present study evaluated several coatings and substrate combinations to assess the modification of the coating and substrate following FSP. Different FSP tool configurations were also considered, to determine the influence of tool geometry and material on the microstructure within the stir zone. The results from this microstructural analysis are presented along with corresponding microhardness data to establish any improvements over the as-received substrate alloy.

6.2 Experimental Methods

This section specifies the different feedstock powders and substrate alloys that were examined in this preliminary study and describes the particular CS and FSP parameters used to manufacture the specimens. The test methods used to evaluate the manufactured samples are also presented herein. A more comprehensive account of these test methods is given in Chapter 4.

6.2.1 Materials

WC-Co cermet powders were selected for the preliminary CS and FSP study as previous work on HVOF deposited WC-Co (Chapter 5) demonstrated its improved erosion and corrosion performance over the as-received substrate. Furthermore, existing research also confirms the beneficial erosion properties of WC-Co [6.20–6.22]. Two grades of WC-Co with different internal morphologies were examined. The first powder (WC-17Co) is comprised of nano- and micro-scale tungsten carbides, evenly distributed throughout a cobalt matrix [6.23]. The second cermet powder (WC-25Co) consists of a tungsten carbide core surrounded by a cobalt binder, as shown in Fig. 6-2. The properties of the two powders are presented in and their chemical composition was verified by SEM. The information concerning the average particle size range was gathered from the powder manufacturer's data sheet [6.24–6.26].

The two WC-Co powders were separately cold sprayed onto three different aluminium alloy substrates. The three grades of aluminium investigated were as follows: AA2024-T3, AA6082-T6 and AA6N01-T6. Table 5-2 [6.24–6.26] presents the chemical composition of each alloy. The substrates were de-greased with methylated spirit before spraying to remove any surface contaminants. Each substrate plate measured 200 x 120 x 6 mm.

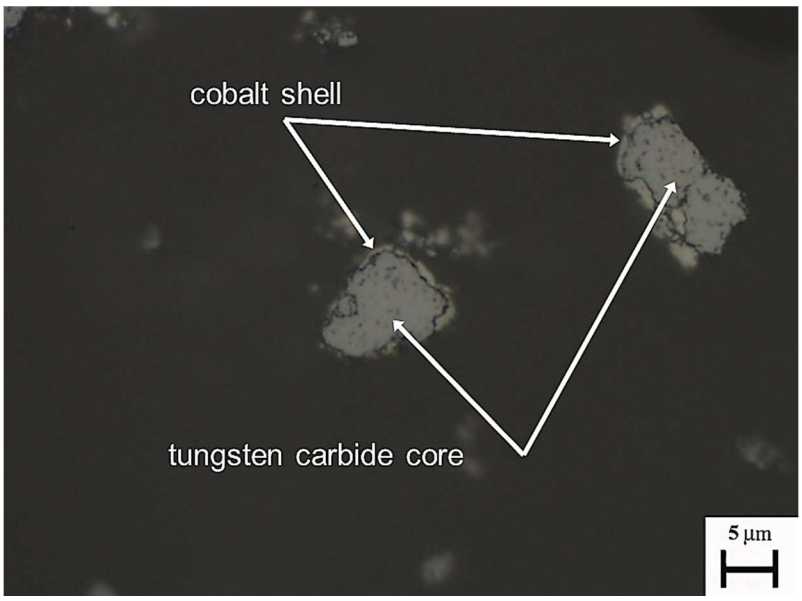

Fig. 6-2 Optical micrograph showing a cross-sectioned WC-25Co particle [x1000]

Table 6-1 Properties of the feedstock powder

Coating material	Composition (wt.%)	Size distribution (µm)	Reinforcement grain
WC-17Co	83W - 17Co	-30 +5	Fine
WC-25Co	75W - 25Co	-25 +5	Coarse

Table 6-2 Properties of the substrate alloy [6.24–6.26]

Alloy	Chemical composition (wt. %)	Heat treatment
AA2024	93.2Al – 0.5Si – 0.5Fe – 4.9Cu – 0.9Mn – 1.8Mg – 0.1Cr – 0.25Zn – 0.15Ti	T3
AA6082	97.15Al – 1.3Si – 0.5Fe – 0.1Cu – 1.0Mn – 1.2Mg – 0.25Cr – 0.2Zn – 0.1Ti	T6
AA6N01	98.46Al – 0.6Si – 0.13Fe – 0.11Mn – 0.64Mg – 0.03Zn – 0.034Ti	T6

*max values unless otherwise stated

6.2.2 Cold spray parameter development and deposition

As discussed in Chapter 4, CS deposition was carried out using a CGT Kinetics 4000/47 CS system, with powders supplied to the nozzle using a PF 4000 Comfort series powder feeder. The CS settings were optimised by measuring the quantity of material deposited for different gas temperatures, gas pressures and nozzle standoff distances. The mass of deposited material was established by weighing the specimens pre- and post-CS. The thickness of the deposited layer was also measured using a micrometer.

By investigating the effect of each parameter on the thickness and mass of the deposited coating, it was established that reducing the standoff distance below 50 mm resulted in a grit blasting effect, similar to what has been demonstrated in existing research [6.7, 6.27]. Grit blasting occurs when the impinging particles impact at too high a velocity causing them to rebound from the surface [6.6.7, 6.27, 6.28]. Spraying at low pressures and temperatures led to only minimal quantities of deposited material due to insufficient deformation of the impinging cermet particles [6.29]. Under these conditions, it was possible to successfully deposit the first coating layer; however, subsequent passes by the CS nozzle did not deposit additional material. This phenomenon has been observed in similar studies [6.7, 6.27], in which the authors attribute the successful deposition of the initial layer to the increased deformability of the substrate alloy (compared to the deformability of the previously deposited cermet layer) [6.28].

Table 6-3 presents the CS parameters used to deposit the two WC-Co powders onto the three substrate alloys. The settings (Table 6-3) were consistent across all of the substrate and coating combinations.

Table 6-3 Optimised CS deposition parameters

Standoff distance (mm)	50
Spray angle (°)	90
Nozzle traverse speed (mm/s)	50
No. of passes	8
Spray overlap (mm)	2
Gas pressure (bar)	30
Gas temperature (°C)	700

6.2.3 FSP process parameters

FSP was performed using a TTI precision spindle FSP machine. The specific details relating to the FSP eqipment and processing stages are discussed in Chapter 4. The parameters presented in Table 6-4 correspond to FSP passes that yielded defect-free processing zones. For this study, the term “defect-free” refers to any FSPed surface that does not exhibit undesirable features such as voids or flash, which are commonly associated with sub-optimal FSP parameters [6.30]. Several other combinations of traverse speed, plunge depth and rotation speed were

examined; however, due to the production of unacceptable surface defects, these FSP passes are not considered herein.

Table 6-4 FSP parameters investigated in the present study

Specimen code	Substrate alloy	Coating material	Tool type	Rotation speed (rpm)	Traverse speed (mm/min)	Plunge depth (mm)	Dwell time (s)
1	AA2024-T3	WC-25Co	pinless	300	50	0.25	0.25
2	AA2024-T3	WC-17Co	pinless	300	50	0.25	5
3	AA6082-T6	WC-17Co	M-series	600	300	5.05	0
4	AA6082-T6	WC-25Co	M-series	600	300	5.05	0
5	AA6N01-T6	WC-25Co	M-series	600	250	5.05	0
6	AA6N01-T6	WC-17Co	M-series	600	250	5.05	0

In addition to the FSP parameters, the material and geometry of the FSP tool have considerable influence over the resultant stir zone [6.31, 6.32]. Therefore, two different tool designs were employed in the present study to investigate the differences between the resulting stir zones. The first tool was a pinless design that was manufactured from H13 tool steel (Fig. 6-3). The shoulder had a concave geometry to force the plasticised material from the outer edge of the stir zone to the centre, thereby increasing the forging pressure during processing [6.31].

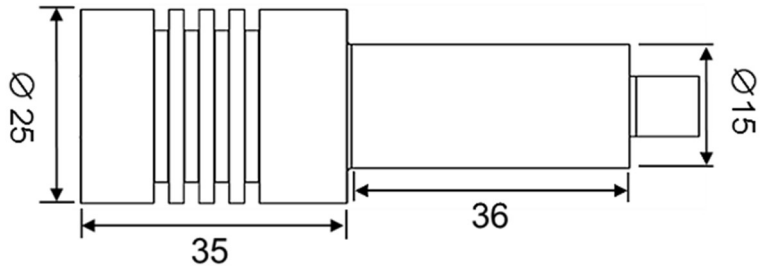

Fig. 6-3 Basic dimensions (mm) of the H13 FSP tool

To prevent chipping of the as-deposited CS coating, a 3° tilt angle was applied during the FSP passes. In addition to the low manufacturing costs associated with the production of an H13 tool, the lack of a pin meant that there was no extraction hole following the withdrawal of the tool from the plate [6.33].

The second tool (Fig. 6-4) employed in the present study, was an M-series tool manufactured by Megastir. This design featured a polycrystalline cubic boron nitride (pcBN) tip and shoulder that offered enhanced resistance to wear and facilitates FSP at higher temperatures (when compared with tools manufactured from steel). The main body of the tool (shank) was manufactured from tungsten carbide. In contrast to the pinless tool, the pcBN tool featured a threaded 5 mm pin to increase movement of the plasticised material within the stir zone [6.34]. The shoulder featured concentric circular grooves to force the softened material from the outer edge of the stir zone to the centre.

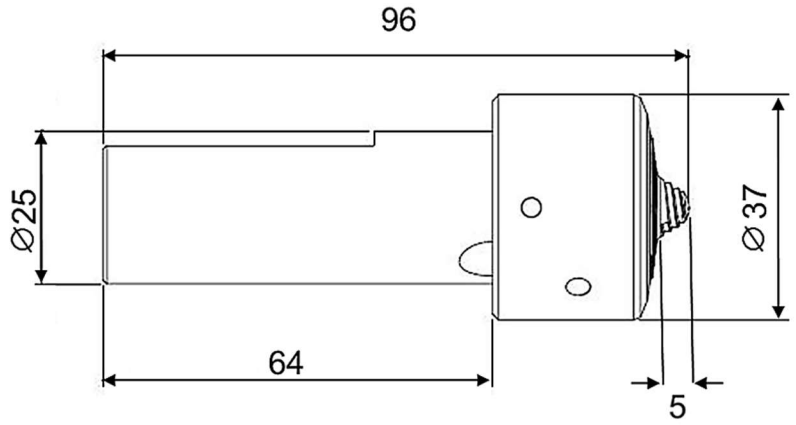

Fig. 6-4 Basic dimensions (mm) of the M-series pcBN tool, adapted from [6.35]

6.2.4 Characterisation of the as-deposited and FSPed specimens

The as-deposited and FSPed specimens were sectioned using a precision cutting wheel (Accutom 5) to examine the microstructure of the coating and stir zone. Standard metallographic preparation techniques were employed to prepare the specimens to a 0.05 μm finish. The specific grinding and polishing stages that were used to prepare the specimens are outlined in Chapter 4.

The microstructure of the test coupons was characterised using light optical and scanning electron microscopy (SEM), facilitated by an Olympus G51X optical microscope and a Hitachi S-3000N SEM. Energy Dispersive Spectroscopy (EDS) provided elemental analysis of the as-deposited coatings and specific regions within the stir zone.

A Mitutoyo MVK-G1 microhardness indenter was used to establish the hardness of the various test specimens. Indents were made using an applied load of 100 gf at specific locations within the CS and FSPed layer. The hardness of the substrate alloys was also measured in the as-received and stirred conditions, without

the addition of any cermet particles. Fig. 6-5 presents a macroscopic view of the stir zone to highlight the different regions that are discussed in Section 6.3. The advancing and retreating sides of the stir zone [6.36] have also been identified. However, the advancing and retreating side of samples W30 and W31 (Table 6-4) were reversed due to the rotation of the pinless tool being opposite to that of the pcBN tool.

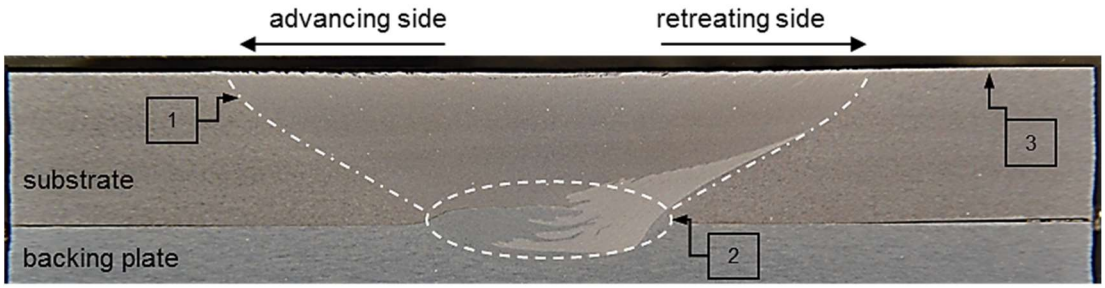

Fig. 6-5 Macrograph highlighting the different areas that will be discussed in the results section; (1) stir zone boundary, (2) root of the stir zone, (3) as-deposited coating

6.3 Results and Discussion

6.3.1 Light optical microscopy

6.3.1.1 Specimens manufactured with a pinless tool

The microstructure of the test specimens was examined using light optical microscopy, to highlight the changes to the microstructure post-FSP. Specifically, the primary aim of this section was to assess whether the particles that comprise the as-deposited coating were successfully embedded within the substrate following FSP, or if the coating was removed by the FSP tool. Light optical microscopy was employed to determine to what extent the internal morphology of the WC-Co particle has affected the microstructure of the as-deposited coating and the distribution of the coating post-FSP.

Fig. 6-6 presents an optical micrograph of the as-deposited WC-17Co coating on AA6082 (T6 condition). The micrograph (Fig. 6-6) illustrates an abrupt interface between the coating and substrate, which is characteristic of low adhesive strength [6.37]. Li et al. [6.37] investigated the microstructure at the coating-to-substrate interface of CS deposited copper onto Q235 mild steel. The authors [6.37] conducted mechanical pull-off testing (in accordance with ASTM C-633-79) to establish the adhesion strength of the coating. Post-test analysis of the specimens confirmed that the location of fracture aligned with the coating-to-substrate interface (as identified

through optical microscopy). Based on these results, the authors [6.37] concluded that the bonding between the copper particles is mechanical (i.e. mechanical interlocking) and that the presence of oxide inclusions prevent adjacent particles from coalescing, thereby reducing the adhesive and cohesive strength of the coating [6.37].

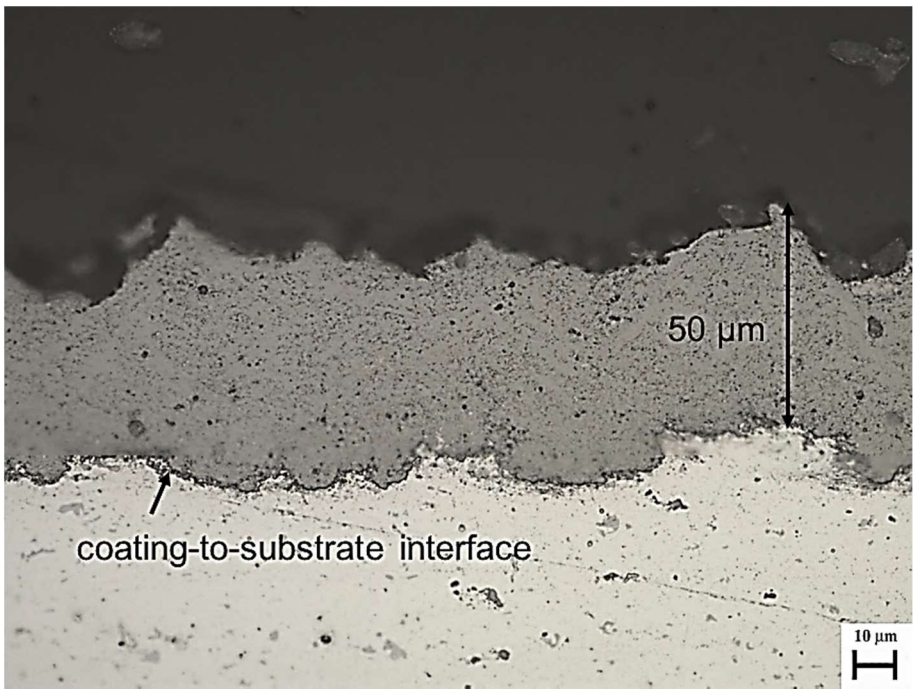

Fig. 6-6 Optical micrograph of the as-deposited WC-17Co coating on AA6082 (Specimen 3 from Table 6-4) [x500, Unetched]

Fig. 6-7 is an optical micrograph showing the stir zone from Specimen 1 in the post-FSP condition. The image (Fig. 6-7) depicts a layer of distributed WC-17Co particles that extend approximately 600 µm from the surface of the specimen. EDS was employed to confirm that the grey particles highlighted in the micrograph (Fig. 6-7) are the deposited WC-17Co particles and not surface contamination. Equally, EDS confirmed that outwith this band of WC-17Co particles in the near-surface region, the substrate was void of reinforcements. The image (Fig. 6-7) demonstrates that reinforcements from the CS coating have been embedded within the AA2024 substrate.

In contrast, Fig. 6-8 shows that, following FSP, the WC-25Co reinforcements have only been embedded within the substrate to a depth of approximately 200 µm. Out-with this narrow band, the substrate is void of reinforcements; as confirmed by EDS. Despite the dissimilarities in the microstructure of each specimen (Fig. 6-7 and Fig. 6-8), it is important to stress that the two micrographs demonstrate that the as-

deposited material has been refined, and successfully embedded in the substrate matrix.

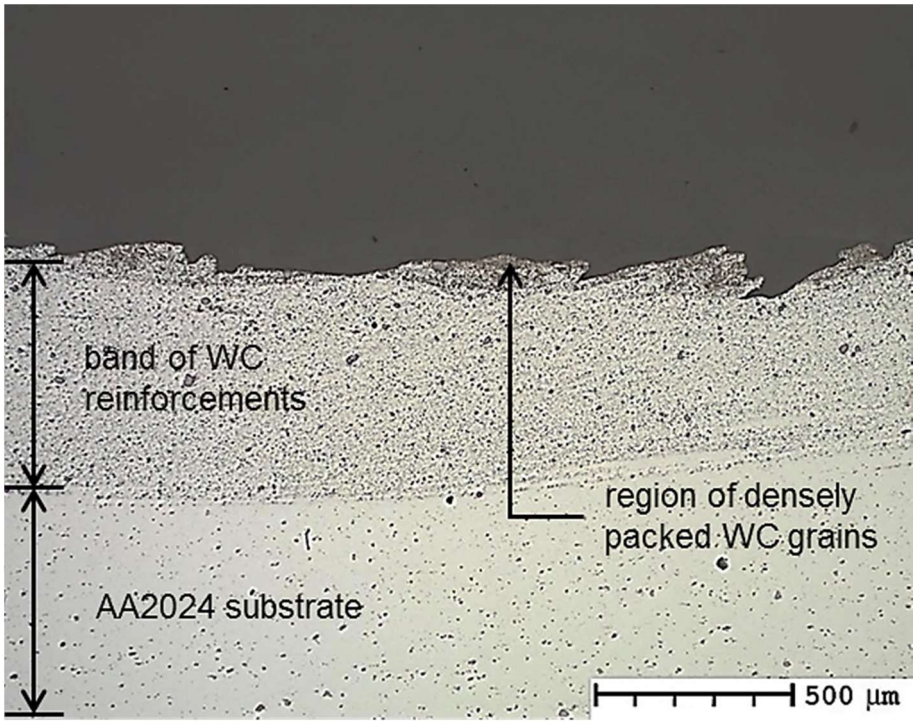

Fig. 6-7 Optical micrograph of the WC-17Co reinforced specimen, post-FSP [x50, Unetched]

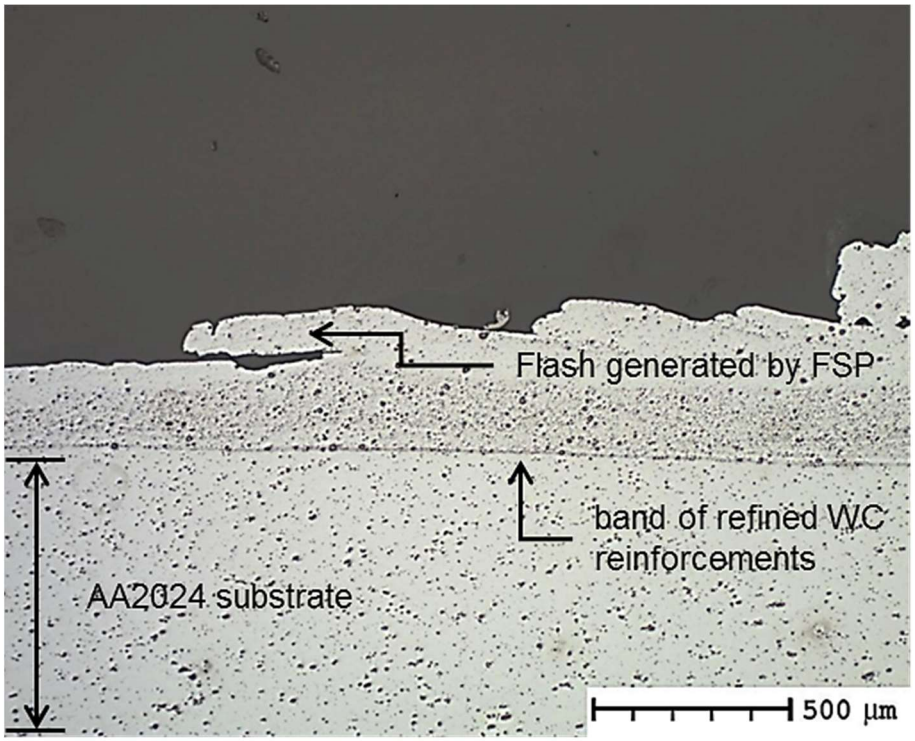

Fig. 6-8 Optical micrograph of the WC-25Co coated specimen post-FSP [x50, Unetched]

6.3.1.2 FSP specimens manufactured with pcBN tool

Fig. 6-9a-b and Fig. 6-10a-b illustrate the top surface of Specimen 3 and Specimen 4 (Table 6-3) respectively, both of which were manufactured using the pcBN tool (Fig. 6-4). The images (Fig. 6-9 and Fig. 6-10) exhibit dissimilar distributions of reinforcements between the advancing and retreating sides of the stir zone. EDS analysis (Section 6.3.2) was employed to confirm that the dark particles embedded within the substrate in the micrographs depict the reinforcements, as opposed to any contaminants that may have been present on the substrate surface prior to FSP.

As discussed in Chapter 2, the difference in the relative motion of the tool, with respect to the direction of traverse, generates dissimilar mechanical and thermal forces on each side of the stir zone [6.38–6.42]. The variation in these forces gives rise to the asymmetric microstructural features [6.38] depicted in Fig. 6-9 and Fig. 6-10. Furthermore, the images (Fig. 6-9 and Fig. 6-10) show that the morphology of the cermet particles has also influenced their distribution post-FSP; the dispersal of the grains in the WC17-Co and WC-25Co reinforced specimens is dissimilar, despite identical processing parameters used for each sample.

Fig. 6-9 depicts large, unrefined particles embedded within the stir zone, as well as refined carbide grains. The presence of these large particles confirms that the FSP parameters employed in this pass have failed to refine all the as-deposited material. Conversely, the WC-25Co reinforced specimen (Fig. 6-10) exhibits no large, as-deposited particles within the stir zone. Therefore, based on the examined micrographs, the WC-17Co particles are more difficult to refine and redistribute by FSP. This difficulty is likely attributed to the greater cohesive strength of the WC-17Co material as a result of the cobalt binder being evenly distributed throughout the particle. This even distribution of carbide grains and the binder is in contrast to the WC-25Co powder, which comprises a single carbide core and surrounding cobalt shell. Considering that no other variables have changed, the different morphologies of the two powders must account for the difference in the resultant microstructure. Corresponding results were also identified when examining the FSPed AA6N01-T6 coated specimens (Specimen 5 and 6 from Table 6-3).

Fig. 6-11 is an optical micrograph of Specimen 4 taken at [x500] magnification showing the distribution of the reinforcements on the advancing side post-FSP. The image (Fig. 6-11) highlights the successful distribution of the carbide grains throughout the substrate matrix. Moreover, the image demonstrates the elimination of the coating-to-substrate interface as seen in the as-deposited coating (Fig. 6-6).

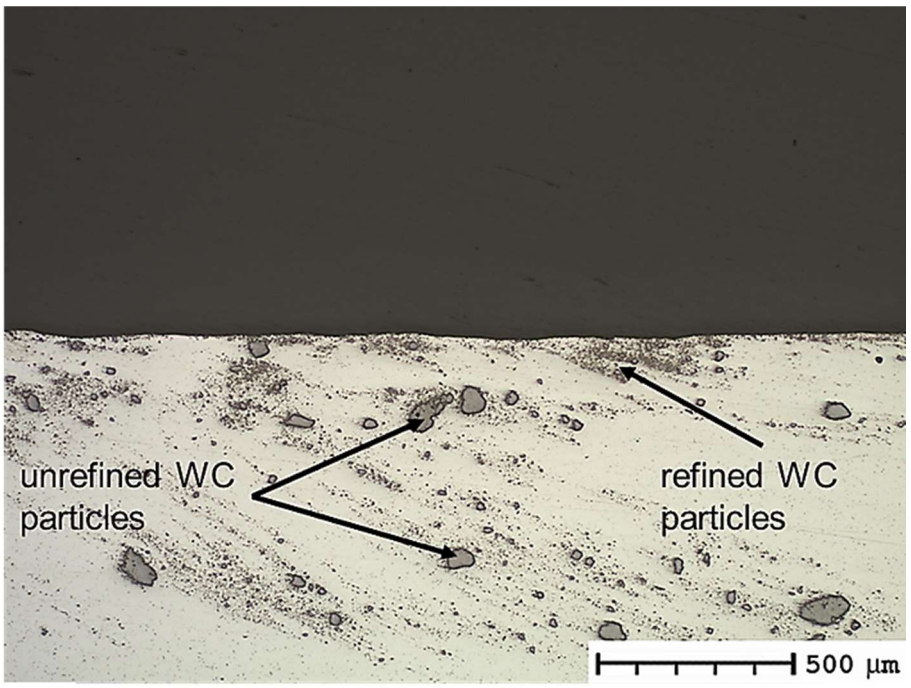

(a)

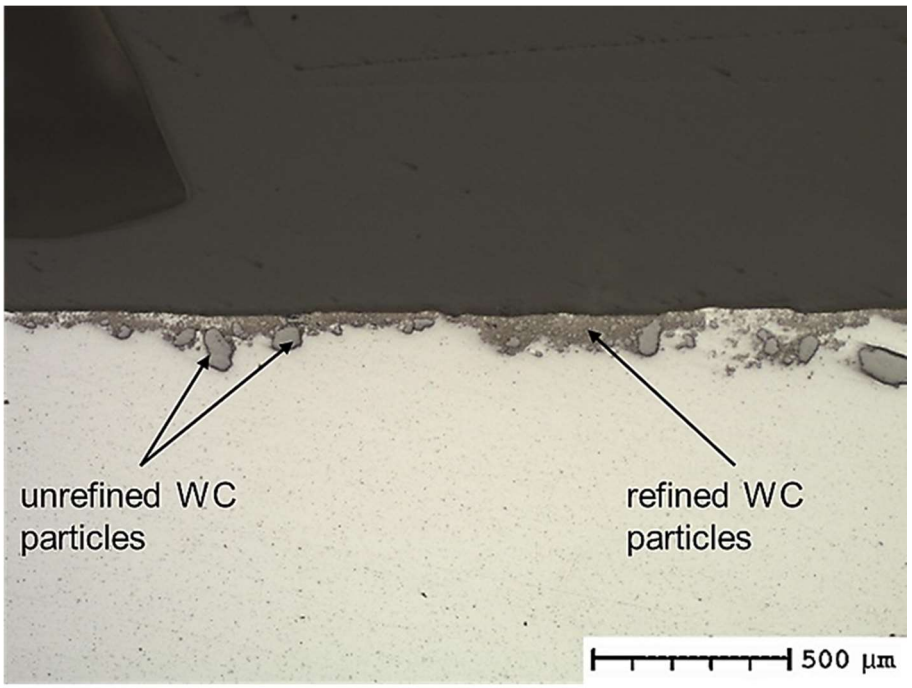

(b)

Fig. 6-9 Optical micrographs showing the distribution of the WC-17Co coating post-FSP; (a) the advancing side; (b) the retreating side of the stir zone [x50, Unetched]

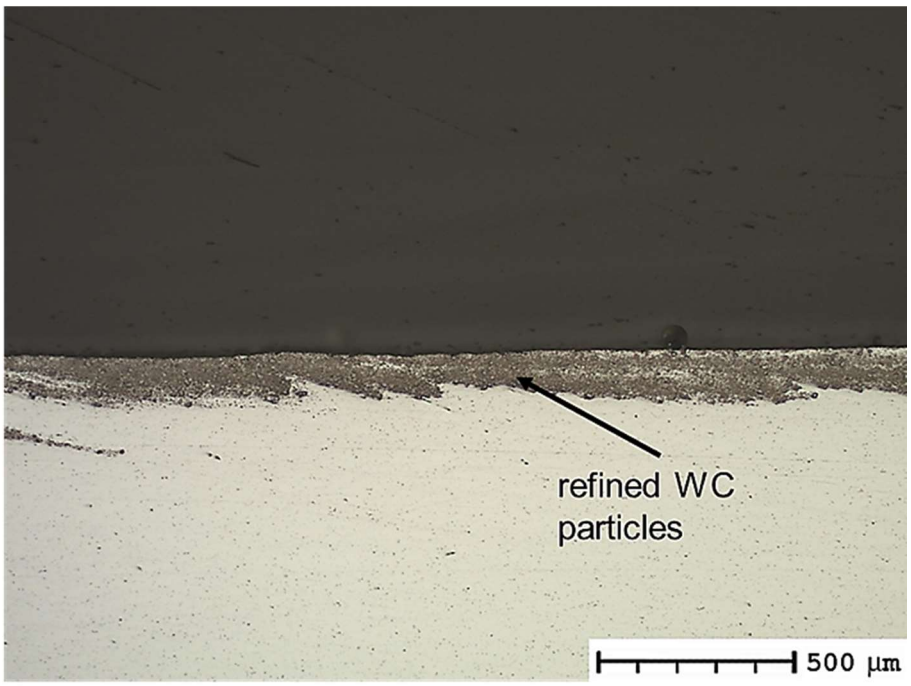

(a)

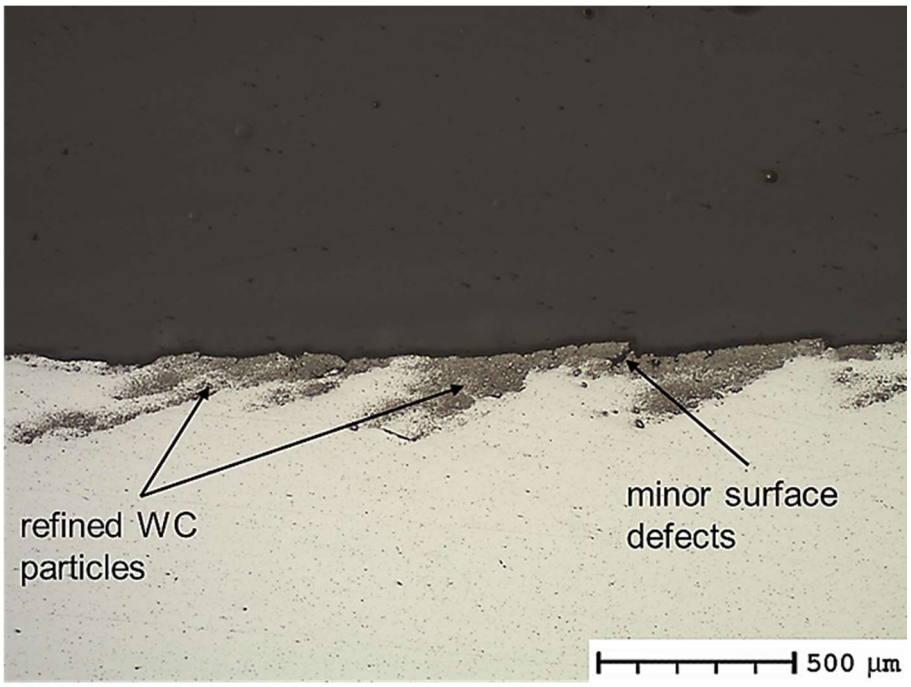

(b)

Fig. 6-10 Optical micrographs showing the distribution of the WC-25Co coating post-FSP; (a) the advancing side; (b) the retreating side of the stir zone [x50, Unetched]

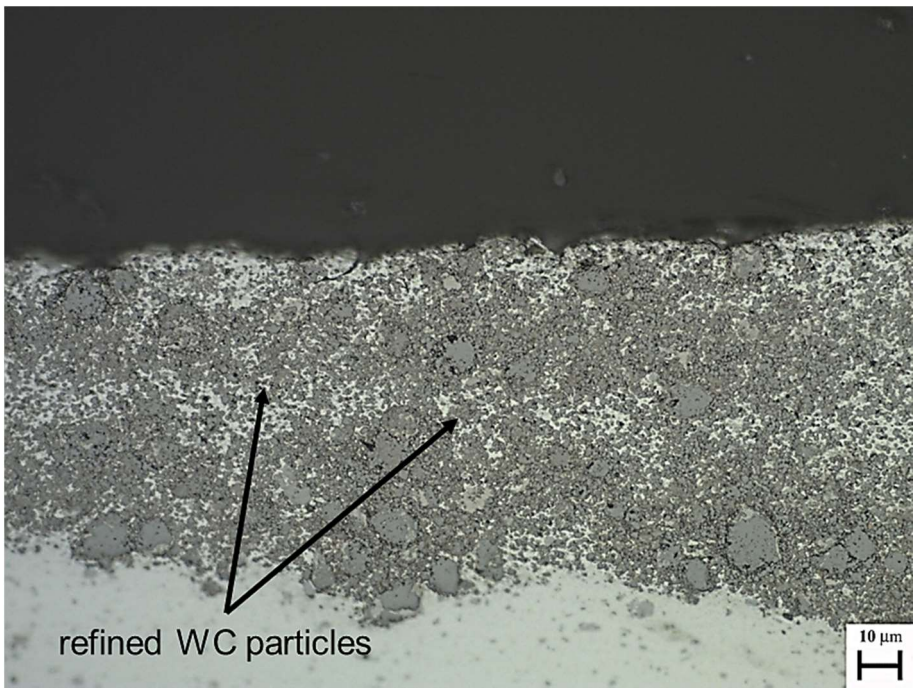

Fig. 6-11 Optical micrograph showing the refinement and distribution of the carbide grains post-FSP [x500, Unetched]

Fig. 6-7 indicates that there is very little coating material embedded within the substrate on the advancing side of the stir zone. However, examination of the as-deposited coatings confirms that the CS deposited material has been evenly distributed across the sprayed area. Therefore, FSP must have removed or redistributed the cermet material that was previously on the advancing side of the stir zone. By inspecting optical micrographs of various regions within the stir zone, cermet material was discovered at the root (base) of the stir zone. Fig. 6-12a-b present images showing the root of the stir zone in Specimen 3 and 4 (Table 6-3).

Both images (Fig. 6-12a-b) show that cermet material from the previously deposited coating has been forced down to the root of the stir zone. This movement of material is attributed to the features present on the shoulder and the probe of the pcBN tool. Considering that FSP is a surface engineering process, modification of the microstructure should be restricted to the surface and near-surface regions. Therefore, the 5 mm probe is unnecessary. In fact, as demonstrated in Fig. 6-12, the incorporation of a 5 mm probe could be considered detrimental to the process by forcing the reinforcing material to the root of the stir zone, away from the surface and near-surface regions.

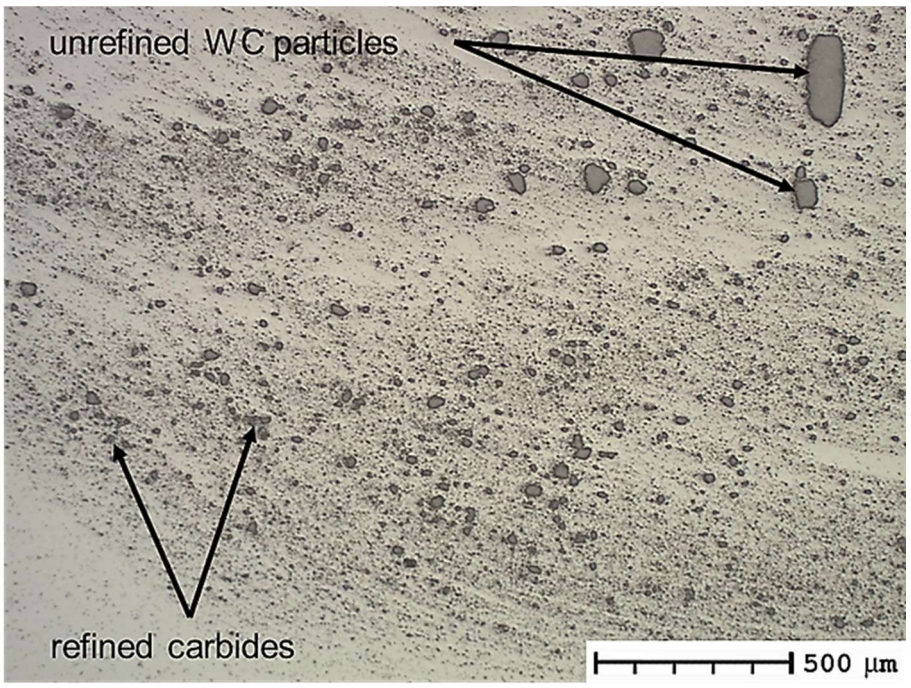

(a)

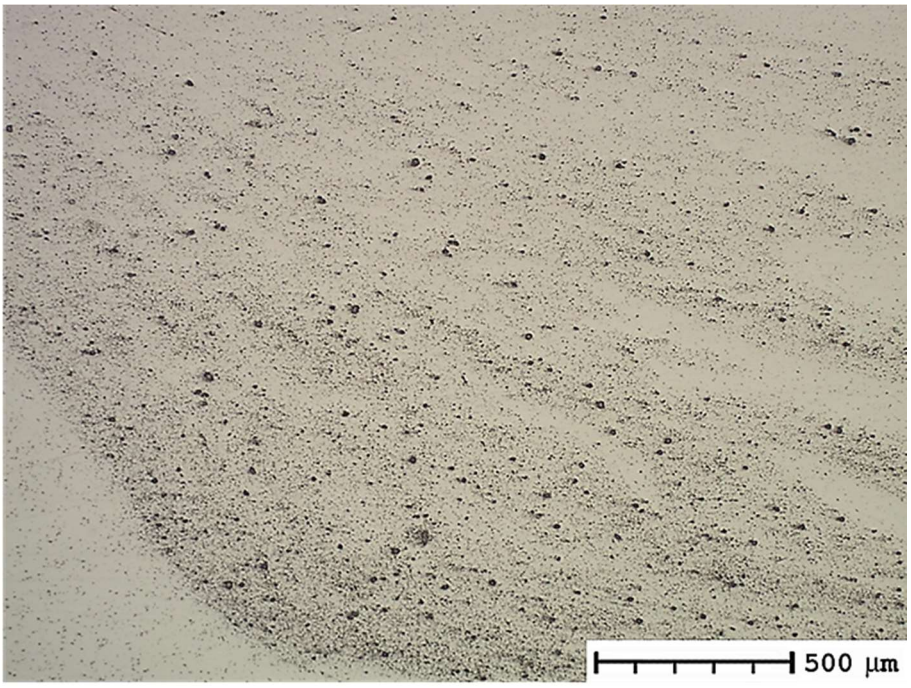

(b)

Fig. 6-12 Optical micrograph exhibiting the microstructure at the root of the stir zone; (a) Specimen 3, (b) Specimen 4 (Table 6-4) [x500, Unetched]

6.3.2 Electron dispersive spectroscopy (EDS) analysis

EDS was employed to substantiate the microstructural features observed in the optical micrographs and to confirm the presence of reinforcements embedded within the substrate at various locations in the stir zone. Specifically, EDS was used to verify that the dark grey particles identified in the optical micrographs are the tungsten carbide reinforcements that were previously deposited on the surface via CS. Fig. 6-13 exhibits an SEM micrograph of the embedded particles and highlights the areas in which the EDS spot analysis was conducted. Through this approach, it was possible to identify the chemical composition of these specific areas within the stir zone and, hence, determine if they represent the carbide reinforcements or other inclusions.

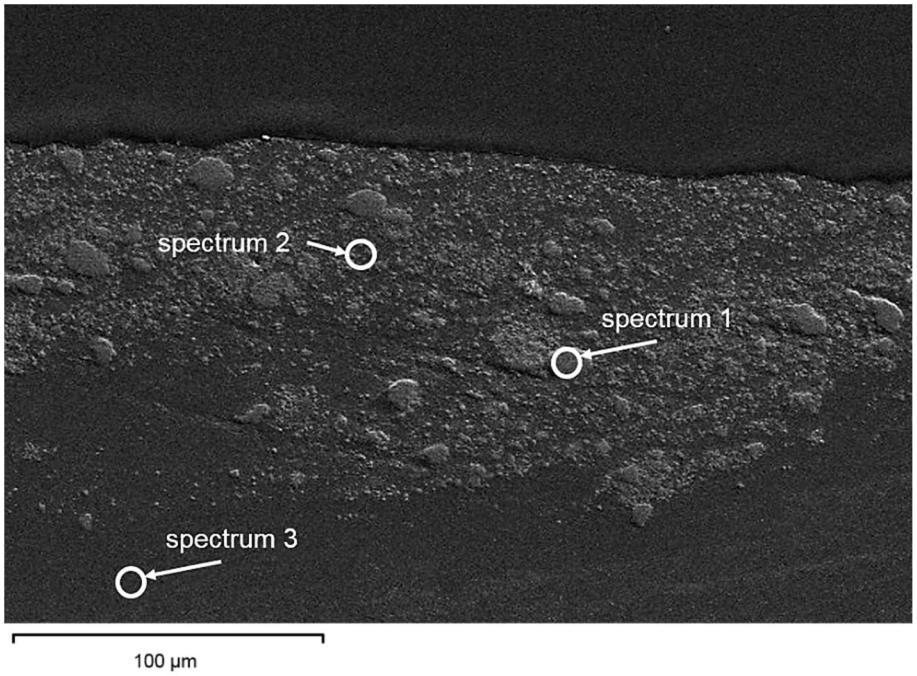

Fig. 6-13 SEM micrograph of the WC-17Co material embedded within the aluminium substrate

The EDS analysis was performed with a fixed element list comprising tungsten, carbon and aluminium, as these are the only elements necessary to prove if the scanned regions depict the carbide reinforcements. Table 6-5 presents the associated chemical composition of the area indicated in the image (Fig. 6-13) and confirmed the presence of tungsten. Thus, it can be stated that the dark grey particles depicted in the optical micrographs do represent the reinforcements.

For the specimens manufactured with the pcBN tool, EDS also confirmed that the particles identified at the root of the stir zone (Fig. 6-12a-b) are the carbide reinforcements. This result confirms that the pcBN tool geometry displaces the coating away from the surface and near-surface regions.

Table 6-5 Chemical composition (wt.%) of locations depicted in Fig. 6-13, obtained by EDS analysis

	W	Co	Al
Spectrum 1	55.4	4.1	40.5
Spectrum 2	12.8	6.0	81.2
Spectrum 3	0	0	100

6.3.3 Coating hardness

The microhardness of the FSPed specimens was measured at various locations within the stir zone to identify the effect of FSP on the hardness of the microstructure. Measurements were also taken on the as-deposited coating (no FSP), on the as-received substrate, and the FSPed substrate without any reinforcements (FSP only). The hardness values presented herein are an average of five measurements.

The as-received substrate (AA2024) from Specimen 1 and Specimen 2 measured 130 HV, and the as-deposited coating measured 900 HV. Post-FSP, the stir zone exhibited a hardness of 190 HV, amounting to a 46% increase over the as-received substrate. This result shows that for the specimens manufactured with the pinless tool, the presence of reinforcements within the aluminium matrix enhances the hardness over the as-received material. This increase is attributed to a load transfer effect (i.e. transfer of the load from the soft matrix to the hard reinforcements) [6.43–6.45] and is comparable to the findings reported by Slipenyuk et al. [6.45].

Fig. 6-14 presents the microhardness values measured in the stir zone of Specimen 3 and Specimen 4 (Table 6-4). The chart (Fig. 6-14) also shows the hardness of the as-received substrate and the FSPed substrate without any reinforcements. Specimens 3 and 4 were manufactured using the M-series pcBN tool. The values presented in Fig. 6-14 were measured 0.1mm from the surface to maintain consistency between the different specimens. For comparison, the microhardness of the as-deposited WC-17Co and WC-25Co coatings (no FSP) was measured as 913 HV and 224 HV respectively. It is important to stress that these measurements

were recorded on the carbide particles alone, i.e. not when distributed throughout a comparably ductile matrix, hence why they are far in excess of any values presented in Fig. 6-14.

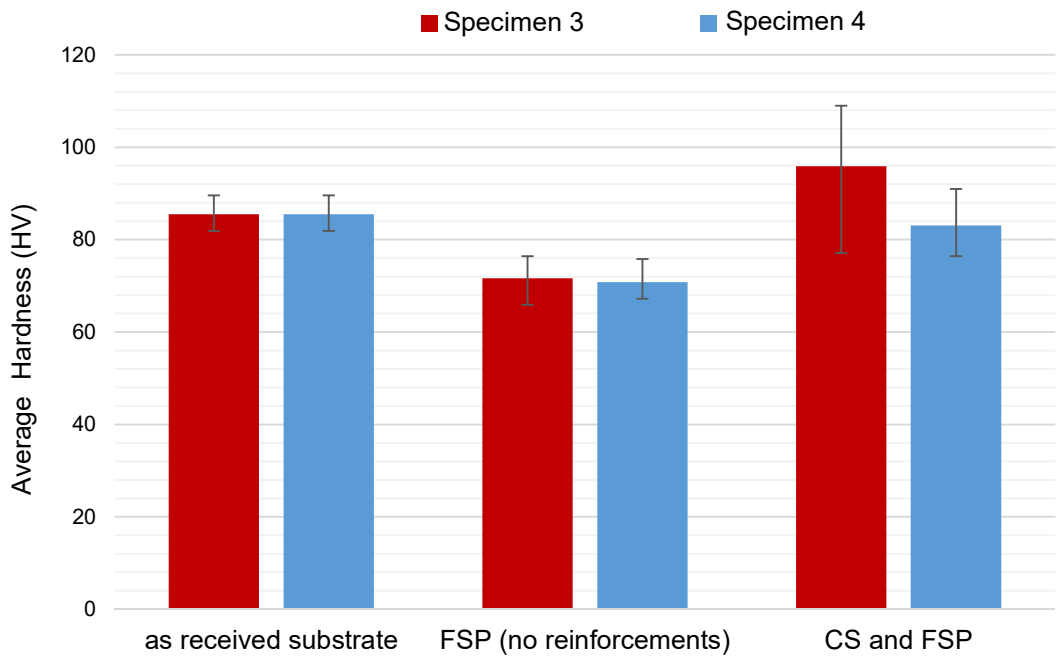

Fig. 6-14 Average hardness of Specimen 3 and Specimen 4 (Table 6-4) in the as-received condition, with FSP only and with combined CS and FSP

The results (Fig. 6-14) demonstrate an increase in hardness with the presence of the reinforcements. However, considering that the cold spray deposited coating measured only 52 µm, and many of the reinforcements have been drawn down to the root of the stir zone, the reinforcements are not present in sufficient quantities in the near-surface region to facilitate load transfer from the matrix to the reinforcements. Hence the hardness within the stir zone exhibits a minor increase (approximately 30%) over the stirred substrate containing no reinforcements (FSP only). This phenomenon is only apparent in the specimens produced using the pcBN tool owing to the incorporation of the 5 mm pin. As highlighted in the existing research [6.45], increasing the quantity of carbides within the matrix leads to an associated increase in hardness. Therefore, future work (Chapter 7 and Chapter 8) will seek to increase the amount of cermet deposited on the surface of the specimen prior to FSP.

The results from the microhardness measurements (Fig. 6-14) also highlight a drop in the hardness of the 6000-grade alloys post-FSP (no reinforcements). However, this finding contrasts with published literature that reports an increase in

hardness post-FSP [6.47]. The hardness increase that is typically measured in materials processed by FSP is attributed to the grain refinement generated within the stir zone [6.47]. In the case of the 6000-grade alloys, the reduction in hardness is potentially attributed to a self-annealing effect arising from the residual heat in the stir zone. The heat causes grain growth, thereby reducing the overall hardness within the stir zone [6.48]. This softened matrix is incapable of supporting the hard carbide grains under the load applied during the microhardness testing and as a result, the reinforcements have little impact on the hardness of the matrix, even in regions of high carbide density. Nevertheless, without physically measuring the temperature at various locations within the stir zone, this cannot be confirmed.

6.4 Conclusions

This chapter has presented the findings from an initial study into the combination of CS and FSP. The aim of this investigation has been to determine the influence of FSP on a CS deposited cermet coating and establish if FSP can refine and redistribute the deposited material, and remove the coating-to-substrate interface. Further, the study sought to determine the effect of the reinforcements on the microstructure within the stir zone, and to what extent the tool geometry has influenced the distribution of the carbide grains.

Based on the results presented herein, the abrupt coating-to-substrate interface has been successfully eliminated post-FSP, with the reinforcements successfully embedded within the aluminium matrix. The incorporation of a 5 mm probe in the pcBN tool adversely affected the distribution of carbides by forcing the reinforcements down to the root of the stir zone. The AA2024-T3 alloy shows a general hardness increase of around 43% in the sprayed and stirred condition, hence providing a proof of concept for combined CS and FSP. The microhardness analysis showed that that hardness of the 6000-grade alloys reduced following the application of FSP. This softened matrix was not capable of supporting the WC-Co particles when under load during the microhardness testing.

Based on the findings presented in this chapter, CS and FSP technologies have successfully been used in combination to embed tungsten carbide reinforcing particles in an aluminium substrate. However, several issues must be addressed in future work. The first issue relates to the quantity of reinforcements deposited on the surface by CS. Therefore, subsequent chapters (Chapter 7 and Chapter 8) utilise an innovative co-deposition process to increase the quantity reinforcing particles

deposited onto the substrate before FSP. Secondly, subsequent chapters incorporate a wider range of examination and analysis methods to evaluate the manufactured specimens. Finally, the use of heat treated aluminium has demonstrated the self-annealing phenomenon. While this discovery is of interest, it does not demonstrate the true capability of CS and FSP. Hence, future work will employ non-heat treated alloys during the investigation to prevent any self-annealing within the stir zone.

6.5 References

[6.1] H. Assadi, F. Gärtner, T. Stoltenhoff, H. Kreye, Bonding mechanism in cold gas spraying, Acta Mater. 51 (2003) 4379–4394.

[6.2] T. Hussain, D.G. McCartney, P.H. Shipway, D. Zhang, Bonding Mechanisms in Cold Spraying : The Contributions of Metallurgical and Mechanical Components, J. Therm. Spray Technol. 18 (2009) 364–379.

[6.3] T. Hussain, A study of bonding mechanisms and corrosion behaviour of cold sprayed coatings, (2011).

[6.4] C. Chen, Y. Xie, S. Yin, M.P. Planche, S. Deng, R. Lupoi, et al., Evaluation of the interfacial bonding between particles and substrate in angular cold spray, Mater. Lett. 173 (2016) 76–79.

[6.5] V.K. Champagne, The cold spray materials deposition process: fundamentals and applications, Woodhead Publishing, 2007.

[6.6] R.C. Dykhuizen, M.F. Smith, D.L. Gilmore, R.A. Neiser, X. Jiang, S. Sampath, Impact of High Velocity Cold Spray Particles, J. Therm. Spray Technol. 8 (1999) 559–564.

[6.7] T.H. Van Steenkiste, J.R. Smith, R.E. Teets, Aluminum coatings via kinetic spray with relatively large powder particles, Surf. Coatings Technol. 154 (2002) 237–252.

[6.8] R.S. Lima, J. Karthikeyan, C.M. Kay, J. Lindemann, C.C. Berndt, Microstructural characteristics of cold-sprayed nanostructured WC-Co coatings, Thin Solid Films. 416 (2002) 129–135.

[6.9] K.J. Hodder, H. Izadi, a. G. McDonald, a. P. Gerlich, Fabrication of aluminum-alumina metal matrix composites via cold gas dynamic spraying at low pressure followed by friction stir processing, Mater. Sci. Eng. A. 556 (2012) 114–121.

[6.10] C. Huang, W. Li, Z. Zhang, M. Fu, M. Planche, H. Liao, et al., Modification of a cold sprayed SiCp/Al5056 composite coating by friction stir processing, Surf. Coatings Technol. 296 (2016) 69–75.

[6.11] H. Ashrafizadeh, A. Lopera-Valle, A. Gerlich, A. McDonald, Effect of friction-stir processing on the wear rate of WC-based MMC coatings deposited by low-pressure cold gas dynamic spraying, in: Int. Therm. Spray Conf., Long Beach, 2015: pp. 41–47.

[6.12] C. Huang, W. Li, Y. Feng, Y. Xie, M.-P. Planche, H. Liao, et al., Microstructural evolution and mechanical properties enhancement of a cold-sprayed CuZn alloy coating with friction stir processing, Mater. Charact. 125 (2017) 76–82.

[6.13] Y. Morisada, H. Fujii, T. Mizuno, G. Abe, T. Nagaoka, M. Fukusumi, Modification of thermally sprayed cemented carbide layer by friction stir processing, Surf. Coatings Technol. 204 (2010) 2459–2464.

[6.14] Y. Mazaheri, F. Karimzadeh, M.H. Enayati, A novel technique for

development of A356/Al2O3 surface nanocomposite by friction stir processing, J. Mater. Process. Technol. 211 (2011) 1614–1619.
[6.15] A. Rahbar-kelishami, A. Abdollah-zadeh, M.M. Hadavi, R.A. Seraj, A.P. Gerlich, Improvement of wear resistance of sprayed layer on 52100 steel by friction stir processing, Appl. Surf. Sci. 316 (2014) 501–507.
[6.16] A. Rahbar-kelishami, A. Abdollah-zadeh, M.M. Hadavi, A. Banerji, A. Alpas, A.P. Gerlich, Effects of friction stir processing on wear properties of WC – 12 % Co sprayed on 52100 steel, Mater. Des. 86 (2015) 98–104.
[6.17] S.R. Anvari, F. Karimzadeh, M.H. Enayati, Wear characteristics of Al-Cr-O surface nano-composite layer fabricated on Al6061 plate by friction stir processing, Wear. 304 (2013) 144–151.
[6.18] Y. Mazaheri, F. Karimzadeh, M.H. Enayati, A novel technique for development of A356/Al2O3 surface nanocomposite by friction stir processing, J. Mater. Process. Technol. 211 (2011) 1614–1619.
[6.19] S.R. Anvari, F. Karimzadeh, M.H. Enayati, Wear characteristics of Al-Cr-O surface nano-composite layer fabricated on Al6061 plate by friction stir processing, Wear. 304 (2013) 144–151.
[6.20] V.A.D. Souza, A. Neville, Aspects of microstructure on the synergy and overall material loss of thermal spray coatings in erosion – corrosion environments, Wear. 263 (2007) 339–346.
[6.21] D.K. Goyal, H. Singh, H. Kumar, V. Sahni, Slurry erosion behaviour of HVOF sprayed WC-10Co-4Cr and Al 2O 3+13TiO 2 coatings on a turbine steel, Wear. 289 (2012) 46–57.
[6.22] A. Neville, F. Reza, S. Chiovelli, T. Revega, Erosion-corrosion behaviour of WC-based MMCs in liquid-solid slurries, Wear. 259 (2005) 181–195.
[6.23] Oerlikon Metco, Material Product Data Sheet Tungsten Carbide – 10 % Cobalt 4 % Chromium Powders, (2015) 1–7.
[6.24] International ASTM Standard, ASTM B209 - 14: Standard Specification for Aluminum and Aluminum-Alloy Sheet and Plate, 2007.
[6.25] International ASTM Standard, ASTM B2221 - 13: Standard Specification for Aluminum and Aluminum-Alloy Extruded Bars, Rods, Wire, Profiles, and Tubes (Metric), 2013.
[6.26] Q. Dai, Z. Liang, G. Chen, L. Meng, Q. Shi, Explore the mechanism of high fatigue crack propagation rate in fine microstructure of friction stir welded aluminum alloy, Mater. Sci. Eng. A. 580 (2013) 184–190.
[6.27] E.J.T. Pialago, C.W. Park, Cold spray deposition characteristics of mechanically alloyed Cu-CNT composite powders, Appl. Surf. Sci. 308 (2014) 63–74.
[6.28] D. Seo, M. Sayar, K. Ogawa, SiO 2 and MoSi 2 formation on Inconel 625 surface via SiC coating deposited by cold spray, Surf. Coatings Technol. 206 (2012) 2851–2858.
[6.29] C.J. Li, Y.Y. Wang, G.J. Yang, A. Ohmori, K.A. Khor, Effect of solid carbide particle size on deposition behaviour, microstructure and wear performance of HVOF cermet coatings, Mater. Sci. Technol. 20 (2004).
[6.30] R. Miranda, J. Gandra, P. Vilaca, L. Quintino, T. Santos, Surface Modification by Solid State Processing, Woodhead Publishing Limited, 2008.
[6.31] Y.N. Zhang, X. Cao, S. Larose, P. Wanjara, Review of tools for friction stir welding and processing, Can. Metall. Q. 51 (2012) 250–261.
[6.32] J.S. De Jesus, a. Loureiro, J.M. Costa, J.M. Ferreira, Effect of tool geometry on friction stir processing and fatigue strength of MIG T welds on Al alloys, J. Mater. Process. Technol. 214 (2014) 2450–2460.
[6.33] J. Gandra, R.M. Miranda, P. Vilaça, Effect of overlapping direction in multipass friction stir processing, Mater. Sci. Eng. A. 528 (2011) 5592–5599.

[6.34] R.S. Mishra, Z.Y. Ma, Friction stir welding and processing, Mater. Sci. Eng. R. 50 (2005) 1–78.
[6.35] A. Toumpis, A. Galloway, S. Cater, N. McPherson, Development of a process envelope for friction stir welding of DH36 steel - A step change, Mater. Des. 62 (2014) 64–75.
[6.36] J. Gandra, H. Krohn, R.M. Miranda, P. Vilaça, L. Quintino, J.F. Dos Santos, Friction surfacing - A review, J. Mater. Process. Technol. 214 (2014) 1062–1093.
[6.37] W.Y. Li, C.J. Li, H. Liao, Significant influence of particle surface oxidation on deposition efficiency, interface microstructure and adhesive strength of cold-sprayed copper coatings, Appl. Surf. Sci. 256 (2010) 4953–4958.
[6.38] J.D. Escobar, E. Velásquez, T.F. a Santos, a. J. Ramirez, D. López, Improvement of cavitation erosion resistance of a duplex stainless steel through friction stir processing (FSP), Wear. 297 (2013) 998–1005.
[6.39] H. Schmidt, J. Hattel, Modelling heat flow around tool probe in friction stir welding Modelling heat flow around tool probe in friction stir welding, Sci. Technol. Weld. Join. 10 (2013).
[6.40] H. Pashazadeh, A. Masoumi, J. Teimournezhad, A study on material flow pattern in friction stir welding using finite element method, Proc. Inst. Mech. Eng. Part B J. Eng. Manuf. 227 (2013) 1453–1466.
[6.41] S. Xu, X. Deng, A.P. Reynolds, T.U. Seidel, Finite element simulation of material flow in friction stir welding, 6 (2001).
[6.42] A.N. Albakri, B. Mansoor, H. Nassar, M.K. Khraisheh, Thermo-mechanical and metallurgical aspects in friction stir processing of AZ31 Mg alloy—A numerical and experimental investigation, J. Mater. Process. Technol. 213 (2013) 279–290.
[6.43] Q. Fang, P. Sidky, M. Hocking, Erosive wear behaviour of aluminium based composites, Mater. Des. 18 (1997) 389–393.
[6.44] H.J. Ryu, H.K. Jung, S.H. Hong, Effect of SiC reinforcement on mechanical properties of SiC/Al metal matrix composites, in: ICCM12 Conf. Paris, 1999: p. Paper 634.
[6.45] A. Slipenyuk, V. Kuprin, Y. Milman, J.E. Spowart, D.B. Miracle, The effect of matrix to reinforcement particle size ratio (PSR) on the microstructure and mechanical properties of a P/M processed AlCuMn/SiCp MMC, Mater. Sci. Eng. A. 381 (2004) 165–170.
[6.46] N. Karni, G.B. Barkay, M. Bamberger, Structure and properties of metal-matrix composite, J. Mater. Sci. Lett. 13 (1994) 541–544.
[6.47] J.-Q. Su, T.W. Nelson, C.J. Sterling, Grain refinement of aluminum alloys by friction stir processing, J. Mater. Sci. Lett. 86 (2006) 1–24.
[6.48] B.M. Darras, M.K. Khraisheh, F.K. Abu-Farha, M.A. Omar, Friction stir processing of commercial AZ31 magnesium alloy, J. Mater. Process. Technol. 191 (2007) 77–81.

Chapter 7 SprayStir of Co-Deposited Metal Matrix Composite Coatings

7.1 Introduction

Based on the findings from the preliminary study presented in Chapter 6, it was necessary to develop a method by which greater quantities of the cermet powder could be deposited on the surface of the substrate, prior to friction stir processing (FSP). Therefore, this chapter will discuss an innovative co-deposition approach to cold spray (CS) reinforcing particles with a comparably ductile binder alloy. This chapter also expands on the experimental work carried out in Chapter 6 by incorporating a more comprehensive test programme (as compared with Chapter 6), to characterise the microstructure of the manufactured specimens and evaluate their erosion performance.

The deposition of erosion resistant coatings by CS has inherent complexities due to the difficulties associated with building up a sufficient coating thickness with wear resistant particles [7.1]. However, within the published literature, two methods have been utilised to enable wear-resistant particles, such as ceramics, to be CS deposited on the surface of a substrate [7.2, 7.3]. The first method involves the use of agglomerated-sintered cermet powders [7.2], such as WC-CoCr and Cr_3C_2-NiCr [7.4]. An overview of cermet powders is presented in Chapter 2. While the use of such powders does enable a wear resistant coating to be produced, the quantity of binder alloy (wt.%) within the cermet may still restrict the amount of flattening (Chapter 2) that that particle can undergo at the point of impact and, hence, limit the coating thickness that can be achieved [7.5]. The second method of incorporating a metallic binder involves mixing two or more powders to a desired ratio prior to CS, thus creating a composite feedstock. Irissou et al. [7.3] employed such a technique to deposit pre-mixed aluminium and Al_2O_3 on steel. However, varying densities of powder particles can cause settling within the powder feeder resulting in inconsistent quantities of ceramic and binder supplied to the nozzle.

The present study aims to overcome the drawbacks associated with these existing approaches using a twin powder feed system (co-deposition) to simultaneously deposit a cermet (or oxide) reinforcing powder with a ductile binder [7.2]. By spraying a binding alloy on the substrate alongside reinforcing particles, the cermet material that would normally rebound from the surface (if deposited alone) is entrapped by the deformed binder particles. The mechanical

interlocking between the binder and reinforcement ensures both materials are retained on the substrate (Chapter 2), resulting in greater quantities of cermet deposited on the substrate.

FSP was subsequently applied to remove the coating-to-substrate interface and disperse the reinforcements homogenously across the stir zone. As-deposited and SprayStirred MMCs were evaluated using light optical and scanning electron microscopy (SEM). The microhardness across the width of the stir zone was measured and compared with the hardness of the as-deposited coatings (CS only) and the as-received material. The erosion performance of the MMC coatings (pre- and post-FSP) was evaluated under erosion slurry conditions and the mechanisms causing the degradation of the coating surface identified through examination of the resulting wear scars. To be clear, within this study four different specimen types are discussed: as-received substrate, as-deposited coating (no FSP), FSPed substrate (no CS) and SprayStirred (CS and FSP).

7.2 Experimental Methods

7.2.1 Materials

Based on the findings from the preliminary study presented in Chapter 6, tungsten carbide (WC-CoCr) powder was co-deposited with AA5083 powder on AA5083 plates. The sprayed section of plate measured approximately 110 x 100 mm. Chromium carbide (Cr_3C_2-NiCr) and aluminium oxide (Al_2O_3) reinforced coatings were also sprayed using the co-deposition approach to compare the slurry erosion performance of the WC-CoCr MMC. Al_2O_3 was included in the study as it provided a low cost alternative to the agglomerated powders and is traditionally difficult to deposit without a suitable binder [7.6]. The properties of the reinforcing particles are presented in Table 7-1. The particle size range was given in the manufacturer's data sheets [7.7, 7.8], and the average carbide size was measured by light optical microscopy. Micrographs of the feedstock powders are presented in Fig. 7-1.

Table 7-1 Feedstock powder properties [7.7, 7.8]

Coating material	Composition (wt.%)	Particle size range (μm)	Average carbide size (μm)
WC-CoCr	W - 10Co - 5.5C - 4.4Cr	15-45	1.07
Cr_3C_2-NiCr	Cr - 20Ni - 9.6C - 0.1Fe	11-45	3.47
Al_2O_3	100Al_2O_3	31-75	N/A

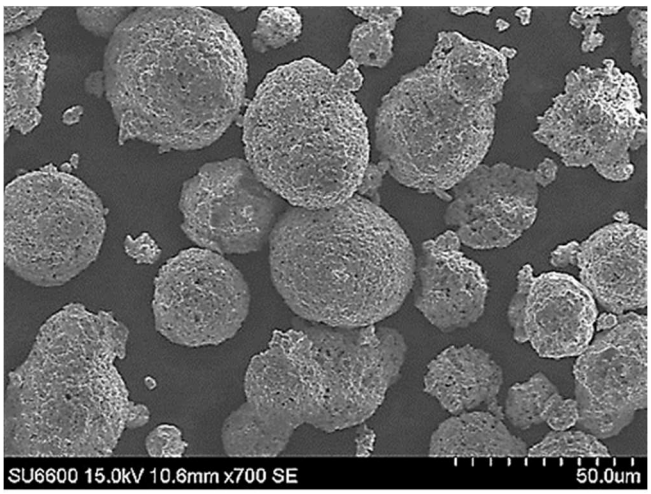

(a)

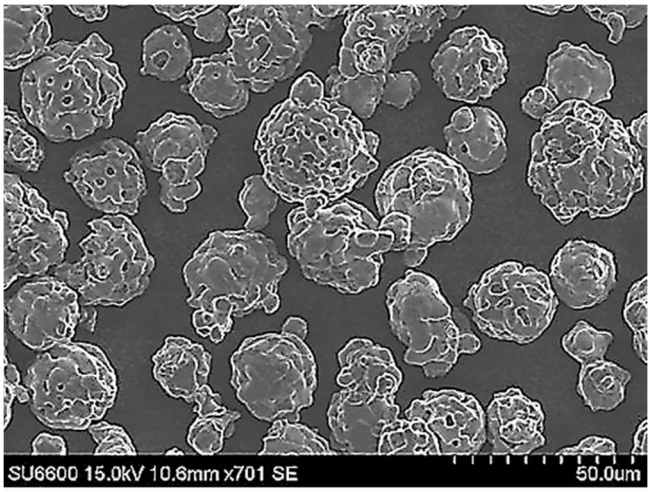

(b)

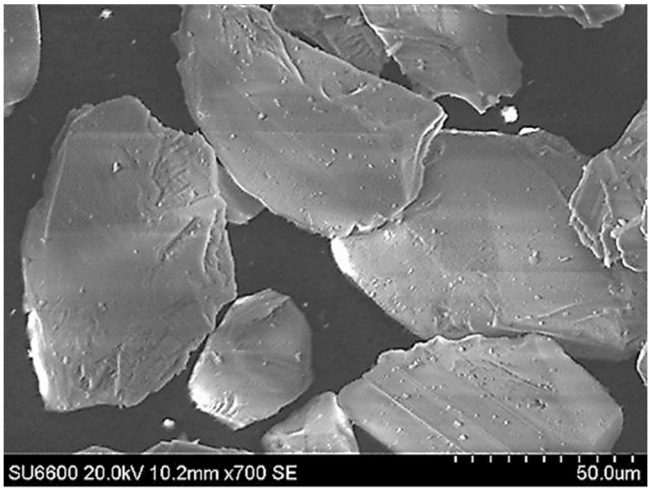

(c)

Fig. 7-1 SEM micrographs of powder particles; a) WC-CoCr; b) Cr_3C_2-NiCr; c) Al_2O_3 [x700]

WC-CoCr and Cr_3C_2-NiCr are agglomerated-sintered powders that comprise hard carbides, retained by a binding alloy (binder) (Fig. 7-1). The WC-CoCr powder particles are spherical and consist of tungsten carbides held together by a cobalt matrix [8]. The addition of chromium decreases the susceptibility to corrosion as demonstrated by Toma et al. [7.9].

The Cr_3C_2-NiCr particles are comparable in size and morphology to WC-CoCr. However, the carbides within the Cr_3C_2-NiCr powder are larger than those contained within the WC-CoCr [7.7, 7.8]. Chromium carbide provides the reinforcing constituent with the nickel-chromium binder retaining the carbides in the observed spheroidal particle profile (Fig. 7-1b). The use of chromium as the reinforcement improves the corrosion resistance over tungsten-based powders, while also increasing the ability of the sprayed coating to withstand greater in-service temperatures [7.7].

Both powders (WC-CoCr and Cr_3C_2-NiCr) are commonly used to enhance the erosion performance of components that are exposed to erosive operating environments, with some existing studies [7.10, 7.11] demonstrating the improved erosion performance of materials that have been coated with WC-CoCr and Cr_3C_2-NiCr.

As indicated in Table 7-1, Al_2O_3 particles are comparably larger and possess no metallic binder, with Fig. 7-1c illustrating the faceted shape of the oxides. The larger Al_2O_3 particles (75.8 µm) have been selected based the reported improved deposition rate when compared with smaller Al_2O_3 particles [7.12]. Post-FSP, the tungsten, chromium and Al_2O_3 grains will be referred to as "*reinforcements*" or "*reinforcing grains*".

7.2.2 Cold spray deposition

The MMC coatings were deposited using a CGT Kinetiks 4000 cold spray system. Two 4000 series powder feeders operating in parallel supplied the AA5083 binder and reinforcement powders simultaneously to the cold spray nozzle. The nozzle design was of a conventional de-Laval shape (Type 24 WC) and accelerated the powders using nitrogen as the process gas. Additional details regarding the CS equipment are presented in Chapter 4.

7.2.3 Co-deposition parameter development

The spraying parameters identified as having the most significant influence on the quality of the deposited coating are gas temperature and pressure, the traverse speed and the nozzle standoff distance [7.13]. An iterative approach was employed

to determine the optimal spray parameters to achieve a dense, well adhered coating. This method involved examining the influence of the identified spraying parameters on the coating microstructure and quantity of material deposited on the substrate. The latter was evaluated by measuring the coating thickness and mass gain following deposition on a series of test coupons. Using the processing parameters outlined in Table 7-2, the three reinforcement powders were independently co-deposited with the AA5083 binder.

Table 7-2 Optimised cold spray deposition parameters

Gas pressure (MPa)	Gas temperature (°C)	Scanning speed (mm/s)	Stand-off distance (mm)
3	500	100	50

The volumetric feed rate for the two powder feeders was calculated based on the total volume of the dosing holes within the conveyor disk of each powder feeder. Through this method, conveyor disk rotational speeds were calculated to deliver a theoretical volume of a compacted powder per unit time, at reinforcement/binder ratios of 30/70, 60/40, and 90/10. Considering that the density of the powders has not been considered, the volumetric feed rate denotes the theoretical volumetric feed rate. In each case, the quantity of reinforcement phase within the deposited layer was examined using optical microscopy to determine the ratio that yielded the highest quantity of reinforcement within each MMC.

Based on the information gathered from this preliminary investigation, a deposition ratio of 60/40 (reinforcement to binder) for the WC-CoCr, Cr_3C_2-NiCr and Al_2O_3 powders was selected for this study. This ratio resulted in a coating thickness measuring 0.38 – 0.44 mm following the deposition of three layers (3 passes of the cold spray gun). Interestingly, co-deposition of the Cr_3C_2-NiCr resulted in a coating thickness approximately 0.2 mm greater than that of WC-CoCr and Al_2O_3. Consequently, only two passes of Cr_3C_2-NiCr were necessary to achieve a similar coating thickness. The likely reason for this enhanced deposition efficiency is explored in Section 7.3.1.

7.2.4 Development of FSP process parameters

FSP of the various test specimens was carried out by a TTI precision spindle friction stir welding/processing machine as discussed in Chapter 4. The FSP tool employed in the present study was based on a modified friction stir welding (FSW)

tool, manufactured from H13 tool steel. The findings from Chapter 6 indicate that, although a pin is necessary to improve material flow within the stir zone, an excessively long pin forces reinforcing material from the surface and near-surface region down to the root for the stir zone. Consequently, the 5 mm pin in the original FSW tool was shortened to 2 mm. The pin was threaded and the tool featured a concave shoulder (Fig. 7-2).

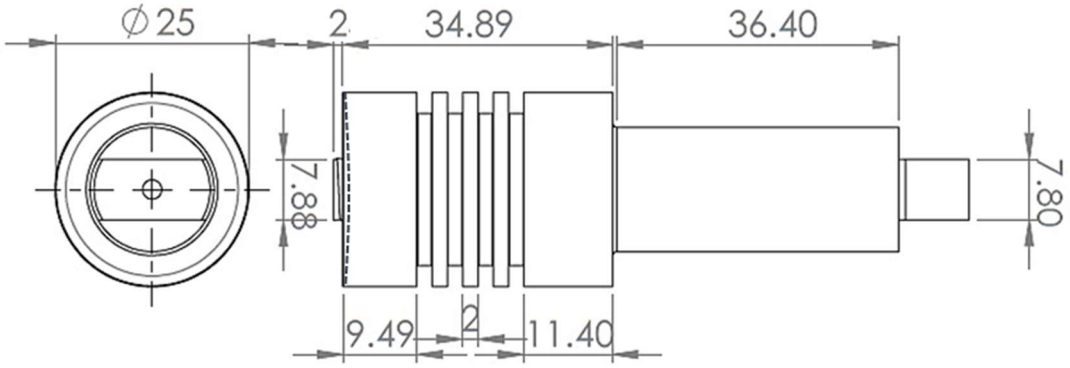

Fig. 7-2 Basic dimensions of the H13 FSP tool

Suitable machine parameters were established for the uncoated AA5083 substrate through an iterative parameter development investigation examining the effect of tool traverse and rotational speed, and plunge depth on the quality of the stir zone. For this investigation (Chapter 7), the tool design and tilt angle were kept constant. The processing parameters that resulted in a high quality stir zone are presented in Table 7-3. For this study, a high quality stir zone was one that exhibited no visible surface voids and minimal quantities of flash [7.14].

Table 7-3 FSP parameters

Rotation speed (RPM)	Traverse speed (mm/min)	Plunge depth (mm)	Tilt angle (°)
600	272	3.8	3

Once suitable parameters were established (Table 7-3), CS coated plates were secured to the machine bed. The tool (Fig. 7-2) was plunged into an uncoated section of the aluminium plate to a depth of 3.8 mm (measured from the tip of the pin) and allowed to stabilise. Moving along a straight path, the tool was traversed from the uncoated aluminium on to the coated section where it continued for a total distance of 100 mm. Upon completion of the traverse, the tool was retracted from the workpiece. The 3° tilt angle was necessary to prevent chipping of the MMC coating as the tool traversed.

7.2.5 Characterisation of the as-deposited and SprayStirred MMCs

Transverse cross-sections of the stir zone were cut from the FSPed plate to examine the microstructure of the as-deposited coating and the microstructure of the stir zone post-FSP. Fig. 7-3 presents a macrograph of a processed plate and indicates the approximate location from which the cross-sections were cut. The image (Fig. 7-3) also highlights the lack of any flash or voids on the surface of the processed material.

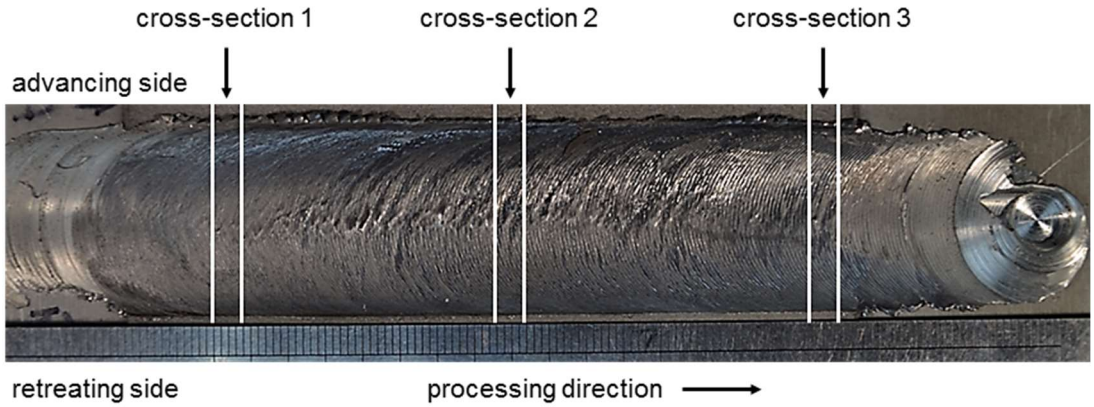

Fig. 7-3 Optical macrograph of the plate post-FSP

A precision cutting wheel (Accutom 5) was used to section the specimens to prevent any cutting damage to the MMC layer. The surface was prepared to a 0.05 μm finish using the standard metallographic preparation techniques discussed in Chapter 4. A macrograph showing a cross-section view of a typical SprayStirred specimen is displayed in Fig. 7-4 depicting the various regions within the stir zone that are discussed throughout this chapter. The pin region denotes the area of the stir zone through which the tool pin traversed.

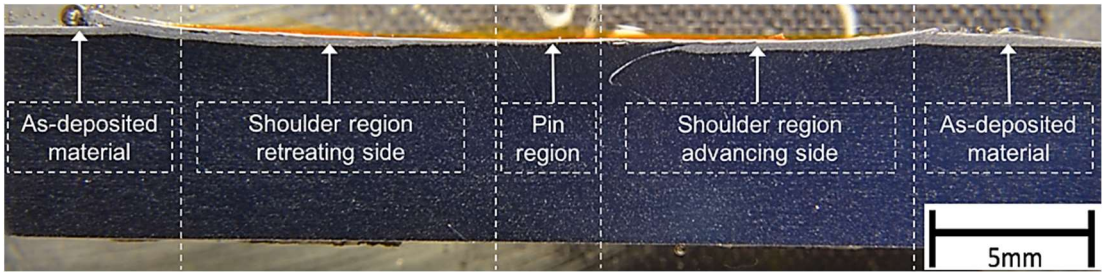

Fig. 7-4 Macroscopic cross section of SprayStirred MMC layer.

The microstructure of the specimens pre- and post- FSP was examined using an Olympus G51X light optical microscope. The distribution of the reinforcements within the MMC was characterised by energy dispersive spectroscopy (EDS), using a Hitachi S-3700 series scanning electron microscope (SEM). EDS using Oxford

Instruments INCA software mapped the positions of the constituent elements and highlighted the distribution of reinforcements throughout the AA5083 matrix. Image analysis software was used to quantify the reinforcing particle content for each MMC before and after FSP (Section 7.3.4). Three micrographs were examined for each specimen to determine the average reinforcing particle content.

Microhardness values were measured across the width of the stir zone and in the as-deposited MMCs. The results were collected using a Mitutoyo MVK-G1 micro-hardness tester with an applied load of 100 gf. The reported hardness of each region is an average of five measurements. The data was analysed to determine the change in average hardness following the application of FSP, as well as the average hardness in the regions depicted in Fig. 7-4.

7.2.6 Experimental analysis of the slurry erosion performance

As discussed in Chapter 4, a closed loop jet impingement rig was used to evaluate the slurry erosion performance of the various test specimens. The dimensions of the test specimens and the specific test parameters used throughout the experimental programme are listed in Table 5-4. The surface of the specimens was lightly abraded with 500-grit SiC paper before testing to produce a uniform surface finish. The specimens were positioned directly beneath the nozzle while fully submerged in the slurry solution. The angle at which with slurry impinged the specimen was 90°.

Table 7-4 Liquid impingement test parameters

Flow velocity (m/s)	Sand concentration (g/l)	Nozzle standoff distance (mm)	Nozzle exit diameter (mm)	Sample diameter (mm)	Test duration (minutes)
22	0.4	20	3	20	20

Three test replicates for each SprayStirred MMC were evaluated to establish the average mass loss. Furthermore, the erosion performance of the as-received AA5083 and as-deposited coatings were assessed to provide a benchmark against which to measure the SprayStirred specimens. Specimens were weighed pre- and post-testing to using a mass balance (accuracy 0.1 mg) to establish the total mass loss.

The measurement of the wear scar was facilitated by a focal variation microscope (Alicona Infinite Focus G4) [7.15]. The wear scar was divided into two distinct regions (impinged and turbulent) corresponding to the different slurry flow

characteristics. The impinged zone is classified as the surface area directly beneath the 3 mm jet nozzle. The volume loss from the entire wear scar and the impinged zone was measured using the Alicona system. The difference between these two values represents the volume loss from the turbulent zone. Subsequent SEM analysis of the wear scar surface was conducted to identify the underlying erosion mechanisms leading to the breakdown of the MMC surface.

7.3 Results and Discussion

7.3.1 Light optical microscopy

The MMCs were examined in the pre- and post-FSP condition to characterise the influence of FSP on the microstructure. Fig. 7-5 presents the approximate location within the CS coated (Fig. 7-5a) and SprayStirred (Fig. 7-5b) specimens from which the micrographs in Fig. 7-6 were captured.

Examination of the as-deposited WC-CoCr coating (Fig. 7-6a) revealed no evidence of defects within the MMC, such as cracking or voids. The lack of any such defects (Fig. 7-6a) is attributed to the deformation experienced by the binder particles (AA5083) at the point of impact [7.16]. However, Fig. 7-6a depicts agglomerates of WC-CoCr particles within the co-deposited material. Consequently, this yields areas within the coating that are void of any reinforcements. Quantitative image analysis of the micrographs revealed that the coating comprises approximately 56% (vol.%) WC-CoCr and 44% binder.

Fig. 7-6b illustrates the WC-CoCr reinforced MMC in the SprayStirred condition. The image (Fig. 7-6b) shows that the as-deposited WC-CoCr agglomerates (Fig. 7-6a) have been refined and redistributed. Further, the areas of unreinforced matrix observed in the co-deposited coating (Fig. 7-6a), have been removed through the application of FSP.

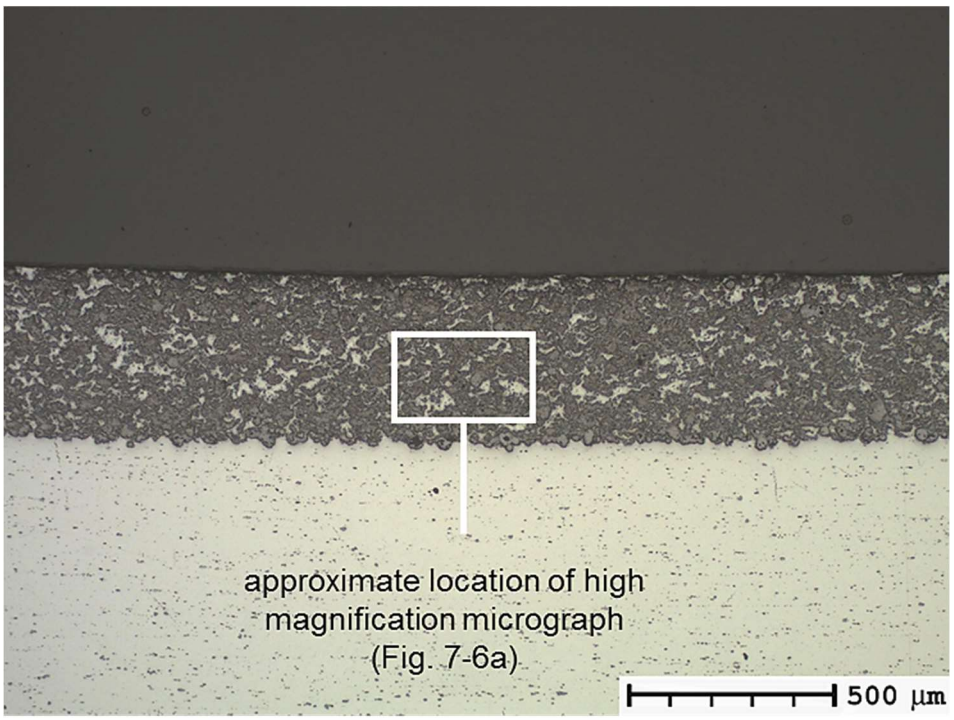

(a)

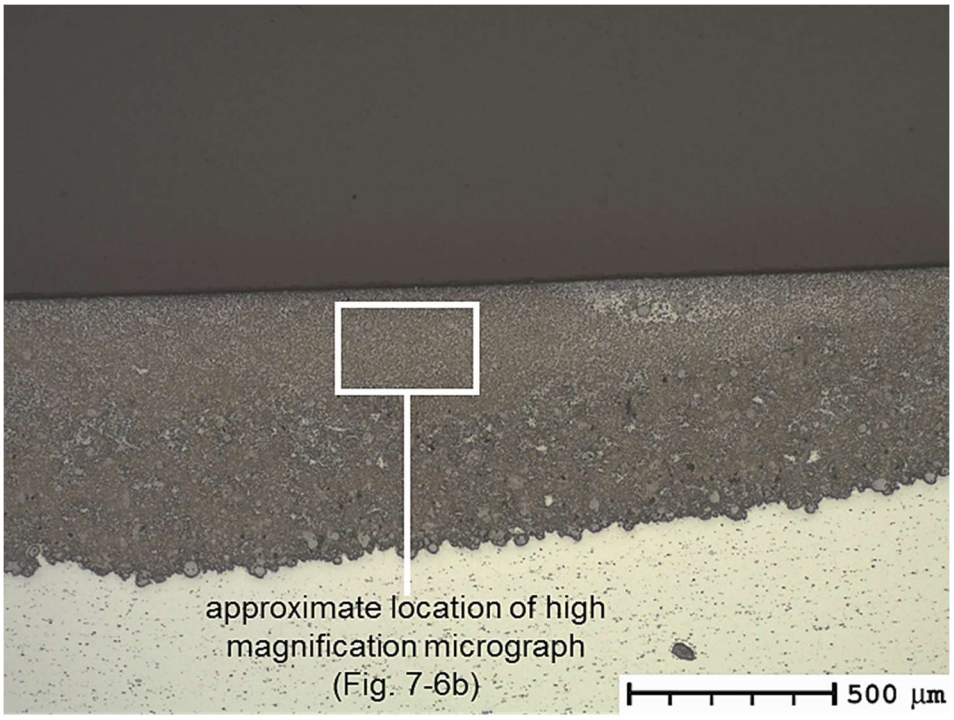

(b)

Fig. 7-5 Optical micrographs highlighting the approximate location of images shown in Fig. 7-6b; (a) as-deposited cold spray coating; (b) SprayStirred layer [x50, Unetched]

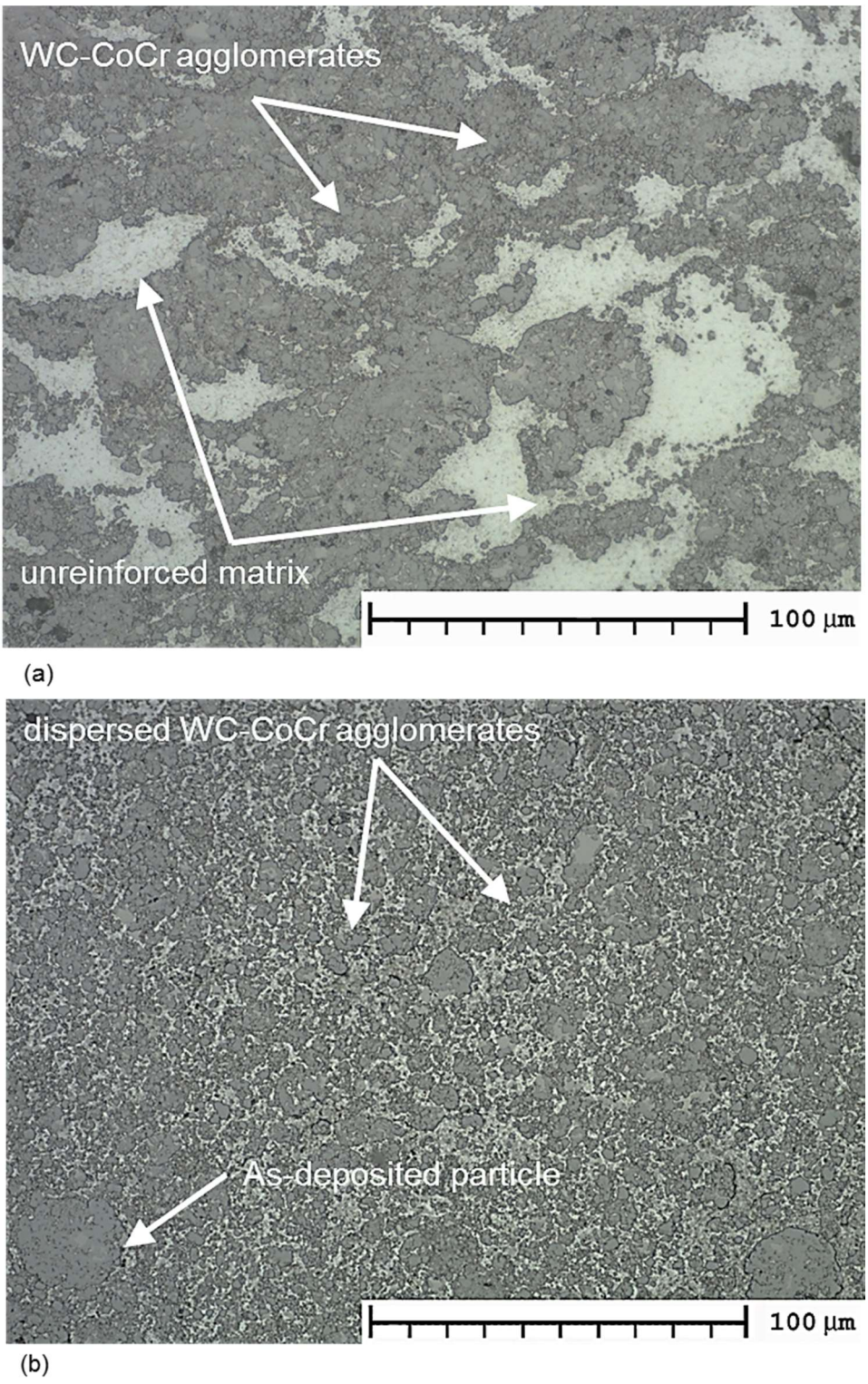

Fig. 7-6 Light optical micrographs of; (a) as-deposited WC-CoCr; (b) SprayStirred WC-CoCr [x500, Unetched]

Image analysis of the Cr_3C_2-NiCr reinforced coating (Fig. 7-7a) measured approximately 48% cermet material within the MMC. The corresponding increase in binder (52%) provides a probable explanation for the increase in coating thickness over WC-CoCr and Al_2O_3 reinforced coatings, as discussed in Section 7.2.3. Similarly, Couto et al. [7.2] reported increased deposition efficiency when greater quantities of ductile binder were CS deposited on the surface of Al-7075.

The reduction in particle agglomeration when compared with the WC-CoCr coating (Fig. 7-6a) is attributed to the larger size of the carbides grains within the Cr_3C_2-NiCr particle. Specifically, the presence of larger carbides reduces the deformation that the Cr_3C_2-NiCr particle can undergo and hence limits its ability to coalesce with the adjoining particles. Post-FSP, the reinforcements within the Cr_3C_2-NiCr MMC (Fig. 7-7b) have been refined and distributed throughout the AA5083 matrix.

The as-deposited Al_2O_3 coating (Fig. 7-8a) comprises approximately 60% binder to 40% oxide particles. Post-FSP, the large Al_2O_3 particles observed in Fig. 7-8b have been refined and dispersed throughout the matrix by the rotating motion of the FSP tool. Therefore, FSP has resulted in a more homogenous distribution of reinforcements when compared to the as-deposited coating (Fig. 7-8a).

For each of the examined MMCs, the refinement observed in the post-FSP condition is attributed to the shear forces that are exerted by the tool as it stirs the plasticised material [7.17, 7.18]. During FSP, the agglomerates are deformed beyond the elastic limit of the binder alloy resulting in the dispersal of the individual carbides (or oxides) throughout the matrix. Nevertheless, some particles approximately 20 μm in diameter can be seen in the micrograph (Fig. 7-6b), thereby indicating that some of the as-deposited material has not been refined by FSP. In existing studies [7.19, 7.20], the extent to which reinforcements are refined increases with the number of FSP passes. Therefore, it is expected that additional FSP passes through the MMC could refine any of the remaining of the as-deposited reinforcing particles.

Fig. 7-7b shows increased particle refinement along the top of the image and corresponded to the region within the stir zone exposed to the greatest temperatures and forces from the tool shoulder [7.13]. This phenomenon is also apparent in WC-CoCr and Al_2O_3 coatings, with both depicting a greater level of refinement towards the top surface. This feature is highlighted in Fig. 7-9.

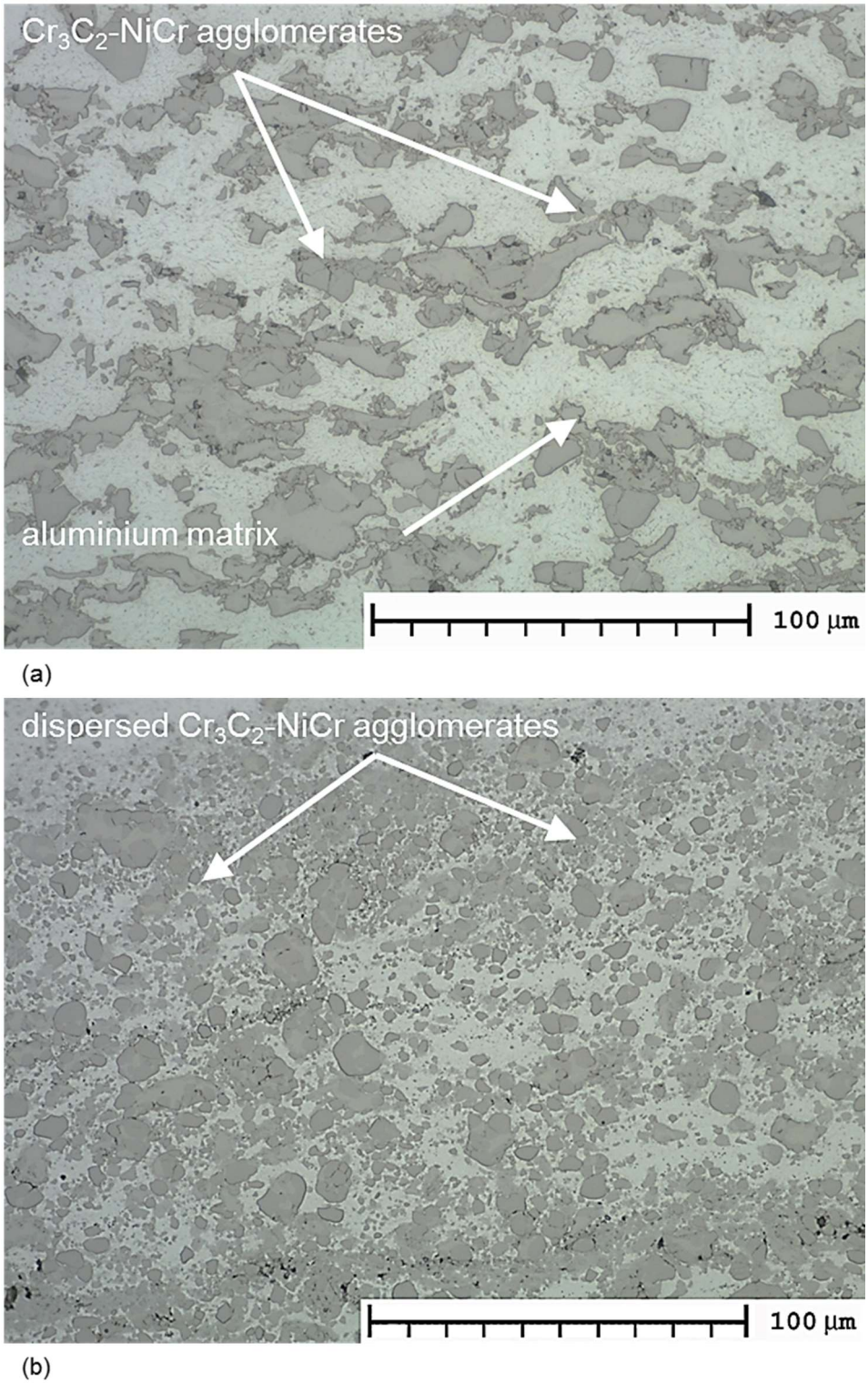

Fig. 7-7 Light optical micrographs of; a) as-deposited Cr_3C_2-NiCr; b) SprayStirred Cr_3C_2-NiCr [x500, Unetched]

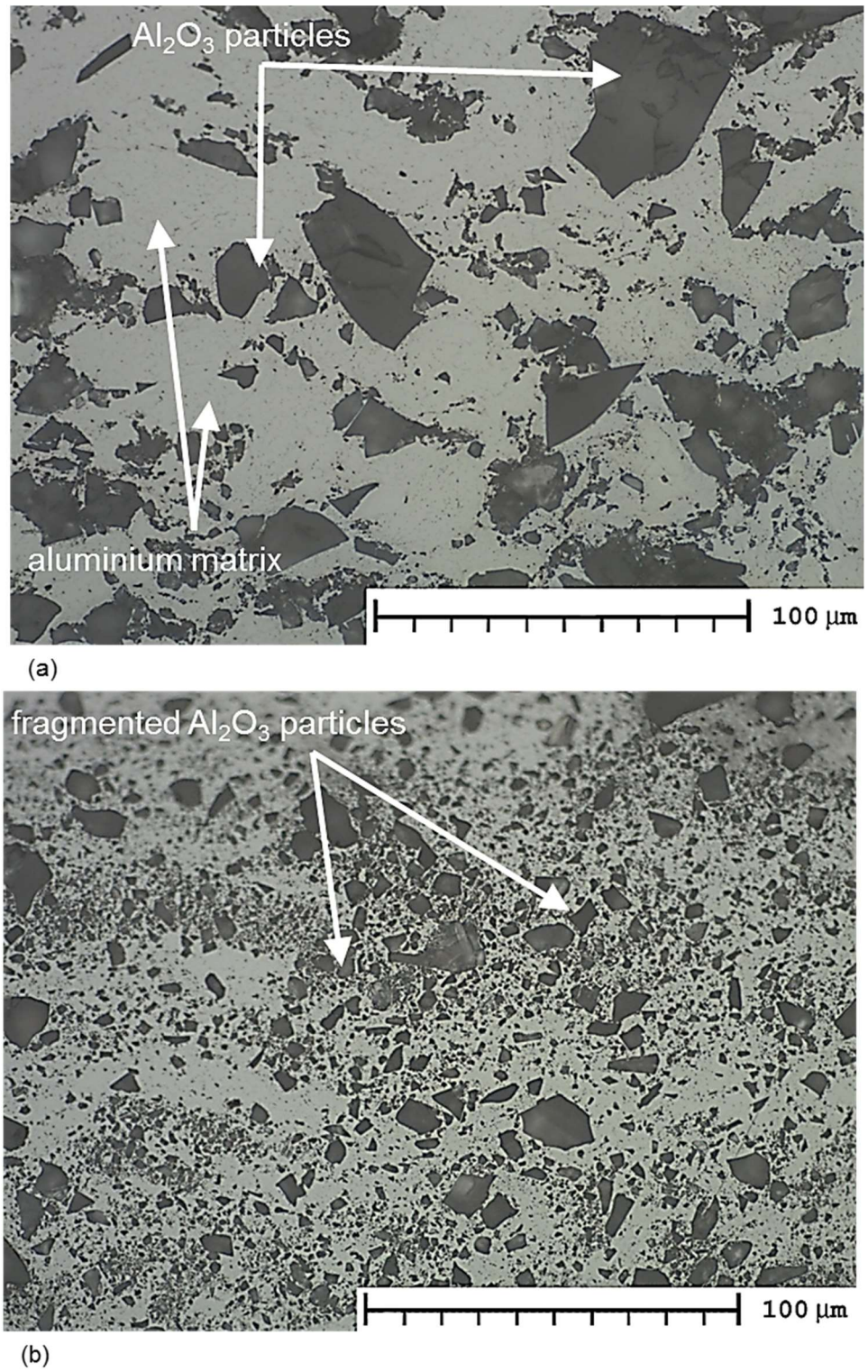

Fig. 7-8 Light optical micrographs of; a) as-deposited Al_2O_3; b) SprayStirred Al_2O_3 [x500, Unetched]

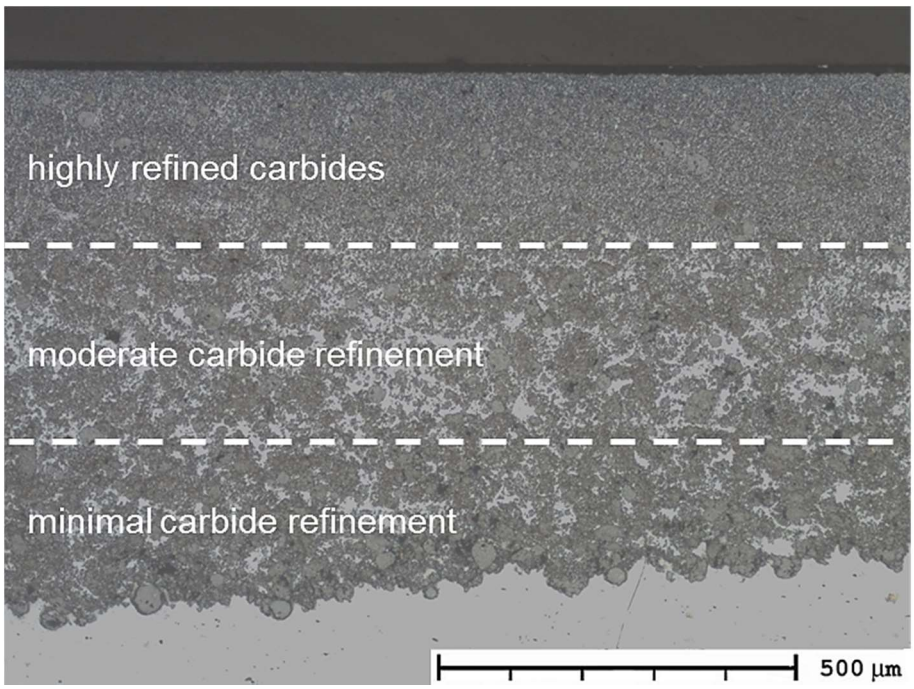

Fig. 7-9 Variation in particle refinement through the depth of the SprayStirred MMC [x100, Unetched]

The micrographs presented in Fig. 7-6, Fig. 7-7 and Fig. 7-8 exhibit a dense MMC layer with the minimal observed porosity attributed to pull-out during the metallographic preparation process [7.21]. This porosity was measured in accordance with ASTM E2109 – 01 [7.22] with the results indicating an area percentage porosity less than 0.5%. As mentioned in the standard [7.22], a value less than 0.5% should be considered zero when calculating the average area percentage of porosity. Hence, the SprayStirred layers can be considered dense. The density of the microstructures depicted in Fig. 7-6, Fig. 7-7 and Fig. 7-8 is attributed to the significant deformation of co-deposited metallic binder particles as they impinge on the substrate surface [7.2, 7.23].

7.3.2 Scanning electron microscopy (SEM)

The as-deposited and SprayStirred MMCs were also examined by SEM to characterise the microstructure at the interface between reinforcement and binder (in the case of the WC-CoCr and Cr_3C_2-NiCr). Moreover, EDS was used to verify several of features highlighted through optical microscopy and map the position of the reinforcements in the as-deposited and post-FSP conditions.

Fig. 7-10a depicts an EDS map of the as-deposited WC-CoCr coating and Fig. 7-10b is an optical micrograph of a corresponding region at identical magnification.

The locations of tungsten and cobalt align with the dark regions shown in the optical micrograph (Fig. 7-10b).

Fig. 7-11 highlights the correlation between dark regions and reinforcing chromium/nickel elements in the Cr_3C_2-NiCr reinforced MMC. Thus, it can be surmised that the dark regions in the optical micrographs depict the locations of the reinforcements, as opposed to pull-out or contamination. Fig. 7-10a also illustrates the agglomeration of reinforcing particles within the matrix. It was not possible to generate an EDS elemental map of the Al_2O_3 reinforced coating due to both matrix and reinforcing particle being comprised of aluminium.

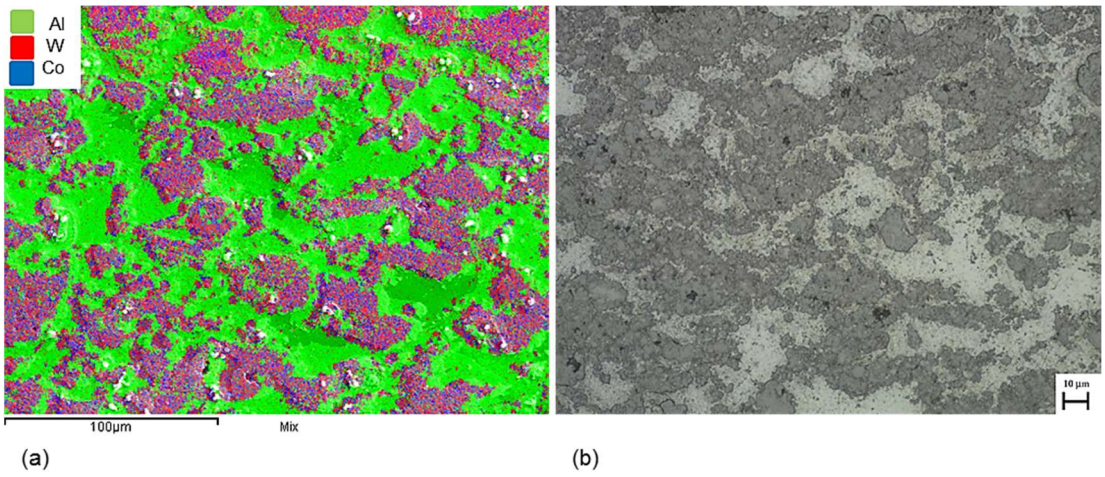

Fig. 7-10 (a) EDS element map of the as-deposited WC-CoCr reinforced coating; (b) light optical micrograph of a comparable region in the WC-CoCr coating [x500]

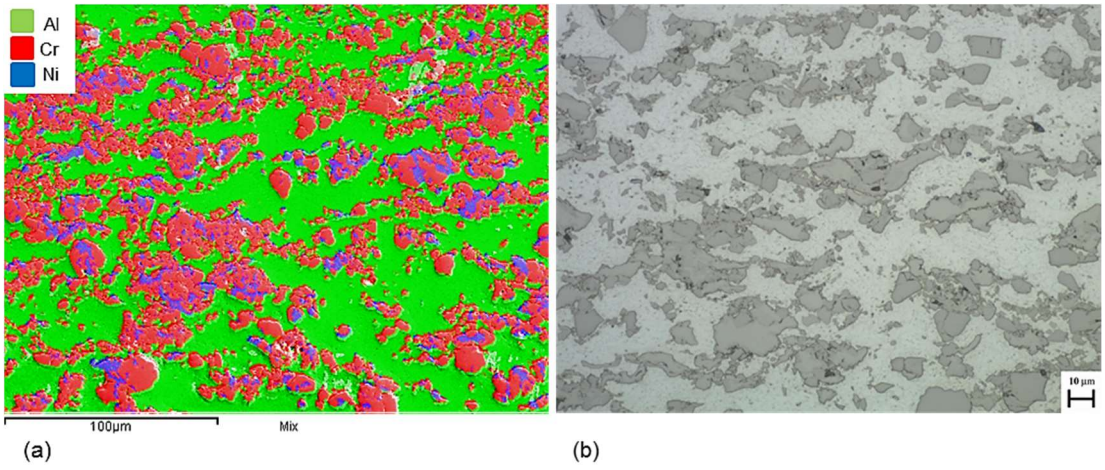

Fig. 7-11 (a) EDS element map of the as-deposited Cr_3C_2-NiCr reinforced coating; (b) light optical micrograph of a comparable region in the Cr_3C_2-NiCr coating [x500]

The SEM micrograph, shown in Fig. 7-12a, demonstrates that the morphology of the WC-CoCr particles has been altered following impact with the surface of the substrate. This is attributed to the deformation of particles upon contact with the substrate and the inability of the cobalt to retain the pre-deposition structure of the WC-CoCr particles. The breakdown of feedstock particles aids the distribution of tungsten carbides throughout the MMC and is therefore deemed to be beneficial in relation to the mechanical (and tribological) properties of the MMC [7.24].

The Cr_3C_2-NiCr has retained more of the original pre-deposition morphology with chromium carbides still surrounded by nickel binder (Fig. 7-12b). This indicates that the Cr_3C_2-NiCr particles possess enhanced ductility due to the increased binder content (Table 7-2), which results in more significant deformation before alteration of the feedstock powder morphology occurs. The location of the constituent elements within the SEM micrographs (Fig. 7-12) was illustrated by EDS mapping, with the resulting element maps presented in Fig. 7-13.

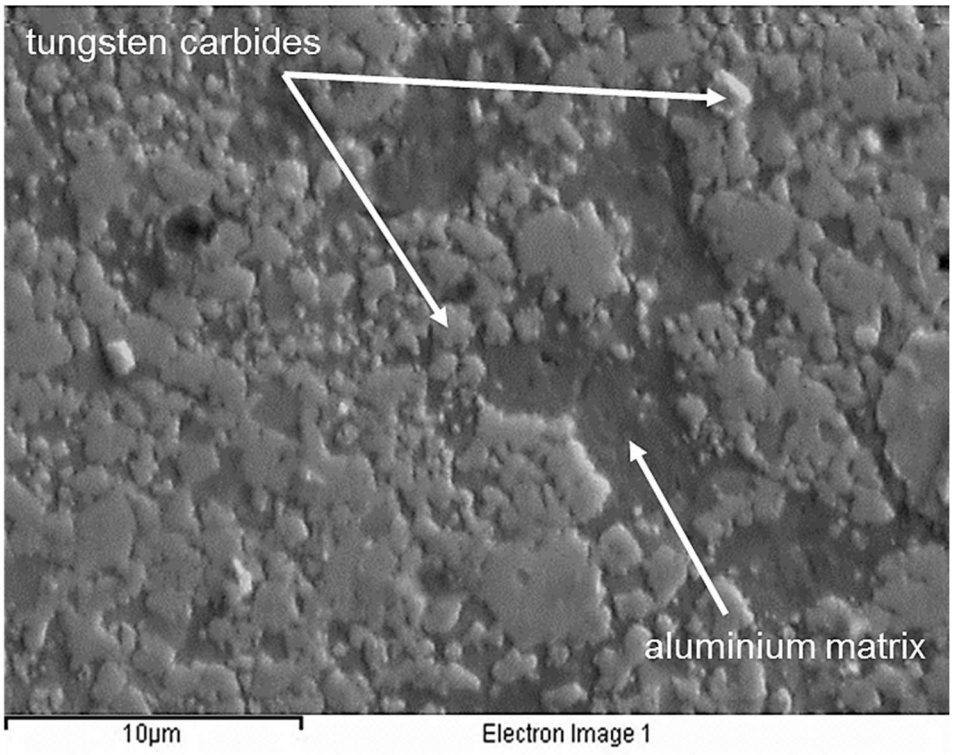

(a)

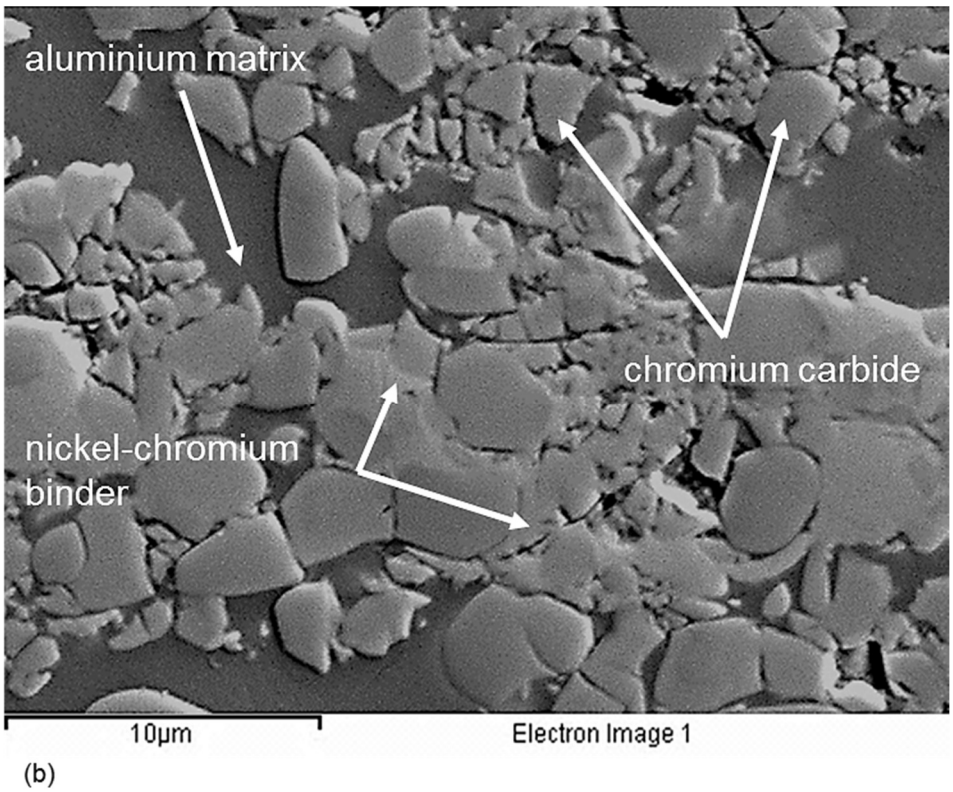

Fig. 7-12 Scanning electron micrographs showing the dispersal of carbides within the aluminium matrix; (a) WC-CoCr; (b) Cr_3C_2-NiCr [x4000]

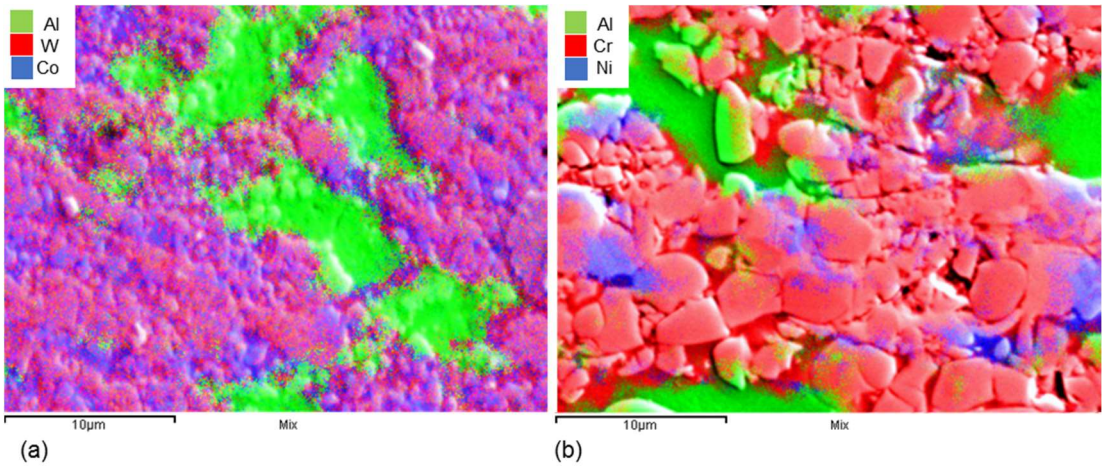

Fig. 7-13 EDS element map showing the distribution of reinforcements within the aluminium matrix; (a) as-deposited WC-CoCr reinforced coating; (b) as-deposited Cr_3C_2-NiCr reinforced coating [x4000]

The particle distribution pre- and post-FSP for the WC-CoCr and Cr_3C_2-NiCr reinforced MMCs is exhibited in the EDS maps depicted in Fig. 7-14, with the corresponding wt.% of the elements presented in Table 7-5. By highlighting the

various elements within the MMC, the distribution of the reinforcements can be observed and hence, the level of refinement achieved by FSP is illustrated.

The values contained in Table 7-5 reveal a drop in the quantity of reinforcement on the advancing side of the stir zone. This is accompanied by a corresponding rise in the quantity of reinforcement on the retreating side, which attributed to the asymmetry within the stir zone during FSP [25]. Under a variety of processing conditions (traverse and rotational speed), Albakari et al. [7.25] discovered that the temperature within the stir zone was elevated on the advancing side of the stir zone. Consequently, the material flow on this side (advancing) was more significant when compared with the retreating side [7.25]. Given this variation in material flow, it follows that any particles embedded within the plasticised material would also exhibit asymmetry between the advancing and retreating sides. Therefore, the variation in reinforcement quantity (wt.%) between the advancing and retreating sides (Table 7-5) is attributed to the asymmetry within the stir zone [7.25].

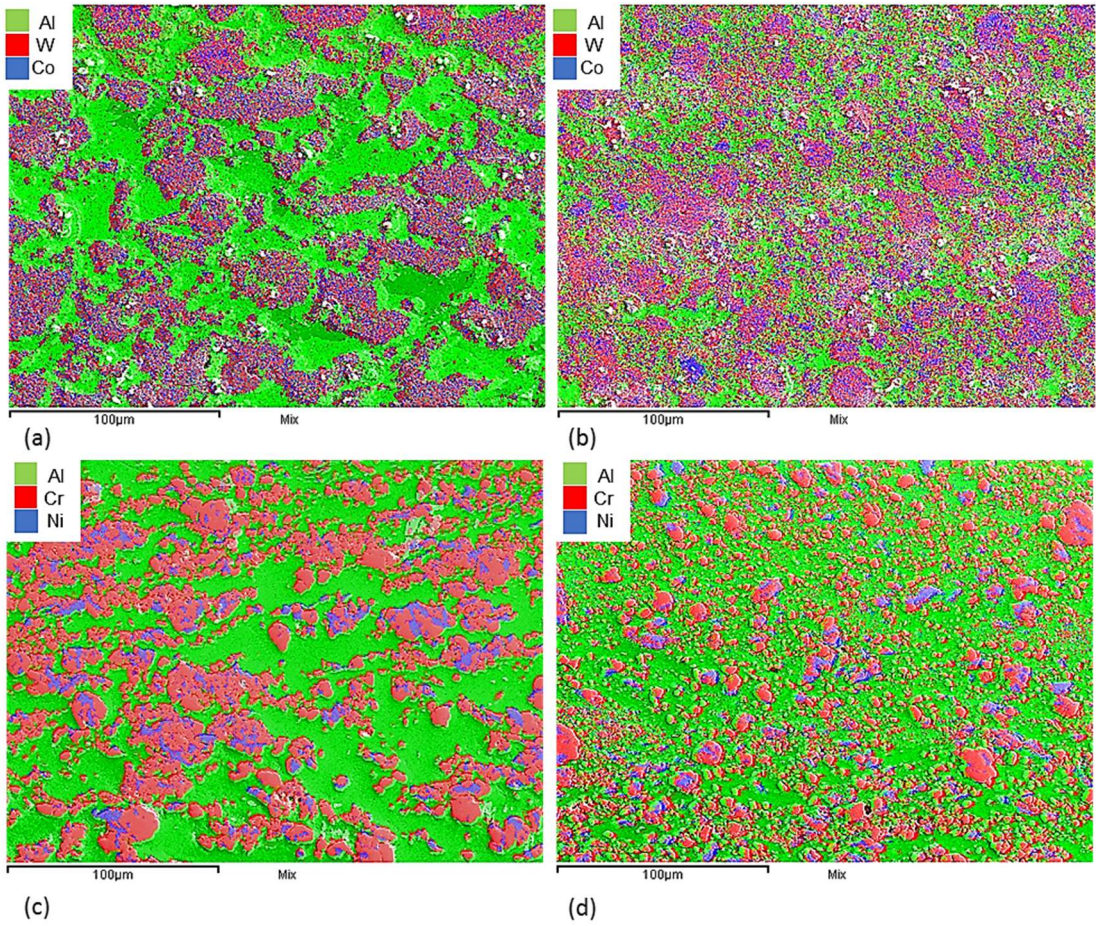

Fig. 7-14 EDS element maps showing reinforcements within; (a) As-deposited WC-CoCr; (b) SprayStirred WC-CoCr; (c) As-deposited Cr_3C_2-NiCr; (d) SprayStirred Cr_3C_2-NiCr [x500]

Table 7-5 EDS elemental analysis (wt.%)

		Mg	Al	Cr	Ni	Co	W	O
As-deposited	WC-CoCr	1.51	32.22	2.54		5.54	58.19	
	Cr_3C_2-NiCr	2.06	39.52	42.92	15.51			
	Al_2O_3	2.60	86.06					11.35
SprayStirred (Retreating)	WC-CoCr	0.83	19.35	3.29		7.68	68.85	
	Cr_3C_2-NiCr	2.09	39.82	41.85	16.23			
	Al_2O_3	2.56	86.48					10.96
SprayStirred (Advancing)	WC-CoCr	1.54	33.79	2.78		5.95	55.95	
	Cr_3C_2-NiCr	2.23	49.51	36.34	11.92			
	Al_2O_3	2.84	90.4					6.67

7.3.3 Microhardness

Fig. 7-15 presents the microhardness distribution across the width of the stir zone (Fig. 7-4) and the average microhardness of the AA5083 substrate (pre- and post-FSP).

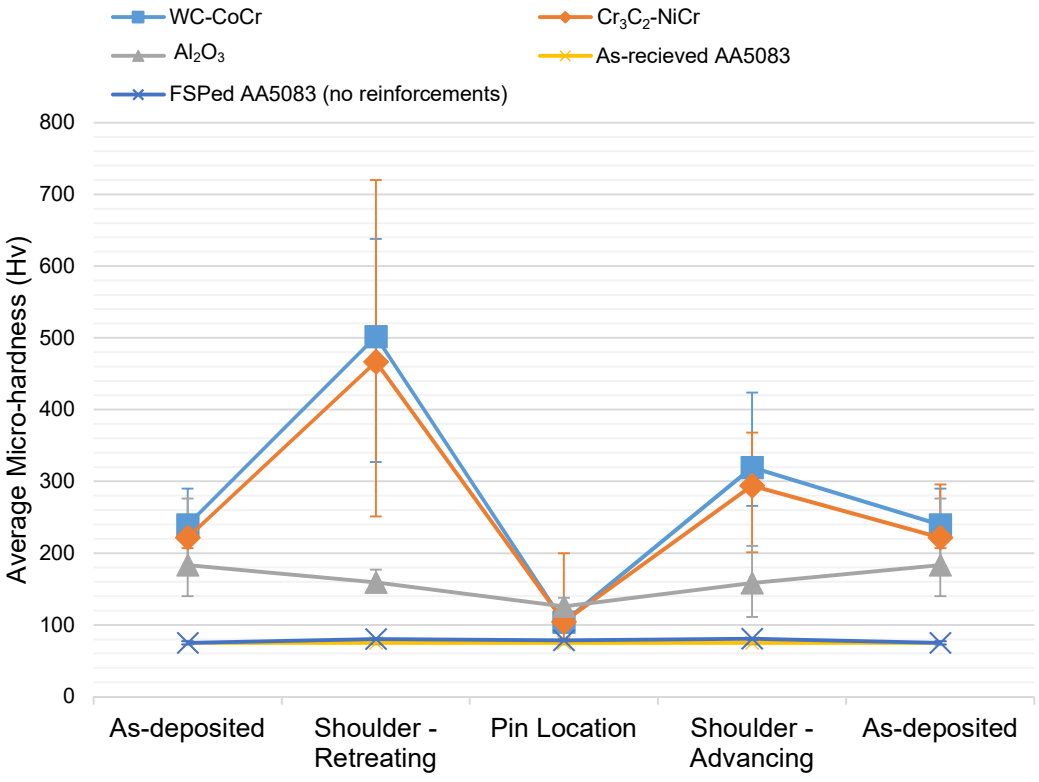

Fig. 7-15 Microhardness measurements from various locations within the stir zone and from the as-received and FSPed AA5083

The results (Fig. 7-15) show that FSP has little effect on the average hardness of the as-received substrate (no reinforcing particles). This outcome is unexpected considering that one of the most widely accepted benefits of FSP is increased hardness within the stir zone [7.26–7.30]; which is typically attributed to grain refinement. For example, Yadav et al. [7.29] measured a 96% reduction in grain size post-FSP (84 μm to 3 μm), corresponding to a 34% increase in hardness over the as-received material. Considering that FSPed AA5083 (with no reinforcements) contradicts the widely accepted understanding that the refined grain structure generated by FSP yields a corresponding hardness increase, it is appropriate to propose a mechanism that explains this outcome.

It is generally known that there are three principal strengthening (hardening) mechanisms that operate within aluminium (and other) alloys [7.31–7.34]; solid solution strengthening, precipitation strengthening and grain boundary strengthening. A fourth mechanism; strain hardening (or cold working), can also be applied to enhance the hardness of metals through plastic deformation processes such as cold rolling. Cold working causes a build-up of dislocations within the grains which inhibits further dislocation motion [7.34].

Within solid solution strengthened alloys (such as AA5083), selected quantities of alloying elements (often referred to as impurities) are added to the aluminium [7.33]. These elements occupy substitutional or interstitial positions within the crystal lattice which impedes dislocation movement when an external load (force) is applied [7.34]. When the temperature of AA5083 is increased above its solubility temperature (approximately 230°C for 4.4 wt.% Mg), magnesium atoms dissolve in the aluminium crystal structure forming a single solid solution. These magnesium atoms remain locked in the single phase when the temperature is lowered [7.34]. The difference in atomic radii between the aluminium and magnesium atoms resists dislocation movement through the grains, thereby increasing the hardness of the alloy [7.33, 7.34]. If too much of the alloying element is added, the solubility limit may be exceeded. Under these conditions, the third strengthening mechanism becomes prevalent – precipitation strengthening (hardening) [7.33].

Precipitation hardening (or age hardening), is when the hardness of the alloy is increased through the addition of small and uniformly distributed second-phase particles (precipitates) within the matrix [7.34]. The purpose of these precipitates is to act as obstacles to dislocation movement, thereby reducing the plasticity of the material (and increasing the hardness) [7.34]. Precipitates are much larger than the

individual atoms utilised in solid solution strengthening and are, in fact, more akin to particle reinforced MMCs.

Nevertheless, the findings of Sato et al. [7.35] indicate that the hardness of precipitation strengthened aluminium alloys (6xxx, 2xxx and 7xxx series) reduced following friction stir welding (FSW). In their study [7.35], the hardness within the stir zone was influenced by the distribution of the precipitates (magnesium and silicon in the case of 6xxx grade aluminium), as opposed to the size of the individual grains. The authors [7.35] attributed the softening to coarsening of these precipitates during the elevated temperatures of, in their case, FSW. Although FSP is not identical to FSW, both are based on the same fundamental theory (as discussed in Chapter 2). Despite not having directly measured the size of the precipitates at the time, the findings presented by Sato et al. [7.35] offer an explanation for the softening measured in the 6xxx and 2xxx grade alloys discussed in Chapter 6.

Grain boundary strengthening is the third mechanism to influence the hardness of alloys; whereby the grain boundaries act as barriers to dislocation movement [34]. As with the previously mentioned strengthening (hardening) mechanisms, these barriers reduce the plasticity of the material thereby increasing its hardness. More grain boundaries (i.e. smaller grains) yield a greater number of dislocation barriers, resulting in a harder alloy; this correlation is often referred to as the Hall-Petch relationship [7.14, 7.33].

Curiously, the hardness of some materials is more closely controlled by grain size than others. For example, many steel alloys exhibit a strong correlation between measured grain size and hardness, i.e. a significant reduction in grain size constitutes a considerable increase in the hardness. For example, Grewal et al. [7.36] measured a 155% (2.6 times) hardness increase in hydroturbine steel (13Cr4Ni) when the grain size was reduced from approximately 25 μm to between 2.6 and 4 μm, by FSP.

Conversely, Sato et al. [7.35] established that, for AA5083-O, grain size reduction from 18 μm to 4.3 μm resulted in a hardness increase of only 4.5 HV. Additionally, Chen et al. [7.37] reported a decrease in the hardness of AA5083 from approximately 90 HV to 84 HV, following a single FSP pass, despite the grain size within the stir zone reducing to 1.88 μm. While the authors [7.37] do not state the grain size of the as-received AA5083, examination of the micrographs included in their article clearly illustrates considerable grain refinement in the stir zone (as shown in Fig. 7-16). The authors [7.37] relate the lack of hardness increase to *“annealing*

softening and recrystallisation", whereby FSP has removed the strain hardening imparted into the alloy by the cold-rolling process.

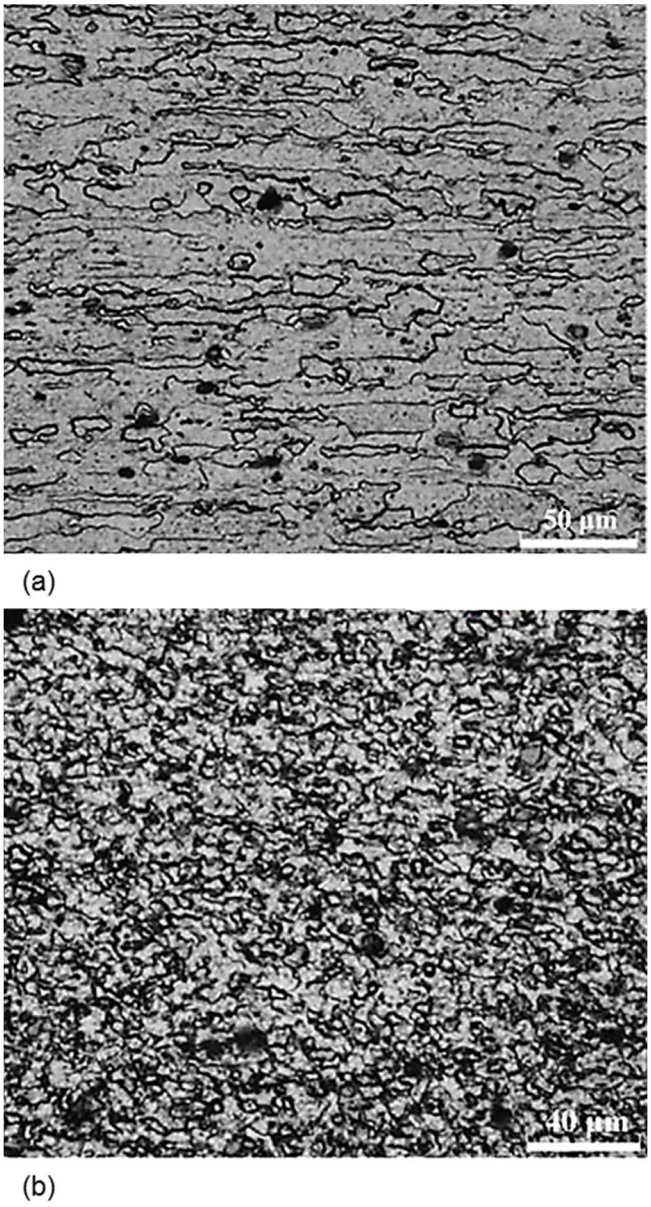

Fig. 7-16 Optical micrographs highlighting the reduction in grain size post-FSP; (a) as-received AA5083; (b) AA5083 post-FSP (adapted from [7.37])

To explain the lack of any hardness increase in the recorded measurements (Fig. 7-15), optical micrographs of the unreinforced AA5083 pre- and post-FSP were etched to highlight the variation in grain structure between the two conditions. Fig. 7-17a shows the grain structure of the as-received AA5083 (pre-FSP). The image (Fig. 7-17a) exhibits directionality within the microstructure which is indicative of cold rolling [7.32]. Existing research [7.38] reports the hardness AA5083 in the cold rolled

(15% reduction) condition as 88 HV. The same report measured the hardness of the as-received AA5083 (no cold rolling) as approximately 78 HV [7.38]. Therefore, the strain hardening [7.32] imparted by the cold rolling process increased the hardness of AA5083 by approximately 10 HV. Fig. 7-17b presents the microstructure of the unreinforced AA5083 post-FSP. The grain structure within FSPed specimen (Fig. 7-17b), does not exhibit the same elongated structure and as the as-received plate (Fig. 7-17a) and, instead, depicts that of strain relieved aluminium [7.32].

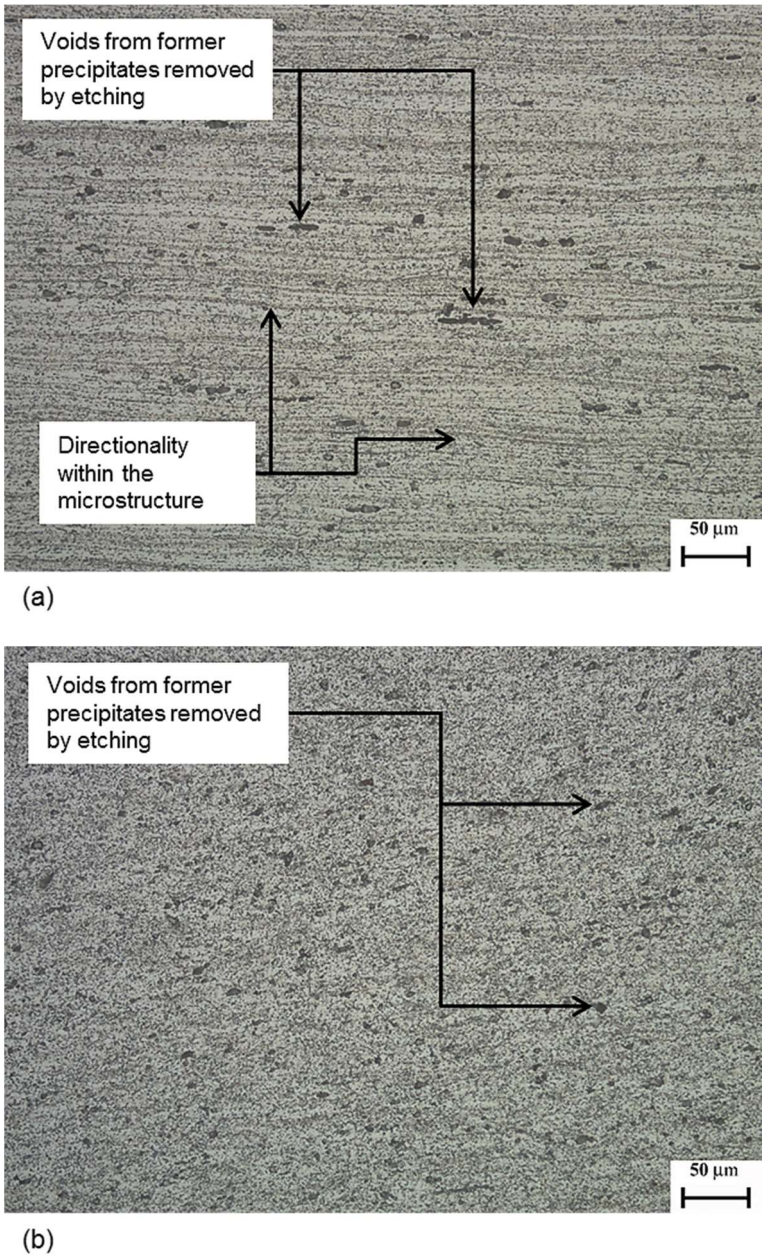

Fig. 7-17 Light optical micrographs depicting the microstructure of; (a) as-received AA50830 rolled plate; (b) stir zone of the unreinforced AA5083 (post-FSP) [x200, Etched using Keller's reagent]

As expected, the grain size within the stir zone has reduced considerably when compared with the as-received alloy (Fig. 7-18). Due to the small size of the grains within the stir zone (Fig. 7-18b), it was not possible to discern the grains boundaries and, hence, measure the drop in grain size in accordance with ASTM E112-13 [7.39].

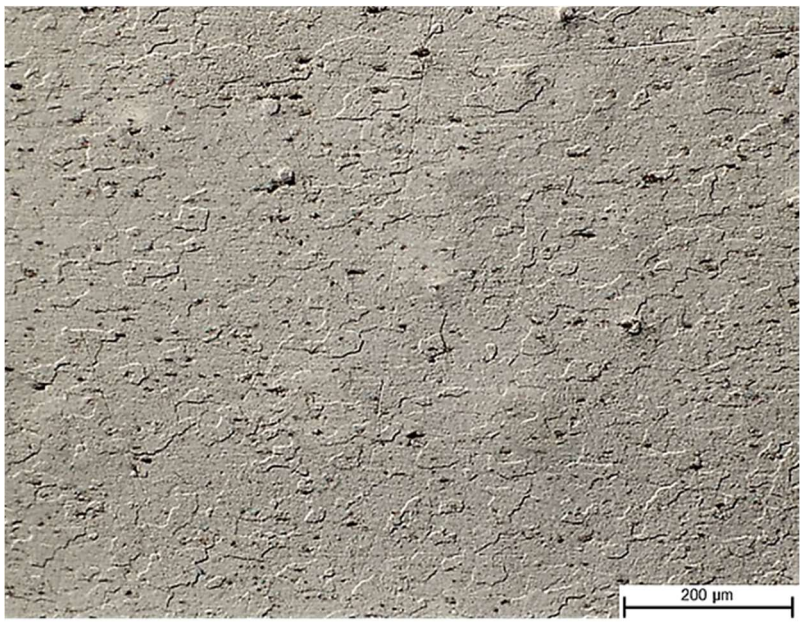

(a)

(b)

Fig. 7-18 Light optical micrographs depicting the microstructure of; (a) as-received AA50830; (b) stir zone of the unreinforced AA5083 (post-FSP) [x100, Etched using Barker's reagent]

However, the images depicted in Fig. 7-18 clearly illustrate that substantial refinement has occurred. While this would generally constitute a corresponding hardness increase (in-line with the Hall-Petch relationship), the existing literature indicates that AA5083 does not harden significantly with a reduction in grain size [7.35, 7.37]. Additionally, the micrographs indicate that FSP has removed the strain hardening imparted by the cold rolling process (Fig. 7-17a). Therefore, it appears as though the two mechanisms (removal of cold work and grain refinement) have effectively countered one another and, hence, explains why FSP has resulted in only a slight hardness increase within the stir zone.

The broad scatter of measurements recorded for the MMCs (as-deposited and SprayStirred) exhibited in Fig. 7-15 is due to the location in which the indenter comes into contact with the surface of the MMC. Indentations made on either a hard reinforcing particle or on the matrix will return correspondingly high and low hardness values.

The SprayStirred WC-CoCr and Cr_3C_2-NiCr reinforced coatings exhibit an average hardness increase of approximately 540% and 495% respectively, over the as-received substrate. However, the Al_2O_3 reinforced specimen yielded a comparatively smaller hardness increase over the as-received AA5083 of only 103%. This lesser hardness increase is attributed to two factors. The first is the lower quantity of reinforcing particles present in the MMC (Section 7.3.1) and the second is the increase in distance between neighbouring particles (Section 7.3.4). The higher hardness measured on the retreating side of the stir zone corresponds to a reduction in the interparticle spacing of the WC-CoCr material post-FSP (Table 7-6).

The results presented in Fig. 7-15 demonstrate the impact of the tool design on the distribution of reinforcing particles. Specifically, the tool design employed in the present study has resulted in more of the reinforcing particles being relocated to the retreating side as opposed to being evenly distributed across the top surface of the specimen. The results (Fig. 7-15) also show a noticeable drop in the microhardness towards the centre of the stir zone.

Fig. 7-19 confirms a lack of reinforcements in the area that the tool pin traverses through. This is attributed to the influence of the tool pin, which forces particles from the surface towards the base of the stir zone. A micrograph showing the region that the pin traverses through (Fig. 7-4), the shown in Fig. 7-20 and highlights the movement of reinforcements from the near-surface region to the root of the stir zone.

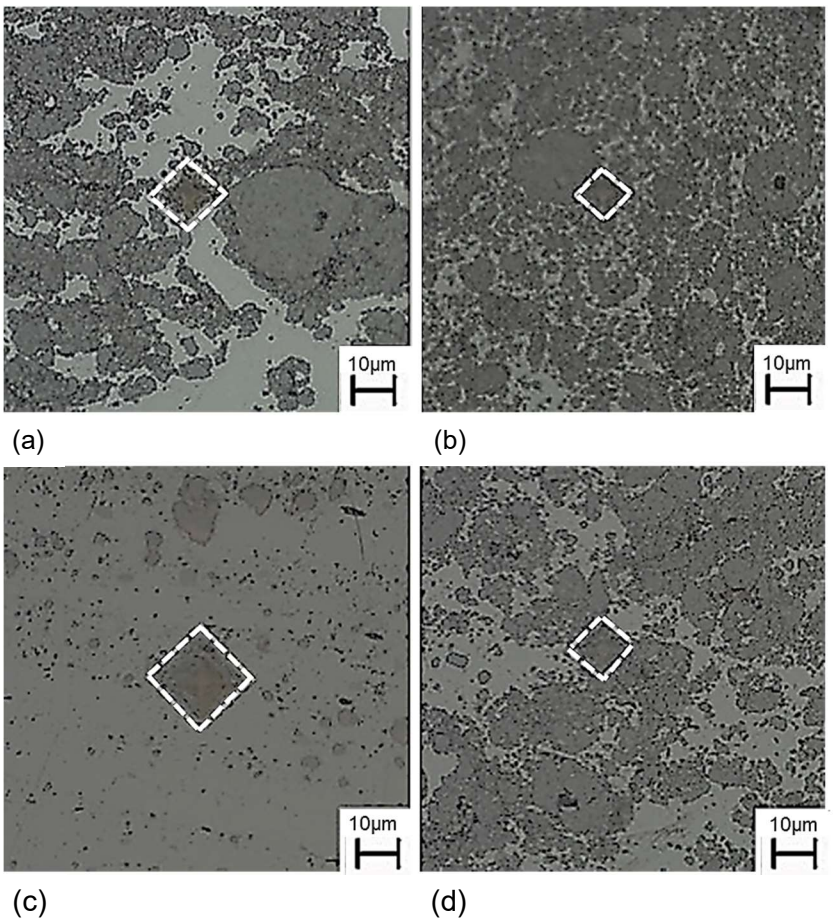

Fig. 7-19 Hardness indents showing the level of surrounding WC-CoCr particles [x500, Unetched]; (a) as-deposited; (b) retreating side; (c) pin location; (d) advancing side

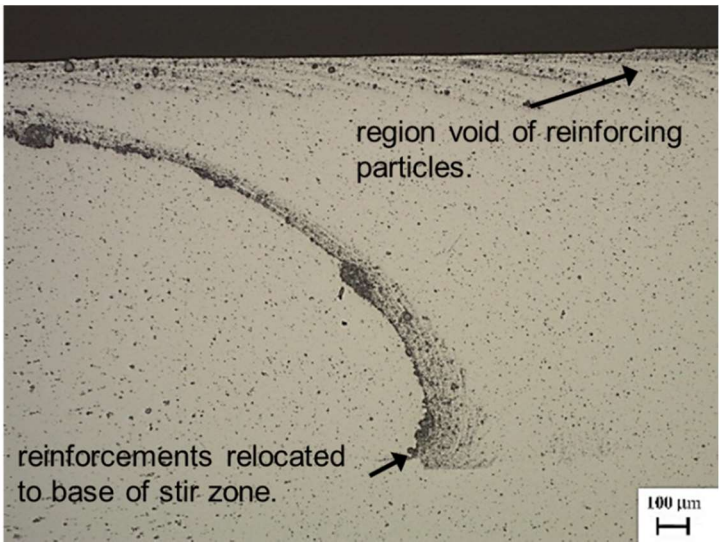

Fig. 7-20 Light optical micrograph showing reinforcing particles being pulled down from the surface [x50, Unetched]

7.3.4 Interparticle spacing

Khare and Burris' method [7.40] was applied to measure the spacing between reinforcements in the MMC and, hence, quantify the variation in interparticle spacing between the as-deposited and SprayStirred MMCs. The results of this analysis are given in Table 7-6. A detailed account of this method [7.40] is presented in Chapter 4.

Table 7-6 Average interparticle spacing

	WC-CoCr	Cr_3C_2-NiCr	Al_2O_3
Interparticle spacing (μm) (as-deposited)	11.5	15.3	13.1
Interparticle spacing (μm) (SprayStirred)	3.7	5.8	8.6
Reduction in interparticle spacing (%)	68	62	34

The results indicate a 68% and 62% decrease in the average interparticle spacing in the WC-CoCr and Cr_3C_2-NiCr coatings following FSP. However, SprayStirred Al_2O_3 resulted in a smaller decrease of 34%. The Al_2O_3 grains are not refined to the same extent as the cermet particles due to the morphology of the oxides. The Al_2O_3 powder is comprised of solid particles with no ductile binder, whereas the cermet powders are agglomerates of smaller carbides retained by a binding alloy. Hence in the case of WC-CoCr, the FSP tool can break down the retaining cobalt binder and distribute the carbide grains that can be further refined through the rotating motion of the FSP tool. Despite the variation in the amount of refinement experienced by each MMC, the results highlight the beneficial effects of FSP by confirming the reduction in the interparticle spacing post-FSP.

7.3.5 Overlapping FSP tracks

Considering that the SprayStir is intended for application to large surface areas (wider than the width of a single FSP track), the results of overlapping multi-pass FSP were evaluated. This section assesses the distribution of WC-CoCr and Cr_3C_2-NiCr particles within the substrate matrix following overlapping multi-pass FSP.

Fig. 7-21 and Fig. 7-22 present images of three overlapping FSP tracks. The photograph in Fig. 7-21 depicts three consecutive tracks with a 10 mm overlap, and Fig. 7-22 depicts three tracks with a 5 mm overlap. In both cases, FSP was conducted using the processing parameters presented in Table 7-3.

Fig. 7-21 Macroscopic image showing the surface of the SprayStirred Cr_3C_2-NiCr specimen with 10 mm overlap

Fig. 7-22 Macroscopic image showing the surface of the SprayStirred Cr_3C_2-NiCr specimen with 5 mm overlap

Fig. 7-23 displays a cross-sectioned view of two overlapping FSP passes, showing the distribution of the reinforcing particles along the top surface of the substrate. The location of the reinforcements within the matrix (post-FSP) indicates that the tool design is effective at retaining the reinforcement particles in the near-surface region while successfully embedding them within the substrate matrix. The images (Fig. 7-23) also show that the amount of overlap between consecutive processing passes appears to have no detrimental effect on the retention of reinforcement particles to the surface of the substrate. Micrographs from the WC-CoCr reinforced specimen (Fig. 7-24) confirm that the reinforcements have been successfully embedded within the substrate matrix.

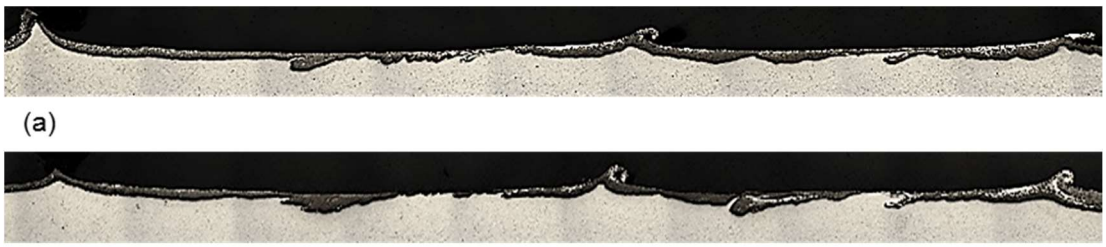

(a)

(b)

Fig. 7-23 Cross-sectional, macroscopic view of Cr_3C_2-NiCr reinforced MMC with; (a) 10mm overlap; (b) 5mm overlap [x5, Unetched]

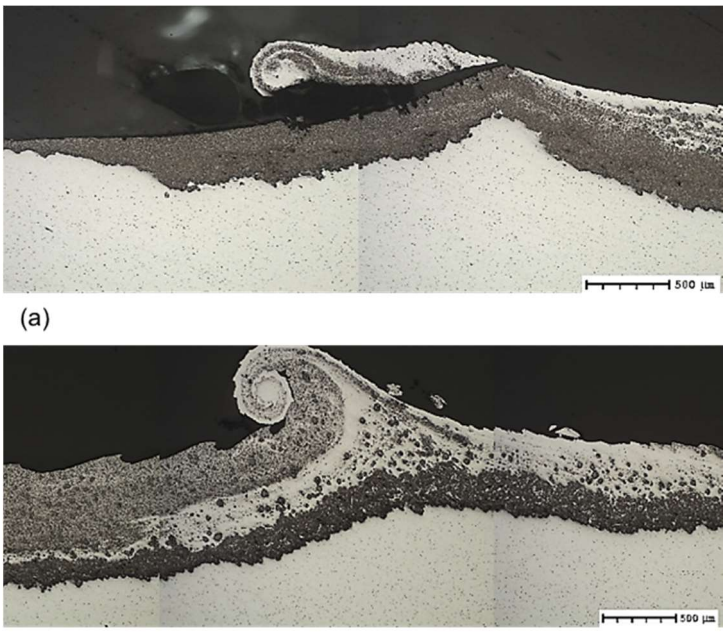

(a)

(b)

Fig. 7-24 Microscopic images at the interface between consecutive FSP passes of WC-Co coated AA5083; (a) 10mm overlap; (b) 5mm overlap [x50, Unetched]

7.3.6 Slurry erosion impingement

The mass and volume loss of each specimen was measured following exposure to free erosion-corrosion test conditions, and the results presented herein. The test was conducted using a recirculating slurry with the specific test parameters offered in Table 5-4.

7.3.6.1 Macro observations

Post-slurry erosion testing, the specimens exhibit two distinct regions on the impinged surface (Fig. 7-25). The central region depicts the direct impingement zone and relates to the area of the test specimen located immediately beneath the jet nozzle. The exit diameter of the nozzle correlates to a directly impinged region of

7.06 mm^2. The outer zone is a turbulent region that experiences significant sliding erosion as particles are forced outwards following impact in the direct zone. The results reported in this section present the mass and volume loss from both the directly impinged and turbulent regions of the wear scar.

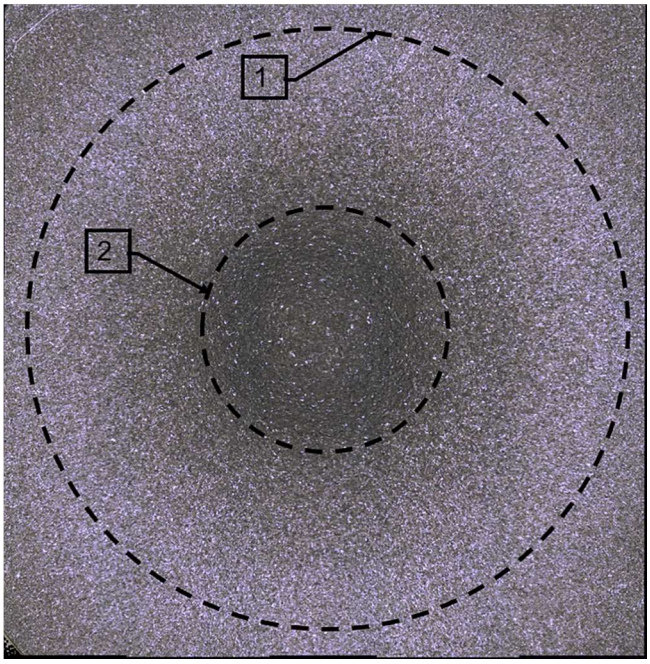

Fig. 7-25 Macrograph of the wear scar on the as-received AA5083 aluminium showing; (1) the turbulent region, (2) the directly impinged region

7.3.6.2 Mass loss

Fig. 7-26 displays the mass loss from the three MMCs and the as-received AA5083 substrate in the pre- and post-FSP condition. The results (Fig. 7-26) show a reduction in the total mass loss of all the MMCs post-FSP. However, the erosion performance of the uncoated substrate exhibits no measurable decline in the mass loss following the application of FSP. This outcome highlights a correlation between the microhardness values (Fig. 7-15) of the AA5083 (no reinforcements) which also show no change in hardness between the pre- and post-FSP conditions. This relationship between hardness and erosion performance has also been reported in existing literature [7.41, 7.42]. Both studies [7.41, 7.42] examined the erosion performance of thermal spray coatings when exposed to a slurry test environment and concluded that the hardness of the impinged surface influences the erosion performance of a specimen.

Post-FSP, the mass loss of the WC-CoCr reinforced MMC has reduced by approximately 75% when compared with the as-deposited coating. This reduction

constitutes the most substantial improvement in erosion performance following FSP out of all the examined coatings and is attributed to the dispersal of the WC-CoCr agglomerates and the corresponding decrease in the interparticle spacing (Table 7-6) [7.43, 7.44]. However, due to the dissimilar density of the three reinforcing particles, the mass loss data cannot be used to compare the erosion performance of the three MMCs. Thus, to enable a comparative analysis of the three different particle reinforced MMCs, the volume loss within the wear scar was measured using a focal variation microscope (Alicona Infinite Focus G4) [7.15].

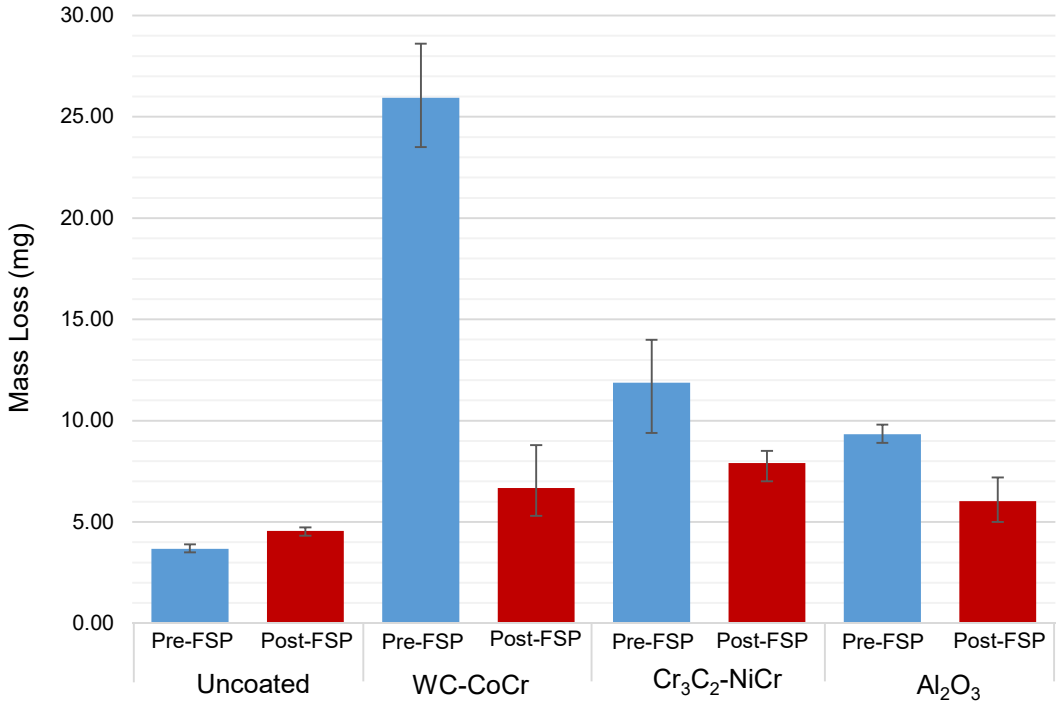

Fig. 7-26 Mass loss of the MMC coatings pre- and post-FSP

7.3.6.3 Volume loss

Fig. 7-27 presents the measured volume loss within the impinged region for each MMC and the as-received substrate. The volume loss in the direct and turbulent regions of the wear scar was measured independently to determine the contribution of each region to the total volume loss. Based on the results (Fig. 7-27), the uncoated AA5083 material has led to similar levels of volume loss in the pre- and post-FSP condition. This finding is somewhat unexpected, considering existing research [7.36, 7.45] reports improved erosion performance of the alloy, post-FSP. However, the results (Fig. 7-27) align with the outcome of the microhardness study, which also demonstrated no change in hardness before and after FSP [7.41, 7.42].

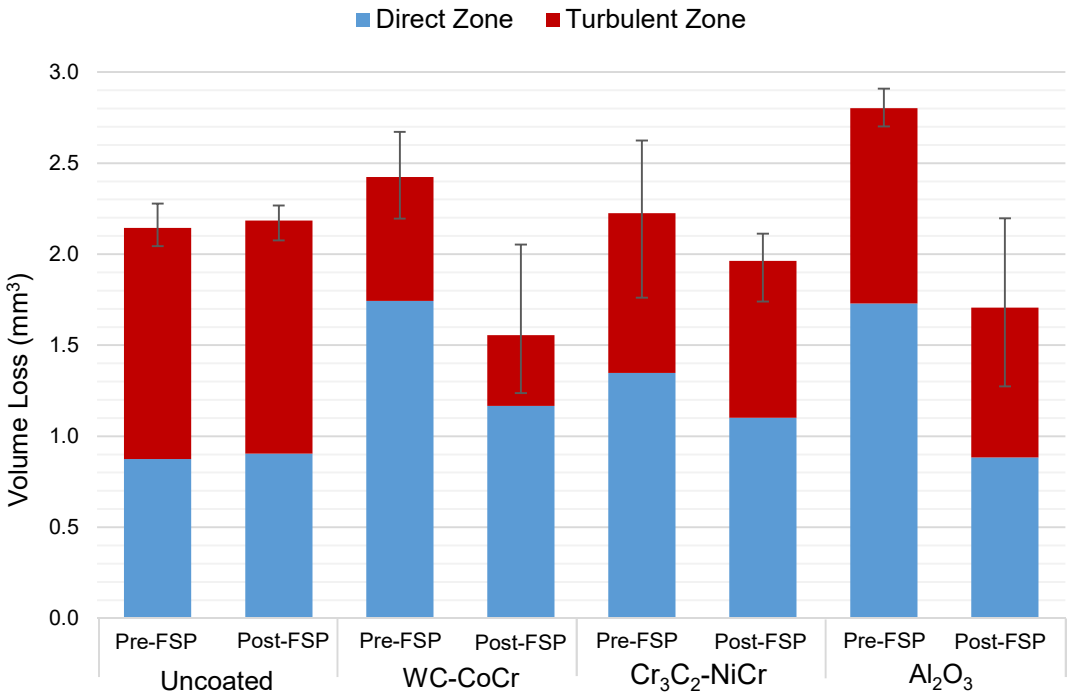

Fig. 7-27 Volume loss in the direct and turbulent regions of the wear scar

The as-deposited Cr_3C_2-NiCr reinforced coating recorded the lowest volume loss when exposed to solid-liquid impingement conditions (Fig. 7-27). Despite this, the resulting volume loss failed to offer any improvement over the as-received substrate. The enhanced erosion performance of this MMC over the WC-CoCr coating is a result of increased quantities of AA5083, which, as shown by the volume loss data, offers comparatively improved erosion resistance at a 90° angle of attack [7.46].

The Al_2O_3 reinforced coating comprises a similar ratio of matrix to reinforcement as the Cr_3C_2-NiCr reinforced coating; however, demonstrates a comparably high volume loss. This outcome is related to the difference in reinforcement particle size between Al_2O_3 and Cr_3C_2-NiCr. As shown in Table 7-1, the average size of Al_2O_3 particles is approximately 180% greater than that of Cr_3C_2-NiCr carbides and is more than the maximum allowable particle size (<1 µm) necessary to result in dispersion strengthening [7.53]. Micrographs of the Al_2O_3 MMC (Fig. 7-8a) exhibit cracking of larger particles which results in the particles being unable to contribute to load transfer strengthening, with the faceted particle shape resulting in lower ductility within the MMC [7.62].

However, the Al_2O_3 reinforced MMC has experienced the greatest improvement in erosion performance post-FSP, recording a 36% decrease in the total

volume loss. The direct and turbulent zones exhibited a drop in volume loss of 33% and 43% respectively. This improvement in erosion performance is attributed to the level of refinement of the oxide particles and the associated drop in the interparticle spacing (Table 7-6).

The unreinforced AA5083 has experienced increased volume loss in the turbulent zone than in the directly impinged zone in both the as-received and FSPed condition. This outcome is a consequence of the ductility of the as-received substrate material which typically exhibits greater erosion at acute angles of attack due to scoring and ploughing acting as the primary erosion mechanism [7.46]. As the vol.% of reinforcing particles is increased, the quantity of material removed from the turbulent zone decreases while the amount removed from the directly impinged zone increases. Specifically, the high hardness of the MMC prevents the erodent from scoring and ploughing the surface, hence reducing the overall material loss from the turbulent region. This shift demonstrates a change in the mechanisms causing material removal from ploughing of the ductile substrate to the fracture and removal of reinforcing particles [46]. The variation in wear mechanisms between the turbulent and directly impinged zones will be expanded on in Section 7.3.7

The as-deposited Al_2O_3 reinforced coating exhibits the most substantial volume loss, with the recorded loss approximately 30% higher than that of the as-received substrate. This increase in volume loss as compared to as-received AA5083 is attributed to two mechanisms. The first is the ploughing and scoring of the ductile AA5083 matrix resulting in the Al_2O_3 reinforcements exposed and subsequently plucked from the matrix by the impinging slurry. Secondly, the dislodged Al_2O_3 particles act as a secondary erodent within the wear scar and hence accelerate the removal of material.

The as-deposited WC-CoCr reinforced MMC has performed poorly in comparison to the as-received substrate and failed to provide increased erosion protection over the Cr_3C_2-NiCr reinforced coating. This contrasts with many studies that state the substantial reduction in erosion rate with the addition of the tungsten carbide cermets [7.47–7.49]. While this outcome is contrary to the findings of these studies [7.50–7.52], the poor performance of the WC-CoCr reinforced MMC is attributed to agglomeration of WC-CoCr particles within the coating matrix. The inhomogeneous distribution of reinforcements in the as-deposited coating has led to the agglomerates being plucked from the matrix due to a lack of supporting binder between the individual carbides.

Post-FSP, the volume loss experienced by the Al_2O_3 coatings is reduced, however, the drop in volume loss measured on the WC-CoCr MMCs is greater still. While the Al_2O_3 particles are refined by FSP, the particles are still larger than the carbides in the WC-CoCr reinforced MMC (Table 7-1). Consequently, the superior erosion performance of the SprayStirred WC-CoCr MMC aligns with the presence of sub-micron reinforcements and reduced interparticle spacing.

The SprayStirred Al_2O_3 MMC has experienced lower volume loss than the SprayStirred Cr_3C_2-NiCr despite the greater interparticle distance between reinforcements. Thus, the interparticle spacing is not the only parameter that governs the erosion performance of the MMC. The refinement of the oxide particles by the FSP has increased the number of particles that are less than 1 μm, and as such, the Al_2O_3 reinforced MMC benefits from increased dispersion strengthening [53], resulting in lower volume loss.

7.3.7 Wear scar examination

7.3.7.1 CS coatings and as-received AA5083 wear scars

The reported mass and volume loss of the CS deposited coatings confirm that, under slurry erosion conditions, the as-deposited MMC coatings fail to provide enhanced erosion protection over the as-received AA5083. SEM micrographs of the impinged region were examined to identify the cause of this unexpected outcome and evaluate the mechanisms resulting in material removal. Furthermore, the erosion mechanisms operating on the as-deposited and SprayStirred MMCs were identified to elucidate the measured drop in volume loss post-FSP (Fig. 7-26).

Fig. 7-28 exhibits scoring and lip formation within the wear scar of the as-received AA5083 substrate. Directionality and parallel scratch patterns are also evident from the image (Fig. 7-28). This scar pattern is consistent with the erosion of ductile materials as noted by Finnie [7.54]. Under near-perpendicular impingement (Fig. 7-28a), silica particle impacts cause craters to form on the surface. Each crater is surrounded by a ring of strained material referred to as lips [7.55] that are removed by subsequent particle impacts. As the impinging particles move outwards from the directly impinged zone, they are travelling near parallel with the substrate surface. Under these conditions, the silica particles score and plough the ductile AA5083 (Fig. 7-28b) which consequently leads to additional material being removed. Fig. 7-29 depicts these features at higher magnification. Hence, the mechanisms causing

material loss, in the as-received AA5083 can be attributed to crater formation, cutting and scoring. This finding is corroborated by previous research [7.56, 7.57].

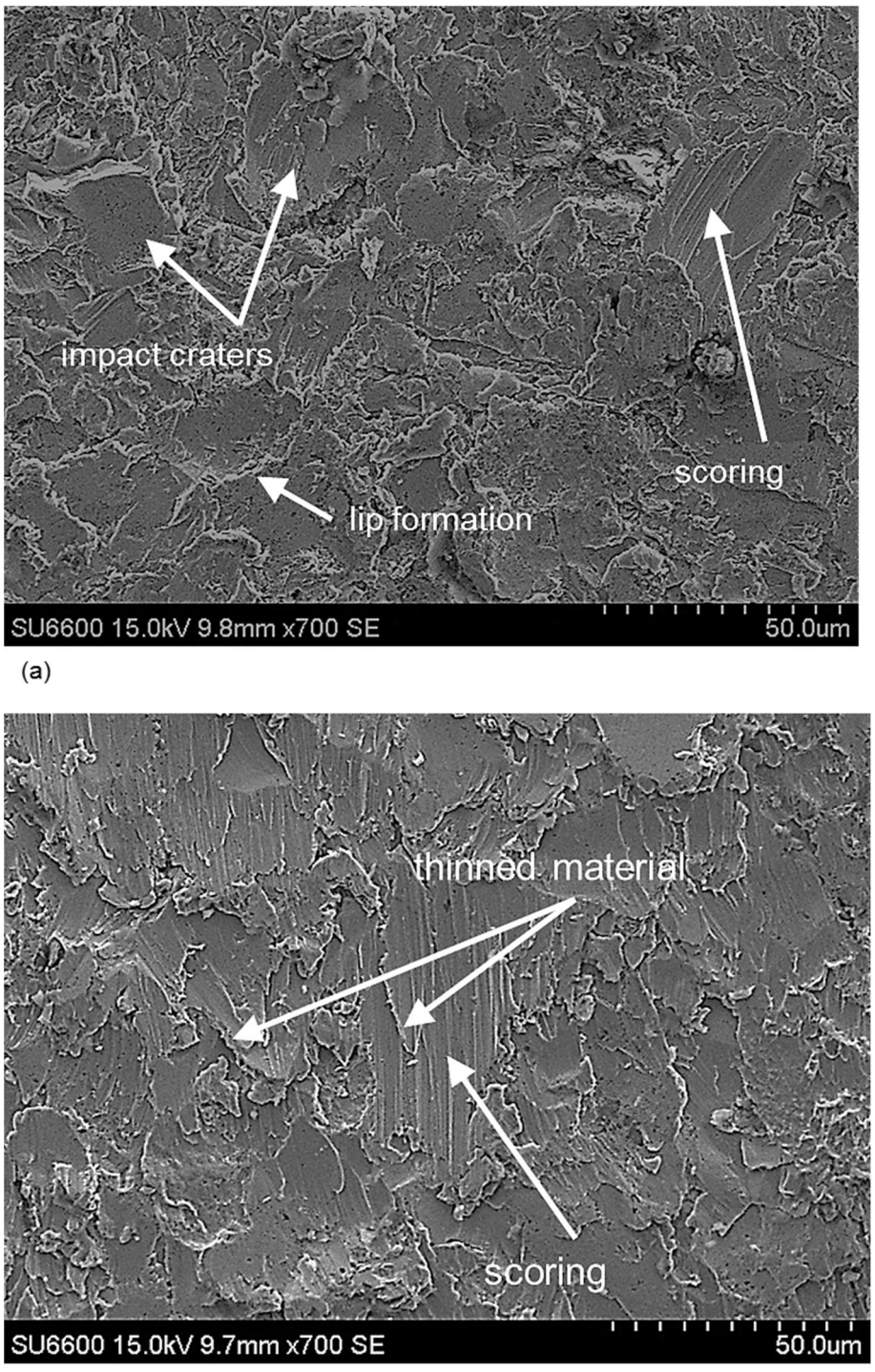

Fig. 7-28 SEM micrograph of the impinged surface of as-received AA5083; (a) directly impinged zone; (b) turbulent region [x700]

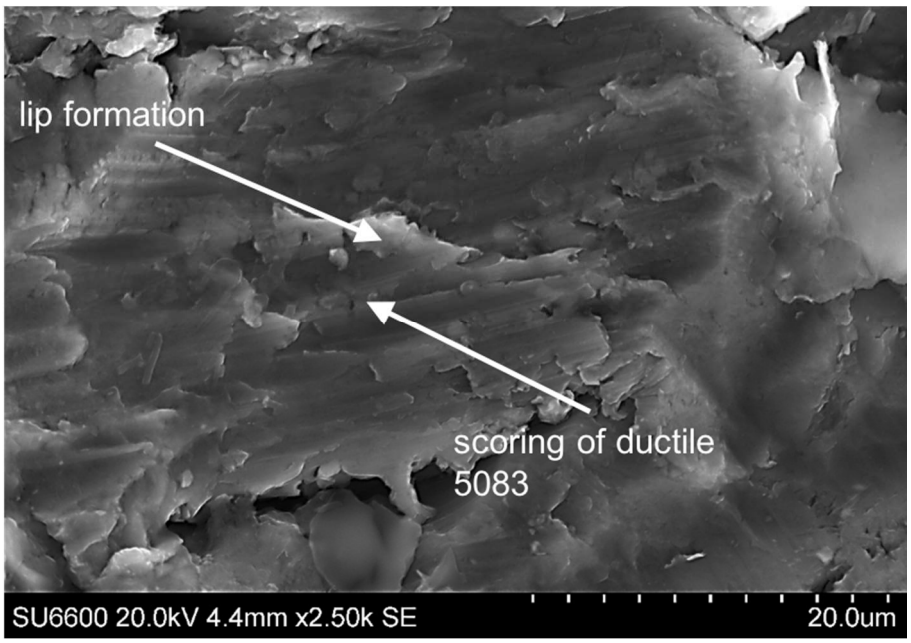

Fig. 7-29 SEM micrograph showing the damage within the wear scar of the as-received AA5083 specimen following slurry erosion testing [x2500]

The CS deposited WC-CoCr reinforced coating (Fig. 7-30) presents signs of damage to the aluminium matrix in the form of scoring and ploughing. This damage is consistent with ductile material removal and is frequently reported in the published literature [7.46, 7.58, 7.59]. Furthermore, Fig. 7-30 shows carbides protruding from the aluminium matrix. EDS analysis reveals high tungsten (approximately 70% wt.%) content in these areas thereby confirming that these protruding features are the carbide reinforcements.

To confirm the presence of ductile erosion, high magnification (x20,000) SEM micrographs were captured of the AA5083 matrix. The image (Fig. 7-31) highlights the presence of ductile scoring within the aluminium matrix. Ramesh et al. [7.60] reported similar findings following examination of HVOF sprayed WC-Co based coatings exposed to dry jet erosion. Particle agglomeration further enhances the rate of material removal as clusters of carbides are removed simultaneously due to the extrusion (ploughing) of the surrounding matrix alloy [7.61]. Consequently, the quantity of eroded material is high with the presence of reinforcement particles offering no measurable improvement to the erosion performance of the MMC.

Fig. 7-32 depicts the damage within the wear scar of the as-deposited Cr_3C_2-NiCr coating. The image (Fig. 7-32) shows the removal of the AA5083 matrix and subsequent exposure of carbides. Hence, this is recognised as the primary wear

mechanism operating on the surface. Pull-out of the large Al_2O_3 particles was identified on the CS deposited Al_2O_3 coating, and is highlighted in Fig. 7-33.

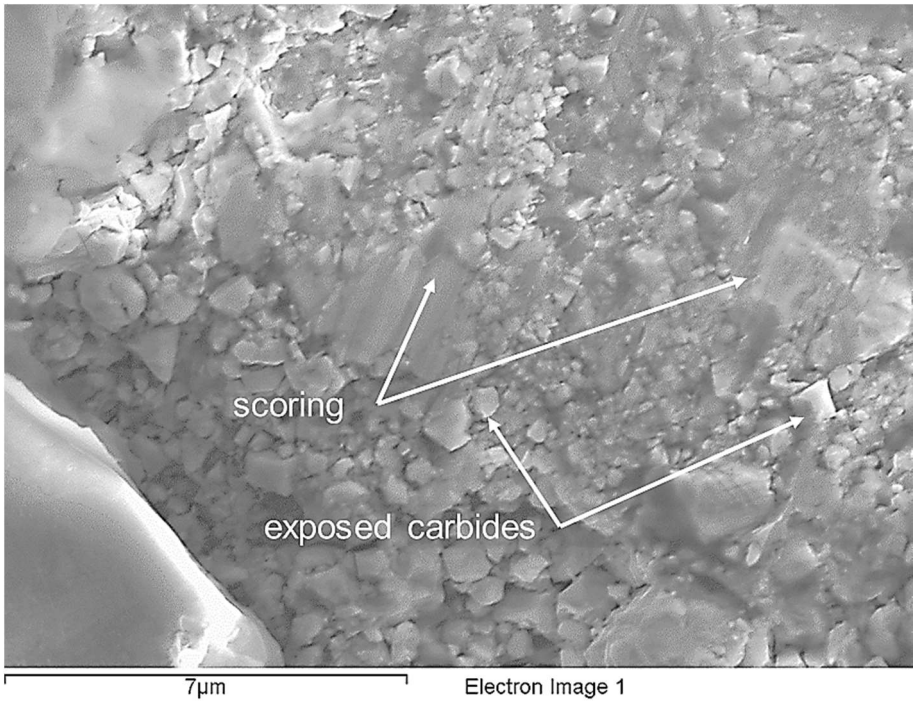

Fig. 7-30 SEM micrograph of the impinged WC-CoCr reinforced CS coating [x8000]

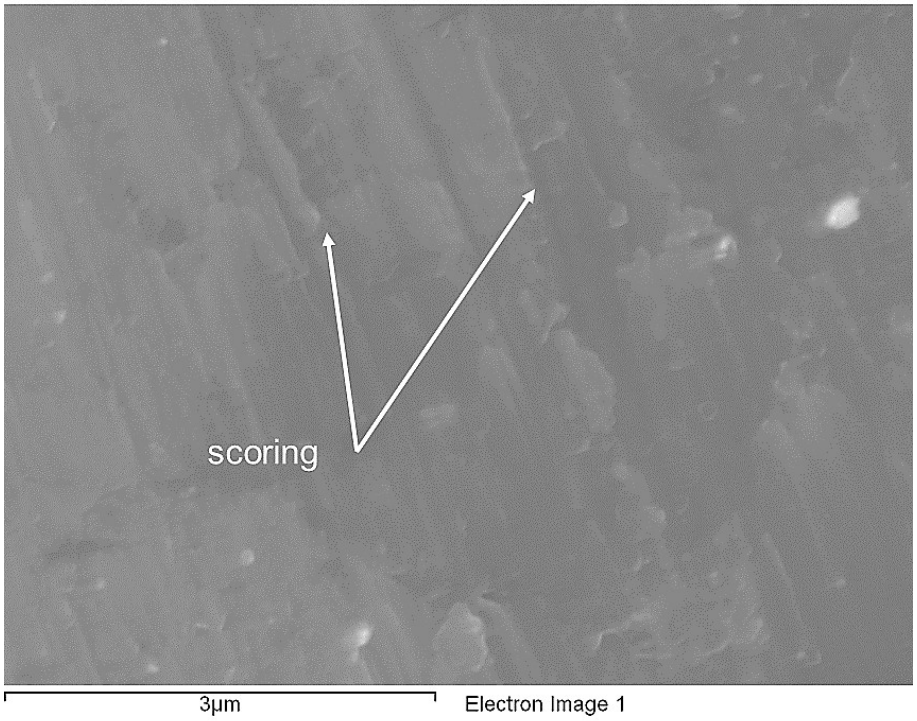

Fig. 7-31 SEM micrograph of the impinged WC-CoCr reinforced CS coating [x20000]

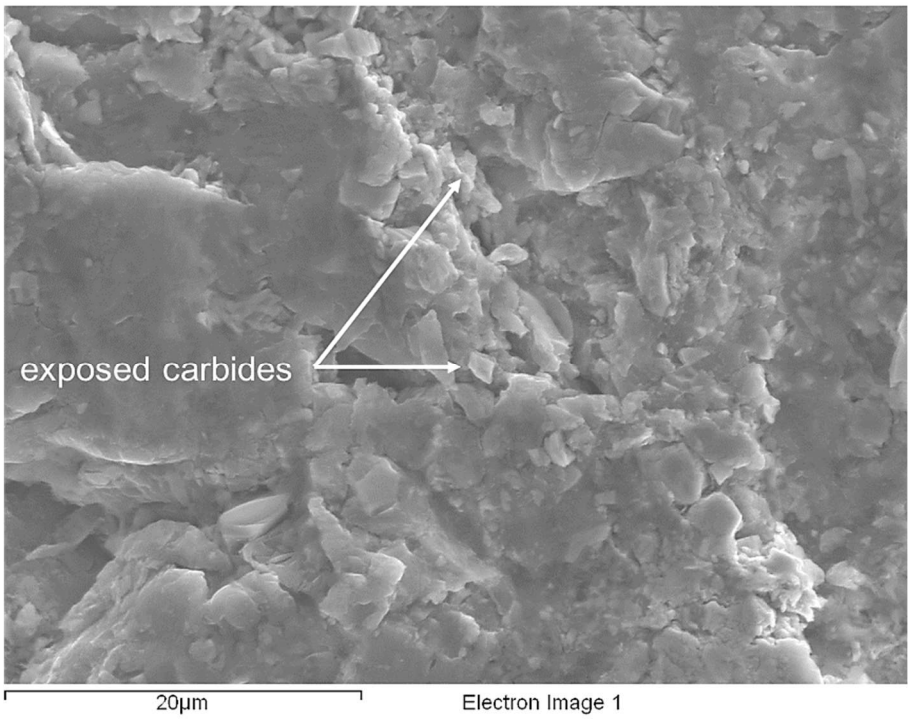

Fig. 7-32 SEM micrograph of the impinged region of the as-deposited Cr_3C_2-NiCr reinforced coating [x2500]

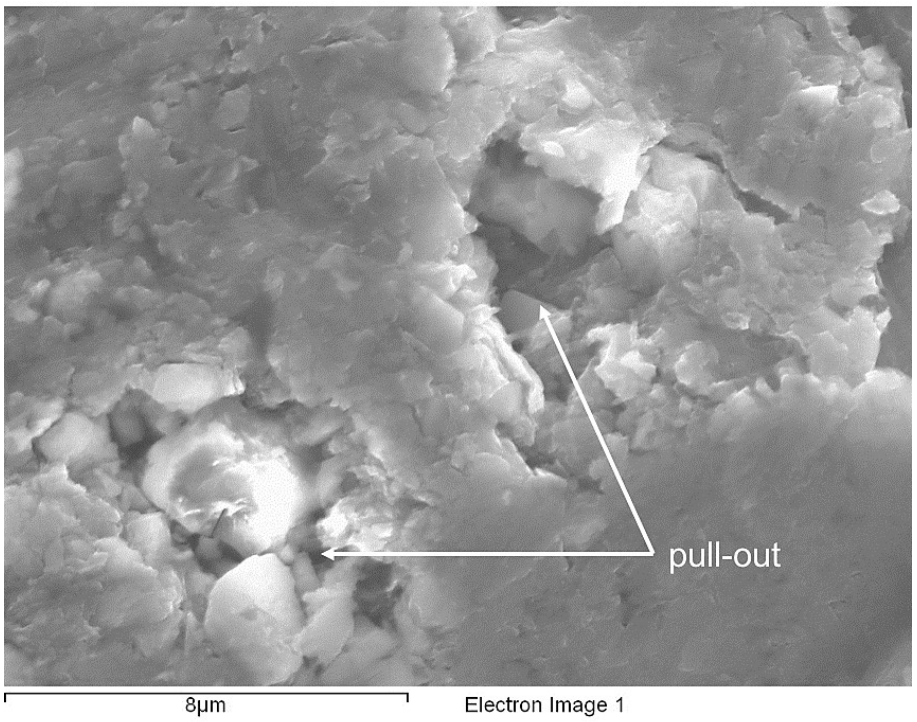

Fig. 7-33 SEM micrograph of the impinged region of the as-deposited Al_2O_3 reinforced coating [x7000]

Numerous authors [7.24, 7.61–7.64] have explored the properties of distributed reinforcing particles in steel and aluminium alloys. In many of these studies [7.24, 7.61–7.65], the addition of reinforcing particles improves the erosion resistance of MMC coatings. However, the results presented herein contradict these findings, thus it is necessary to elucidate this phenomenon.

Ninham et al. [7.61] evaluated the erosion performance of reinforced carbon steel with varying quantities of tungsten carbide based cermet particles under dry jet erosion conditions. The authors discovered that, for tungsten carbide content below 30% (wt.%), the coatings exhibited a ductile degradation mechanism with the retaining matrix removed by the erodent, and the carbides subsequently pulled from the matrix [7.61]. For WC content greater than 70%, the breakdown of the MMC occured through the brittle fracture of the carbide particles [7.61]. The erosion resistance was enhanced with the addition of either of these respective quantities (<30% or >70%) when compared with the as-received substrate. However, Ninham et al. [61] discovered that for MMCs alloys containing approximately 60% reinforcing particles, the erosion rate was higher than MMCs containing high (>70%) and low (<30%) quantities of carbide reinforcements.

The authors [7.61] attributed this observation to ductile and brittle erosion mechanisms both operating on the surface, resulting in the displacement of the matrix alloy and subsequent removal of carbides. Considering that the quantities of reinforcements measured in the MMCs examined in the present study is lies within this range (>70% <30%) [7.61], it is probable that the same mechanism was responsible for the poor erosion performance of MMC coatings recorded. By increasing the quantity of reinforcing particle to a value around 80% (vol.%), the authors [7.61] discovered that the MMC demonstrates superior resistance to the erosive medium.

Moreover, Singh et al. [7.66] reported enhanced tribological performance with the homogeneous spatial distribution of reinforcing particles. Similar findings are reported by Machio et al. [7.67] under erosive slurry conditions. The authors [7.67] state that the lower volume fraction of matrix leads to reduced free space between adjacent reinforcement particles within the matrix, hence resulting in improved erosion resistance. Based on this work [7.61, 7.66, 7.67], a reduction in the interparticle spacing between the reinforcement particles while increasing the vol.% of reinforcement within the matrix would likely lead to improvement in the erosion performance of the MMC. As demonstrated in Table 7-6, the application of FSP has

successfully reduced the interparticle spacing between the reinforcements in all three MMCs and has resulted in a corresponding drop in the quantity of material removed by the impinging slurry (Fig. 7-27).

7.3.7.2 SprayStir wear scars

The impinged region of the SprayStirred specimens has been examined to identify the mechanisms leading to the loss of material and hence provide an explanation for the measured improvements to the erosion performance (Fig. 7-27). The impinged region of the WC-CoCr reinforced SprayStirred surface is presented in Fig. 7-34 and reveals a significant quantity of tungsten carbides exposed to the impinging slurry. To generate this damage, the slurry has removed the comparably soft, ductile matrix that surrounds the carbides. Without this retaining matrix, continued exposure to the impinging jet causes the carbides to be pulled from the surface.

Furthermore, the matrix alloy within the SprayStirred WC-CoCr reinforced MMC (Fig. 7-35) exhibited signs of scoring that are consistent with ductile material removal. Scoring is commonly reported as the primary erosion mechanism for particle reinforced alloys in existing literature [7.42, 7.58–7.60]. However, the exposure of carbides does highlight their uniform distribution in the MMC and explains the enhanced erosion performance recorded during the slurry erosion study.

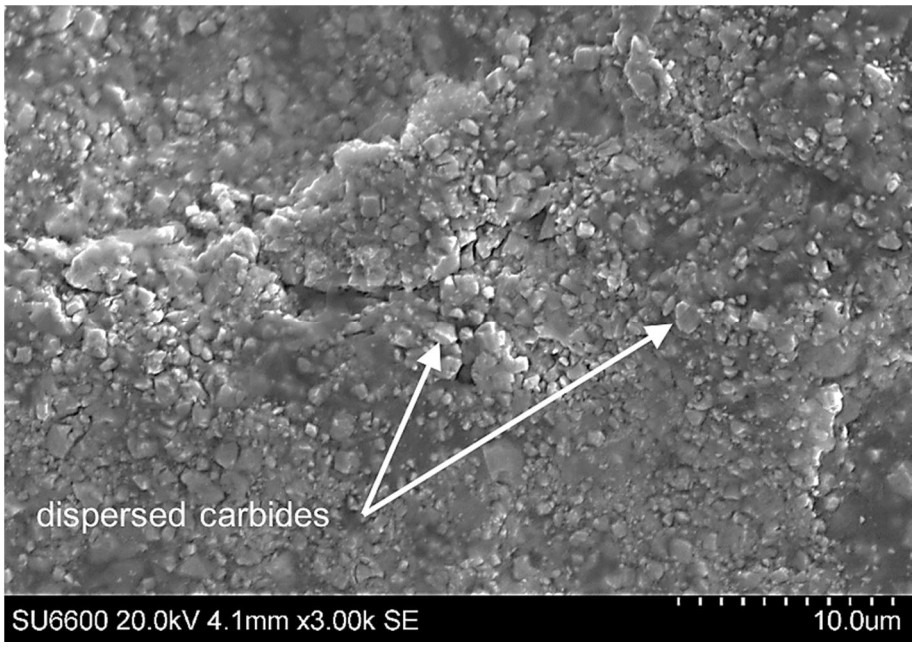

Fig. 7-34 SEM micrograph of the impinged SprayStirred WC-CoCr reinforced MMC [x3000]

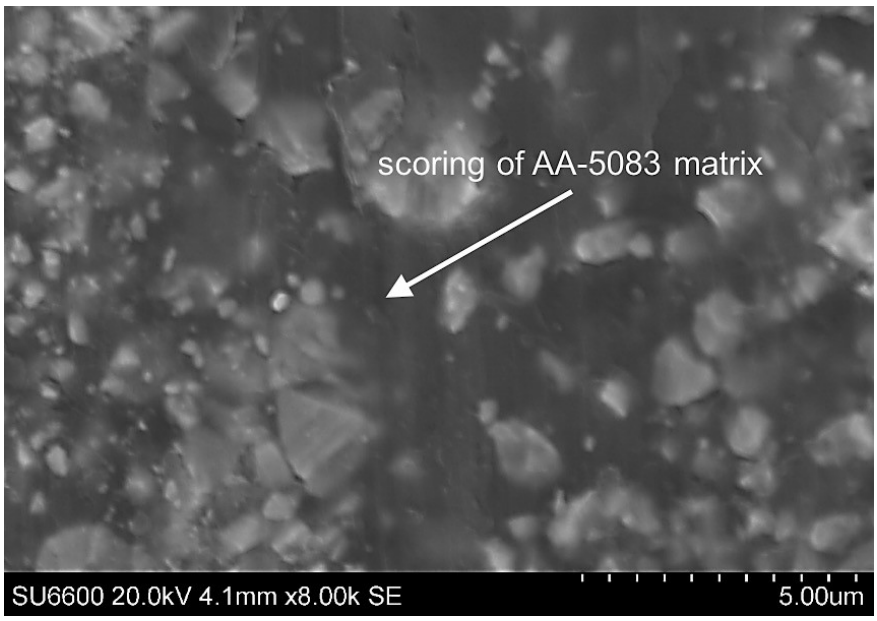

Fig. 7-35 SEM micrograph of the impinged SprayStirred WC-CoCr reinforced MMC [x8000]

Evidence of the same erosion mechanism was found on the surface of SprayStirred Cr_3C_2-NiCr, as demonstrated by the exposed carbides shown in Fig. 7-36. The level of damage experienced by this coating is attributed to the increased interparticle spacing (Table 7-6) and the lower hardness of the chromium carbides (as compared with WC-CoCr). The greater distance between adjacent particles (Table 7-6) has led to a larger surface area of the matrix being exposed to the impinging slurry.

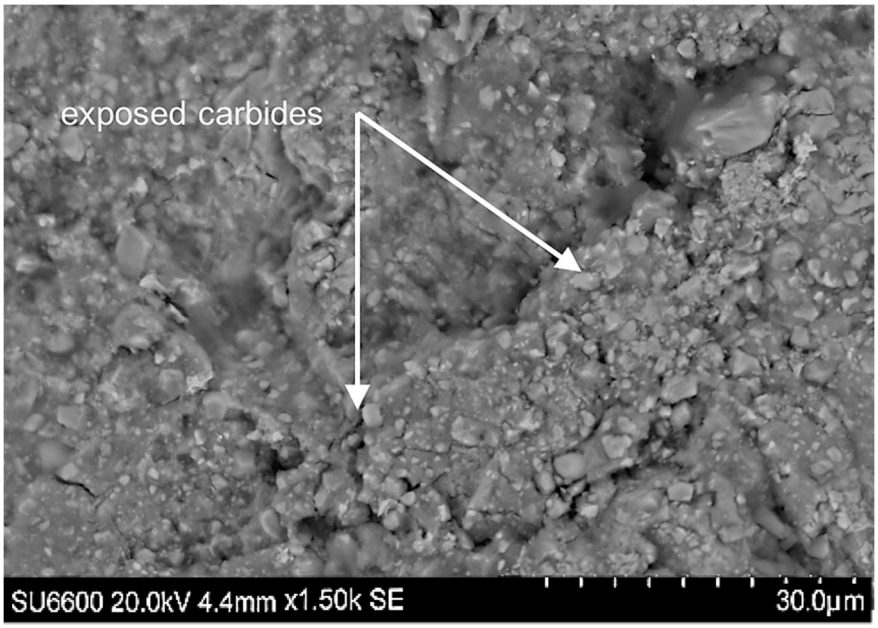

Fig. 7-36 SEM micrograph of the impinged SprayStirred Cr_3C_2-NiCr MMC [x1500]

7.4 Conclusions

By co-depositing reinforcing particles with a ductile metallic binder, a thick, dense coating has been achieved. The successful build-up of a coating is attributed to the deformation of the binding alloy that increases the contact area with adjacent particles. Subsequent FSP has successfully refined the as-deposited reinforcements. Micrographs reveal that the particles have been homogeneously dispersed throughout the MMC matrix. Moreover, the WC-CoCr agglomerates present in the as-deposited coating have been refined by FSP. The results presented herein confirm that FSP has successfully reduced the average interparticle spacing of all three coatings, with the WC-CoCr reinforced MMC exhibiting a reduction of 65%. FSP has resulted in approximately 120% increase in the average hardness over the as-deposited MMC in the WC-CoCr reinforced MMC. This increase is attributed to the particle refinement and reduction in the interparticle distance of the reinforcements.

Volumetric analysis of the SprayStirred wear scar has highlighted the improved performance of the SprayStirred specimens over the CS deposited coatings. The findings of this study attribute the improved performance of these specimens to the uniform dispersal of the reinforcing particles. The Al_2O_3 reinforced specimens exhibited the most significant improvement in erosion performance following FSP with the volume loss decreasing by approximately 40%. Despite this, WC-CoCr recorded the lowest volume loss out of all the examined coatings. The superior erosion properties of this MMC are attributed to the uniform distribution of micro and sub-micron reinforcing particles and the higher hardness of the tungsten carbide reinforcements.

Examination of the wear scars highlighted damage to the softer matrix alloy in the form of ploughing which subsequently exposed the reinforcements to the impinging slurry. The SprayStirred surfaces presented a reduction in the interparticle spacing, hence less of the matrix alloy was exposed to the impinging slurry.

7.5 References

[7.1] R.S. Lima, J. Karthikeyan, C.M. Kay, J. Lindemann, C.C. Berndt, Microstructural characteristics of cold-sprayed nanostructured WC-Co coatings, Thin Solid Films. 416 (2002) 129–135.

[7.2] M. Couto, S. Dosta, M. Torrell, J. Fernández, J.M. Guilemany, Cold spray deposition of WC-17 and 12Co cermets onto aluminum, Surf. Coatings Technol. 235 (2013) 54–61.

7. [3] E. Irissou, J.G. Legoux, B. Arsenault, C. Moreau, Investigation of Al-Al 2O 3

cold spray coating formation and properties, J. Therm. Spray Technol. 16 (2007) 661–668.
[7.4] R.S. Lima, B.R. Marple, Thermal spray coatings engineered from nanostructured ceramic agglomerated powders for structural, thermal barrier and biomedical applications: A review, J. Therm. Spray Technol. 16 (2007) 40–63.
[7.5] H.-T. Wang, X. Chen, X.-B. Bai, G.-C. Ji, Z.-X. Dong, D.-L. Yi, Microstructure and properties of cold sprayed multimodal WC–17Co deposits, Int. J. Refract. Met. Hard Mater. 45 (2014) 196–203.
[7.6] R. Fernandez, B. Jodoin, Effect of Particle Morphology on Cold Spray Deposition of Chromium Carbide-Nickel Chromium Cermet Powders, J. Therm. Spray Technol. 26 (2017) 1356–1380.
[7.7] Oerlikon Metco, Material Product Data Sheet Chromium Carbide – Nickel Chromium Powder Blends, 2 (2014) 2–7.
[7.8] Oerlikon Metco, Material Product Data Sheet Tungsten Carbide – 10 % Cobalt 4 % Chromium Powders, (2015) 1–7.
[7.9] D. Toma, W. Brandl, G. Marginean, Wear and corrosion behaviour of thermally sprayed cermet coatings, Surf. Coat. Technol. (2001) 149–158.
[7.10] L. Thakur, N. Arora, R. Jayaganthan, R. Sood, An investigation on erosion behavior of HVOF sprayed WC-CoCr coatings, Appl. Surf. Sci. 258 (2011) 1225–1234.
[7.11] S. Hong, Y. Wu, Q. Wang, G. Ying, G. Li, W. Gao, et al., Microstructure and cavitation-silt erosion behavior of high-velocity oxygen-fuel (HVOF) sprayed Cr3C2-NiCr coating, Surf. Coatings Technol. 225 (2013) 85–91.
[7.12] H.Y. Lee, S.H. Jung, S.Y. Lee, Y.H. You, K.H. Ko, Correlation between Al2O3 particles and interface of Al-Al2O3 coatings by cold spray, Appl. Surf. Sci. 252 (2005) 1891–1898.
[7.13] H. Assadi, T. Schmidt, H. Richter, J.O. Kliemann, K. Binder, F. Gartner, et al., On parameter selection in cold spraying, J. Therm. Spray Technol. 20 (2011) 1161–1176.
[7.14] R. Miranda, J. Gandra, P. Vilaca, L. Quintino, T. Santos, Surface Modification by Solid State Processing, Woodhead Publishing Limited, 2008.
[7.15] R.S. Bolton-King, J.P.O. Evans, C.L. Smith, J.D. Painter, D.F. Allsop, W.M. Cranton, What are the Prospects of 3D Profiling Systems Applied to Firearms and Toolmarks Identification?, AFTE J. 42 (2010) 23–33.
[7.16] W. Li, K. Yang, D. Zhang, X. Zhou, X. Guo, Interface behavior of particles upon impacting during cold spraying of Cu/Ni/Al mixture, Mater. Des. 95 (2016) 237–246.
[7.17] C.J. Lee, J.C. Huang, P.J. Hsieh, Mg based nano-composites fabricated by friction stir processing, Scr. Mater. 54 (2006) 1415–1420.
[7.18] A. Toumpis, A. Galloway, S. Cater, N. McPherson, Development of a process envelope for friction stir welding of DH36 steel - A step change, Mater. Des. 62 (2014) 64–75.
[7.19] S.R. Sharma, Z.Y. Ma, R.S. Mishra, Effect of friction stir processing on fatigue behavior of A356 alloy, Scr. Mater. 51 (2004) 237–241.
[7.20] Z.Y. Ma, S.R. Sharma, R.S. Mishra, Effect of multiple-pass friction stir processing on microstructure and tensile properties of a cast aluminum-silicon alloy, Scr. Mater. 54 (2006) 1623–1626.
[7.21] Struers, Metallographic preparation of thermal spray coatings, 2014.
[7.22] International ASTM Standard, ASTM E2109 − 01: Standard Test Methods for Determining Area Percentage Porosity in Thermal Sprayed Coatings, (2006) 1–8.
[7.23] H. Assadi, F. Gärtner, T. Stoltenhoff, H. Kreye, Bonding mechanism in cold

gas spraying, Acta Mater. 51 (2003) 4379–4394.
[7.24] A. Slipenyuk, V. Kuprin, Y. Milman, J.E. Spowart, D.B. Miracle, The effect of matrix to reinforcement particle size ratio (PSR) on the microstructure and mechanical properties of a P/M processed AlCuMn/SiCp MMC, Mater. Sci. Eng. A. 381 (2004) 165–170.
[7.25] A.N. Albakri, B. Mansoor, H. Nassar, M.K. Khraisheh, Thermo-mechanical and metallurgical aspects in friction stir processing of AZ31 Mg alloy—A numerical and experimental investigation, J. Mater. Process. Technol. 213 (2013) 279–290.
[7.26] R. Bauri, D. Yadav, G. Suhas, Effect of friction stir processing (FSP) on microstructure and properties of Al-TiC in situ composite, Mater. Sci. Eng. A. 528 (2011) 4732–4739.
[7.27] H.S. Arora, H. Singh, B.K. Dhindaw, Wear behaviour of a Mg alloy subjected to friction stir processing, Wear. 303 (2013) 65–77.
[7.28] B.M. Darras, M.K. Khraisheh, F.K. Abu-Farha, M.A. Omar, Friction stir processing of commercial AZ31 magnesium alloy, J. Mater. Process. Technol. 191 (2007) 77–81.
[7.29] D. Yadav, R. Bauri, Effect of friction stir processing on microstructure and mechanical properties of aluminium, Mater. Sci. Eng. A. 539 (2012) 85–92.
[7.30] C.I. Chang, X.H. Du, J.C. Huang, Achieving ultrafine grain size in Mg-Al-Zn alloy by friction stir processing, Scr. Mater. 57 (2007) 209–212.
[7.31] J.D. Embury, D.J. Lloyd, T.R. Ramachandran, 22 - Strengthening Mechanisms in Aluminum Alloys, in: A.K. Vasudevan, R.D. Docherty (Eds.), Alum. Alloy. Res. Appl., Elsevier, 1989: pp. 579–601.
[7.32] J.E. Hatch, Aluminium: Properties and Physical Metallurgy, American Society for Metals, 1984.
[7.33] D.R. Askeland, P.P. Fulay, D.K. Bhattacharya, Essentials of Materials Science and Engineering, Second Edi, Cengage Learning, Canada, 2010.
[7.34] W.D.J. Callister, Fundamentals of Materials Science and Engineering, 2001.
[7.35] Y.S. Sato, S.H.C. Park, H. Kokawa, Microstructural factors governing hardness in friction-stir welds of solid-solution-hardened Al alloys, Metall. Mater. Trans. A. 32 (2001) 3033–3042.
[7.36] H.S. Grewal, H.S. Arora, H. Singh, a. Agrawal, Surface modification of hydroturbine steel using friction stir processing, Appl. Surf. Sci. 268 (2013) 547–555.
[7.37] Y. Chen, H. Ding, J. Li, Z. Cai, J. Zhao, W. Yang, Influence of multi-pass friction stir processing on the microstructure and mechanical properties of Al-5083 alloy, Mater. Sci. Eng. A. 650 (2016) 281–289.
[7.38] C.N. Panagopoulos, E.P. Georgiou, Cold rolling and lubricated wear of 5083 aluminium alloy, Mater. Des. 31 (2010) 1050–1055.
[7.39] ASTM International, ASTM E112-13: Standard test methods for determining average grain size, ASTM Int. (2013) 1–28.
[7.40] H.S. Khare, D.L. Burris, A quantitative method for measuring nanocomposite dispersion, Polymer (Guildf). 51 (2010) 719–729.
[7.41] K. Sugiyama, S. Nakahama, S. Hattori, K. Nakano, Slurry wear and cavitation erosion of thermal-sprayed cermets, Wear. 258 (2005) 768–775.
[7.42] H.M. Hawthorne, B. Arsenault, J.P. Immarigeon, J.G. Legoux, V.R. Parameswaran, Comparison of slurry and dry erosion behaviour of some HVOF thermal sprayed coatings, Wear. 225–229 (1999) 825–834.
[7.43] A. V. Levy, The solid particle erosion behavior of steel as a function of microstructure, Wear. 68 (1981) 269–287.
[7.44] K. Ghosh, T. Troczynski, A.C.D. Chaklader, Aluminum-Silicon Carbide Coatings by Plasma Spraying, 7 (1998) 78–86.

[7.45] S. Dodds, A.H. Jones, S. Cater, Tribological enhancement of AISI 420 martensitic stainless steel through friction-stir processing, Wear. 302 (2013) 863–877.
[7.46] D. Aquaro, E. Fontani, Erosion of ductile and brittle materials, Meccanica. 36 (2001) 651–661.
[7.47] S.A. Alidokht, P. Manimunda, P. Vo, S. Yue, R.R. Chromik, Cold spray deposition of a Ni-WC composite coating and its dry sliding wear behavior, Surf. Coatings Technol. 308 (2016) 424–434.
[7.48] S. Ahmad Alidokht, P. Vo, S. Yue, R.R. Chromik, Erosive wear behavior of Cold-Sprayed Ni-WC composite coating, Wear. 376–377 (2017) 566–577.
[7.49] D. Deschuyteneer, F. Petit, M. Gonon, F. Cambier, Influence of large particle size – up to 1.2 mm – and morphology on wear resistance in NiCrBSi/WC laser cladded composite coatings, Surf. Coatings Technol. 311 (2017) 365–373.
[7.50] S.A. Alidokht, P. Manimunda, P. Vo, S. Yue, R.R. Chromik, Cold spray deposition of a Ni-WC composite coating and its dry sliding wear behavior, Surf. Coatings Technol. 308 (2016) 424–434.
[7.51] S. Ahmad Alidokht, P. Vo, S. Yue, R.R. Chromik, Erosive wear behavior of Cold-Sprayed Ni-WC composite coating, Wear. 376–377 (2017) 566–577.
[7.52] D. Deschuyteneer, F. Petit, M. Gonon, F. Cambier, Influence of large particle size – up to 1.2 mm – and morphology on wear resistance in NiCrBSi/WC laser cladded composite coatings, Surf. Coatings Technol. 311 (2017) 365–373.
[7.53] Z. Zhang, D.L. Chen, Contribution of Orowan strengthening effect in particulate-reinforced metal matrix nanocomposites, Mater. Sci. Eng. A. 483–484 (2008) 148–152.
[7.54] I. Finnie, Erosion of surfaces by solid particles, Wear. 3 (1960) 87–103.
[7.55] M.A. Al-Bukhaiti, S.M. Ahmed, F.M.F. Badran, K.M. Emara, Effect of impingement angle on slurry erosion behaviour and mechanisms of 1017 steel and high-chromium white cast iron, Wear. 262 (2007) 1187–1198.
[7.56] Z.B. Zheng, Y.G. Zheng, W.H. Sun, J.Q. Wang, Erosion-corrosion of HVOF-sprayed Fe-based amorphous metallic coating under impingement by a sand-containing NaCl solution, Corros. Sci. 76 (2013) 337–347.
[7.57] N. Andrews, L. Giourntas, A.M. Galloway, A. Pearson, Effect of impact angle on the slurry erosion-corrosion of Stellite 6 and SS316, Wear. 320 (2014) 143–151.
[7.58] W. Wu, K.C. Goretta, J.L. Routbort, Erosion of 2014 Al reinforced with SiC or Al2O3 particles, Mater. Sci. Eng. A. 151 (1992) 85–95.
[7.59] Q. Fang, P. Sidky, M. Hocking, Erosive wear behaviour of aluminium based composites, Mater. Des. 18 (1997) 389–393.
[7.60] M.R. Ramesh, S. Prakash, S.K. Nath, P.K. Sapra, B. Venkataraman, Solid particle erosion of HVOF sprayed WC-Co/NiCrFeSiB coatings, Wear. 269 (2010) 197–205.
[7.61] A.J. Ninham, A. V Levy, The erosion of carbide-metal composites, Wear. 121 (1988) 347–361.
[7.62] N. Chawla, Y. Shen, Mechanical Behavior of Particle Reinforced Metal Matrix Composites, Adv. Eng. Mater. 3 (2001) 357–370.
[7.63] R. Miranda, Surface reinforcements of light alloys, in: Surf. Modif. by Solid State Process., Woodhead Publishing Limited, 2014: pp. 113–152.
[7.64] P.A. Karnezis, G. Durrant, B. Cantor, Characterization of Reinforcement Distribution in Cast Al-Alloy/SiCp Composites, Mater. Charact. 40 (1998) 97–109.
[7.65] H. Gül, F. Kili, M. Uysal, S. Aslan, A. Alp, H. Akbulut, Effect of particle

concentration on the structure and tribological properties of submicron particle SiC reinforced Ni metal matrix composite (MMC) coatings produced by electrodeposition, Appl. Surf. Sci. 258 (2012) 4260–4267.
[7.66] J. Singh, A. Chauhan, Overview of wear performance of aluminium matrix composites reinforced with ceramic materials under the influence of controllable variables, Ceram. Int. 42 (2015) 56–81.
[7.67] C.N. Machio, G. Akdogan, M.J. Witcomb, S. Luyckx, Performance of WC-VC-Co thermal spray coatings in abrasion and slurry erosion tests, Wear. 258 (2005) 434–442.

Chapter 8 Development of SprayStir on AISI 316 Stainless Steel

8.1 Introduction

The results presented previously (Chapter 6 and Chapter 7) demonstrate that combined cold spray (CS) and friction stir processing (FSP) (SprayStir) can successfully embed and distribute cermet and oxide reinforcements within an aluminium substrate, thereby producing an engineered metal matrix composite (MMC) surface layer. The work presented herein expands on the study detailed in Chapter 7 by investigating the application of SprayStir to AISI 316 steel. AISI 316 steel is used extensively in corrosive environments; however, its low erosion performance (in contrast to other readily available steels) limits its use in environments where erosion and corrosion both operate, for example within pipelines transporting aqueous slurry. Therefore, the aim of this chapter is to demonstrate if, and to what extent, SprayStir can enhance the erosion performance of AISI 316 over the as-received material.

Before discussing the results of this investigation, the current state-of-the-art research concerning the FSP of CS co-deposited coatings comprising a steel matrix will be discussed. Thereafter, the current state-of-the-art research on the erosion performance of steel-based MMCs will be presented.

8.1.1 A review of cold spray and friction stir processing of steel

Despite the reported improvements to the tribological and microstructural properties of different alloys by FSP [8.1, 8.2], the use of FSP on CS coated steel has not been extensively examined. In fact, it has not been possible to identify any studies that manufacture MMC surfaces using the SprayStir technique and evaluate their performance under slurry erosion conditions. The lack of research concerning the slurry erosion performance of SprayStirred steel MMCs is potentially due to the difficulties associated with FSP of steel alloys. For example, the high mechanical loads required to generate sufficient heat to plasticise the steel [8.3], in addition to the increased temperature of the tool (as compared to aluminium) during processing, necessitate the use of bespoke FSP machinery [8.3, 8.4]. This equipment requires considerable investment, whereas FSP of aluminium can be completed on modified milling machines. Consequently, the existing research regarding cold spray deposited MMCs with subsequent FSP is mainly limited to aluminium based MMCs [8.5–8.8].

However, one study was identified that assessed the effect of FSP on the tribological performance of mild steel reinforced with Al_2O_3 nano-composites [8.9]. The research group [8.9] introduced these reinforcements by manufacturing a channel along the length of the plate, which was subsequently packed with Al_2O_3 particles, and then traversed by the FSP tool. The authors [8.9] discovered that FSP generated a composite layer on the surface consisting of ultra-fine grains and the dispersed Al_2O_3 nanoparticles. The hardness of this reinforced composite surface was approximately three times greater than the as-received substrate [8.9]. Equally, the wear resistance of the reinforced MMC (assessed by pin-on-disc testing) was superior to the unreinforced alloy by measuring substantially lower weight loss (practically two or three times) when compared with the unreinforced steel substrate [8.9]. This result was attributed to higher hardness from the refined microstructure and the homogeneously dispersed Al_2O_3 nanoparticles [8.9].

FSP has also been applied to HVOF deposited cermet coatings. For example, Morisada et al. [8.10] reported a 65% increase in the hardness of a friction stir processed, HVOF deposited MMC over the as-deposited coating. The authors [8.10] attributed this to the refinement and improved distribution of the tungsten and chromium carbides. Additionally, defects such as microcracking and porosity were eliminated post-FSP [8.10].

8.1.2 Erosion and corrosion performance of steel MMCs

Steel-based MMCs have gathered interest in recent years due to the increased erosion performance that they offer over unreinforced steel [8.11–8.15]. The present study examines MMCs produced by SprayStir. However, MMCs can be produced using several different manufacturing processes. Therefore, to explain the mechanisms that enhance the erosion performance of the SprayStirred MMCs (when compared with the as-received steel), this section will discuss steel MMCs produced by alternative surface engineering processes.

Betts et al. [8.16] manufactured MMC surfaces from AISI 316 powder, reinforced with either alumina, tungsten carbide or chromium carbide by direct laser deposition [8.16]. The MMCs reinforced with tungsten carbide or chromium carbide enhanced the erosion performance of AISI 316 by up to 100% and 150% respectively, over the as-received material. Furthermore, chromium carbide offered improved corrosion properties when compared with the as-received AISI 316 [8.16]. However, the authors [8.16] discovered that the addition of alumina offered no improvements to

the hardness or erosion performance of the MMC. Moreover, the erosion performance of the tungsten carbide and chromium carbide reinforced MMCs varied substantially depending on the deposition parameters, the total surface area exposed to the slurry and the orientation of the MMC surface with respect to the direction of flow [8.16].

The results presented in their study [8.16] highlight the benefits to the erosion performance of the alloy when different types of reinforcement are embedded in the substrate. While these results [8.16] show that particle reinforced MMC surfaces do improve the erosion performance of the as-received substrate, the study failed to examine the erosion performance of their specimens under direct impingement at a consistent angle of attack. Instead, the authors [8.16] measured the erosion rate by slurry pot testing; a method that impinges erodent particles at random angles of attack [8.17]. Using this method, the influence of the angle of attack cannot be determined [8.17, 8.18]. Furthermore, the relative erosion performance of each specimen was established by measuring the mass loss following pot-slurry testing [8.16]. This approach does not consider the variance in density between the different reinforcements and the as-received AISI 316. Therefore, the results [8.16] do not represent the actual quantity of material removed by the slurry from each specimen. Finally, the corrosion rate in Betts' study was established by salt spray testing [8.16]. As stated in Chapters 3 and 5, the combined effects of erosion and corrosion give rise to increased material loss, through a synergistic effect between the two degradation mechanisms; this has not been considered in Betts' study [8.16].

The present study advances the existing knowledge by assessing the effect of FSP on cold spray co-deposited MMCs on AISI 316 stainless steel. The erosion performance of the MMCs (pre- and post-FSP) was evaluated using the same approach as is detailed in previous chapters. However, the present study expands the breadth of analysis and investigation methods over those presented in Chapter 7 by establishing the contributing factors of erosion, corrosion and synergy to the total mass loss experienced by each specimen. The erosion performance of the various specimens was also measured under two different impingement angles (90° and 30°). Finally, nanoindentation was employed to precisely measure the hardness of the reinforcements and matrix in the as-deposited coatings and the SprayStirred MMCs.

8.2 Experimental Methods

8.2.1 Materials

WC-CoCr and Al_2O_3 reinforced MMC coatings were co-deposited on AISI 316 plates measuring approximately 250 x 130 x 6 mm, with the sprayed region measuring approximately 210 x 90 mm. The austenitic stainless steels (of which AISI 316 is a member), have been shown to exhibit excellent corrosion properties which make them suitable for use in the fabrication of components used within the mineral extraction industry [8.13, 8.14, 8.19]. However, the low hardness and poor erosion performance of AISI 316 make it unsuitable for use in highly erosive working environments [8.14, 8.16]. To overcome this deficiency, the present study seeks to enhance the erosion performance of AISI 316 through the addition of an MMC surface layer, produced by SprayStir. The co-deposited binder comprised AISI 316 powder particles [8.20]. This material was selected to ensure the stir zone would maintain the same chemical composition as the as-received AISI 316 substrate alloy.

The chemical composition of the co-deposited powders and the substrate is presented in Table 8-1 and Table 8-2 respectively. The average particle size was obtained from the powder manufacturer's data sheets [8.20–8.22] and validated by light optical microscopy. Additional information relating to the morphology of the reinforcing particles can be found in Chapter 7. The dissimilar size (Table 8-1) of the WC-CoCr and Al_2O_3 particles employed in this study is due to the reported enhanced deposition efficiency and increased adhesive strength of larger grades of Al_2O_3 [8.23].

Table 8-1 Powder composition [8.20–8.22]

Coating material	Composition (wt.%)	Average particle size (μm)
WC-CoCr	W - 10Co - 5.5C - 4.4Cr	31
Al_2O_3	$100Al_2O_3$	76
AISI 316	Fe – 17Cr - 12Ni – 12.5Mo – 1.5Mn – 0.7Si	20

Table 8-2 Chemical composition of AISI 316 substrate [8.24]

Element	C	Mn	P	S	Si	Cr	Ni	Mo
wt.%	0.08	2	0.045	0.03	0.75	16-18	10-14	2-3

*max values unless otherwise stated

8.2.2 Cold spray parameter development and deposition

The CS parameter development for co-deposition followed the same steps as those outlined in Chapter 7. Equally, the same CS equipment (CGT Kinetiks 4000 cold spray system and two 4000 series powder feeders) was employed to spray the feedstock powders. As before (Chapter 7), three reinforcement/binder ratios (30/70, 60/40, 90/10) were examined. However, unlike in previous chapters, the quantity (vol.%) of reinforcements within the deposited coating was measured using optical image analysis software (ImageJ).

The measured volume fractions of reinforcement phase for coatings produced using the three dosing ratios (30/70, 60/40, 90/10) are presented in Table 8-3. Table 8-4 contains the cold spray parameters used to deposit the three dosing ratios.

Fig. 8-1 and Fig. 8-2 depict the microstructure of the as-deposited WC-CoCr and Al_2O_3 MMCs when sprayed with the three reinforcement/binder ratios (30/70, 60/40, 90/10). Based on the results from the studies detailed in previous chapters (Chapter 7) and from the information gathered in this preliminary investigation, a deposition ratio of 90/10 (reinforcement to binder) for both the Al_2O_3 and WC-CoCr was selected for this study.

Using the processing parameters outlined in Table 8-4, the two reinforcement powders were independently co-deposited with the AISI 316 binder, resulting in a coating thickness of approximately 0.3 mm for both WC-CoCr and Al_2O_3 reinforced MMCs.

Table 8-3 Measured quantity (Vol.%) of reinforcement particles within the CS deposited coating for the three powder feeder dosing ratios (average over 3 measurements) (σ = std. deviation).

	Measured reinforcement concentration for each volumetric flow rate ratio (Vol.%)					
	30/70		60/40		90/10	
	Average	σ	Average	σ	Average	σ
WC-CoCr	20.8	1.6	41.4	2.3	68.4	1.1
Al_2O_3	4.6	0.5	11.7	1.6	23.7	1.7

Table 8-4 Optimised cold spray deposition parameters

Gas Pressure (MPa)	Gas Temperature (°C)	Scanning Speed (mm/s)	Stand-off Distance (mm)	Track spacing (mm)
4	800	500	20	1.5

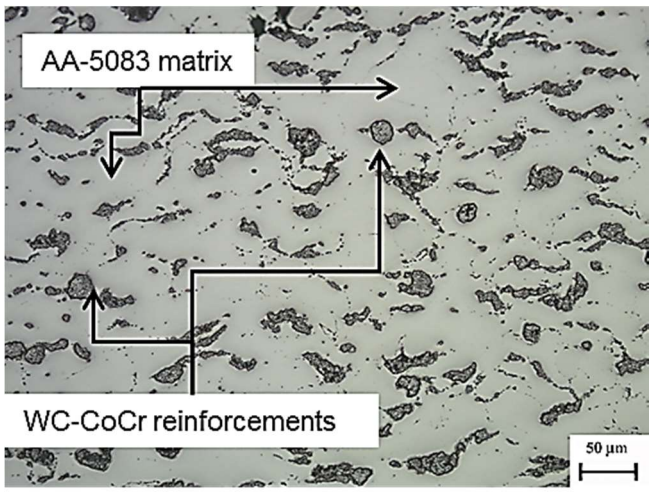

(a)

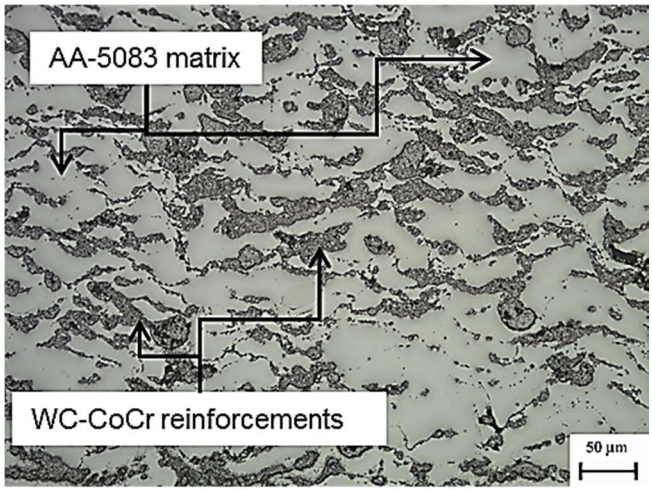

(b)

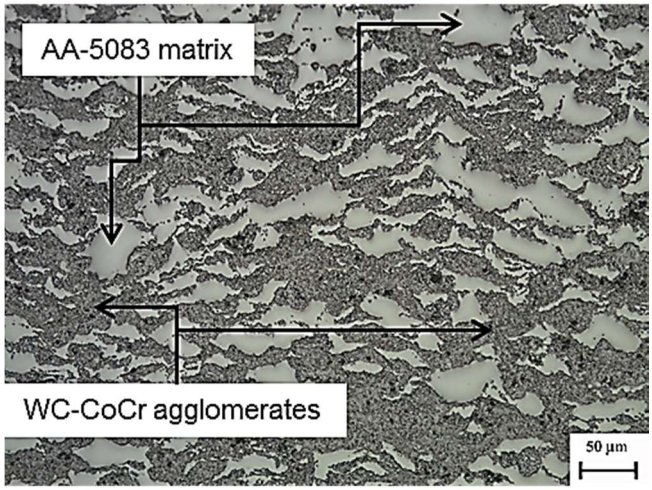

(c)

Fig. 8-1 Optical micrographs of the WC-CoCr reinforced MMC deposited using; (a) 30/70; (b) 60/40; (c) 90/10 (reinforcement to binder) dosing ratios [x500, Unetched]

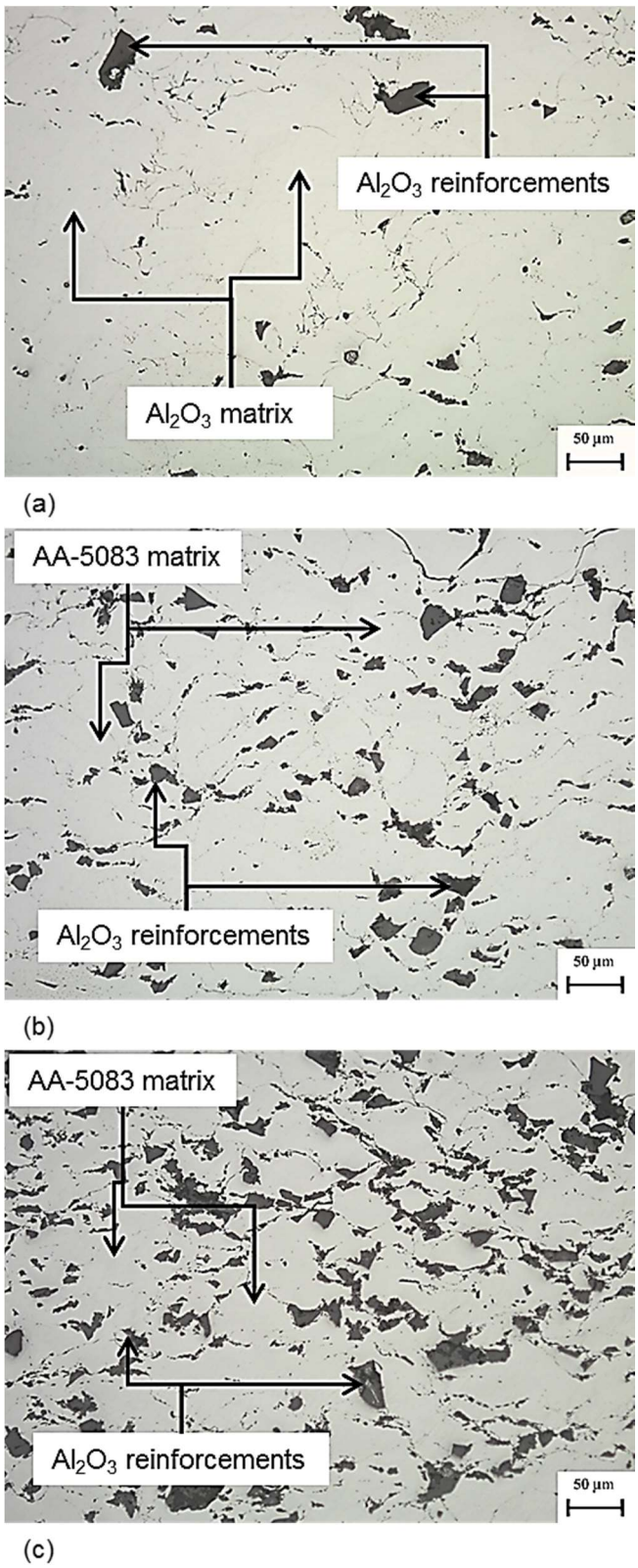

Fig. 8-2 Optical micrographs of the Al_2O_3 reinforced MMC deposited using; (a) 30/70; (b) 60/40; (c) 90/10 (reinforcement to binder) [x500, Unetched]

8.2.3 FSP process parameters

FSP of the coated plates was carried out using a TTI precision spindle friction stir welding/processing machine. In the present study, two tool configurations were utilised. The first, made of tungsten carbide and rhenium (W-Re), was used to process the uncoated AISI 316 and Al_2O_3 coated plates. This tool featured a threaded 5 mm pin [8.25] and incorporated a concentric circular pattern on the shoulder.

FSP of the WC-CoCr reinforced coating was initially attempted with a tungsten-rhenium (W-Re) tool. However, complete removal of the pin and shoulder features after approximately 40 mm of traverse necessitated the use of a polycrystalline boron nitride (pcBN) tool. To maintain consistency in the investigation, the pcBN tool had similar geometry to the W-Re tool, incorporating a 5 mm threaded pin and concentric circular features on the shoulder. However, due to the design of the cooling system for the pcBN tool, no tilt angle was applied. Additionally, the pcBN tool rotated in an anti-clockwise direction.

FSP processing parameters were established for the uncoated (as-received) AISI 316 by examining the effect of tool traverse and rotational speed, and plunge depth on the stir zone. The processing parameters that resulted in a high quality stir zone are offered in Table 8-5. For this study, the quality of the stir zone was based on the lack of surface voids and minimal flash [8.26].

Table 8-5 FSP parameters

Tool type	Pin length (mm)	Shoulder diameter (mm)	Rotational speed (rpm)	Traverse speed (mm/min)	Plunge depth (mm)	Tilt angle (°)
W-Re	5.7	18	250	100	5.9	2
pcBN	5.75	25.4	800	76	N/A	0

8.2.4 Characterisation of the MMCs

8.2.4.1 Microstructural characterisation

The steps employed to prepare the transverse cross-sections were identical to those used in previous chapters and the specific preparation stages are discussed in Chapter 4. The various regions within the stir zone that are discussed throughout this work are depicted in Fig. 8-3.

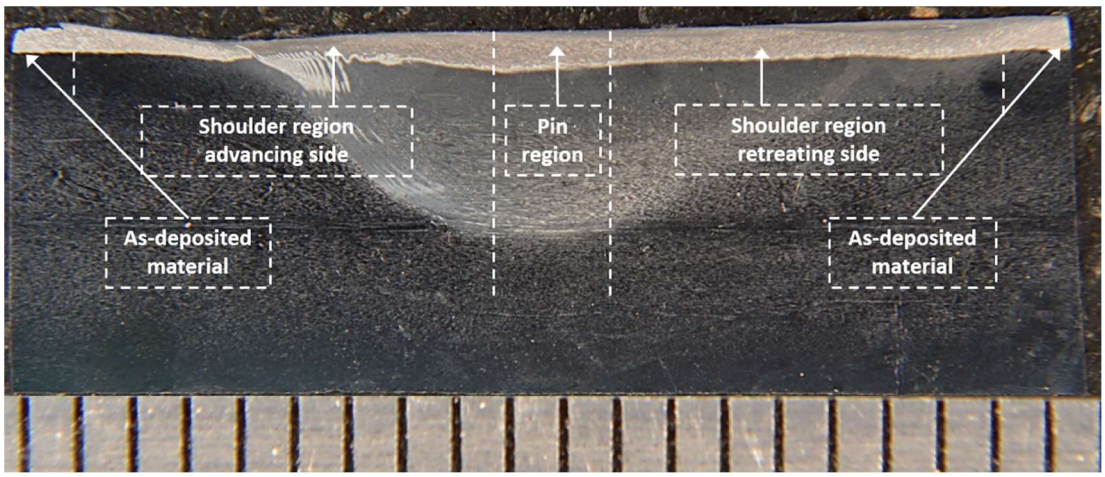

Fig. 8-3 Macroscopic cross-section of the SprayStirred WC-CoCr MMC

Micrographs of the prepared cross sections were captured using an Olympus G51X light optical microscope. The ratio of matrix to reinforcements within the pre- and post-FSP specimens was measured at [x500] magnification using image analysis software (ImageJ). Three micrographs were examined for each MMC, to establish the average reinforcing particle content. The coating porosity was measured by the method outlined in ASTM E2109 – 01 [8.27]. High magnification electron micrographs of the MMCs depicting the distribution of carbides and oxides within the matrix were obtained using a scanning electron microscope (SEM), (Hitachi S-3700). Energy dispersive spectroscopy (EDS), using Oxford Instruments INCA software, was employed to map the positions of various elements within the MMC and highlighted the distribution of the reinforcements. The average interparticle spacing between the reinforcing particles was established pre- and post-FSP using a statistical analysis approach developed by Khare & Burris [8.28]. This method [8.28] is expanded upon in Chapter 4 and Chapter 7.

8.2.4.2 Microhardness and nanoindentation analysis

The microhardness of the as-deposited and SprayStirred MMCs was measured using a Mitutoyo MVK-G1 microhardness tester with a 4-sided diamond indenter. Indents were made using an applied load of 200 gf at several locations across the width of the stir zone (Fig. 8-3).

The specific hardness of the reinforcements and matrix was determined using a nanoindentation system (Agilent Nano Indenter G200). The extended methodology for this process was developed by Oliver and Pharr [8.29, 8.30–8.33] and is discussed in Chapter 4. The surface of each specimen was indented at 10 μm intervals with the

indentations covering a total surface area of 100 μm^2. To directly compare the microhardness and nanohardness results, the nanohardness measurements were converted from GPa to HV using the conversion factor stated in ASTM E92 – 16 [8.34].

8.2.5 Experimental analysis of the erosion and corrosion

8.2.5.1 Slurry erosion assessment

Erosion testing was carried out using a recirculated slurry comprising 3.5% NaCl solution and FS9 grade angular silica particles with an average size of 0.4 mm. A detailed description and schematic diagram of the test apparatus are presented in Chapter 4.

The test coupons were sectioned from the CSed and SprayStirred plates using water-jet cutting equipment and any surface roughness was removed with 500-grit SiC paper. During testing, the test coupons were secured directly beneath the jet nozzle and fully submerged in the slurry solution. Specimen holders positioned at 30° and 90° to the slurry facilitated the assessment of different angles of attack.

The mass was established pre- and post-testing using a mass balance (calibrated to an accuracy of 0.1 mg) to calculate the total mass loss. Three specimens for each MMC were assessed to establish an average mass loss. The mass loss from an AISI 316 control specimen was measured before the assessment of the MMCs to ensure the erosive conditions remained consistent. Table 8-6 presents the specific test parameters for the erosion study and the approximate dimensions of the test coupons (samples).

Table 8-6 Solid liquid impingement test parameters.

Flow velocity (m/s)	Sand concentration (g/l)	Standoff distance (mm)	Duration (min)	Sample dimensions (mm)	Nozzle diameter (mm)
18	1	5	60	20x20	2.95

8.2.5.2 Volume loss assessment

The volume of the wear scars generated by the impinging slurry was established using a focal variation microscope (Alicona Infinite Focus G4) [8.35]. The system [8.35] constructs a digital 3D model by layering multiple images of the wear scar region at different focal lengths. This model contains numerous data points that are measured in relation to a reference plane that represents the original top

surface of the specimen. The volume of the wear scar is calculated by measuring the distance between the data points and the reference plane. An expanded description of the Alicona system is presented in Chapter 4.

8.2.5.3 Corrosion measurement

The contribution of erosion, corrosion and synergy [8.36–8.39] to the total mass loss from each specimen was established using the electrochemical test method discussed in Chapter 4. The mass loss from pure erosion (with no corrosion operating on the surface) was measured by applying cathodic protection (CP) to the specimen [8.40]. A potential of -1 V was applied to the sample (working electrode) which suppressed any anodic reaction thus preventing any corrosion from taking place on the specimen.

Anodic/cathodic polarisation scans were conducted under flowing slurry test conditions to establish the corrosion rate of each sample. Details concerning the specific test equipment and method are presented in Chapter 4. The corrosion mass loss rate was calculated in accordance with ASTM G102 - 89(2010) [8.41] using the measured current density and the equivalent weight. The equivalent weight (EW) of the various elements within the MMCs was established using the method outlined in Chapter 4.

The mass loss attributed to the synergistic effect of combined erosion-corrosion was calculated by subtracting the mass loss associated with pure erosion (CP) and corrosion (anodic polarisation) from the mass loss measured under free erosion-corrosion conditions (total mass loss).

8.3 Results and Discussion

8.3.1 Light optical microscopy

Before assessing the as-deposited and SprayStirred MMCs, it is of interest to first examine the microstructure when only the AISI 316 material (binder) is CS deposited. The micrographs presented in Fig. 8-4 show the as-deposited AISI 316 coating produced using the parameters presented in Table 8-4. Fig. 8-4b is a high magnification micrograph [x500] showing the deformation of the AISI 316 particles that comprise the as-deposited coating (Fig. 8-4a), as well as the porosity within the coating. The images (Fig. 8-4) exhibit only minimal particle deformation and approximately 3% porosity in the coating.

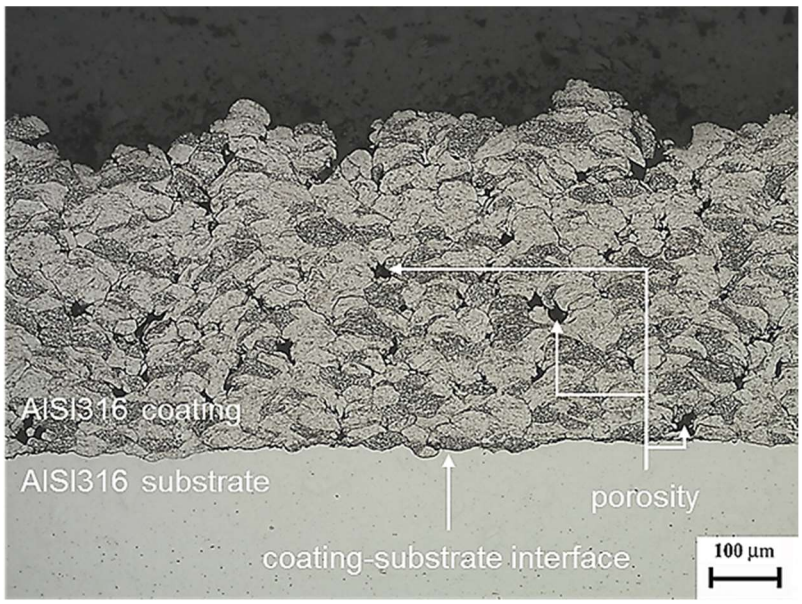

(a)

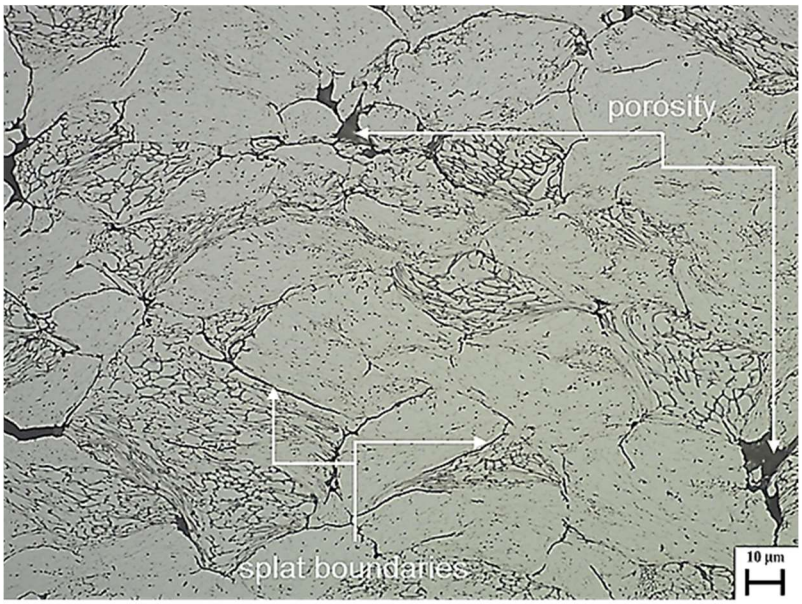

(b)

Fig. 8-4 Optical micrographs of the cold sprayed AISI 316 coating (unreinforced) on AISI 316 substrate; (a) [x100]; (b) high magnification micrograph of the coating denoted in (a) [x500] [Both electrolytically etched with 10% oxalic acid]

The presence of voids within the unreinforced AISI 316 coating is attributed to the deposition parameters used to deposit the feedstock powder. Specifically, the CS parameters used to manufacture the unreinforced AISI 316 coating were optimised for co-deposition; not for binder alone. As discussed in Chapter 2, when non-optimal spray parameters are used for a particular feedstock, the material may rebound from the surface [8.42, 8.43], or the coating may contain voids as the particles do not flatten

sufficiently upon contact with the substrate [8.44–8.46]. Therefore, it is not entirely unexpected that these parameters, when used to spray unreinforced AISI 316 (binder) alone, would not produce a defect-free coating.

Optical micrographs of the co-deposited WC-CoCr and Al_2O_3 reinforced MMCs are presented in Fig. 8-5 and Fig. 8-6 respectively. Both MMCs (Fig. 8-5 and Fig. 8-6) depict minimal observable porosity and no cracking within the AISI 316 matrix. The porosity was measured in accordance with ASTM E2109 – 01 [8.27] with the results indicating an area percentage porosity less than 0.5%.

The lower porosity measured in the co-deposited coatings (near fully dense vs. 3% in the binder alone) was due to the continuous high velocity impact of the hard reinforcing particles on the previously deposited AISI 316 binder [8.47]. When the reinforcements impinge on the previously deposited material, they impart further deformation to the AISI 316 binder particles. This process is akin to shot peening and reduces the porosity within the coating [8.47–8.51]. Without the added shot peening effect [8.47] generated by the reinforcements, the AISI 316 binder particles are not travelling at sufficient velocity to fully deform and coalesce with the surrounding material, hence, giving rise to the porous microstructure depicted in Fig. 8-4. Additionally, the plasticity of the AISI 316 binder can retain the WC-CoCr and Al_2O_3 particles as they impact during the co-deposition process. Without the binder, the reinforcing particles would rebound from the surface, resulting in a reduced deposition efficiency.

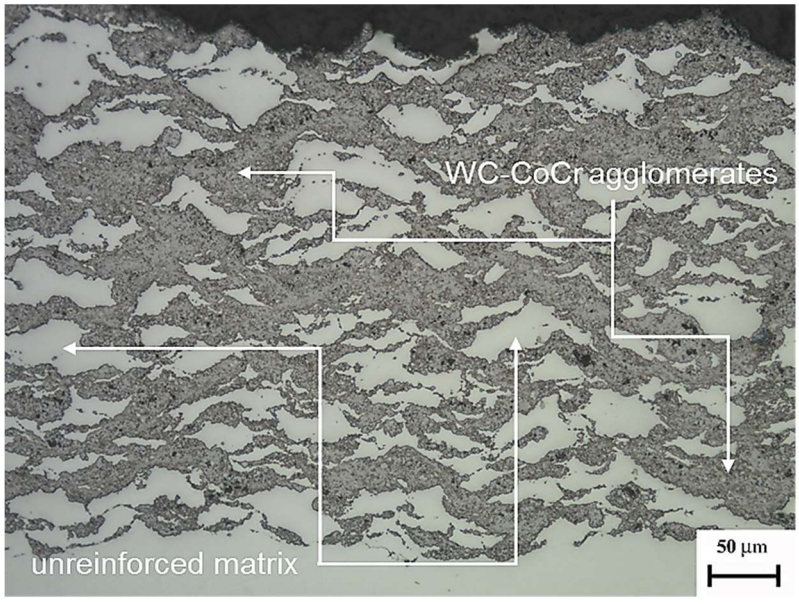

Fig. 8-5 Light optical micrograph showing the dark-shaded WC-CoCr reinforcement particles dispersed throughout the light-shaded AISI 316 matrix [x200, Unetched]

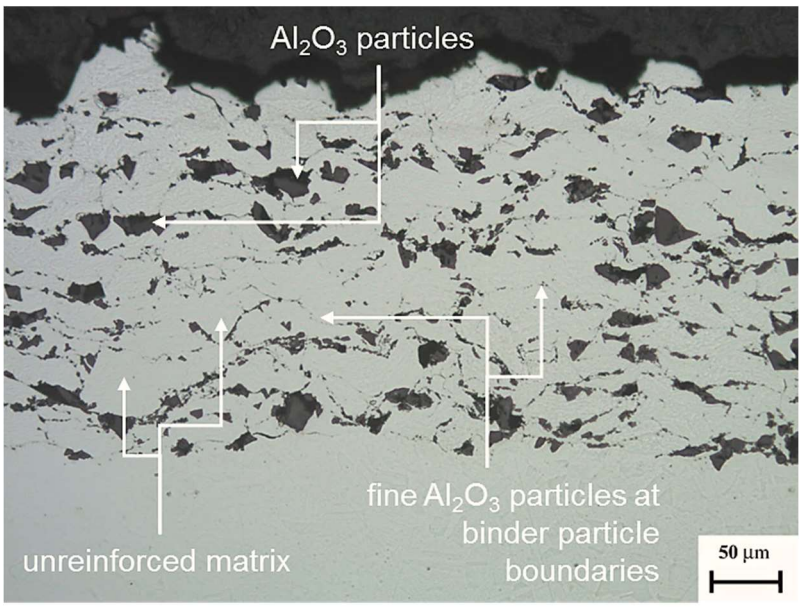

Fig. 8-6 Light optical micrograph showing the dark-shaded Al_2O_3 reinforcement particles dispersed throughout the light-shaded AISI 316 matrix [x200, Unetched]

As shown in Table 8-3, the concentration of reinforcing particles in the WC-CoCr reinforced coating (Fig. 8-5) was measured to be 68% (vol.%). While this represents a significant quantity of reinforcement, it is less than the 90% ratio that was supplied to the nozzle by the powder feeder.

According to Grigoriev et al. [8.52], the variation between the vol.% of reinforcement (68%) measured in the deposited coating and the quantity of feedstock delivered to the CS nozzle by the powder feeder (90%) is a consequence of the dissimilar material properties of the reinforcement and the binder. The authors [8.52] explain that, owing to the variation in critical velocity for the binder and reinforcement, the comparably ductile AISI 316 powder experiences greater deformation in contrast to the WC-CoCr particles. Therefore, the AISI 316 material deposits preferentially to the WC-CoCr. Another important observation from the micrographs (Fig. 8-5) is the agglomeration of WC-CoCr particles within the MMC. This agglomeration has given rise to regions containing high concentrations of carbide and regions that contain no observable reinforcing material.

The as-deposited Al_2O_3 MMC (Fig. 8-6) comprises 25% oxide and 75% matrix (Table 8-3). As with the WC-CoCr MMC, the quantity of reinforcements is significantly less than the quantity supplied by the powder feeder, and less still than the quantity of WC-CoCr deposited on the surface. Unlike the WC-CoCr particles, which can deform to some extent due to their CoCr binder, the Al_2O_3 particles experience no deformation upon contact with the AISI 316 [8.23]. As a result, the particles are more

susceptible to rebounding from the surface of the substrate [8.53] or fracturing on impact. Furthermore, the larger size of the Al_2O_3 oxides would result in them impacting the surface at a lower velocity [8.54]. Hence, the particles have less energy to embed in the AISI 316 binder. Fig. 8-7 depicts the approximate location within the as-deposited, and SprayStirred WC-CoCr reinforced MMCs from which the micrographs in Fig. 8-8 were taken.

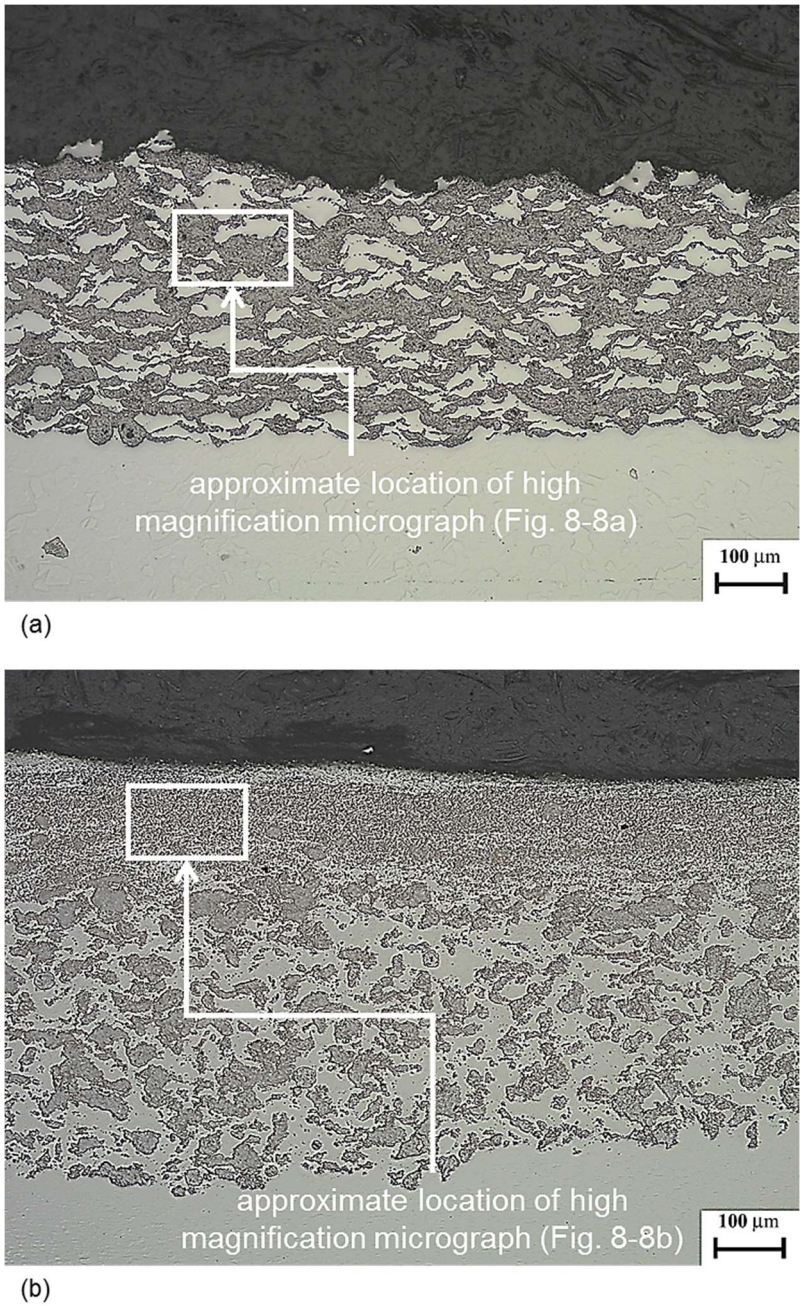

Fig. 8-7 Micrographs highlighting the approximate location of images shown in Fig. 8-8; (a) as-deposited cold spray coating; (b) SprayStirred MMC [x100, Unetched]

Fig. 8-7a exhibits the microstructure of the as-deposited WC-CoCr MMC in which no cracking is observed. Fig. 8-7a also illustrates the abrupt interface between the CS coating and the substrate. This abrupt change in material properties at this interface is a typical cause of coating delamination [8.55–8.58], which is discussed further in Chapter 2. Fig. 8-7b shows that post-FSP, the reinforcements are embedded within the AISI 316 matrix.

Fig. 8-8 presents higher magnification micrographs [x500] of the WC-CoCr reinforced MMC in the as-deposited (Fig. 8-8a) and SprayStirred condition (Fig. 8-8b). Fig. 8-8b demonstrates the significant dispersal of the WC-CoCr agglomerates observed in the as-deposited condition (Fig. 8-8a). This dispersal is restricted to the top surface of the stir zone, with larger as-deposited agglomerates located further from the surface (Fig. 8-7b).

Variation in temperature and material plasticity between the root and surface of the stir zone produced the dissimilar microstructure observed through the depth of the stir zone (Fig. 8-7b). The refinement of the agglomerates on the top surface is associated with increased temperature and shear force exerted by the shoulder as it stirs the plasticised material [8.59, 8.60]. During FSP, this shearing by the rotating tool deforms the agglomerates beyond the elastic limit of the Co-Cr binder and AISI 316 resulting in the dispersal of the individual carbides throughout the matrix. The deformation of the WC-CoCr agglomerates is highlighted in Fig. 8-9.

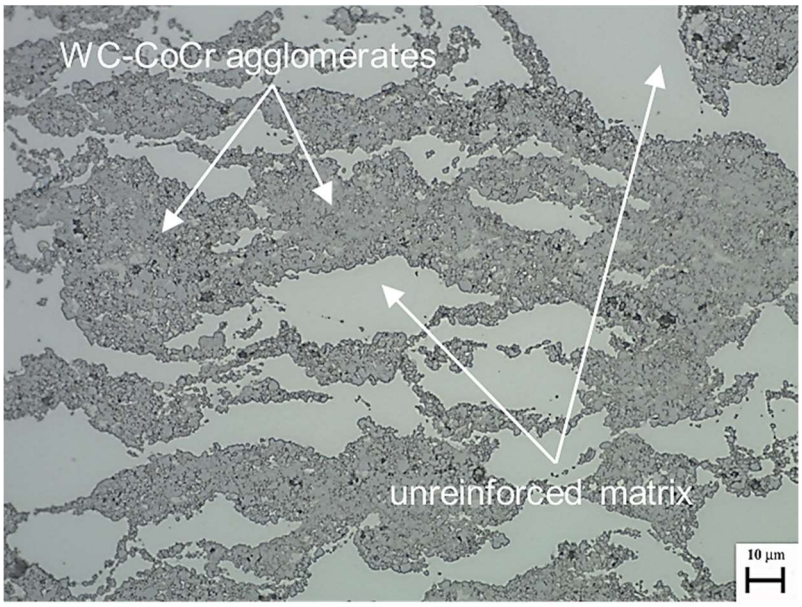

(a)

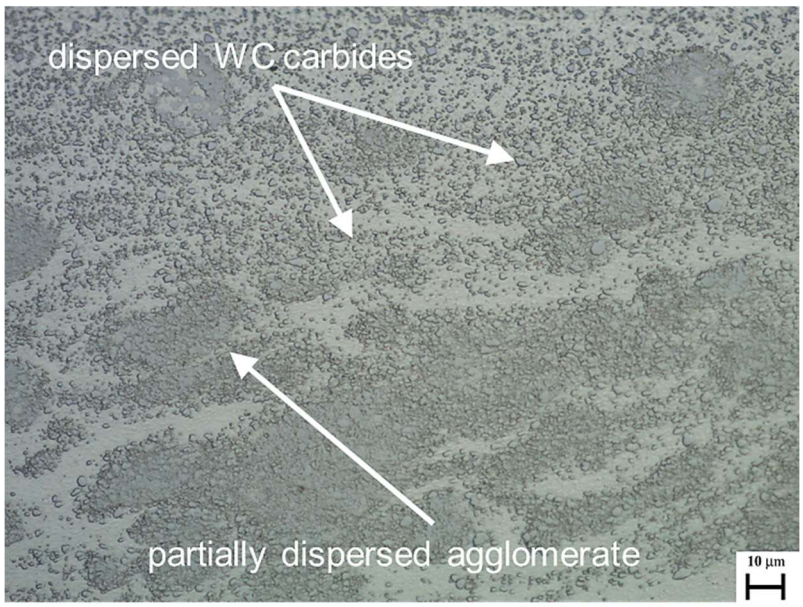

(b)

Fig. 8-8 Light optical micrographs of the WC-CoCr reinforced MMC; (a) As-deposited; (b) SprayStirred [x500, Unetched]

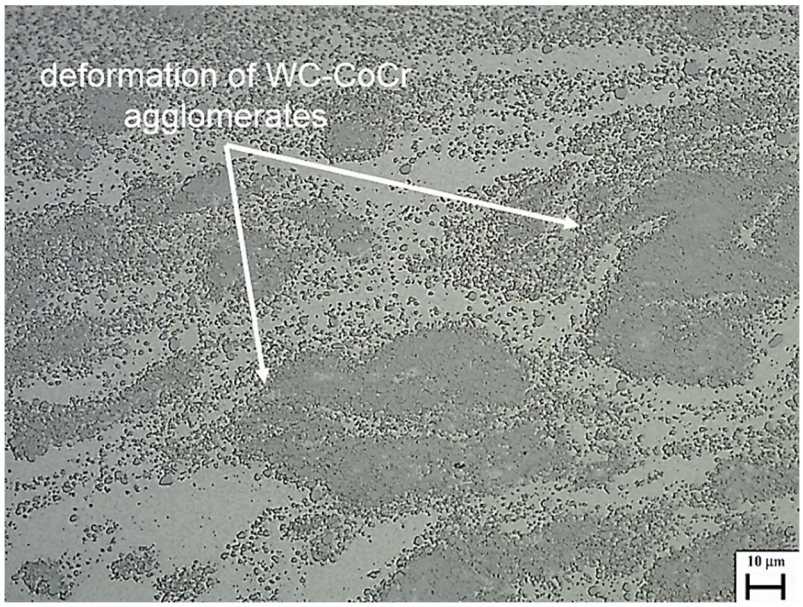

Fig. 8-9 Deformation of the WC-CoCr agglomerates [x500, Unetched]

The microstructure of the as-deposited and SprayStirred Al_2O_3 reinforced MMCs are exhibited in Fig. 8-10. Fig. 8-10a shows the as-deposited Al_2O_3 reinforcements and the areas of unreinforced AISI 316 matrix. Fig. 8-10b depicts the refinement of the as-deposited oxides (in contrast to Fig. 8-10a). During FSP, the shear force exerted by the tool fractured the large particles and distributed them

throughout the plasticised AISI 316 matrix, consequently homogenising the distribution of the reinforcements.

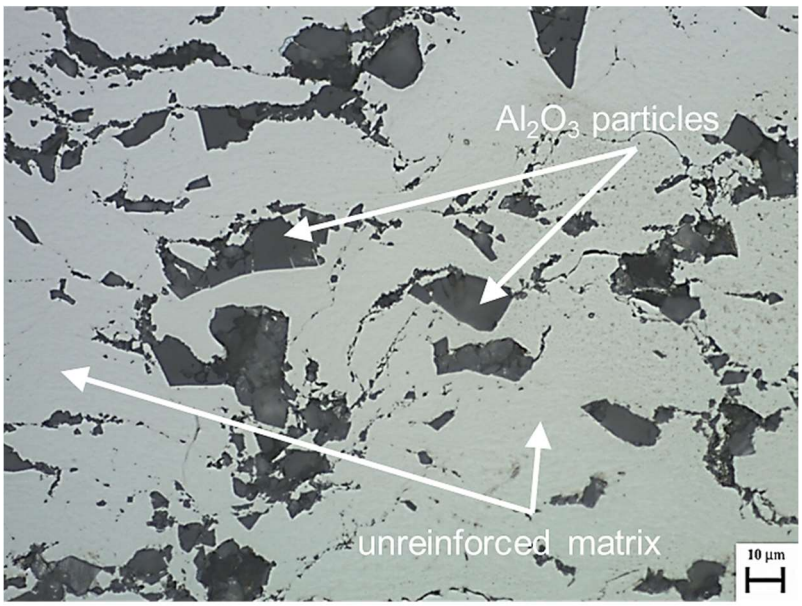

(a)

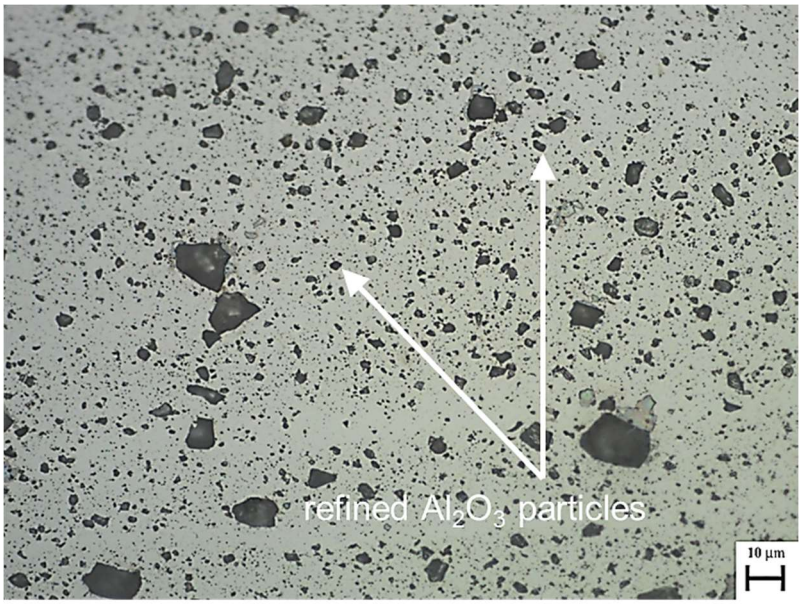

(b)

Fig. 8-10 Light optical micrographs of the Al_2O_3 reinforced MMC; (a) as-deposited; (b) SprayStirred [x500, Unetched]

8.3.2 Scanning electron microscopy

The as-deposited and SprayStirred MMCs were examined by SEM to characterise the distribution of carbide and oxide reinforcements within the AISI 316 matrix. Further, EDS facilitated mapping of the different elements within the MMCs to highlight the position of the reinforcements in the as-deposited and SprayStirred conditions. SEM micrographs of the as-deposited WC-CoCr and Al_2O_3 reinforced MMCs are depicted in Fig. 8-11 and Fig. 8-12.

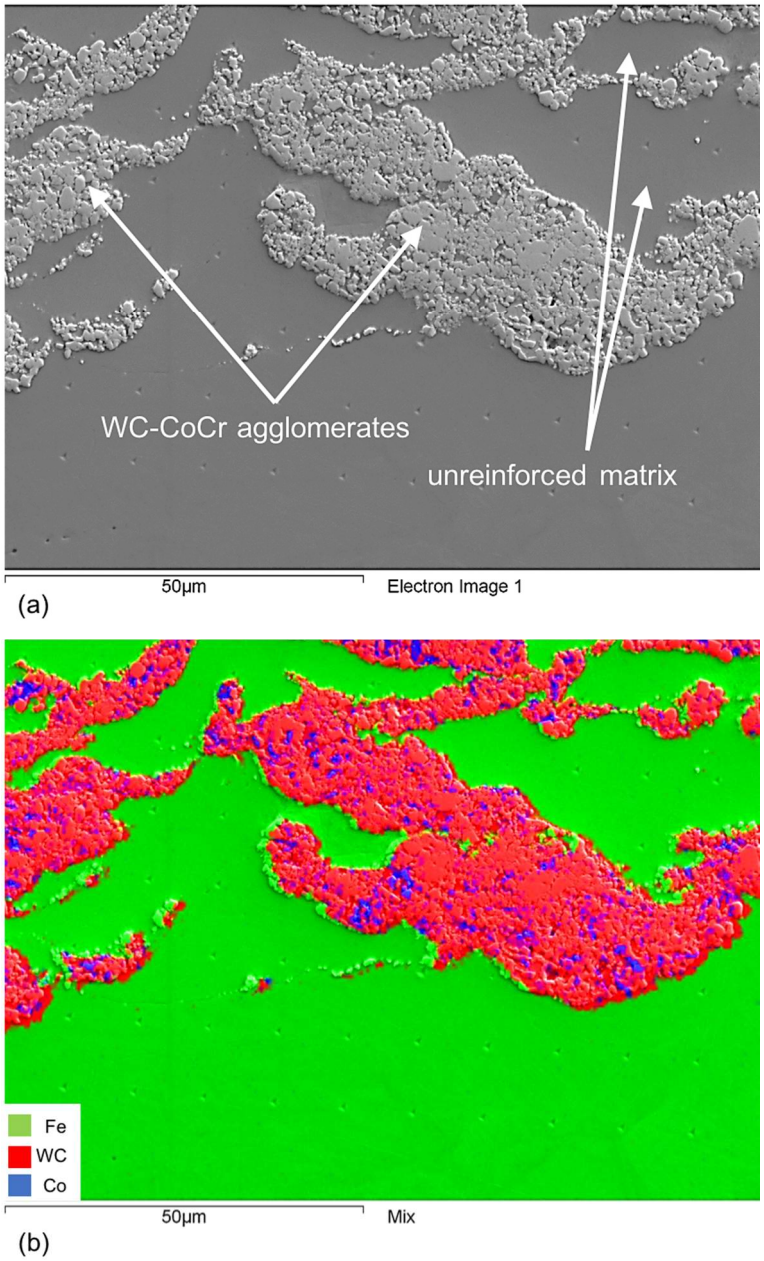

Fig. 8-11 As-deposited WC-CoCr reinforced coating; (a) SEM micrograph; (b) EDS elemental map [x500]

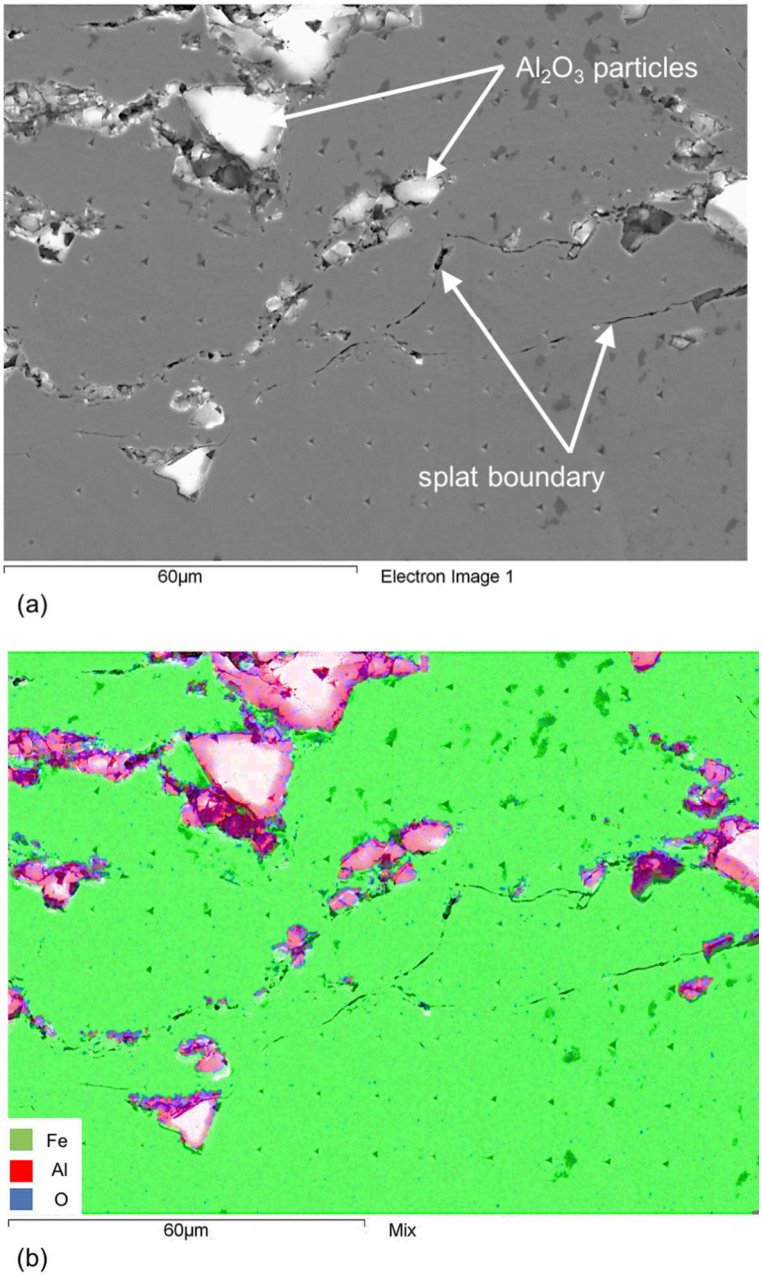

Fig. 8-12 As-deposited Al_2O_3 reinforced coating; (a) SEM micrograph; (b) EDS elemental map [x500]

The images (Fig. 8-11 and Fig. 8-12) confirm that the dark-shaded regions visible in the optical micrographs are the reinforcements. Moreover, the EDS map (Fig. 8-11) shows the agglomeration of the WC-CoCr particles. This occurs when multiple WC-CoCr particles coalesce upon impact with the surface of the substrate due to the plastic deformation of the WC-CoCr cermet. This deformation is only possible due to the presence of the comparably ductile cobalt-chromium binder [8.61].

Fig. 8-11a demonstrates the deformation of the cermet particles. The change in the pre-deposition powder morphology enhances the dispersion strengthening effect of the carbides, and is, therefore beneficial to the mechanical properties of the MMC as they act as an effective barrier to dislocation movement through the matrix [8.62]. However, due to the nature of the co-deposition process and the initial powder particle size, it was unavoidable that the coating would consist of discrete regions of AISI 316 and WC-CoCr. Consequently, the dispersion and load transfer strengthening generated by the reinforcements is limited [8.63, 8.64].

Fig. 8-12 depicts the distribution of reinforcements in the as-deposited Al_2O_3 coating. Unlike the WC-CoCr coating (Fig. 8-11), the Al_2O_3 oxides do not coalesce with one another when deposited on the surface. Instead, they are positioned between the AISI 316 binder particles. The oxides do not coalesce in the same manner at the WC-CoCr cermet feedstock, due to their lack of any inherent metallic binder [8.48].

The SEM micrograph of the as-deposited WC-CoCr reinforced MMC (Fig. 8-13a) highlights the distribution of individual carbides within the agglomerates. EDS analysis recorded only cobalt and chromium between adjacent carbides, thus confirming the lack of AISI 316 matrix.

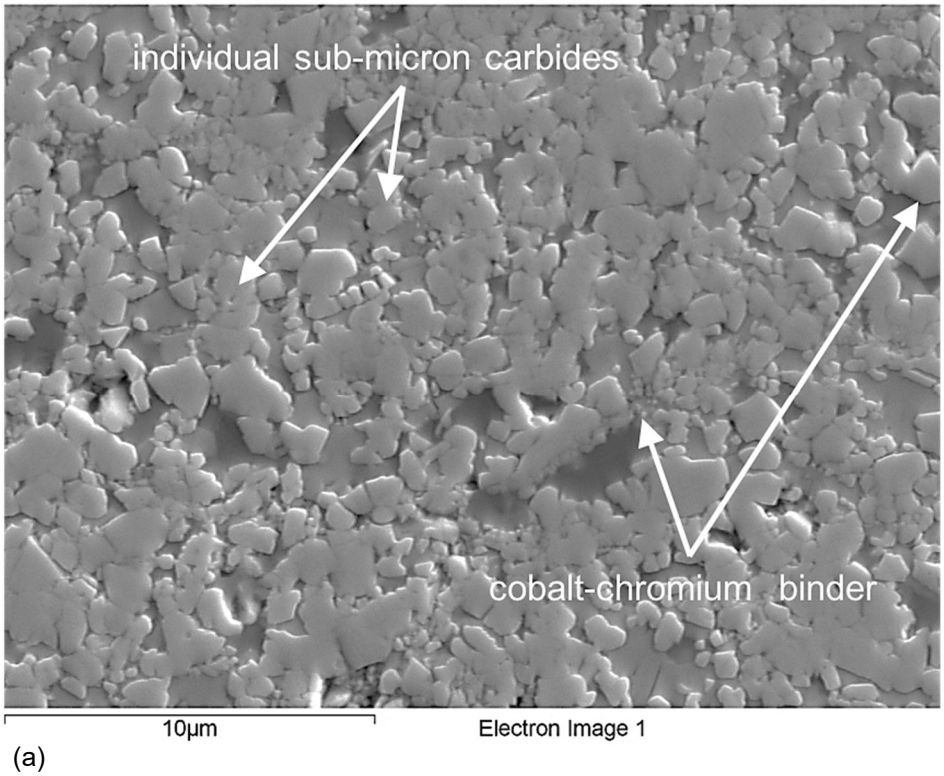

(a)

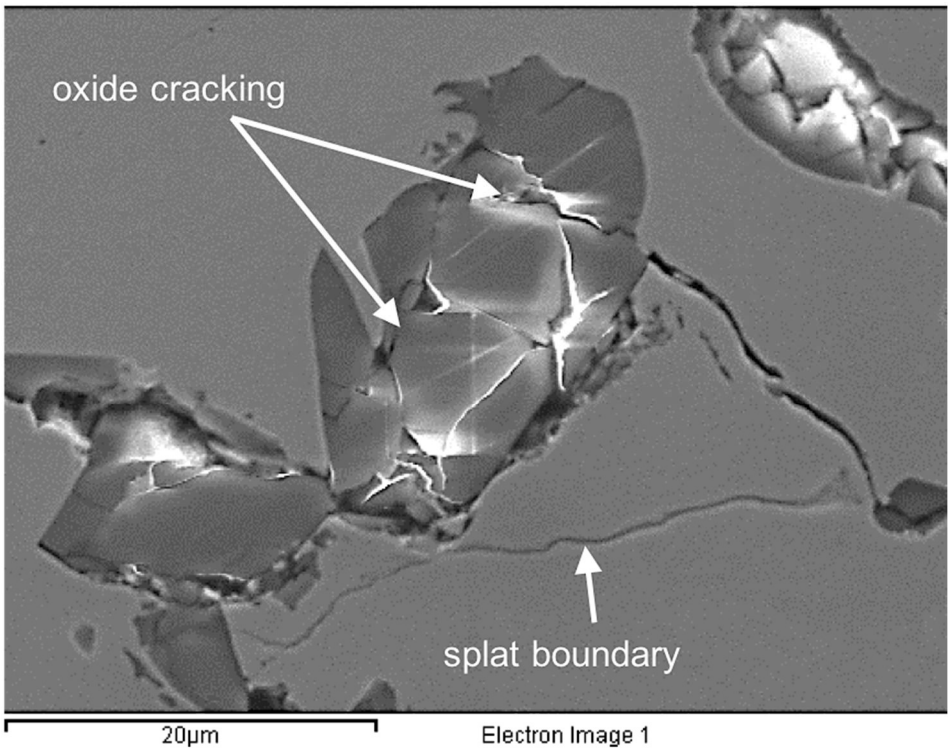

(b)

Fig. 8-13 SEM micrograph of; (a) WC-CoCr agglomerate [x5000]; (b) Al_2O_3 oxide particle [x2500]

Fig. 8-13b depicts Al_2O_3 particles at the boundaries of the deformed binder particles (splat boundaries). The presence of oxides at the boundary limits the contact area of adjacent AISI 316 binder particles. Additionally, the optical micrographs (Fig. 8-10) illustrate a decrease in the size of the Al_2O_3 within the coating, when compared to the feedstock powder. This size reduction is likely a consequence of the reinforcements colliding with one another and fracturing as they impact the surface of the substrate. Evidence of this can be seen in Fig. 8-13b which depicts cracking in the oxide particles. Shockley et al. also confirmed that some particle fracture takes place during the CS deposition of Al_2O_3 [8.65].

EDS element mapping was also employed to depict the position of specific elements within the MMC, and hence highlight the distribution of reinforcements pre- and post-FSP. The particle distribution before and after FSP for the Al_2O_3 reinforced MMC is exhibited in Fig. 8-14 and shows that FSP has successfully refined and improved the dispersion of the as-deposited reinforcing particles. EDS software calculated the wt.% of the various elements within the MMC coating, with the results offered in Table 8-7.

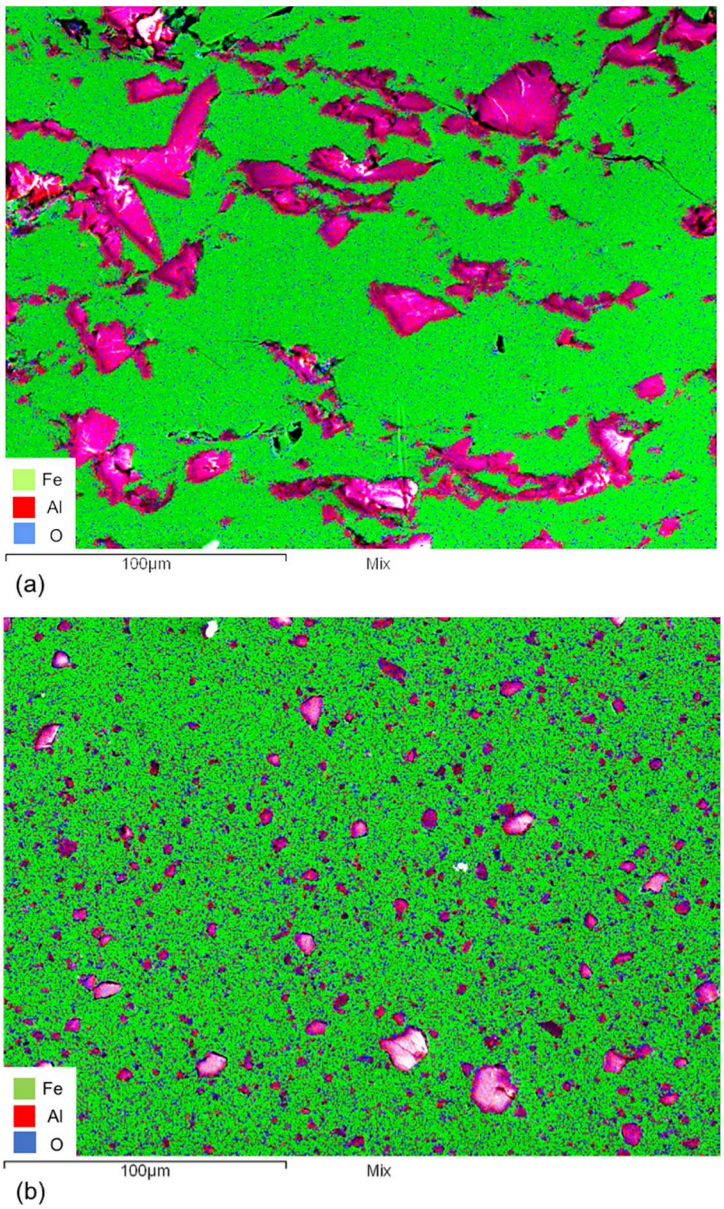

Fig. 8-14 EDS element maps showing the distribution of Al_2O_3 reinforcing particles; a) as-deposited; b) SprayStirred [x500]

Table 8-7 EDS elemental analysis (wt.%)

		Mn	Al	Cr	Ni	Co	W	Fe	O	Mo
As-deposited	WC-CoCr	0.62		10.46	4.73	4.91	49.63	28.60		
	Al_2O_3		10.56	14.72	9.80			54.01	7.12	2.51
SprayStirred (Retreating)	WC-CoCr	0.77		9.71	5.01	5.92	51.27	27.32		
	Al_2O_3	1.12	6.56	16.06	10.03			58.47	5.23	2.53
SprayStirred (Advancing)	WC-CoCr	0.57		10.16	5.08	5.46	50.24	28.49		
	Al_2O_3	1.33	9.18	15.71	10.22			56.02	5.52	2.02

Analysis of the EDS maps established that equivalent quantities of reinforcements were present in the as-deposited and SprayStirred MMCs. This outcome confirms that the reinforcing particles are redistributed during FSP, as opposed to being removed by the tool. A similar wt.% of reinforcing particles was measured in the retreating and advancing sides of the stir zone, thus demonstrating that the carbide and oxide reinforcements have been evenly distributed across the top surface of the stir zone.

8.3.3 Interparticle spacing

Existing research [8.66, 8.67] correlates the increased hardness of MMCs to improved homogeneity in particle distribution. Moreover, these studies [8.66, 8.67, 8.68] highlight enhanced hardness with decreasing interparticle spacing. A statistical method (discussed in Chapter 4) [8.28] was employed to evaluate the distribution of reinforcements and calculate the interparticle spacing in the as-deposited and SprayStirred MMCs. The results are presented in Table 8-8.

Table 8-8 Average interparticle spacing

	WC-CoCr	Al_2O_3
As-deposited (μm)	15.3	22.6
SprayStirred (μm)	1.4	2.6
Reduction in spacing (%)	91	88

In the as-deposited condition, the WC-CoCr reinforcements exhibit smaller interparticle spacing than was measured between the as-deposited Al_2O_3 particles. This outcome is primarily attributed to the lower vol.% of Al_2O_3 oxides within the MMC (Section 8.3.1). Furthermore, the structure of the WC-CoCr particles allows for slight deformation upon contact with the surface. This deformation enables the carbides to coalesce with surrounding particles and hence contributes to the reduced spacing between the WC-CoCr reinforcements.

The WC-CoCr cermet is comprised of micro and sub-micron carbides retained by a CoCr binder. Therefore, it is not necessary for FSP to refine any of the carbides. Instead, FSP deforms the WC-CoCr agglomerates beyond their elastic limit, thereby allowing the carbides to be distributed throughout the plasticised AISI 316 matrix. This requires less energy than what would be necessary to fracture particles and, therefore, accounts for the significant drop in the interparticle spacing in the WC-CoCr MMC.

8.3.4 Microhardness

The average hardness of the co-deposited MMC coatingss and the as-received AISI 316 are presented in Fig. 8-15. Based on the recorded measurements (Fig. 8-15), the as-deposited WC-CoCr coating possesses an average hardness of 580 HV, with the Al_2O_3 reinforced coating measuring 385 HV. These results correspond to a respective increase of 225% and 115% over the as-received AISI 316 substrate. The broad scatter of microhardness results presented in Fig. 8-15 is related to the specific locations on which the indents were produced and the highly dissimilar hardness of the reinforcements and AISI 316 matrix. Regions with increased carbide density, i.e. the agglomerates, measured a high hardness (due to the higher hardness of the carbides) and areas void of reinforcements exhibit a comparably low hardness.

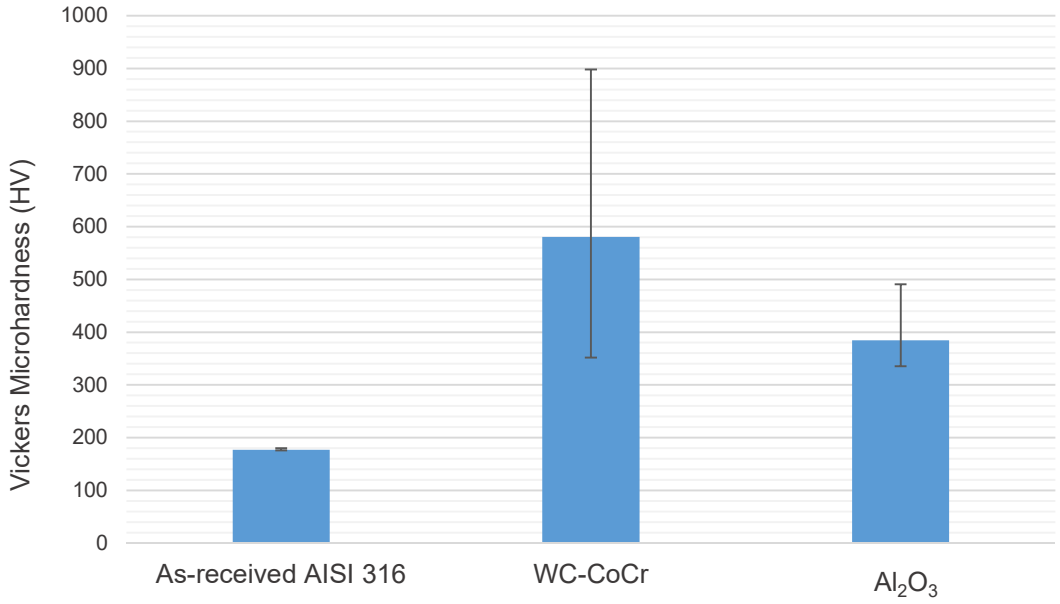

Fig. 8-15 Average hardness of the co-deposited MMC coatings with the associated maximum and minimum recorded microhardness values

Despite the broad scatter of measurements, the lowest recorded hardness of both MMCs is approximately 340 HV. This value corresponds to regions void of any reinforcing particles. Given that this is in excess of the 177 HV hardness of AISI 316, it can be inferred that the cold spray process imparted significant work hardening into the deposited AISI 316 particles as they deformed upon contact with the surface of the substrate (or previously deposited particles). A study by Hodder et al. [8.5] indicated that the addition of reinforcing particles increases the level of work hardening, as these hard particles impart further deformation to the previously deposited binder particles through a shot peening effect [8.5].

The microhardness results for the SprayStirred MMCs are presented in Fig. 8-16. For the as-received AISI 316 (no coating), FSP has increased the average hardness within the stir zone by approximately 27%. Similar increases in hardness have been widely reported in existing literature [8.69, 8.70] and are attributed to the grain refinement generated by FSP. To illustrate the grain refinement within the stir zone, etched optical micrographs of the as-received plate and the stir zone were examined (Fig. 8-17). The grain size was measured using the circular intercept approach outlined in ASTM E112-13 [8.71]. The measurement process [8.71] is discussed in detail in Chapter 4.

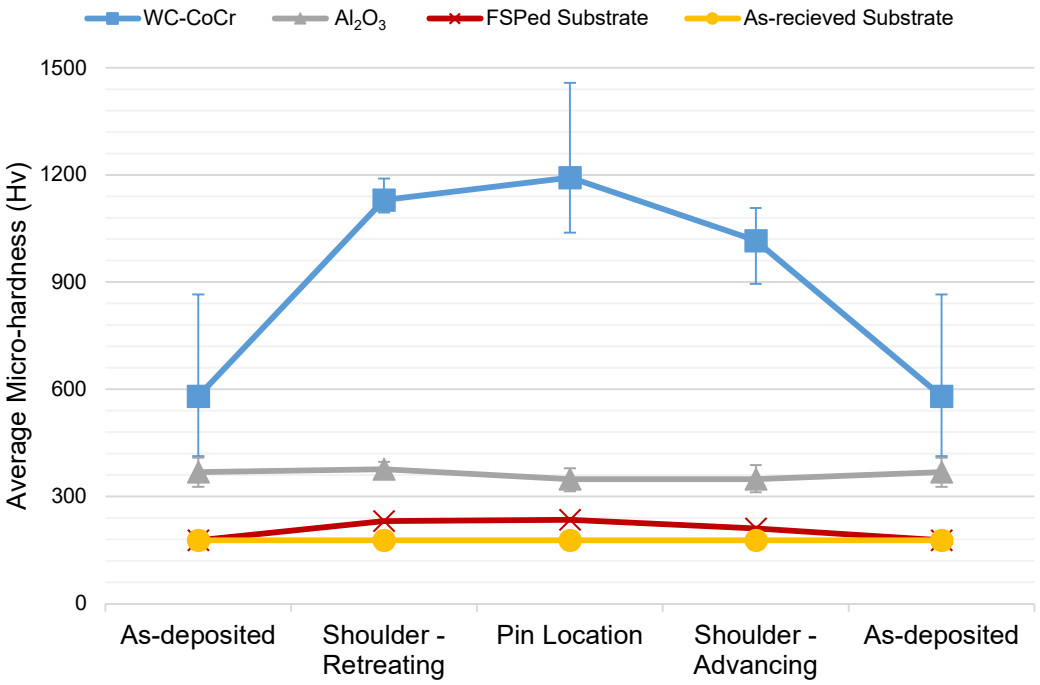

Fig. 8-16 Average microhardness values across the stir zone (Fig. 8-3)

The micrographs of the etched specimen (Fig. 8-17) confirm that grain refinement has occurred at the near-surface region of the stir zone (Fig. 8-17b). Moreover, grain size measurements of the as-received substrate and stir zone (Table 8-9) indicate that the average grain size has reduced correspondingly from approximately 22.2 μm to 10 μm. The hardness at the root of the stir zone (Fig. 8-17c), measured approximately 255 HV. The grain size measurements (Table 8-9) show that the average grain size at the root of the stir zone is approximately 68% smaller than in the near surface region, and 86% smaller than the as-received AISI 316.

Existing research indicates that cooling rate has a significant influence on the resulting grain structure of a material post-FSP. For instance, Chabok et al. [8.69]

reported a reduction in grain size of interstitial-free steel when active cooling (water and ice) was applied to the surface of the steel after the FSP tool shoulder had passed over. The authors [8.69] discovered that the region within the stir zone that experienced the highest cooling rate (near surface region) the grain size ranged from 30 to 50 nm. Further from the near-surface region, i.e. in the region with lower cooling rate, the grain size was found to range from 100 to 300 nm [8.69]. This difference in grain size corresponded to increased hardness (approximately 30%) in the near-surface region when compared with the hardness at the root of the stir zone [8.69].

Therefore, one possible explanation for the increased grain refinement identified at the root of the stir zone in this study is that the backing plate and tool bed acted as a heat sink. Consequently, the cooling rate was greater than at the near surface region which was allowed to air-cool once the shoulder has passed over. However, without measuring the temperature distribution at various points in the stir zone, it is not possible to discern precisely why increased grain refinement has occurred at the root of the stir zone.

The SprayStirred WC-CoCr specimen demonstrated a hardness increase of approximately 575% over the as-received AISI 316 in the centre of the stir zone (Fig. 8-16). This location correlates to the region (Fig. 8-3) that has experienced the most considerable particle refinement. Thus, the result is in agreement with previous work which attributes the increased hardness to the presence of fine, homogeneously dispersed reinforcements [8.67]. Furthermore, the SprayStirred WC-CoCr MMC was found to be approximately 105% harder than the as-deposited WC-CoCr coating, thereby highlighting the benefits of the SprayStir process over CS alone.

In the centre of the stir zone, the SprayStirred Al_2O_3 exhibited a 95% increase in hardness over the as-received AISI 316. This increase is a consequence of the matrix grain refinement (over the as-received AISI 316), as discussed above, and the presence of homogeneously distributed reinforcing particles within the stir zone.

The results indicate that there is no discernible difference in the hardness of the as-deposited Al_2O_3 coating and the SprayStirred Al_2O_3 MMC. The existing research indicates that the improved dispersion of reinforcements, in addition to the grain refinement achieved by FSP (as shown in Fig. 8-17), should yield higher hardness [8.69, 8.70, 8.72–8.73]. Therefore, it is necessary to explain why the results presented in Fig. 8-16 are not in agreement.

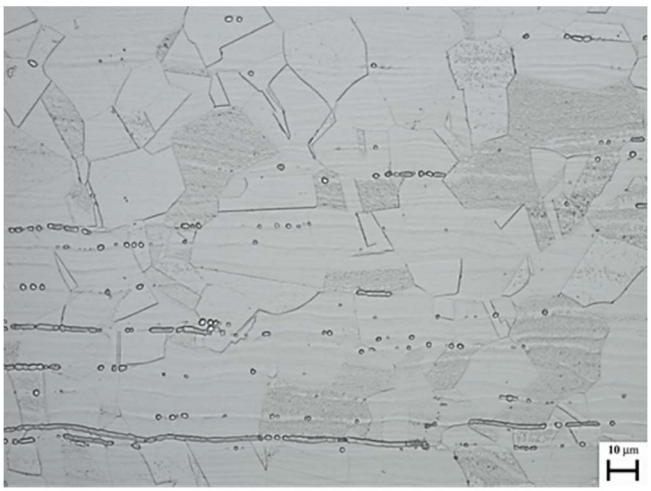

(a)

(b)

(c)

Fig. 8-17 Micrographs highlighting the grain structure of the unreinforced AISI 316; (a) as-received condition; (b) post-FSP in the near-surface region; (c) post-FSP at the root of the stir zone [x200 Electrolytic etch with 10% oxalic acid]

Table 8-9 Average grain size of unreinforced AISI 316 and the corresponding microhardness

	Average grain size (μm)	Average microhardness (HV)
As-received AISI316	22.2	177
Post-FSP, near-surface region	10.0	225
Post-FSP, root of the stir zone	3.2	255

Fig. 8-18 presents etched micrographs of the Al_2O_3 reinforced specimen in the as-deposited and SprayStirred condition. The images show that the as-deposited coating (Fig. 8-18a) has been embedded within the substrate by FSP (Fig. 8-18b). Furthermore, the highly-strained binder particles, visible in the as-deposited coating (Fig. 8-18c), have been mixed with the underlying substrate during FSP, forming the recrystallised grain structure observed in the stir zone (Fig. 8-18b). Consequently, the strain hardening in the coating (imparted by the plastic deformation of the AISI 316 binder during CS) has been removed post-FSP. Therefore, the hardening mechanism attributed to FSP (grain refinement) has effectively superseded the hardening mechanism associated with CS (strain hardening). Fig. 8-19 depicts the transition between the stir zone and the unaffected parent material. The image illustrates the grain refinement within the stir zone and the corresponding refinement of the Al_2O_3 oxides.

In the case of the WC-CoCr reinforced MMC, this same mechanism (grain refinement following the recrystallisation of the strain hardened binder particles) also likely occurs. However, the greater quantity of small, homogeneously distributed carbide reinforcements (as stated in Table 8-3) increases the hardness of the SprayStirred MMC through dispersion strengthening (hardening), whereby the hardness of the alloy is enhanced through the addition of small and uniformly distributed second-phase particles (precipitates) within the matrix [8.74]. These precipitates obstruct dislocation movement within the grains, thereby reducing the plasticity of the material (and increase the hardness) [8.74]. The lack of any apparent precipitation strengthening in SprayStirred Al_2O_3 is attributed to an insufficient quantity of reinforcements to impart hardening through this mechanism.

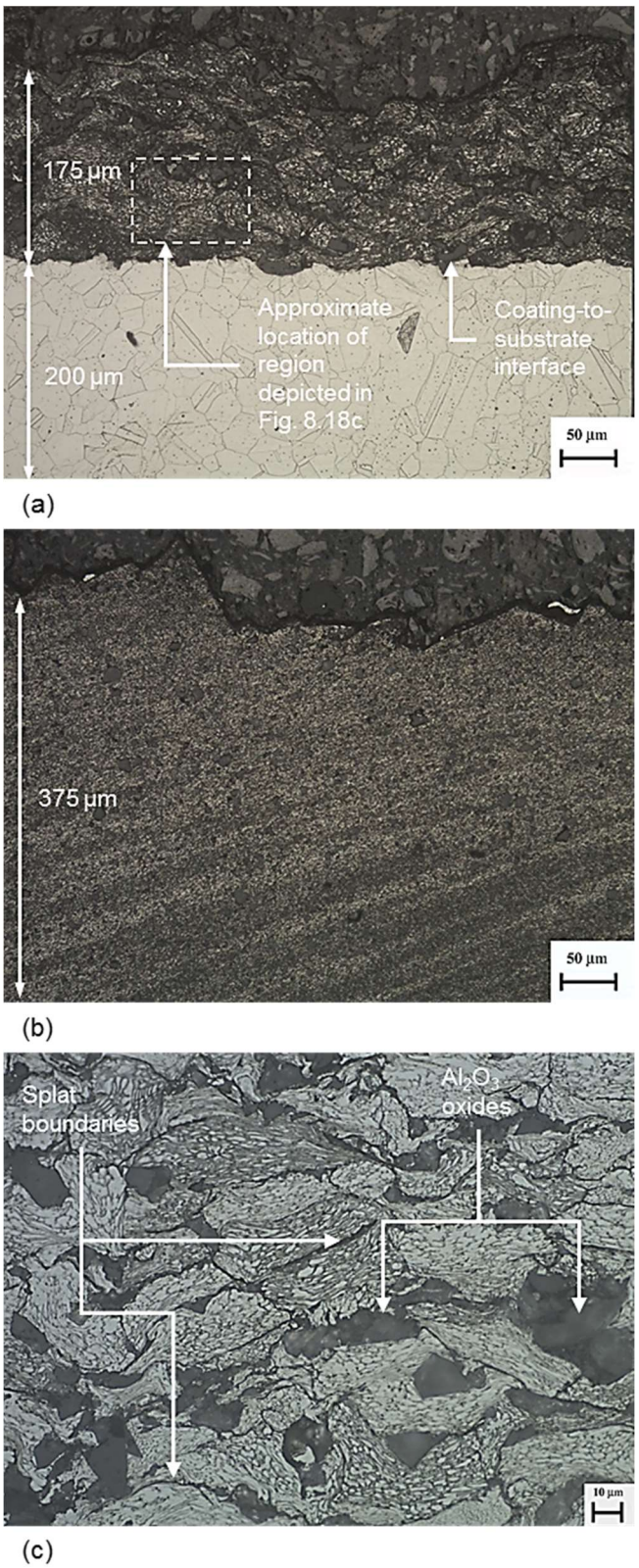

Fig. 8-18 Optical micrographs of the Al_2O_3 reinforced MMC; (a) as-deposited Al_2O_3 coating (no FSP) [x200]; (b) SprayStirred Al_2O_3 [x200]; (c) high-magnification micrograph of the as-deposited Al_2O3 coating [x500] [All electrolytically etched with 10% oxalic acid]

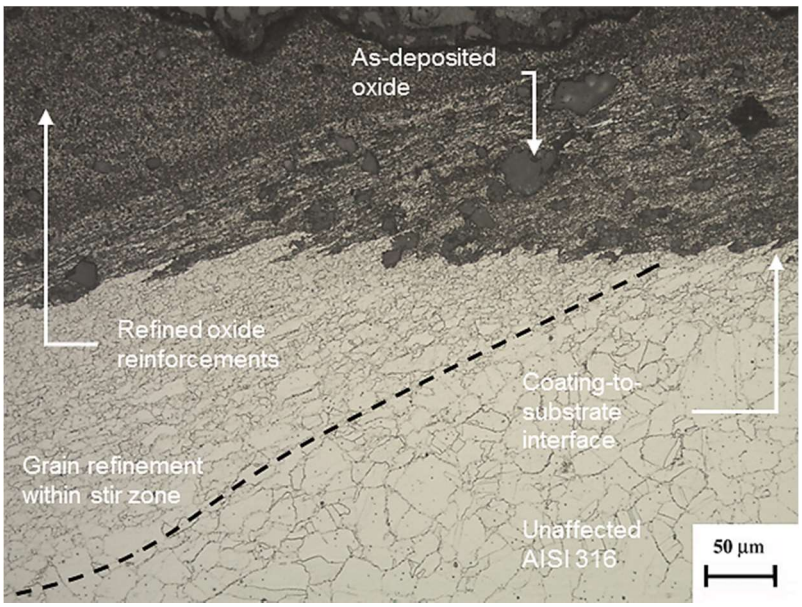

Fig. 8-19 Optical micrograph showing the transition region of SprayStirred Al_2O_3 [x200, Electrolytic etch with 10% oxalic acid]

8.3.5 Nanoindentation study

Due to the size of the microhardness indenter being greater than a single reinforcing grain or particle, it was not possible to measure the hardness of the matrix or reinforcement separately. Hence, nanoindentation was employed to establish the hardness of the matrix and reinforcements respectively.

Fig. 8-20a and Fig. 8-20b depict the nanoindents on the as-deposited WC-CoCr, and Al_2O_3 reinforced MMC coatings. Previous EDS analysis (Section 8.3.2) confirmed that the dark regions correspond to the reinforcements, with the light-shaded regions representing the AISI 316 matrix. Fig. 8-21a and Fig. 8-21b present the hardness of the indented region depicted in Fig. 8-20a and Fig. 8-20b as a hardness map.

The correlation between the location of the reinforcements (Fig. 8-20) and corresponding regions of high hardness (Fig. 8-21) is evident. For example, the maximum recorded hardness of the as-deposited WC-CoCr MMC was found to be in the range of 3500-4000 HV and was located at point g11 (Fig. 8-21a). Examination of the matching optical micrograph (Fig. 8-20a) highlights that this value aligns with the location of a large carbide dense region within the MMC.

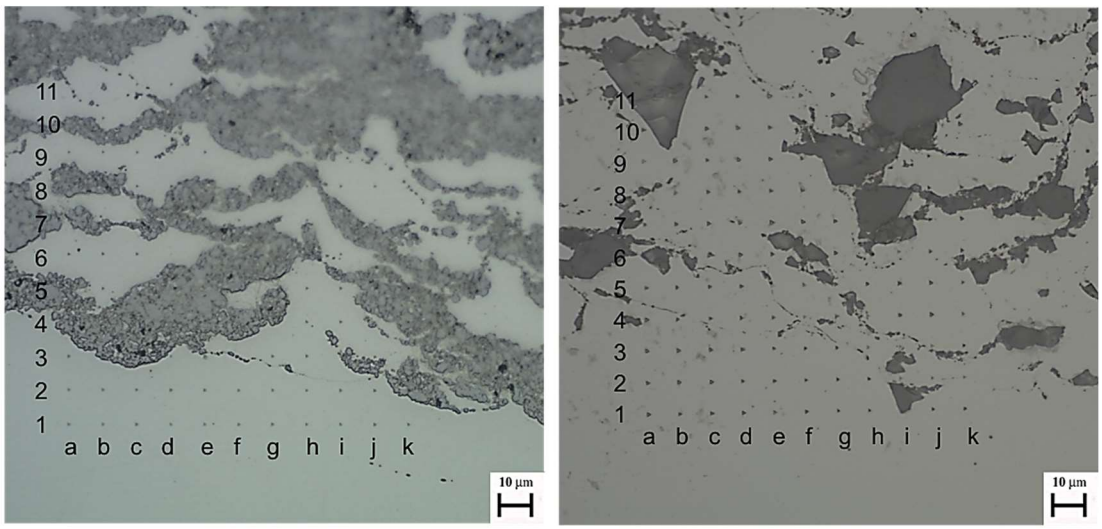

Fig. 8-20 Optical micrographs of nanoindentation impressions on; (a) WC-CoCr reinforced MMC; (b) Al_2O_3 reinforced MMC [x500, Unetched]

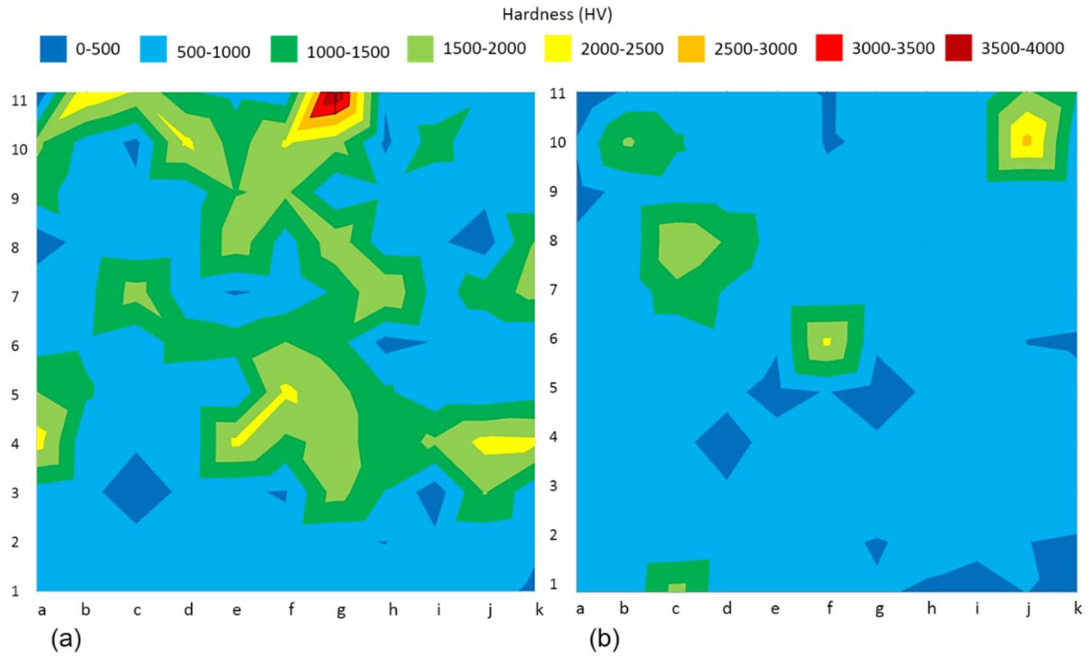

Fig. 8-21 Hardness maps of the examined area (Fig. 8-20); (a) WC-CoCr reinforced MMC; (b) Al_2O_3 reinforced MMC

The higher hardness measured by nanoindentation, in contrast to microhardness, is attributed to the inability of the AISI 316 matrix to support the reinforcing particles under load from the microhardness apparatus. The matrix located behind the reinforcing particles plastically deforms with the applied load. Consequently, the measurement is an average of the reinforcement and underlying

supporting matrix. This issue is not apparent in nanoindentation due to the low loads applied to the surface and the comparably small indenter tip [8.31]. Therefore, the supporting matrix does not deform, and the resultant values provide a more precise indication of the hardness of the specific regions within the MMC. Similar findings have been reported in the published literature [8.75]. However, studies [8.76, 8.77] examining the influence of indentation size on hardness show a direct correlation between reducing indentation depth and increasing hardness. Consequently, the substantial reduction in indentation depth in the nanoindentation, when compared with microhardness is expected to contribute to the measured increase in hardness [8.76, 8.77].

Optical micrographs depicting the nanoindentation impressions on the as-deposited and SprayStirred WC-CoCr reinforced MMCs are exhibited in Fig. 8-22, with corresponding hardness maps illustrated in Fig. 8-23a and Fig. 8-23b. Both high and low hardness values, shown in Fig. 8-23a correlate to the locations of reinforcements depicted in the micrograph (Fig. 8-22a). In contrast, the hardness map of the SprayStirred surface (Fig. 8-23b) highlights a more uniform hardness distribution throughout the examined region. Post-FSP (Fig. 8-23b), there are no high peaks. Instead, the WC-CoCr agglomerates, on which these peak values were measured, have been redistributed throughout the MMC by FSP, hence demonstrating the homogenising effect of FSP.

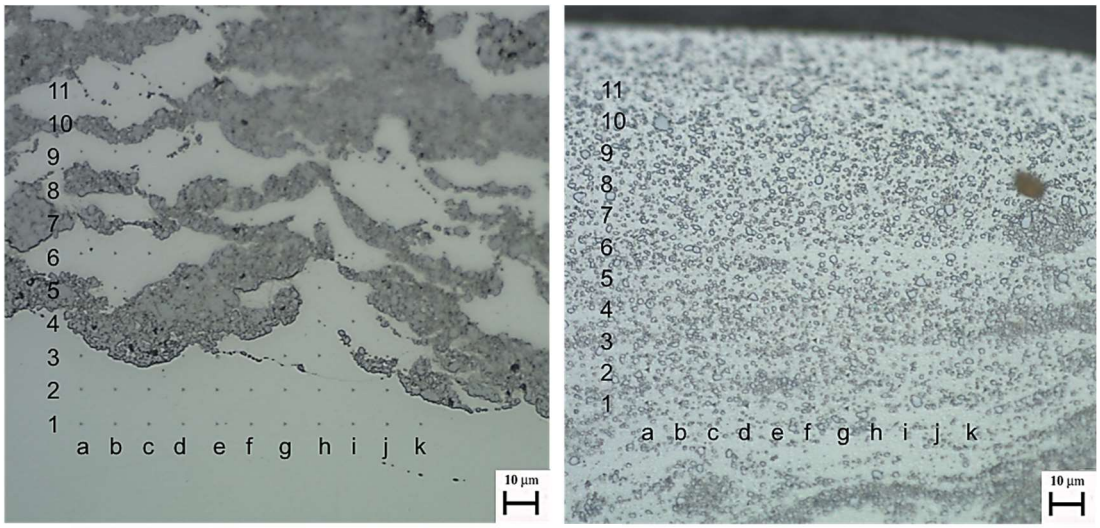

(a) (b)

Fig. 8-22 Optical micrographs of nanoindentation impressions on the WC-CoCr reinforced MMC; (a) as-deposited; (b) SprayStirred [x500 Unetched]

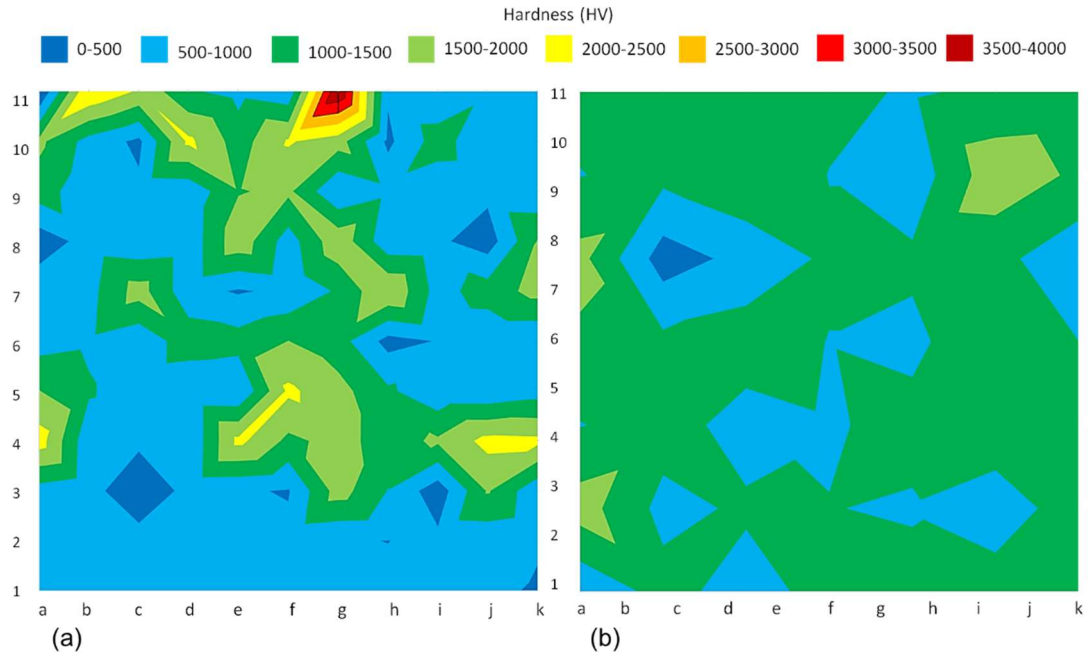

Fig. 8-23 Hardness maps of the area measured by nanoindentation; (a) as-deposited WC-CoCr reinforced MMC; b) SprayStirred WC-CoCr reinforced MMC

8.3.6 Slurry erosion testing

8.3.6.1 Mass Loss

The influence of FSP on the mass loss of the two MMCs and AISI 316 (under free erosion-corrosion conditions) has been measured following impingement at 90° and 30° and is shown in Fig. 8-24 and Fig. 8-25. Due to the dissimilar densities of the WC-CoCr and Al_2O_3 reinforcements, the mass loss cannot be used to compare the two MMCs and the AISI 316. However, the measurements provide an indication as to the relative erosion performance of each coating under 90° and 30° angle of attack.

For both MMCs (WC-CoCr and Al_2O_3), the SprayStirred specimen exhibited a reduction in mass loss over the as-deposited coating and the as-received AISI 316. In the case of the uncoated AISI 316, the improved erosion performance measured in the FSPed specimen is accredited to the grain refinement and corresponding hardness increase [8.7].

The mass loss results (Fig. 8-24 and Fig. 8-25) highlighted the superior erosion resistance of the SprayStirred MMC as compared to the corresponding CS coating. This improvement is related to the homogeneous distribution of the reinforcements throughout the MMC. This distribution reduced the surface area of unreinforced material that is exposed to the impinging slurry and also increased the hardness of the matrix through dispersion strengthening [8.66]. The harder matrix is

more resistant to erosion at shallow angles of attack, owing to the different erosion mechanisms operating at shallow and steep angles of impingement [8.78]. These mechanisms are discussed further in Section 8.3.8.

Although not directly comparable, the results from Betts et al. [8.16] demonstrate that, under slurry pot erosion testing, WC-CoCr reinforced AISI 316 increased the erosion performance (measured by mass loss) by approximately 1.5 – 3 times. In contrast, the results from this study indicate that SprayStirred WC-CoCr reduced the mass loss of as-received AISI 316 by up to 3.5 times. While the comparison of these two results is in no way systematic, it does provide an indication as to the relative erosion performance of SprayStir, in contrast to existing state-of-the-art surface engineering methods.

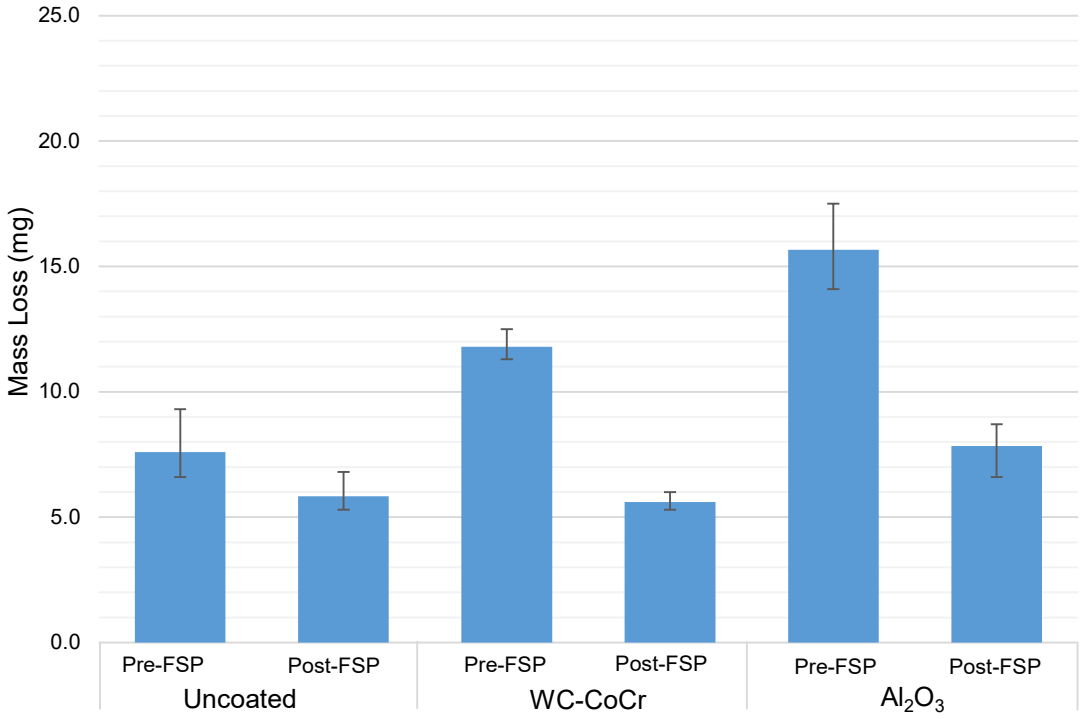

Fig. 8-24 Mass loss of the MMC specimens pre- and post-FSP under 90° impingement

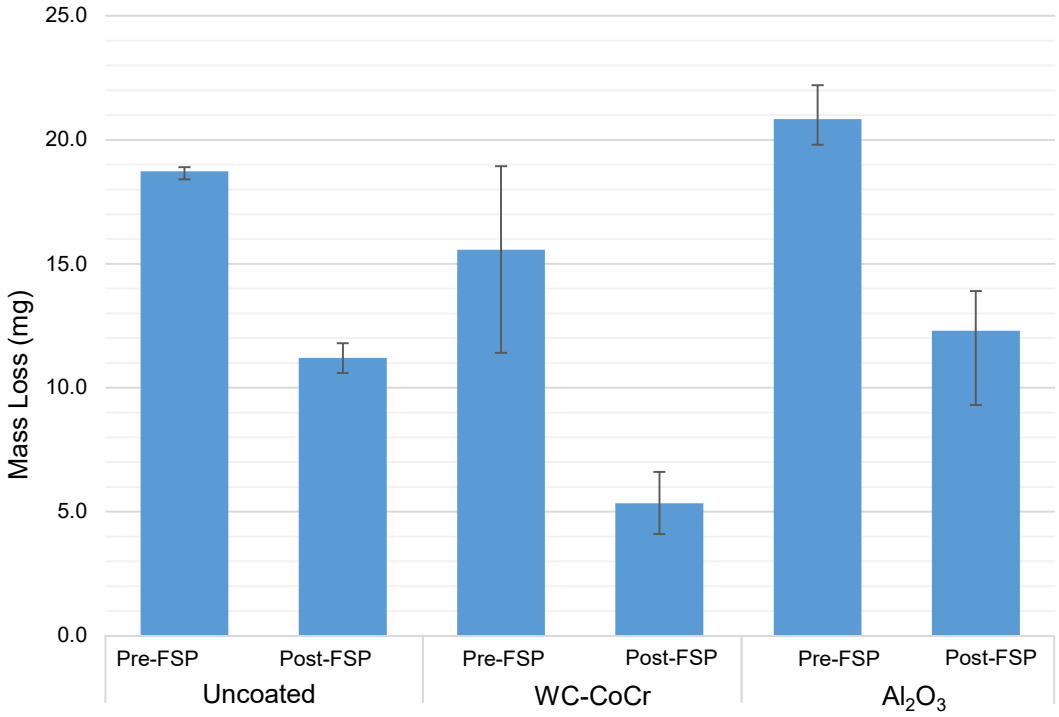

Fig. 8-25 Mass loss of the MMC specimens pre- and post-FSP under 30° impingement

8.3.6.2 Volume Loss

To directly compare the erosion performance of the different MMCs, the volume of the wear scar produced by the slurry was measured for each specimen following 90° (Fig. 8-26) and 30° (Fig. 8-27) impingement. Post-FSP, the uncoated AISI 316 experienced a significant reduction (45%) in volume loss under a 30° angle of attack (Fig. 8-27). However, under 90° impingement (Fig. 8-26), the FSPed AISI 316 only exhibited a 6% drop in volume loss over the as-received specimen. This outcome is a consequence of the grain refinement within the stir zone (as shown in Section 8.2.4.2) and corresponding hardness increase (Fig. 8-16).

The SprayStirred WC-CoCr MMC has yielded a 52% and 70% reduction in volume loss at 90° and 30° impingement, over the unreinforced AISI 316 post-FSP. Additionally, a 77% and 67% reduction in the volume loss has been recorded for the SprayStirred WC-CoCr MMC, over the as-deposited WC-CoCr. These results demonstrate the beneficial impact of FSP on the erosion performance of the engineered surface and confirm the significant influence of particle distribution on the erosion performance of the MMC.

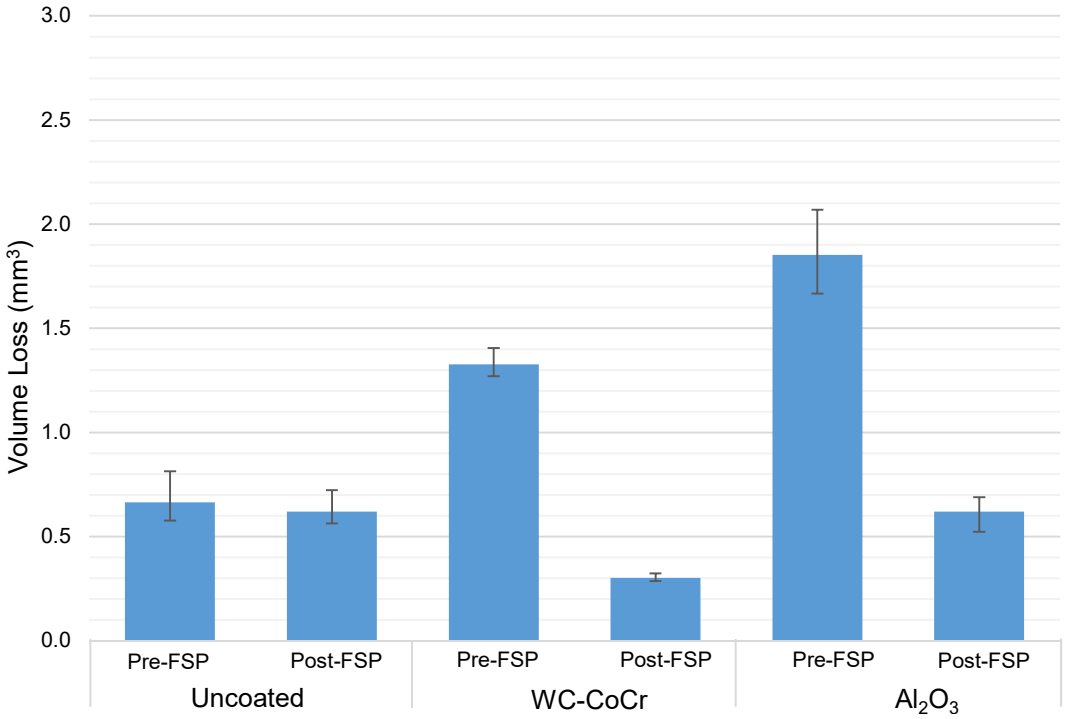

Fig. 8-26 Volume loss of the MMC specimens pre- and post-FSP under 90° impingement

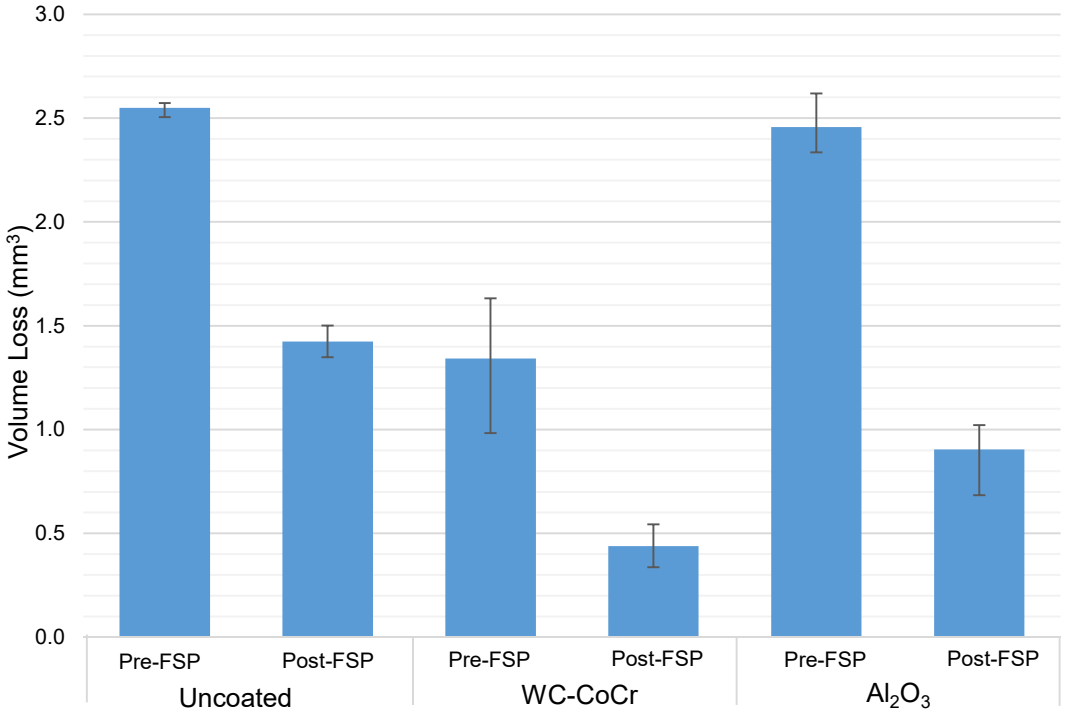

Fig. 8-27 Volume loss of the MMC specimens pre- and post-FSP under 30° impingement

Under 90° impingement (Fig. 8-26), the SprayStirred Al_2O_3 reinforced MMC offered no measurable improvement to the erosion performance over the as-received AISI 316. However, at 30° (Fig. 8-27) the SprayStirred Al_2O_3 measures a 36% drop in the volume loss. This outcome is attributed to the specific erosion mechanisms that operate at high (near 90°) and low impingement [8.78, 8.79] and will be discussed in Section 8.3.8.

The SprayStirred Al_2O_3 has provided greater erosion resistance at 30° impingement due to the refined oxides limiting the depth of the cutting and ploughing produced by the silica particles. The fracture and pull out of the oxides under 90° impingement has resulted in no change to the volume loss when compared with the as-received AISI 316. Despite the significant refinement of the Al_2O_3 oxides, the particles are still larger than the tungsten carbides (Table 8-1). Consequently, the superior erosion performance of the SprayStirred WC-CoCr MMC aligns with a greater quantity of reinforcements, smaller particle size and reduced interparticle spacing (Table 8-8).

8.3.6.3 Impressed current cathodic protection

Mass Loss

The slurry erosion test was repeated with applied cathodic protection (CP) [8.80] to establish the mass loss attributed to pure erosion (no corrosion acting on the surface of the specimen). Fig. 8-28 presents the mass loss of the various test specimens under free erosion-corrosion and with applied CP, thereby demonstrating the change in the mass loss when only mechanical erosion acts on the specimen.

The results (Fig. 8-28) indicate that all of the specimens suffer reduced levels of mass loss when corrosion is not permitted to act on the surface. Furthermore, the Al_2O_3 reinforced MMCs (as-deposited and SprayStirred) exhibited the most significant reduction in mass loss following the application of CP. This outcome implies that the addition of Al_2O_3 particles reduces the corrosion performance of the coating below that of the unreinforced AISI 316.

The impinging slurry removed similar quantities of material from the as-received AISI 316, and WC-CoCr reinforced MMC when exposed to free erosion-corrosion conditions and CP. The negligible difference in the mass loss with and without applied CP in the SprayStirred and co-deposited MMCs demonstrates the superior corrosion performance of the AISI 316, and WC-CoCr reinforced specimens in contrast to Al_2O_3.

Finally, the SprayStirred WC-CoCr MMC measured the lowest overall mass loss under free erosion-corrosion conditions, and with applied CP. This finding is attributed to the high hardness and the homogenous distribution of carbide reinforcements. The benefits of the SprayStirred WC-CoCr reinforced MMC are further illustrated by the negligible impact of the reinforcements on the corrosion performance of the coating.

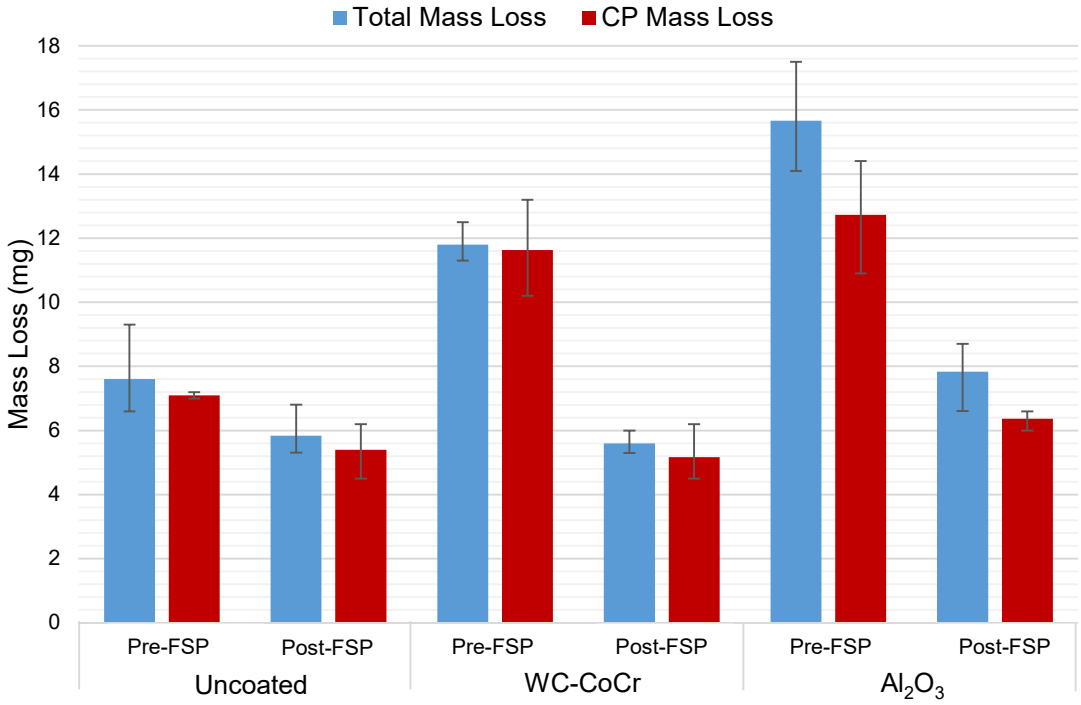

Fig. 8-28 Mass loss measured on the AISI 316 and MMC specimens pre- and post-FSP under free erosion-corrosion conditions and with applied CP (90° impingement)

8.3.7 Corrosion rate

To evaluate the influence of synergy on the total mass loss, the mass loss attributed to pure corrosion was established by anodic polarisation [8.81]. The corrosion rate (mg/hr) was measured under static and flowing conditions (90° impingement) for each of the coatings, and for the unreinforced AISI 316. To calculate the mass loss rate, it was necessary to establish the corrosion current (I_{corr}) of the different specimens. The specific details concerning the measurement of I_{corr} are presented in Chapter 3 and Chapter 4. The corrosion current density was calculated by dividing the I_{corr} by the specimen area (3.8 cm^2).

The polarisation curves for uncoated AISI 316, WC-CoCr at Al_2O_3 are shown in Fig. 8-29, Fig. 8-30 and Fig. 8-31 respectively. The fluctuations in the current density illustrated in Fig. 8-30 and Fig. 8-31 are indicative of particle impingement,

which disrupted the passive layer [8.82]. The current density values were established by identifying the point at which lines, extrapolated from the straight line on the anodic and cathodic curves, intersect. The x-coordinate of this intersection denotes the current density of the specimen. The total anodic current and current density results for static and flowing test conditions are presented in Table 8-10 and Table 8-11 respectively.

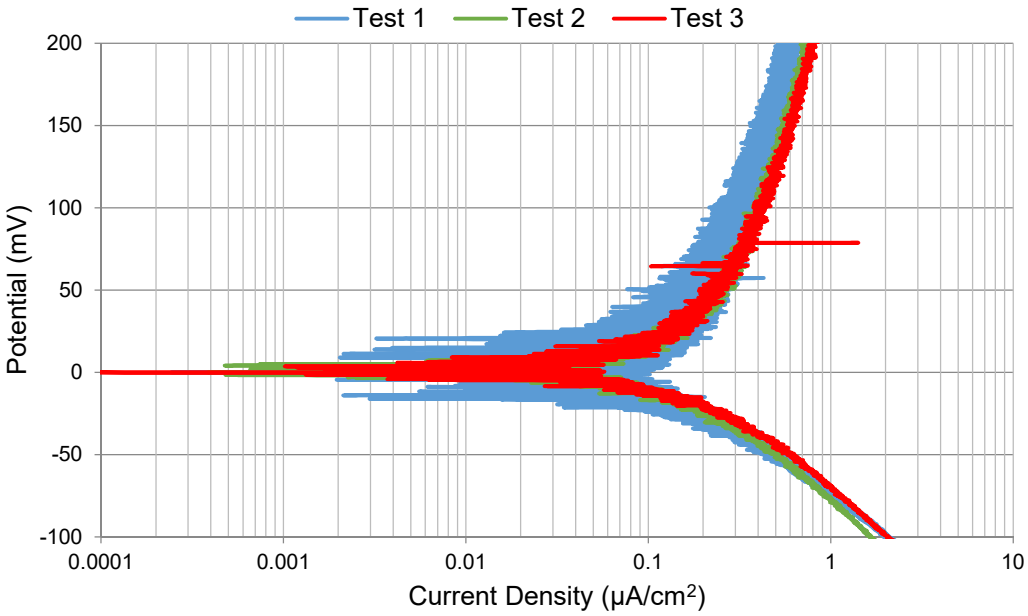

Fig. 8-29 As-received AISI 316 when exposed to static test conditions (90° impingement)

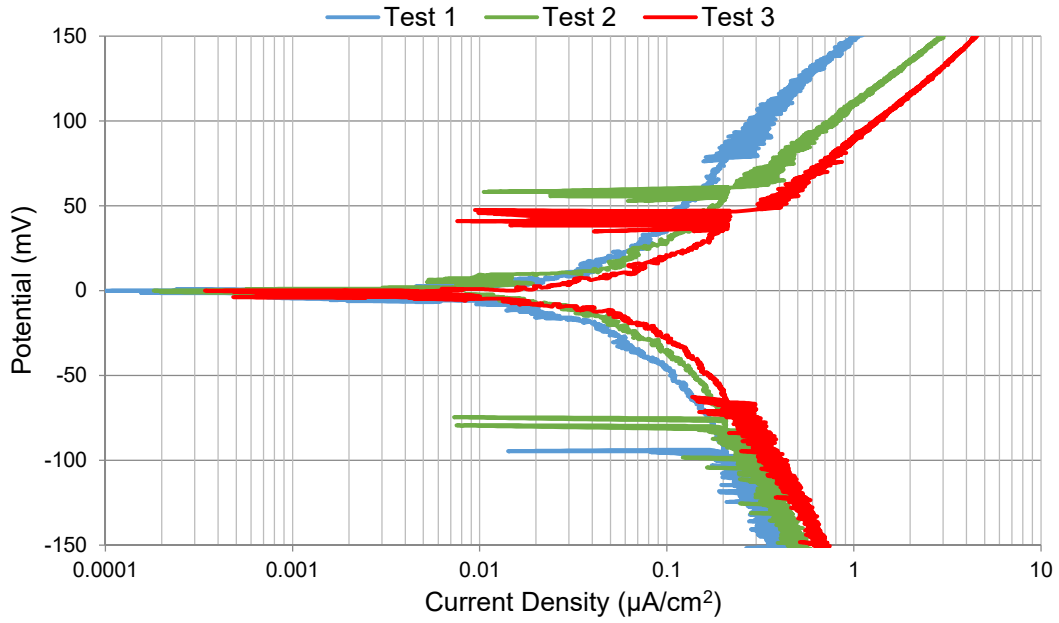

Fig. 8-30 SprayStirred WC-CoCr exposed to flowing test conditions (90° impingement)

The results (Table 8-10 and Table 8-11) indicate that the corrosion performance WC-CoCr and Al_2O_3 reinforced AISI 316 is adversely affected by the addition of reinforcements; for both the as-deposited CS coating and the SprayStirred MMC. This is in agreement with the published literature, which attributes this inferior performance of MMCs to corrosion attack at the interface between the reinforcement and matrix [8.80, 8.83, 8.84]. The substantial increase in corrosion rates (Table 8-11) measured between the static and slurry tests are a consequence of the continuous removal of the passive layer by the erosive particles [8.82]. The published literature suggests that corrosion occurs in the matrix, whereby the impinging particle removes the passive film, thus, exposing the underlying metal to the corrosive slurry [8.80].

However, determination of the specific corrosion mechanism operating on the SprayStirred and CS deposited MMCs is beyond the scope of the current investigation. Instead, the corrosion data has been collected to identify any detrimental effects of the reinforcements in terms of corrosion performance and to establish the influence of synergy on the total mass loss.

The corrosion rate was also measured under 30° impingement on the unreinforced AISI 316 specimens. The results from this trial highlighted no change in the corrosion rate between 90° and 30° impingement. Hence, it was not necessary to measure the corrosion rate of the MMCs under 30° impingement. For subsequent mass loss calculations, the same corrosion rate was used for 90° and 30° impingement.

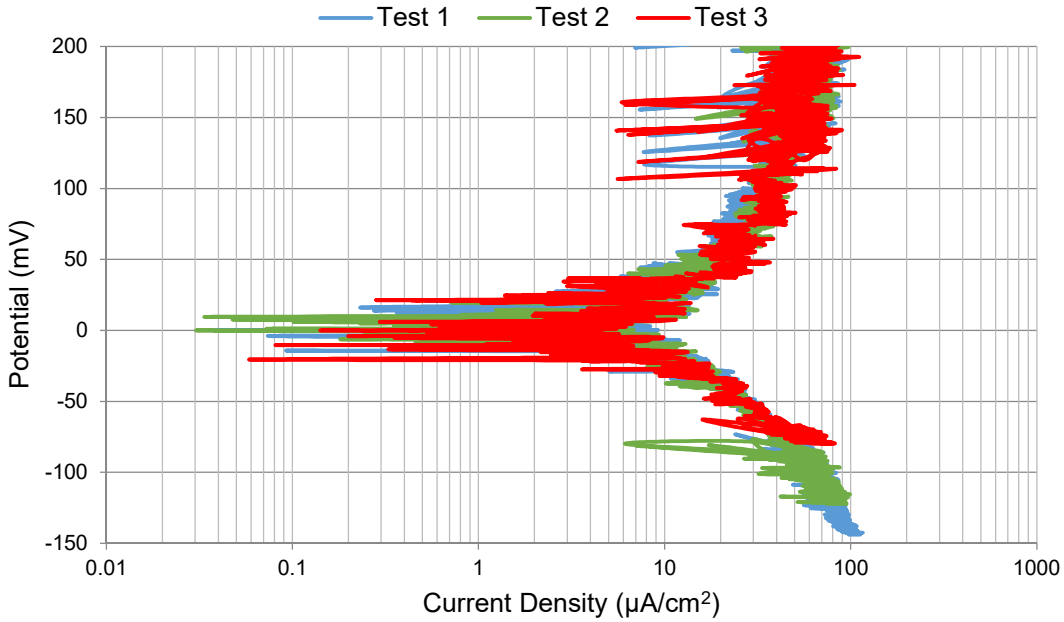

Fig. 8-31 SprayStirred Al_2O_3 when exposed to flowing test conditions (90° impingement)

Table 8-10 Corrosion current density for specimens under static corrosion test conditions

	No FSP			Post-FSP		
	AISI 316	WC-CoCr	Al_2O_3	AISI 316	WC-CoCr	Al_2O_3
Total anodic current (μA)	0.0006	0.01	0.005	0.0014	0.0078	0.0021
Current density (μA/cm^2)	0.16	2.63	1.31	0.37	2.05	0.55

Table 8-11 Corrosion current density for specimens under flowing test conditions

	No FSP			Post-FSP		
	AISI 316	WC-CoCr	Al_2O_3	AISI 316	WC-CoCr	Al_2O_3
Total anodic current (μA)	0.0036	0.046	0.12	0.032	0.061	0.10
Current density (μA/cm^2)	9.47	12.10	31.56	8.42	16.05	26.32

8.3.7.1 Effect of synergy

The method outlined in ASTM G102 - 89 [8.41] was employed to calculate hourly mass loss rates for each MMC based on the extrapolated current density. The specific calculation steps are detailed in Chapter 4. Table 8-12 and Table 8-13 present the contribution of each wear mechanism (erosion, corrosion, and synergy) to the total mass loss under flowing erosion-corrosion conditions. The mass loss generated by the slurry is erosion dominant, with the synergistic effect of combined corrosion and erosion (synergy) contributing between 1 and 18% of the total mass loss.

While the unreinforced AISI 316 specimen demonstrates the highest resistance to corrosion, the comparatively poor erosion performance of the alloy, when exposed to the impinging slurry, makes it unsuitable for use in erosive environments. The SprayStirred WC-CoCr MMC measured only a minor increase in the corrosion rate over the AISI 316 but demonstrated considerable improvement to the erosion performance over the AISI 316, and Al_2O_3 reinforced specimens, as shown in Fig. 8-26 and Fig. 8-27. Therefore, based on the results presented herein, the SprayStirred WC-CoCr MMC offers the highest resistance to combined erosion and corrosion.

Table 8-12 Percentage contribution of erosion, corrosion and synergy to total mass loss of the as-received substrate and the as-deposited coatings under flowing conditions

	Total mass loss (%)	Erosion (%)	Corrosion (%)	Synergy (%)
Uncoated	100	93.4	0.07	6.51
WC-CoCr	100	98.6	0.09	1.35
Al_2O_3	100	87.0	0.16	12.9

Table 8-13 Percentage contribution of erosion, corrosion and synergy to total mass loss of the FSPed AISI 316 and SprayStirred MMCs under flowing conditions

	Total mass loss (%)	Erosion (%)	Corrosion (%)	Synergy (%)
Uncoated	100	92.6	0.08	7.29
WC-CoCr	100	92.3	0.25	7.43
Al_2O_3	100	81.4	0.27	18.4

8.3.8 Post-test wear scar examination

To elucidate the findings of the volume loss analysis, micrographs of the impinged region were examined to identify the mechanisms resulting in the removal of material from the surface of the specimens.

8.3.8.1 CS coatings and as-received AISI 316 wear scars

Fig. 8-32 presents macroscopic images of the examined wear scar surfaces on the as-received AISI 316. The images (Fig. 8-32) highlight the variation in the profile of the wear scar between the 90° and 30° impingement. Corresponding wear scar patterns were identified on all of the examined specimens.

SEM micrographs of the impinged region of the as-received AISI 316 are presented in Fig. 8-33 and Fig. 8-34 to demonstrate the dissimilar erosion mechanisms operating on the surface under each angle of impingement. The wear scar topography for as-received AISI 316 eroded at 90° (Fig. 8-33) exhibits several distinct crater and lip features that are consistent with the erosion of ductile materials [8.85–8.87].

An SEM micrograph showing the wear scar of the as-received AISI 316 substrate eroded at 30° is presented in Fig. 8-34. This image depicts numerous ploughing and scoring marks which are consistent with the erosion of ductile alloys at shallow angles of attack [8.78, 8.85]. Material removal was caused by the thinning of the material around the periphery of the surface damage (ploughing and scoring)

generated by the silica particles, with subsequent impacts removing the weakened material.

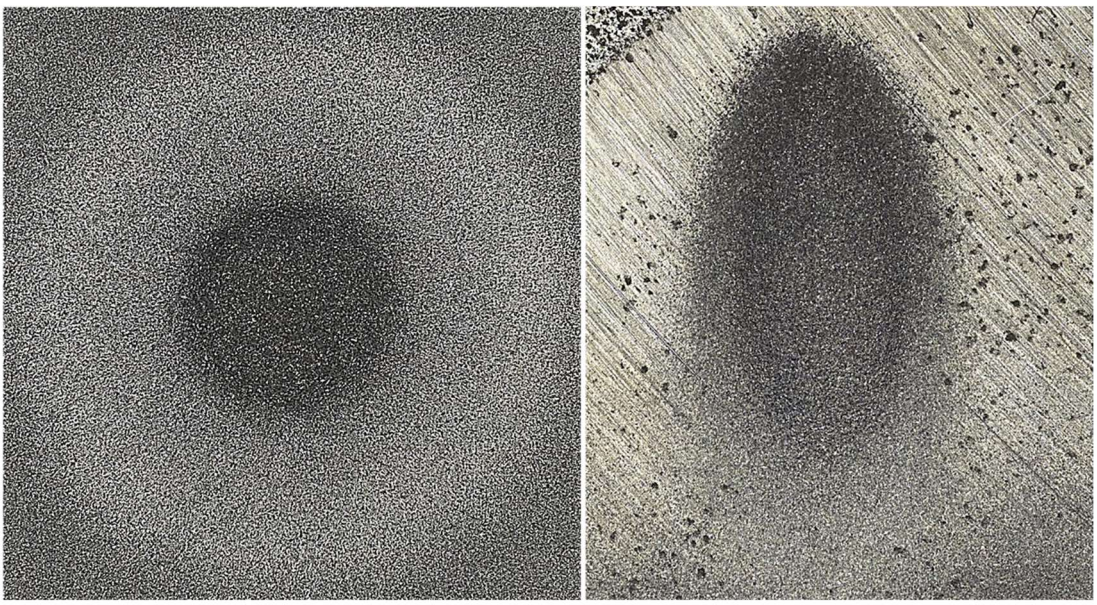

Fig. 8-32 Macroscopic images of the wear scar on the as-received AISI 316; (a) 90° impingement; (b) 30° impingement

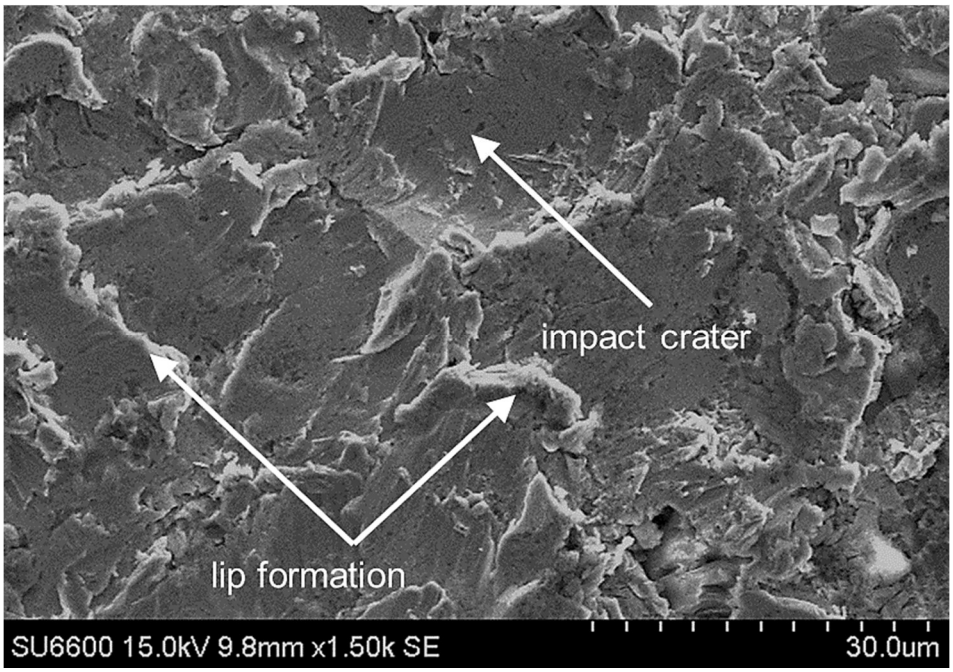

Fig. 8-33 SEM micrograph depicting the surface of as-received AISI 316 exposed to 90° impingement [x1500]

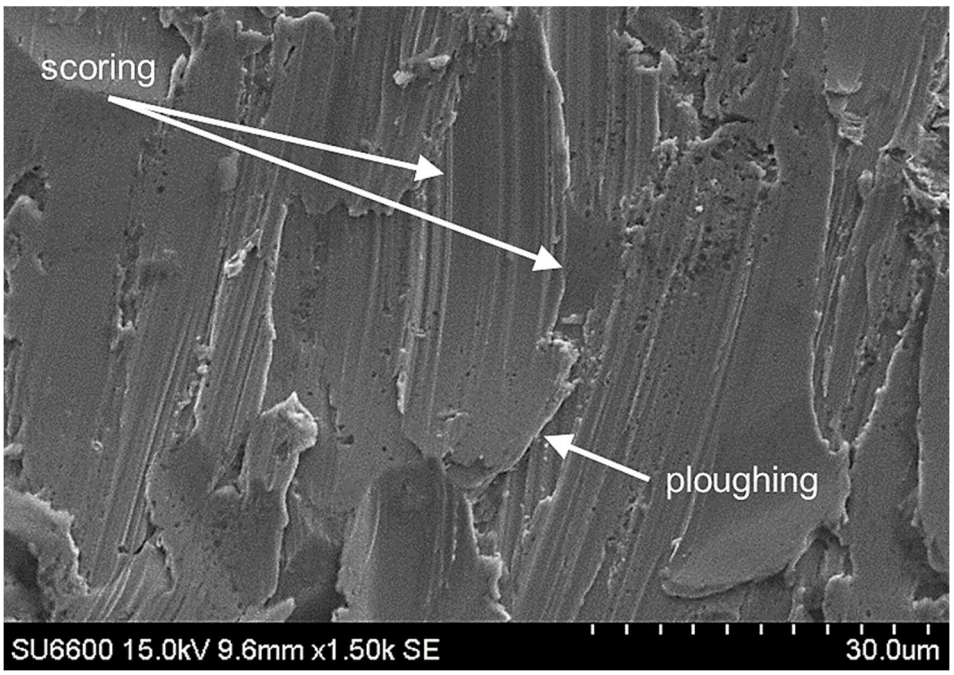

Fig. 8-34 SEM micrograph depicting the surface of as-received AISI 316 exposed to 30° impingement [x1500]

The wear scar of the as-deposited WC-CoCr reinforced MMC exposed to slurry impingement at 90° is illustrated in Fig. 8-35. The image depicts evidence of both ductile and brittle erosion mechanisms operating on the surface. Ductile erosion is characterised by the presence of scoring and lip formation on the AISI 316 matrix. Equally, the eroded surface presents evidence of brittle erosion in the form of cracking and pull-out. However, due to the quantity of WC contained in the MMC (Section 8.3.1) erosion is dominated by cracking and pull out of the carbides from the matrix.

Repeated impact by the silica particles causes cracking in the brittle carbide agglomerates which propagate with successive impacts. As the cracks intersect with the AISI 316 matrix, the WC agglomerates are loosened and eventually dislodged from the MMC leaving a void (as shown in Fig. 8-35). This wear mechanism is enhanced by the clustering of reinforcements, whereby large agglomerates of WC-CoCr particles can be dislodged simultaneously should the cracking caused by the impinging particles intersect with the boundary between the matrix and the reinforcement.

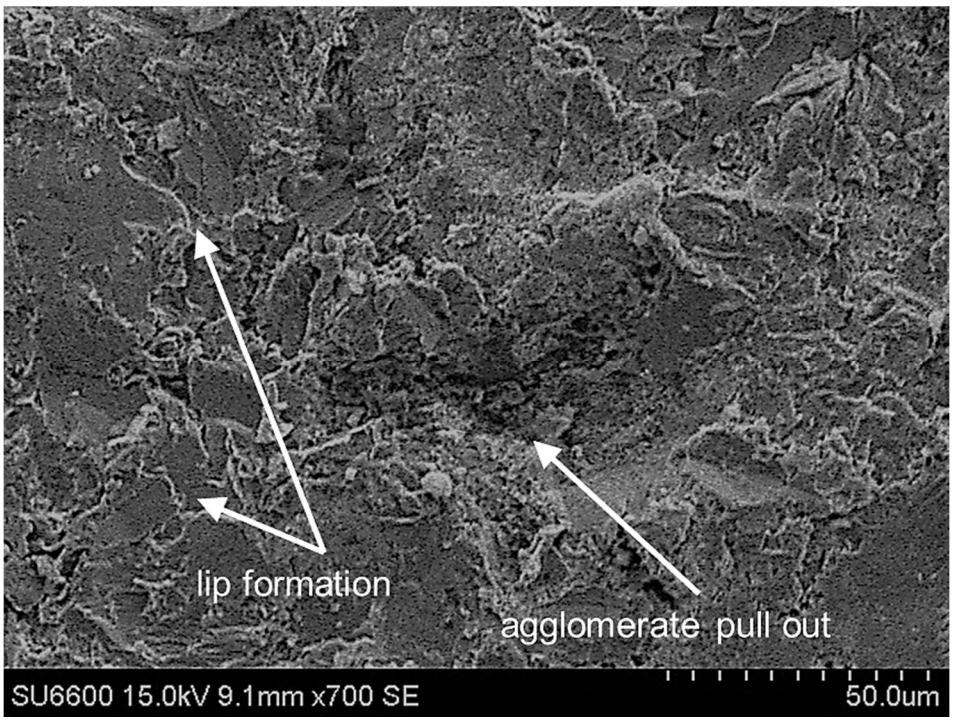

Fig. 8-35 SEM micrograph of the wear scar on the as-deposited WC-CoCr coating exposed to 90° impingement [x700]

Fig. 8-36 illustrates the eroded region of the WC-CoCr coating following impingement at 30° and depicts ductile erosion of the matrix. However, the depth of the ploughing and scoring damage is noticeably less than is present on the surface of the AISI 316 (Fig. 8-34). Furthermore, carbides protruding from the AISI 316 matrix can be seen in Fig. 8-36. EDS analysis recorded approximately 70% tungsten, thus confirming these protruding particles are the deposited reinforcements. Fig. 8-36 highlights the deflection of the scoring around the carbides, indicating that their presence actively reduces the erosive damage on the surface of the specimen.

The examination of the Al_2O_3 reinforced specimens also reveals brittle and ductile erosion damage (Chapter 3) at high (90°) and low angles of impact (30°). At 90°, an initial silica particle generates an indent and simultaneously produces cracks in the brittle Al_2O_3 reinforcements. Subsequent impacts lead to complete fracture, forming a chip of material that is removed by the slurry (Fig. 8-37). At low impact angle (30°), there is evidence of ductile scoring in the matrix and large voids signifying the former location of dislodged oxide particles (Fig. 8-38). The increased volume loss associated with the Al_2O_3 reinforced coating (Fig. 8-26 and Fig. 8-27) is attributed to the presence of oxide particles at the boundaries of the deformed AISI 316 binder particles, thereby reducing the cohesive strength of the coating.

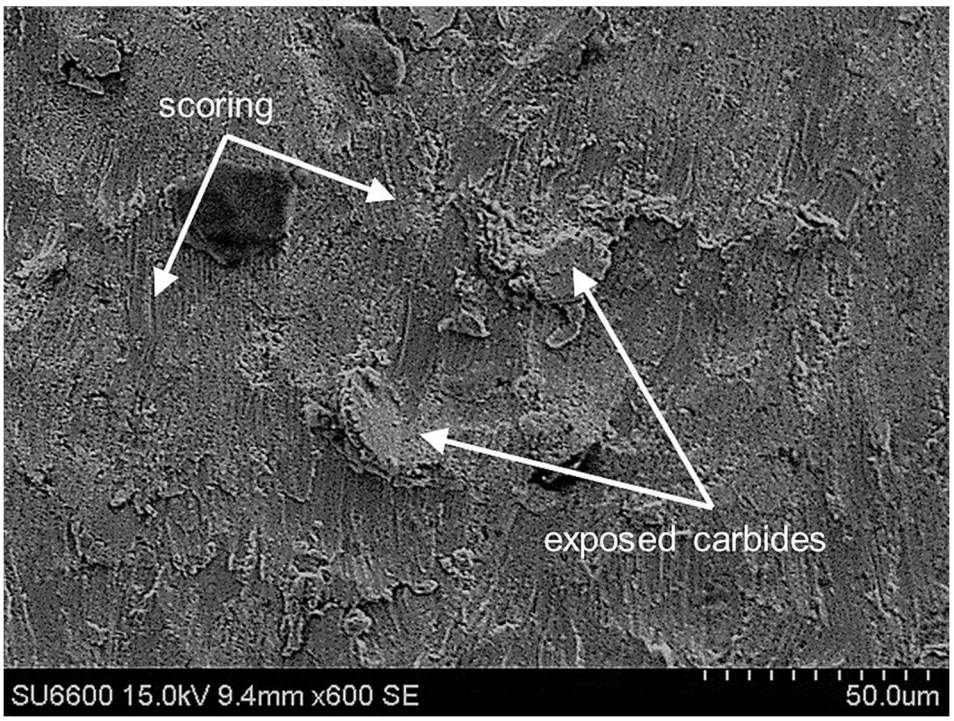

Fig. 8-36 SEM micrograph of the wear scar on the as-deposited WC-CoCr coating exposed to 30° impingement [x600]

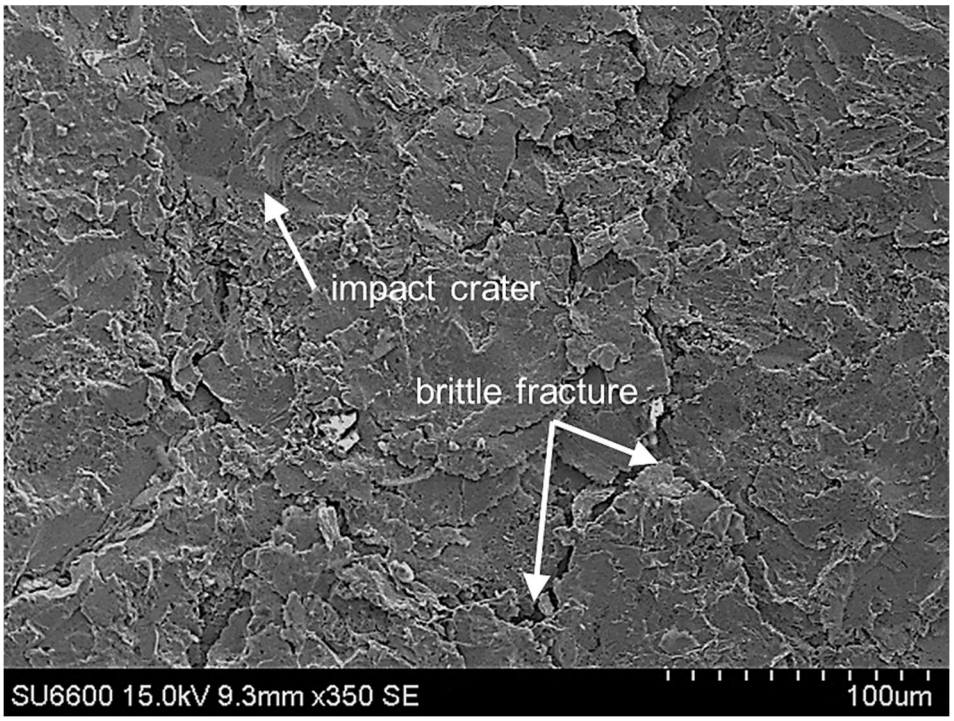

Fig. 8-37 SEM micrograph of the wear scar on the surface of the Al_2O_3 reinforced MMC following 90° impingement [x350]

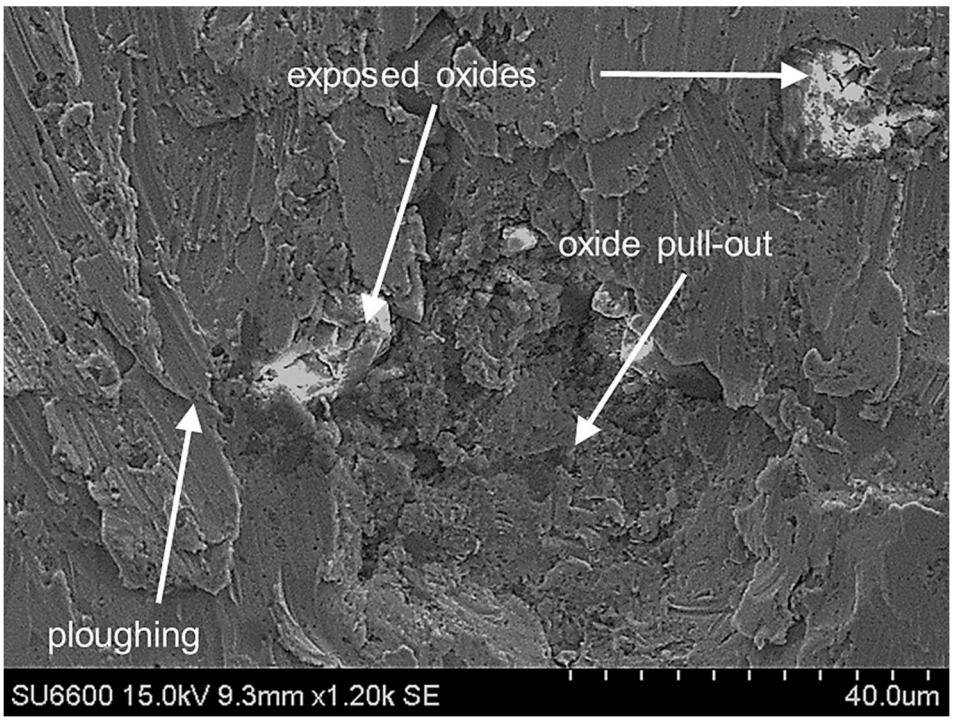

Fig. 8-38 SEM micrograph of the wear scar on the Al_2O_3 reinforced MMC following 30° impingement [x1200]

8.3.8.2 SprayStir wear scars

The impinged region of the SprayStirred WC-CoCr specimen following impingement at 90° presented in Fig. 8-39. The image depicts the distributed carbides on the surface of the sample. In contrast to the as-deposited WC-CoCr reinforced coating (Fig. 8-35), there is no evidence of any voids on the surface that correspond to removed agglomerates. Thus, the SEM micrographs of the wear scar corroborate the findings from the microstructural analysis (Section 8.3.1), that the as-deposited agglomerates have been dispersed by FSP. Further, the image shows scoring on the surface of the specimen. Considering this specimen was impinged at 90°, these features are attributed to dislodged carbides scoring the surface as they are transported by the slurry.

Following 30° impingement, the damage on the SprayStirred WC-CoCr specimen (Fig. 8-40) shows directionality in the score pattern that aligns with the flow of the slurry. The deep ploughing observed in the as-deposited coating (Fig. 8-36) is less pronounced on the surface of the SprayStirred WC-CoCr MMC (Fig. 8-40). When the size of the eroding particles is substantially greater than the refined reinforcements, the carbides are incapable of deflecting the impinging particles. Instead, the carbides increase the hardness of the matrix through dispersion

strengthening [8.66]. This subsequently reduces the depth of the surface damage, thus, decreasing the volume of the wear scar. Similar erosion mechanisms have been reported in existing literature [8.80, 8.88]. Additionally, uniform distribution of the reinforcing particles reduces the surface area of the unreinforced matrix that was exposed to the slurry solution, thus reducing the damage on the surface of the specimen.

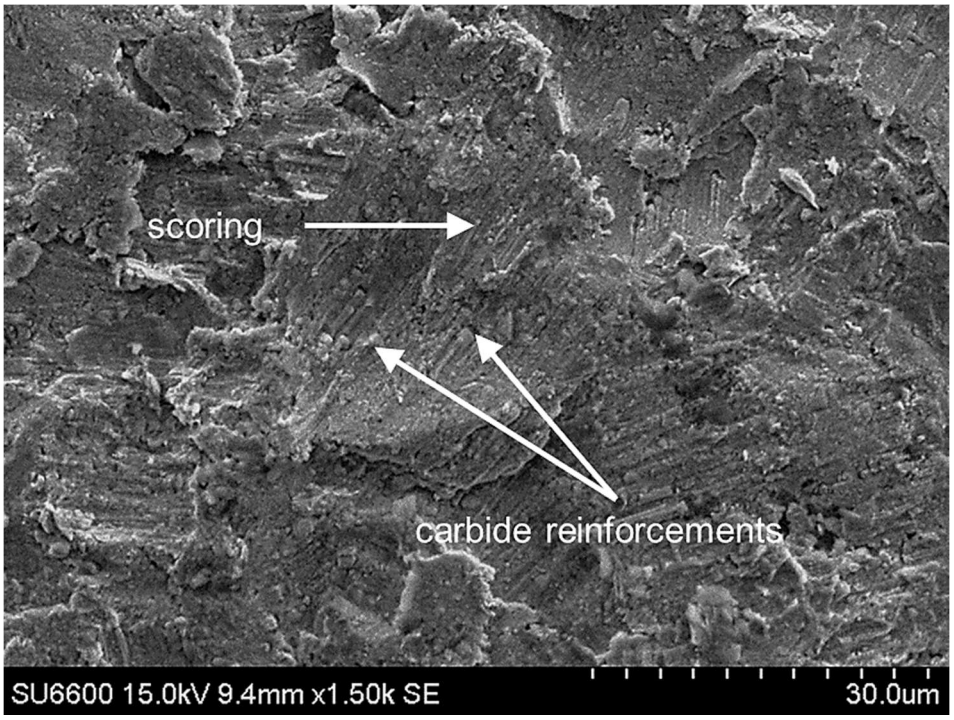

Fig. 8-39 SEM micrograph of the wear scar on the SprayStirred WC-CoCr specimen following 90° impingement [x1500]

Fig. 8-41 highlights the damage to the SprayStirred Al_2O_3 reinforced MMC following impact at 30°. The micrograph (Fig. 8-41) exhibits similar damage to the uncoated AISI 316, specifically illustrating evidence of ploughing and cutting. The reduced volume loss measured on the SprayStirred Al_2O_3 specimen is attributed to the homogeneous distribution of the refined oxide particles imparting hardening through dispersion strengthening [8.67]; thereby making the surface more resistant to ploughing and cutting by the silica particles.

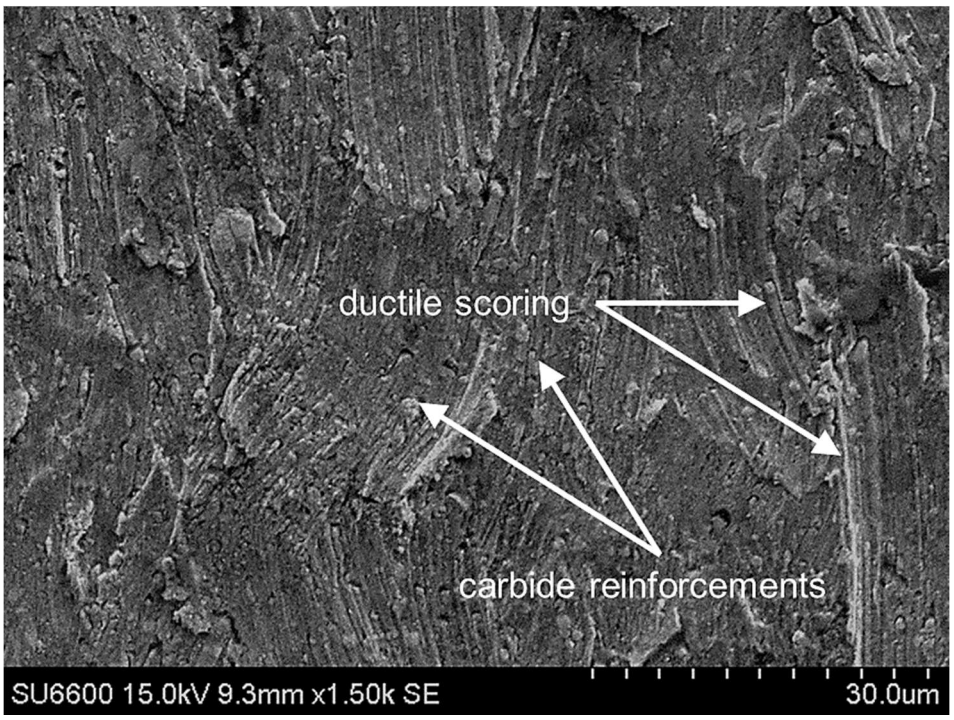

Fig. 8-40 SEM micrograph of the wear scar on the surface of the SprayStirred WC-CoCr specimen following 30° impingement [x1500]

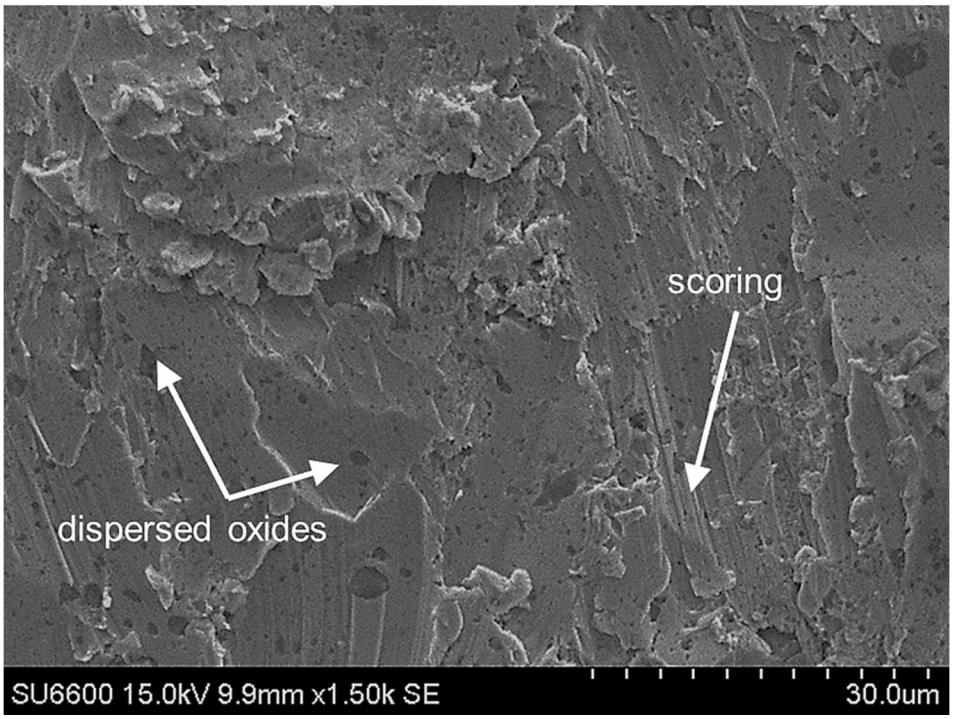

Fig. 8-41 SEM micrograph of the wear scar on the SprayStirred Al_2O_3 specimen following 30° impingement [x1500]

8.4 Conclusions

In this study WC-CoCr and Al_2O_3 feedstock powder particles were successfully CS co-deposited with AISI 316 binder particles to produce particle reinforced MMC coatings. The coatings were subsequently modified using FSP to embed, refine and redistribute the reinforcing particles. FSP has resulted in the dispersion of the as-deposited WC-CoCr agglomerates and refinement of the Al_2O_3 particles.

The average microhardness of the SprayStirred WC-CoCr was 1120 HV. This result correlates to a 50% increase over the CS coating (no FSP) and a 500% increase over the as-received AISI 316. The results from nanoindentation confirm a significant reduction in the range of the measured hardness values in the SprayStirred MMCs. Therefore, the SprayStir process has improved the hardness homogeneity in both the WC-CoCr and Al_2O_3 reinforced MMCs. The interparticle spacing measurements demonstrate a 91% and 88% reduction in the spacing of the WC-CoCr and Al_2O_3 reinforced MMCs post-FSP.

The as-deposited WC-CoCr reinforced coating (no FSP) demonstrated an 80% decrease in volume loss over the as-received AISI 316 at 30° impingement. However, through combined CS and FSP, the SprayStirred WC-CoCr specimen exhibited a further 75% reduction in volume loss over the as-deposited coating (CS only).

At 90°, erosion was dominated by the removal of weakened material on the periphery of impact craters. The presence of the carbide/oxide reinforcements reduced the depth of the craters owing to their increased hardness, while the small size of the particles prevented them from being easily dislodged from the matrix. Under 30° impingement, the refined reinforcements limited the depth of the surface damage caused by the erosive slurry by increasing the hardness of the SprayStirred MMC. Furthermore, the homogeneous distribution of carbide/oxides reduced the surface area of unreinforced AISI 316 exposed to the slurry. Both mechanisms contribute to the measured reduction in volume loss associated with SprayStir.

8.5 References

[8.1] H.S. Arora, H. Singh, B.K. Dhindaw, Wear behaviour of a Mg alloy subjected to friction stir processing, Wear. 303 (2013) 65–77.

[8.2] C. Lorenzo-Martin, O.O. Ajayi, Rapid surface hardening and enhanced tribological performance of 4140 steel by friction stir processing, Wear. 332–333 (2015) 962–970.

[8.3] S.H. Aldajah, O.O. Ajayi, G.R. Fenske, S. David, Effect of friction stir

processing on the tribological performance of high carbon steel, Wear. 267 (2009) 350–355.
[8.4] Y.S. Sato, H. Yamanoi, H. Kokawa, T. Furuhara, Microstructural evolution of ultrahigh carbon steel during friction stir welding, Scr. Mater. 57 (2007) 557–560.
[8.5] K.J. Hodder, H. Izadi, A.G. McDonald, A.P. Gerlich, Fabrication of aluminum-alumina metal matrix composites via cold gas dynamic spraying at low pressure followed by friction stir processing, Mater. Sci. Eng. A. 556 (2012) 114–121.
[8.6] C. Huang, W. Li, Z. Zhang, M. Fu, M. Planche, H. Liao, et al., Modification of a cold sprayed SiCp/Al5056 composite coating by friction stir processing, Surf. Coatings Technol. 296 (2016) 69–75.
[8.7] R. Bauri, D. Yadav, G. Suhas, Effect of friction stir processing (FSP) on microstructure and properties of Al-TiC in situ composite, Mater. Sci. Eng. A. 528 (2011) 4732–4739.
[8.8] O.S. Salih, H. Ou, W. Sun, D.G. Mccartney, A review of friction stir welding of aluminium matrix composites, Mater. Des. 86 (2015) 61–71.
[8.9] A. Ghasemi-kahrizsangi, S.F. Kashani-Bozorg, M. Moshref-Javadi, Effect of friction stir processing on the tribological performance of Steel/Al2O3 nanocomposites, Surf. Coatings Technol. 276 (2015) 507–515.
[8.10] Y. Morisada, H. Fujii, T. Mizuno, G. Abe, T. Nagaoka, M. Fukusumi, Modification of thermally sprayed cemented carbide layer by friction stir processing, Surf. Coatings Technol. 204 (2010) 2459–2464.
[8.11] A. Rokanopoulou, P. Skarvelis, G.D. Papadimitriou, Improvement of the tribological properties of Al2O3 reinforced duplex stainless steel MMC coating by the addition of TiS2 powder, Surf. Coat. Technol. 289 (2016) 144–149.
[8.12] A. Neville, F. Reza, S. Chiovelli, T. Revega, Assessing metal matrix composites for corrosion and erosion-corrosion applications in the oil sands industry, J. Sci. Eng. 62 (2006) 657–675.
[8.13] S. Buytoz, M. Ulutan, In situ synthesis of SiC reinforced MMC surface on AISI 304 stainless steel by TIG surface alloying, Surf. Coatings Technol. 200 (2006) 3698–3704.
[8.14] F.T. Cheng, C.T. Kwok, H.C. Man, Cavitation erosion resistance of stainless steel laser-clad with WC-reinforced MMC, Mater. Lett. 57 (2002) 969–974.
[8.15] S.C. Tjong, K.C. Lau, Sliding wear of stainless steel matrix composite reinforced with TiB2 particles, Mater. Lett. 41 (1999) 153–158.
[8.16] J.C. Betts, B.L. Mordike, M. Grech, Characterisation, wear and corrosion testing of laser-deposited AISI 316 reinforced with ceramic particles, Surf. Eng. 26 (2010) 21–29.
[8.17] A.A. Gadhikar, A. Sharma, D.B. Goel, C.P. Sharma, Fabrication and testing of slurry pot erosion tester, Trans. Indian Inst. Met. 64 (2011) 493–500.
[8.18] H.M. Clark, Particle velocity and size effects in laboratory slurry erosion measurements OR... do you know what your particles are doing? Tribol. Int. 35 (2002) 617–624.
[8.19] R.J.K. Wood, Y. Puget, K.R. Trethewey, K. Stokes, The performance of marine coatings and pipe materials under fluid-borne sand erosion, Wear. 219 (1998) 46–59.
[8.20] Sandvik Osprey, Material Product Data Sheet 316L Powder, 2015.
[8.21] Oerlikon Metco, Material Product Data Sheet Chromium Carbide – Nickel Chromium Powder Blends, 2 (2014) 2–7.
[8.22] Oerlikon Metco, Material Product Data Sheet Tungsten Carbide – 10 % Cobalt 4 % Chromium Powders, (2015) 1–7.

[8.23] H.Y. Lee, S.H. Jung, S.Y. Lee, Y.H. You, K.H. Ko, Correlation between Al2O3 particles and interface of Al-Al2O3 coatings by cold spray, Appl. Surf. Sci. 252 (2005) 1891–1898.
[8.24] International ASTM Standard, ASTM A666 - 15 Standard specification for annealed or cold-worked austenitic stainless steel, 1 (1999) 1–7.
[8.25] Y.N. Zhang, X. Cao, S. Larose, P. Wanjara, Review of tools for friction stir welding and processing, Can. Metall. Q. 51 (2012) 250–261.
[8.26] R. Miranda, J. Gandra, P. Vilaca, L. Quintino, T. Santos, Surface Modification by Solid State Processing, Woodhead Publishing Limited, 2008.
[8.27] International ASTM Standard, ASTM E2109 − 01: Standard Test Methods for Determining Area Percentage Porosity in Thermal Sprayed Coatings, (2006) 1–8.
[8.28] H.S. Khare, D.L. Burris, A quantitative method for measuring nanocomposite dispersion, Polymer (Guildf). 51 (2010) 719–729.
[8.29] W.C. Oliver, G.M. Pharr, An improved technique for determining hardness and elastic modulus using load and displacement sensing indentation experiments, J. Mater. Res. 7 (1992) 1564–1583.
[8.30] W.C. Oliver, G.M. Pharr, Measurement of hardness and elastic modulus by instrumented indentation: Advances in understanding and refinements to methodology, J. Mater. Res. 19 (2004) 3–20.
[8.31] A.C. Fischer-Cripps, Mechanical Engineering Series: Nanoindentation, 2011.
[8.32] G.M. Pharr, W.C. Oliver, F.R. Brotzen, On the generality of the relationship among cantact stiffness,contact area, and elastic-modulus during indentation, J. Mater. Res. 7 (1992) 613–617.
[8.33] G.M. Pharr, W.C. Oliver, Measurement of thin film mechanical properties using nanoindentation, Mrs Bull. 17 (1992) 28–33.
[8.34] International ASTM Standard, ASTM E92-16 Standard Test Methods for Vickers Hardness and Knoop Hardness of Metallic, 2016.
[8.35] R.S. Bolton-King, J.P.O. Evans, C.L. Smith, J.D. Painter, D.F. Allsop, W.M. Cranton, What are the Prospects of 3D Profiling Systems Applied to Firearms and Toolmarks Identification?, AFTE J. 42 (2010) 23–33.
[8.36] L. Giourntas, T. Hodgkiess, A.M. Galloway, Comparative study of erosion–corrosion performance on a range of stainless steels, Wear. 332–333 (2015) 1051–1058.
[8.37] A. Neville, X. Hu, Mechanical and electrochemical interactions during liquid–solid impingement on high-alloy stainless steels, Wear. 251 (2001) 1284–1294.
[8.38] V.A.D. Souza, A. Neville, Corrosion and synergy in a WC-Co-Cr HVOF thermal spray coating - Understanding their role in erosion-corrosion degradation, Wear. 259 (2005) 171–180.
[8.39] V.A.D. Souza, A. Neville, Aspects of microstructure on the synergy and overall material loss of thermal spray coatings in erosion – corrosion environments, Wear. 263 (2007) 339–346.
[8.40] H. Xu, A. Neville, An electrochemical and microstructural assessment of erosion-corrosion of austenitic cast iron for marine applications, Mater. Corros. 53 (2002) 5–12.
[8.41] I.A. Standard, ASTM G102 - 89 Standard Practice for Calculation of Corrosion Rates and Related Information from Electrochemical Measurements, 2015.
[8.42] D. Seo, M. Sayar, K. Ogawa, SiO 2 and MoSi 2 formation on Inconel 625 surface via SiC coating deposited by cold spray, Surf. Coatings Technol. 206 (2012) 2851–2858.

[8.43] V.K. Champagne, The cold spray materials deposition process: fundamentals and applications, Woodhead Publishing, 2007.
[8.44] H. Assadi, T. Schmidt, H. Richter, J.O. Kliemann, K. Binder, F. Gartner, et al., On parameter selection in cold spraying, J. Therm. Spray Technol. 20 (2011) 1161–1176.
[8.45] S.H. Zahiri, C.I. Antonio, M. Jahedi, Elimination of porosity in directly fabricated titanium via cold gas dynamic spraying, J. Mater. Process. Technol. 209 (2009) 922–929.
[8.46] S.H. Zahiri, D. Fraser, S. Gulizia, M. Jahedi, Effect of processing conditions on porosity formation in cold gas dynamic spraying of copper, J. Therm. Spray Technol. 15 (2006) 422–430.
[8.47] K. Spencer, V. Luzin, N. Matthews, M.-X. Zhang, Residual stresses in cold spray Al coatings: The effect of alloying and of process parameters, Surf. Coatings Technol. 206 (2012) 4249–4255.
[8.48] E.J.T. Pialago, C.W. Park, Cold spray deposition characteristics of mechanically alloyed Cu-CNT composite powders, Appl. Surf. Sci. 308 (2014) 63–74.
[8.49] P. Coddet, C. Verdy, C. Coddet, F. Debray, F. Lecouturier, Mechanical properties of thick 304L stainless steel deposits processed by He cold spray, Surf. Coatings Technol. 277 (2015) 74–80.
[8.50] S.A. Alidokht, P. Manimunda, P. Vo, S. Yue, R.R. Chromik, Cold spray deposition of a Ni-WC composite coating and its dry sliding wear behavior, Surf. Coatings Technol. 308 (2016) 424–434.
[8.51] F. Sevillano, P. Poza, C.J. Múnez, S. Vezzù, S. Rech, A. Trentin, Cold-sprayed Ni-Al2O3 coatings for applications in power generation industry, J. Therm. Spray Technol. 22 (2013) 772–782.
[8.52] S. Grigoriev, A. Okunkova, A. Sova, P. Bertrand, I. Smurov, Cold spraying: From process fundamentals towards advanced applications, Surf. Coatings Technol. 268 (2015) 77–84.
[8.53] K. Spencer, D.M. Fabijanic, M.X. Zhang, The use of Al-Al2O3 cold spray coatings to improve the surface properties of magnesium alloys, Surf. Coatings Technol. 204 (2009) 336–344.
[8.54] S. Yin, M. Meyer, W. Li, H. Liao, R. Lupoi, Gas Flow, Particle Acceleration, and Heat Transfer in Cold Spray: A review, J. Therm. Spray Technol. 25 (2016) 874–896.
[8.55] M. Couto, S. Dosta, M. Torrell, J. Fernández, J.M. Guilemany, Cold spray deposition of WC-17 and 12Co cermets onto aluminum, Surf. Coatings Technol. 235 (2013) 54–61.
[8.56] R. Ghelichi, D. MacDonald, S. Bagherifard, H. Jahed, M. Guagliano, B. Jodoin, Microstructure and fatigue behavior of cold spray coated Al5052, Acta Mater. 60 (2012) 6555–6561.
[8.57] E. Irissou, J.G. Legoux, B. Arsenault, C. Moreau, Investigation of Al-Al2O3 cold spray coating formation and properties, J. Therm. Spray Technol. 16 (2007) 661–668.
[8.58] S. Dosta, M. Couto, J.M. Guilemany, Cold spray deposition of a WC-25Co cermet onto Al7075-T6 and carbon steel substrates, Acta Mater. 61 (2013) 643–652.
[8.59] C.J. Lee, J.C. Huang, P.J. Hsieh, Mg based nano-composites fabricated by friction stir processing, Scr. Mater. 54 (2006) 1415–1420.
[8.60] A. Toumpis, A. Galloway, S. Cater, N. McPherson, Development of a process envelope for friction stir welding of DH36 steel - A step change, Mater. Des. 62 (2014) 64–75.
[8.61] S.A. Alidokht, P. Manimunda, P. Vo, S. Yue, R.R. Chromik, Cold spray

deposition of a Ni-WC composite coating and its dry sliding wear behavior, Surf. Coatings Technol. 308 (2016) 424–434.
[8.62] A. Slipenyuk, V. Kuprin, Y. Milman, J.E. Spowart, D.B. Miracle, The effect of matrix to reinforcement particle size ratio (PSR) on the microstructure and mechanical properties of a P/M processed AlCuMn/SiCp MMC, Mater. Sci. Eng. A. 381 (2004) 165–170.
[8.63] Q. Fang, P. Sidky, M. Hocking, Erosive wear behaviour of aluminium based composites, Mater. Des. 18 (1997) 389–393.
[8.64] M.K. Surappa, Aluminium matrix composites: Challenges and opportunities, Sadhana. 28 (2003) 319–334.
[8.65] J.M. Shockley, S. Descartes, P. Vo, E. Irissou, R.R. Chromik, The influence of Al2O3 particle morphology on the coating formation and dry sliding wear behavior of cold sprayed Al–Al2O3 composites, Surf. Coatings Technol. 270 (2015) 324–333.
[8.66] X.T. Luo, G.J. Yang, C.J. Li, Multiple strengthening mechanisms of cold-sprayed cBNp/NiCrAl composite coating, Surf. Coatings Technol. 205 (2011) 4808–4813.
[8.67] A.M. Redsten, E.M. Klier, A.M. Brown, D.C. Dunand, Mechanical properties and microstructure of cast oxide-dispersion-strengthened aluminum, Mater. Sci. Eng. A. 201 (1995) 88–102.
[8.68] M. Kouzeli, A. Mortensen, Size dependent strengthening in particle reinforced aluminium, Acta Mater. 50 (2002) 39–51.
[8.69] A. Chabok, K. Dehghani, Formation of nanograin in IF steels by friction stir processing, Mater. Sci. Eng. A. 528 (2010) 309–313.
[8.70] B.M. Darras, M.K. Khraisheh, F.K. Abu-Farha, M.A. Omar, Friction stir processing of commercial AZ31 magnesium alloy, J. Mater. Process. Technol. 191 (2007) 77–81.
[8.71] ASTM International, ASTM E112-13: Standard test methods for determining average grain size, ASTM Int. (2013) 1–28.
[8.72] D. Yadav, R. Bauri, Effect of friction stir processing on microstructure and mechanical properties of aluminium, Mater. Sci. Eng. A. 539 (2012) 85–92.
[8.73] C.I. Chang, X.H. Du, J.C. Huang, Achieving ultrafine grain size in Mg-Al-Zn alloy by friction stir processing, Scr. Mater. 57 (2007) 209–212.
[8.74] W.D.J. Callister, Fundamentals of Materials Science and Engineering, 2001.
[8.75] L. Qian, M. Li, Z. Zhou, H. Yang, X. Shi, Comparison of nano-indentation hardness to microhardness, Surf. Coatings Technol. 195 (2005) 264–271.
[8.76] J. Swadener, E.P. George, G.M. Pharr, The correlation of the indentation size effect measured with indenters of various shapes, J. Mech. Phys. Solids. 50 (2002) 681–694.
[8.77] Y. Huang, F. Zhang, K.C. Hwang, W.D. Nix, G.M. Pharr, G. Feng, A model of size effects in nano-indentation, J. Mech. Phys. Solids. 54 (2006) 1668–1686.
[8.78] I. Finnie, Erosion of surfaces by solid particles, Wear. 3 (1960) 87–103.
[8.79] P. Kulu, I. Hussainova, R. Veinthal, Solid particle erosion of thermal sprayed coatings, Wear. 258 (2005) 488–496.
[8.80] A. Neville, F. Reza, S. Chiovelli, T. Revega, Erosion-corrosion behaviour of WC-based MMCs in liquid-solid slurries, Wear. 259 (2005) 181–195.
[8.81] International ASTM Standard, ASTM G102 - 89 Standard Practice for Calculation of Corrosion Rates and Related Information from Electrochemical Measurements, 2015.
[8.82] International ASTM Standard, ASTM G46 - 94 (2013): Standard Guide for Examination and Evaluation of Pitting Corrosion, 2017.
[8.83] V.A.D. Souza, A. Neville, Linking electrochemical corrosion behaviour and

corrosion mechanisms of thermal spray cermet coatings (WC-CrNi and WC/CrC-CoCr), Mater. Sci. Eng. A. 352 (2003) 202–211.
[8.84] J.F. Flores, A. Neville, N. Kapur, A. Gnanavelu, Erosion-corrosion degradation mechanisms of Fe-Cr-C and WC-Fe-Cr-C PTA overlays in concentrated slurries, Wear. 267 (2009) 1811–1820.
[8.85] D. Aquaro, E. Fontani, Erosion of ductile and brittle materials, Meccanica. 36 (2001) 651–661.
[8.86] A. V. Levy, The platelet mechanism of erosion of ductile metals, Wear. 108 (1986) 1–21.
[8.87] A. V. Levy, P. Chik, The effects of erodent composition and shape on the erosion of steel, Wear. 89 (1983) 151–162.
[8.88] L. Thakur, N. Arora, R. Jayaganthan, R. Sood, An investigation on erosion behavior of HVOF sprayed WC-CoCr coatings, Appl. Surf. Sci. 258 (2011) 1225–1234.

Chapter 9 Conclusions and Proposed Future Work

9.1 Concluding Remarks

This thesis has reported on the development of an innovative surface engineering technology (SprayStir) to deposit an erosion resistant coating by cold spray (CS) and subsequently embed and redistribute the reinforcements by friction stir processing (FSP). Based on the findings from the research completed to date, SprayStir has been shown to successfully embed and distribute reinforcing particles within the matrix of aluminium and steel alloys. The aim of this new process was to enhance the erosion performance of the as-received substrate alloy.

The preliminary investigation presented in Chapter 6 highlighted the ability of FSP to embed and redistribute the CS deposited reinforcements within the aluminium matrix and hence remove the coating-to-substrate interface. Moreover, the incorporation of 5 mm probe in the pcBN tool adversely affected the distribution of carbides by relocating the reinforcements to the root of the stir zone. The AA2024-T3 alloy measured an average hardness increase of approximately 43% in the sprayed and stirred condition and hence provided proof of concept for combined CS and FSP. The microhardness results confirmed that hardness of the 6000-grade alloys reduced following the application of FSP. Based on the findings from this preliminary study, co-deposition was employed in subsequent chapters to manufacture coatings comprising reinforcing particles and a ductile binder alloy.

Thereafter, MMC coatings reinforced with WC-CoCr, Cr_3C_2-NiCr or Al_2O_3 particles were successfully co-deposited on AA5083 aluminium and subsequently FSPed. By co-depositing reinforcing particles with the comparably ductile AA5083 binder, the quantity of cermet and oxide particles deposited on the substrate was greater than by deposition of the reinforcement alone (Chapter 6). The application of FSP resulted in refinement of the deposited reinforcements and dispersal of the WC-CoCr agglomerates previously observed in the as-deposited coating. The reduction in interparticle spacing, post-FSP, was quantified and confirmed that the WC-CoCr reinforced MMC experienced a reduction of approximately 65% in contrast to the as-deposited coating. Consequently, the hardness of the SprayStirred WC-CoCr MMC, was approximately 120% greater than the as-deposited coating.

Volumetric analysis of the wear scars on the as-deposited and SprayStirred AA5083 based MMCs demonstrated the improvements to the erosion performance post-FSP. The Al_2O_3 reinforced specimens exhibited the greatest improvement in

erosion performance following FSP with the volume loss decreasing by approximately 40%. Despite this, SprayStirred WC-CoCr recorded the lowest volume loss of all the examined MMCs.

The wear mechanisms operating on the surface of the CS deposited and SprayStirred AA5083 based MMCs were evaluated through examination of the wear scar. The findings highlighted damage to the softer matrix alloy (AA5083) in the form of ploughing which subsequently exposes carbide/oxide particles to the impinging slurry. The SprayStirred surfaces presented a reduction in the interparticle spacing, hence less of the matrix alloy was exposed to the impinging slurry. The superior erosion performance was, therefore, attributed to the uniform distribution of micro and sub-micron reinforcing particles.

For the final phase of the investigation, the co-deposition method developed on AA5083 (Chapter 7) was applied to a steel substrate (AISI 316). WC-CoCr and Al_2O_3 reinforcements were successfully co-deposited with AISI 316 binder particles to produce particle reinforced MMC coatings. The coatings were subsequently modified using FSP to refine and redistribute the reinforcing particles. The average hardness of the SprayStirred WC-CoCr MMC was 50% greater than the CS coating and a 500% greater than the as-received AISI 316. This increase was achieved through dispersion strengthening imparted into the matrix by the nano and micro scale carbide reinforcements. Furthermore, nanoindentation recorded a significant reduction in the range of the measured hardness values in the SprayStirred MMC. This homogenising effect was exhibited in both the WC-CoCr and Al_2O_3 reinforced MMCs. The grain refinement within the stir zone of unreinforced AISI 316 generated only a minor increase in hardness when compared with the as-received AISI 316; hence confirming that the increased hardness of the SprayStirred MMCs is attributable to the reinforcements present within the matrix.

FSP resulted in the dispersion of the CS co-deposited WC-CoCr agglomerates and refinement of the Al_2O_3 particles. Moreover, examination of optical and scanning electron micrographs revealed a homogeneous distribution of reinforcements on the top surface of the stir zone. The interparticle spacing measurements demonstrated a 91% and 88% reduction in the spacing of the WC-CoCr and Al_2O_3 reinforced MMCs post-FSP. In both cases, FSP successfully refined the as-deposited particles and distributed them throughout the MMC.

The SprayStirred WC-CoCr reinforced MMC demonstrated an 83% decrease in volume loss over the as-received AISI 316 under 30° impingement and a 67%

reduction in volume loss over the as-deposited CS coating (no FSP). The improved erosion performance was directly related to the reduction in interparticle spacing and matrix hardening through dispersion strengthening. In comparison, the HVOF deposited WC-CoCr coating (evaluated in Chapter 5) reduced the volume loss of the EN:10025 steel by 75% and 90% for 90° and 30° impingement respectively. Although the results are not directly comparable given the differences in the grade of substrate alloy and slurry erosion test conditions, they do indicate that SprayStir provides a similar level of erosion resistance to that of an existing state-of-the-art surface engineering technology.

At 90°, erosion was dominated by the removal of weakened material on the periphery of impact craters. The presence of the carbide/oxide reinforcements reduced the depth of the craters owing to their increased hardness, while the small size of the particles prevented them from being easily dislodged from the matrix. At 30°, the refined reinforcements limited the depth of the surface damage by imparting dispersion strengthening into the MMC. Additionally, the homogeneous distribution of carbide/oxides reduced the surface area of unreinforced AISI 316 exposed to the slurry.

9.2 Recommendations for Future Work

The scope of work presented herein documents the successful development and application of SprayStir to several CS coating and substrate combinations. In this study, WC-CoCr reinforced MMCs exhibited superior erosion performance when exposed to the impinging slurry in the SprayStirred condition. However, assessment of a broader range of reinforcement materials would likely be of interest to the surface engineering community.

Considering that the current study does not incorporate any mechanical testing, a future study could consist of a comprehensive evaluation of the mechanical properties (tensile strength, fatigue and residual stress) of SprayStirred MMCs; possibly including a comparison with CS coatings (no FSP) and an existing state-of the-art surface engineering process such as HVOF.

This study has identified the strong correlation with FSP parameters (including FSP tool geometry) and the resulting distribution of reinforcements within the stir zone. Therefore, it would also be of interest to examine a wider range of FSP parameters (plunge depth, rotational and traverse speeds) and tool geometries, to assess their effect on the distribution of reinforcements within the stir zone.

Appendix A: Research Output

Journal Articles

T. Peat, A.M. Galloway, A. Toumpis, D. Harvey, W.H. Yang, Performance evaluation of HVOF deposited cermet coatings under dry and slurry erosion, Surf. Coatings Technol. 300 (2016) 118–127. (Impact Factor: 2.1)

T. Peat, A.M. Galloway, A. Toumpis, D. Harvey, Evaluation of the synergistic erosion-corrosion behaviour of HVOF thermal spray coatings, Surf. Coatings Technol. 299 (2016) 37–48. (Impact Factor: 2.1)

T. Peat, A.M. Galloway, A. Toumpis, P. McNutt, N. Iqbal, The erosion performance of particle reinforced metal matrix composite coatings produced by co-deposition cold gas dynamic spraying, Appl. Surf. Sci. (2016) 1623–1634. (Impact Factor: 3.2)

T. Peat, A.M. Galloway, A. Toumpis, P. McNutt, N. Iqbal, The erosion performance of cold spray deposited metal matrix composite coatings with subsequent friction stir processing, Appl. Surf. Sci. (2016) 1635–1648. (Impact Factor: 3.2)

T. Peat, A.M. Galloway, A. Toumpis, R. Steel, W. Zhu, N. Iqbal, Enhanced erosion performance of cold spray co-deposited AISI316 MMCs modified by friction stir processing, Mater. Des. 120 (2017) 22–35. (Impact Factor: 4.0)

Conference Proceedings

T. Peat, A.M. Galloway, T. Marrocco, N. Iqbal, Microstructural Evaluation of Cold Spray Deposited WC with Subsequent Friction Stir Processing, Frict. Stir Weld. Process. VIII. (2015).

T. Peat, A.M. Galloway, A. Toumpis, P. McNutt, N. Iqbal, Cold gas dynamic spraying of metal matrix composite coatings with subsequent friction stir processing, in: 11th Int. Symp. Frict. Stir Weld. (2016).